

Iowa State University

From the Selected Works of Jeramy C. Ashlock

June, 2015

Low-Cost Rural Surface Alternatives: Demonstration Project

Cheng Li, *Iowa State University*

Jeramy C Ashlock, *Iowa State University*

David White, *Iowa State University*

Pavana Vennapusa, *Iowa State University*



Available at: https://works.bepress.com/jeramy_ashlock/13/

Low-Cost Rural Surface Alternatives: Demonstration Project

**Final Report
June 2015**



IOWA STATE UNIVERSITY
Institute for Transportation

Sponsored by
Iowa Highway Research Board
(IHRB Project TR-664)
Iowa Department of Transportation
(InTrans Project 13-479)

About the Institute for Transportation

The mission of the Institute for Transportation (InTrans) at Iowa State University is to develop and implement innovative methods, materials, and technologies for improving transportation efficiency, safety, reliability, and sustainability while improving the learning environment of students, faculty, and staff in transportation-related fields.

Disclaimer Notice

The contents of this report reflect the views of the authors, who are responsible for the facts and the accuracy of the information presented herein. The opinions, findings and conclusions expressed in this publication are those of the authors and not necessarily those of the sponsors.

The sponsors assume no liability for the contents or use of the information contained in this document. This report does not constitute a standard, specification, or regulation.

The sponsors do not endorse products or manufacturers. Trademarks or manufacturers' names appear in this report only because they are considered essential to the objective of the document.

Non-Discrimination Statement

Iowa State University does not discriminate on the basis of race, color, age, ethnicity, religion, national origin, pregnancy, sexual orientation, gender identity, genetic information, sex, marital status, disability, or status as a U.S. veteran. Inquiries regarding non-discrimination policies may be directed to Office of Equal Opportunity, Title IX/ADA Coordinator, and Affirmative Action Officer, 3350 Beardshear Hall, Ames, Iowa 50011, 515-294-7612, email eooffice@iastate.edu.

Iowa Department of Transportation Statements

Federal and state laws prohibit employment and/or public accommodation discrimination on the basis of age, color, creed, disability, gender identity, national origin, pregnancy, race, religion, sex, sexual orientation or veteran's status. If you believe you have been discriminated against, please contact the Iowa Civil Rights Commission at 800-457-4416 or the Iowa Department of Transportation affirmative action officer. If you need accommodations because of a disability to access the Iowa Department of Transportation's services, contact the agency's affirmative action officer at 800-262-0003.

The preparation of this report was financed in part through funds provided by the Iowa Department of Transportation through its "Second Revised Agreement for the Management of Research Conducted by Iowa State University for the Iowa Department of Transportation" and its amendments.

The opinions, findings, and conclusions expressed in this publication are those of the authors and not necessarily those of the Iowa Department of Transportation.

Technical Report Documentation Page

1. Report No. IHRB Project TR-664	2. Government Accession No. 	3. Recipient's Catalog No. 	
4. Title and Subtitle Low-Cost Rural Surface Alternatives: Demonstration Project		5. Report Date June 2015	
		6. Performing Organization Code 	
7. Author(s) Cheng Li, Jeramy Ashlock, David White, and Pavana Vennapusa		8. Performing Organization Report No. InTrans Project 13-479	
9. Performing Organization Name and Address Institute for Transportation Iowa State University 2711 South Loop Drive, Suite 4700 Ames, IA 50010-8664		10. Work Unit No. (TRAIS) 	
		11. Contract or Grant No. 	
12. Sponsoring Organization Name and Address Iowa Highway Research Board Iowa Department of Transportation 800 Lincoln Way Ames, IA 50010		13. Type of Report and Period Covered Final Report	
		14. Sponsoring Agency Code IHRB Project TR-664	
15. Supplementary Notes Visit www.intrans.iastate.edu for color pdfs of this and other research reports.			
16. Abstract <p>The goals of this project were to implement several stabilization methods for preventing or mitigating freeze-thaw damage to granular surfaced roads and identify the most effective and economical methods for the soil and climate conditions of Iowa. Several methods and technologies identified as potentially suitable for Iowa were selected from an extensive analysis of existing literature provided with Iowa Highway Research Board (IHRB) Project TR-632.</p> <p>Using the selected methods, demonstration sections were constructed in Hamilton County on a heavily traveled two-mile section of granular surfaced road that required frequent maintenance during previous thawing periods. Construction procedures and costs of the demonstration sections were documented, and subsequent maintenance requirements were tabulated through two seasonal freeze-thaw periods.</p> <p>Extensive laboratory and field tests were performed prior to construction, as well as before and after the two seasonal freeze-thaw periods, to monitor the performance of the demonstration sections. A weather station was installed at the project site and temperature sensors were embedded in the subgrade to monitor ground temperatures up to a depth of 5 ft and determine the duration and depths of ground freezing and thawing.</p> <p>An economic analysis was performed using the documented construction and maintenance costs, and the estimated cumulative costs per square yard were projected over a 20-year timeframe to determine break-even periods relative to the cost of continuing current maintenance practices.</p> <p>Overall, the sections with biaxial geogrid or macadam base courses had the best observed freeze-thaw performance in this study. These two stabilization methods have larger initial costs and longer break-even periods than aggregate columns, but counties should also weigh the benefits of improved ride quality and savings that these solutions can provide as excellent foundations for future paving or surface upgrades.</p>			
17. Key Words freeze-thaw—granular surfaced roads—low-volume roads—mechanistic-based performance—soil stabilization—thaw weakening		18. Distribution Statement No restrictions.	
19. Security Classification (of this report) Unclassified.	20. Security Classification (of this page) Unclassified.	21. No. of Pages 240	22. Price NA

LOW-COST RURAL SURFACE ALTERNATIVES: DEMONSTRATION PROJECT

**Final Report
June 2015**

Principal Investigator

Jeremy C. Ashlock, Assistant Professor of Geotechnical Engineering
Civil, Construction, and Environmental Engineering, Iowa State University

Co-Principal Investigators

David J. White, R. L. Handy Professor and Director
Center for Earthworks Engineering Research, Iowa State University

Pavana Vennapusa, Research Assistant Professor and Assistant Director
Center for Earthworks Engineering Research, Iowa State University

Research Assistant

Cheng Li

Authors

Cheng Li, Jeremy Ashlock, David White, and Pavana Vennapusa

Sponsored by
the Iowa Department of Transportation and
the Iowa Highway Research Board
(IHRB Project TR-664)

Preparation of this report was financed in part
through funds provided by the Iowa Department of Transportation
through its Research Management Agreement with the
Institute for Transportation
(InTrans Project 13-479)

A report from
Institute for Transportation
Iowa State University
2711 South Loop Drive, Suite 4700
Ames, IA 50010-8664
Phone: 515-294-8103 / Fax: 515-294-0467
www.intrans.iastate.edu

TABLE OF CONTENTS

ACKNOWLEDGMENTS	xv
EXECUTIVE SUMMARY	xvii
CHAPTER 1. INTRODUCTION	1
1.1 Problem Statement	1
1.2 Goal and Objectives of the Research	1
1.3 Site Selection	2
1.4 Significance of the Research.....	2
1.5 Organization of the Report.....	2
CHAPTER 2. BACKGROUND	4
2.1 Freeze-Thaw Damage of Unpaved Roads	4
2.2 Macadam Stone Base Course.....	5
2.3 Chemical Stabilization	8
2.4 Geotextiles and Geogrids.....	9
2.5 Geocomposite Drainage Layers	9
2.6 MASW and FWD Tests	10
CHAPTER 3. METHODS	13
3.1 Laboratory Tests	13
3.2 Field Tests	25
CHAPTER 4. MATERIALS	36
4.1 Geomaterials	36
4.2 Chemical Stabilizers	46
4.3 Geosynthetics.....	52
CHAPTER 5. CONSTRUCTION METHODS	55
5.1 Macadam Stone Base: Sections 1 through 8.....	55
5.2 Aggregate Column Drains: Sections 12 and 13.....	58
5.3 Chemical Stabilization: Sections 15 through 17.....	59
5.4 Geosynthetic Interlayers: Sections 18, 19A, and 19B	61
5.5 QC/QA Methods	63
CHAPTER 6. RESULTS AND DISCUSSION.....	65
6.1 Pre-Construction Conditions of Existing Roadway	65
6.2 Laboratory Mix Design for Chemical Stabilization Sections (Sections 16 and 17)....	73
6.3 Laboratory Permeameter Tests for Geocomposite Drain Section (Section 18).....	83
6.4 Performance of As-Constructed Demonstration Sections	84
6.5 Evaluation of Post-Thawing Durability	106
6.6 Construction Costs and Economic Analysis	157
CHAPTER 7. CONCLUSIONS AND RECOMMENDATIONS	165
7.1 Construction Processes and Requirements	165
7.2 Laboratory Test Results	165

7.3 Weather and Ground Temperature Profile Results	166
7.4 Field Test Results.....	166
7.5 Economic Analysis Results.....	167
7.6 Recommendations.....	168
REFERENCES	169
APPENDIX A: RECEIPTS FOR CHEMICAL STABILIZERS AND PRODUCT DATASHEETS FOR GEOSYNTHETICS	175
APPENDIX B: HORIZONTAL PERMEAMETER TEST (HPT) SPECIMEN PREPARATION PROCEDURE	183
APPENDIX C: SURVEY PHOTOS OF VAIL AVENUE DEMONSTRATION SECTIONS	187

LIST OF FIGURES

Figure 1. Schematic of near field and far field characteristics	11
Figure 2. (a) Sieve analysis and (b) hydrometer test devices used in this study.....	14
Figure 3. Liquid limit test device used in this study	15
Figure 4. Micro-Deval testing machine used in this study	16
Figure 5. (a) Hobart mixer and (b) automated mechanical rammer used in this study.....	17
Figure 6. Unconfined compressive strength test on a fly ash-treated soil specimen	18
Figure 7. CBR tests conducted on (a) OMC and (b) saturated specimens	19
Figure 8. Vail Avenue subgrade specimens (a) before, (b) during, and (c) after vacuum saturation (compacted moisture contents are indicated on specimens)	21
Figure 9. Rigid-wall compaction mold permeameter test device used in this study	23
Figure 10. (a) Photo and (b) schematic of the large-scale HPT device used in this study	24
Figure 11. Dynamic cone penetrometer (DCP) test.....	25
Figure 12. Example of DCP depth profiles: (a) cumulative blows and (b) DCP-CBR	26
Figure 13. Kuab falling weight deflectometer setup.....	27
Figure 14. MASW test setup with landstreamer	30
Figure 15. Example of experimental dispersion image from MASW test on granular surfaced road	31
Figure 16. Example of experimental dispersion curve (target) and theoretical dispersion curve from inversion procedure	31
Figure 17. Air permeameter test	33
Figure 18. (a) Weather station, (b) thermocouples and data loggers, and (c) layout of thermocouples	34
Figure 19. Example of estimating field freeze-thaw cycles from ground temperature data	35
Figure 20. (a) Air-dried existing surface aggregate, (b) 1 in. road stone, (c) 0.75 in. choke stone, and (d) clean aggregate-column fill	38
Figure 21. Particle size distribution curves of the four aggregate materials.....	39
Figure 22. Proctor compaction curve for existing surface aggregate	39
Figure 23. Samples of road stone (a) before and (b) after Micro-Deval tests, and choke stone (c) before and (d) after Micro-Deval tests.....	41
Figure 24. Air-dried samples of (a) dirty, (b) clean, and (c) RPCC macadam materials	42
Figure 25. Particle size distribution curves of the three macadam types.....	42
Figure 26. Dirty, clean, and RPCC macadam specimens after L.A. abrasion tests.....	44
Figure 27. (a) Existing subgrade with 9.0% moisture content and (b) SG+AGG mixture with 1.0% moisture content.....	44
Figure 28. Particle size distribution curves of existing subgrade, surface aggregate, and subgrade-aggregate mixture	45
Figure 29. Proctor compaction curves for subgrade and subgrade-aggregate mixture.....	46
Figure 30. Fly ash set-time test.....	47
Figure 31. Set time of fly ash used for construction of Section 16.....	48
Figure 32. XRD results for fly ash of Section 16	50
Figure 33. XRD results for bentonite of Section 15	51
Figure 34. Macdrain W1051 geocomposite material: (a) top view and (b) side view.....	53
Figure 35. Tensar Roadrain RD-5 geocomposite: (a) top view and (b) side view	54

Figure 36. Plan view of demonstration sections on Vail Avenue in Ellsworth, Iowa	56
Figure 37. Construction procedures and equipment for Sections 1-8 with macadam base courses: (a) placing macadam with Jersey spreader, (b) non-woven geotextile interlayer, (c) spreading choke stone with Jersey spreader, and (d) shaping with motor grader	57
Figure 38. Cross-sectional profiles with nominal thicknesses for Sections 1A through 9	58
Figure 39. Construction procedures and equipment for aggregate columns in Sections 12 and 13: (a) drilling columns, (b) placing geocomposite lining, (c) filling with clean aggregate, and (d) column layout pattern	59
Figure 40. Construction procedures and equipment for chemically stabilized Sections 15, 16, and 17: (a) powder truck for spreading bentonite, fly ash, and cement, (b) full depth reclaimer connected to water truck milling chemical stabilizers to the specified depth and water content, (c) vibratory pad-foot roller following the full depth reclaimer, and (d) 1 in.-thick road-stone wearing surface	60
Figure 41. Typical surface course cross-sectional profiles of chemically-stabilized Sections 15, 16, and 17	61
Figure 42. Construction procedures and equipment for geosynthetically stabilized sections: (a) removal of existing surface, (b) geocomposite in Section 18, (c) replacement of surface course by earth mover for geocomposite Section 18, (d) BX geogrid in Section 19B on left with added non-woven geotextile in Section 19A on right, (e) replacement of surface course by motor grader for Sections 19A and 19B, and (f) compaction by rubber-tire compactor	62
Figure 43. Typical surface course cross-sectional profiles of geosynthetically stabilized Sections 18, 19A, and 19B	63
Figure 44. Pre-construction DCP test results for the three representative road sections (Sections 10, 18, and 19): (a) cumulative blows, (b) DCPI, and (c) DCP-CBR versus depth	66
Figure 45. Pre-construction FWD and DCP test results of the three representative sections: (a) $E_{FWD-Composite}$, (b) $E_{FWD-AGG}$ and $DCP-CBR_{AGG}$ of surface aggregate, and (c) E_{FWD-SG} and $DCP-CBR_{SG}$ of subgrade	68
Figure 46. Summary boxplots of pre-construction FWD test results for the three representative sections: (a) $E_{FWD-Composite}$, (b) $E_{FWD-AGG}$, and (c) E_{FWD-SG}	69
Figure 47. Uncorrected stress on piston versus penetration depth from CBR tests on surface aggregate and subgrade	70
Figure 48. (a) Standard Proctor compaction and (b) UCS test results for the as-compacted and vacuum-saturated subgrade	72
Figure 49. Uncorrected stress on piston versus penetration depth for CBR tests on untreated, fly ash-stabilized, and cement-stabilized subgrade	73
Figure 50. Moisture-density-UCS relationships of as-compacted and saturated subgrade specimens: (a and b) untreated, (c and d) fly ash-stabilized, and (e and f) cement-stabilized (optimum moisture content $w_{opt(UCS)}$ for peak saturated UCS shown)	75
Figure 51. Uncorrected stress on Piston versus penetration depth for CBR tests on untreated and fly ash-stabilized surface aggregate specimens	76

Figure 52. Moisture-density-UCS relationships of as-compacted and saturated surface aggregate: (a and b) fly ash-stabilized and (c and d) cement-stabilized	78
Figure 53. Moisture-density-UCS relationships of as-compacted and saturated SG+AGG mixtures: (a and b) untreated, (c and d) fly ash-stabilized, and (e and f) cement-stabilized	81
Figure 54. Moisture-density-UCS relationships of as-compacted and saturated subgrade and SG+AGG mixtures: (a and b) untreated, (c and d) fly ash-stabilized, and (e and f) cement-stabilized	82
Figure 55. Large-scale horizontal permeameter test (HPT) results of existing surface aggregate and surface aggregate with embedded geocomposite drainage layer	84
Figure 56. DCP test results for as-constructed Sections 1 through 5: (a) cumulative blows, (b) DCPI, and (c) DCP-CBR versus depth	86
Figure 57. DCP test results for as-constructed Sections 6 through 9: (a) cumulative blows, (b) DCPI, and (c) DCP-CBR versus depth	87
Figure 58. 2013 FWD and DCP test results for as-constructed first-mile Sections 1–9: (a) $E_{FWD-Composite}$, (b) $E_{FWD-AGG}$ and $DCP-CBR_{AGG}$ of combined surface course, and (c) E_{FWD-SG} and $DCP-CBR_{SG}$ of subgrade	89
Figure 59. Comparison of 2013 and 2014 FWD test results for first-mile Sections 1A–9: (a) $E_{FWD-Composite}$, (b) $E_{FWD-AGG}$, and (c) E_{FWD-SG}	91
Figure 60. Summary boxplots of 2013 and 2014 FWD test results for first-mile sections: (a) $E_{FWD-Composite}$, (b) $E_{FWD-AGG}$, and (c) E_{FWD-SG}	92
Figure 61. 2014 FWD test results for second-mile Sections 10–20: (a) $E_{FWD-Composite}$, (b) $E_{FWD-AGG}$, and (c) E_{FWD-SG}	93
Figure 62. Summary boxplots of 2014 FWD tests on all demonstration sections: (a) $E_{FWD-Composite}$, (b) $E_{FWD-AGG}$, and (c) E_{FWD-SG}	95
Figure 63. FWD and MASW back-calculated moduli for first-mile Sections 1A–9: (a) surface course modulus and (b) subgrade modulus	97
Figure 64. FWD and MASW back-calculated moduli for second-mile Sections 10–20: (a) surface course modulus, (b) subgrade modulus	98
Figure 65. Summary boxplots of back-calculated FWD and MASW moduli: (a) first mile Sections 1A–9, (b) second mile Sections 10–20	99
Figure 66. Statistical correlations between mean MASW and FWD back-calculated moduli: (a) for surface course materials, (b) for subgrade	100
Figure 67. Back-calculated moduli of surface course and subgrade from MASW tests during curing of chemically stabilized sections: (a and b) fly ash Section 16 and (c and d) cement Section 17	101
Figure 68. Standard Proctor test results for subgrade, surface aggregate, and lab- and field-compacted subgrade-surface aggregate mixture: (a) fly ash-stabilized and (b) cement-stabilized	102
Figure 69. UCS test results of field-compacted (a) fly ash-stabilized and (b) cement-stabilized SG+AGG specimens at 7 days curing	103
Figure 70. Comparison of UCS and MASW results for (a) fly ash-stabilized Section 16 and (b) cement-stabilized Section 17	103
Figure 71. APT locations (indicated by black dots) and cross-section profiles of the geocomposite drain Section 18 and control Section 17	104

Figure 72. Saturated hydraulic conductivity versus depth for aggregate layers of geocomposite drain Section 18 and control Section 17	105
Figure 73. Mass changes of (a) fly ash-stabilized and (b) cement-stabilized aggregate-subgrade mixture specimens during freeze-thaw cycling	107
Figure 74. Mass changes of (a) fly ash-stabilized and (b) cement-stabilized aggregate-subgrade mixture specimens during wet-dry cycling.....	108
Figure 75. Photos of fly ash-stabilized specimens after freeze-thaw cycles.....	109
Figure 76. Photos of cement-stabilized specimens after freeze-thaw cycles.....	110
Figure 77. Photos of fly ash-stabilized specimens after wet-dry cycles	113
Figure 78. Photos of cement-stabilized specimens after wet-dry cycles	115
Figure 79. Air and ground temperature data during 2013-2014 seasonal freeze-thaw period.....	119
Figure 80. Ground temperature profiles at three different dates during 2013-2014 seasonal freeze-thaw period	120
Figure 81. 2013–2014 ground freezing-thawing period of the project site	121
Figure 82. Precipitation rates during 2014 thawing period measured every 15 minutes at the project site	122
Figure 83. 2014 Post-thawing DCP test results versus depth for Sections 1–6: (a) cumulative blows, (b) DCPI, and (c) DCP-CBR.....	124
Figure 84. 2014 Post-thawing DCP test results versus depth for Sections 7–9: (a) cumulative blows, (b) DCPI, and (c) DCP-CBR.....	125
Figure 85. 2014 Post-thawing DCP test results versus depth for Sections 10–12: (a) cumulative blows, (b) DCPI, and (c) DCP-CBR.....	126
Figure 86. 2014 Post-thawing DCP test results versus depth for Sections 13–18: (a) cumulative blows, (b) DCPI, and (c) DCP-CBR.....	127
Figure 87. 2014 Post-thawing DCP test results versus depth for Sections 19A–20: (a) cumulative blows, (b) DCPI, and (c) DCP-CBR.....	128
Figure 88. 2014 Post-thawing FWD and DCP results for Sections 1–9: (a) $E_{FWD-Composite}$, (b) $E_{FWD-AGG}$ and $DCP-CBR_{AGG}$ of combined surface course, and (c) E_{FWD-SG} and $DCP-CBR_{SG}$ of subgrade.....	132
Figure 89. 2014 Post-thawing FWD and DCP results for Sections 10–20: (a) $E_{FWD-Composite}$, (b) $E_{FWD-AGG}$ and $DCP-CBR_{AGG}$ of surface course, and (c) E_{FWD-SG} and $DCP-CBR_{SG}$ of subgrade (Sections 15–18 not yet stabilized at time of tests)	133
Figure 90. Comparison of 2013 pre-freezing and 2014 post-thawing FWD test results for Sections 1A–9: (a) $E_{FWD-Composite}$, (b) $E_{FWD-AGG}$, and (c) E_{FWD-SG}	134
Figure 91. Summary boxplots of 2013 pre-freezing and 2014 post-thawing FWD test results for Sections 1A–9: (a) $E_{FWD-Composite}$, (b) $E_{FWD-AGG}$, and (c) E_{FWD-SG}	135
Figure 92. Survey photos of Vail Avenue demonstration sections (March 11, 2014).....	137
Figure 93. Air and ground temperature data during 2014-2015 seasonal freeze-thaw period.....	139
Figure 94. Ground temperature profiles at three different dates during 2014-2015 seasonal freeze-thaw period	140
Figure 95. 2014–2015 ground freezing-thawing period of the project site compared with the 2013-2014 period	141

Figure 96. Precipitation rates during 2015 thawing period measured every 15 minutes at the project site	142
Figure 97. Comparison of 2014 pre-freezing and 2015 post-thawing FWD tests on Sections 1A–9: (a) $E_{FWD-Composite}$, (b) $E_{FWD-AGG}$, and (c) E_{FWD-SG}	143
Figure 98. Comparison of 2014 pre-freezing and 2015 post-thawing FWD tests on Sections 10–20: (a) $E_{FWD-Composite}$, (b) $E_{FWD-AGG}$, and (c) E_{FWD-SG}	144
Figure 99. Summary boxplots of 2014 pre-freezing and 2015 post-thawing FWD tests on all sections: (a) $E_{FWD-Composite}$, (b) $E_{FWD-AGG}$, and (c) E_{FWD-SG}	145
Figure 100. Boxplots of surface course modulus of fly ash- and cement-stabilized sections from MASW and FWD tests during curing and after 2014-2015 seasonal freeze-thaw cycles	146
Figure 101. Surface conditions of dirty macadam plus chloride Section 2 during (a) freezing period (February 24, 2015) and (b) thawing period (March 10, 2015)	148
Figure 102. Surface condition of geocomposite drain Section 18 showing rutting (April 21, 2015).....	149
Figure 103. Surface condition of BX-geogrid+NW-geotextile Section 19A showing exposed geosynthetics (May 20, 2015).....	149
Figure 104. Surface conditions of dirty macadam, dirty macadam with bentonite, and calcium chloride Sections 1A, 1B, and 2 during 2015 thawing period (March 28, 2015)	150
Figure 105. Particle size distribution curves of surface aggregate from dirty macadam Section 1A and dirty macadam with bentonite Section 1B	151
Figure 106. Comparison of X-ray spectra normalized to (a) background and (b) Ca content for the different surface course materials (collected at 50x magnification of SEM scan area).....	153
Figure 107. SEM images (1500x magnification) of (a and b) dirty macadam, (c and d) dirty macadam with chloride, and (d and e) bentonite-treated surface course samples.....	155
Figure 108. SEM images (5000x magnification) of surface course samples from (a and b) fly ash and (c and d) cement-stabilized sections.....	156
Figure 109. Construction costs (\$/sq. yd.) of the Vail Avenue demonstration sections.....	157
Figure 110. Projected cumulative (construction + annual maintenance) costs for the (a) first mile and (b) second mile stabilization sections, compared to cumulative cost of continuing pre-2013 maintenance practices	163
Figure 111. Receipt for bentonite used on Sections 1B, 4, and 15	175
Figure 112. Receipt for class C fly ash used on Section 16.....	176
Figure 113. Receipt for type I/II cement used on Section 17	177
Figure 114. Product datasheet for NW-geotextile used on Sections 3, 4, 5, 8, and 19A.....	178
Figure 115. Product datasheet for BX-geogrid used on Sections 19A and 19B.....	179
Figure 116. Product datasheet for NW-geotextile used on Sections 3, 4, 5, 8, and 19A.....	180
Figure 117. Product datasheet for geocomposite used on Section 18.....	181
Figure 118. Product datasheet for geocomposite used on Section 12.....	182
Figure 119. HPT soil tank set up: (a) place fine screen and screen support on top of inlet and outlet, (b, c, d, and e) place three screens with different opening sizes next to the screen support, (e) place specimen material in soil tank.....	183

Figure 120. HPT specimen compaction: (a) compact specimen in several lifts, (b) scarify surface after each compaction lift, and (c) place geocomposite at middle of specimen and seal gaps between geocomposite and soil tank using closed-cell foam	184
Figure 121. HPT specimen sealing: (a) level the specimen surface, (b) pre-soak specimen, and (c) seal top surface with closed-cell foam	185
Figure 122. HPT specimen saturation and examination: (a) soak specimen using water supply placed on top of specimen, then vacuum saturate specimen, (b) examine specimen surface after test to check if water channeling occurred.....	186
Figure 123. Survey photos of Vail Avenue demonstration sections (March 8, 2014).....	187
Figure 124. Survey photos of Vail Avenue demonstration sections (March 20, 2014).....	190
Figure 125. Survey photos of Vail Avenue demonstration sections (April 21, 2014).....	193
Figure 126. Survey photos of Vail Avenue demonstration sections (May 8, 2014).....	196
Figure 127. Survey photos of Vail Avenue demonstration sections (June 6, 2014).....	199
Figure 128. Survey photos of Vail Avenue demonstration sections (July 3, 2014)	202
Figure 129. Survey photos of Vail Avenue demonstration sections (September 2, 2014).....	205
Figure 130. Survey photos of Vail Avenue demonstration sections (January 20, 2015).....	208
Figure 131. Survey photos of Vail Avenue demonstration sections (February 24, 2015).....	211
Figure 132. Survey photos of Vail Avenue demonstration sections (March 10, 2015).....	214
Figure 133. Survey photos of Vail Avenue demonstration sections (April 21, 2015).....	217
Figure 134. Survey photos of Vail Avenue demonstration sections (May 19, 2015).....	220

LIST OF TABLES

Table 1. Summary of previous field research projects involving macadam stone base layers	6
Table 2. Relative ratings of subbase and subgrade layers based on CBR values (SUDAS 2015)	19
Table 3. Frost susceptibility classification system (ASTM D 5918-13).....	20
Table 4. Configuration used for MASW tests	30
Table 5. Soil index properties of the nine geomaterials used in this project	37
Table 6. Initial gradations and masses of Micro-Deval test specimens	40
Table 7. Laboratory Micro-Deval abrasion test results for choke stone and road stone	40
Table 8. Initial gradations and masses of L.A. abrasion test specimens.....	43
Table 9. L.A. abrasion test results for the three macadam types	43
Table 10. Sources of chemical stabilizers used in this study	46
Table 11. Chemical composition of fly ash for Section 16 compared to typical Iowa self-cementing fly ash (Barnes 1997), 13 Iowa self-cementing fly ash samples from seven sources (White et al. 2005a), and ASTM C618 requirements for Class C fly ash	49
Table 12. Chemical composition of bentonite used for Sections 1B, 4, and 15	51
Table 13. D ₅₀ and 2 times D ₈₅ of existing surface aggregate and 1 in. road stone	52
Table 14. Summary of preconstruction DCP test results	67
Table 15. Summary of pre-construction FWD test results for three representative sections	68
Table 16. Laboratory CBR test results for as-compacted and soaked surface aggregate and subgrade.....	71
Table 17. Laboratory CBR test results for untreated and stabilized subgrade.....	74
Table 18. Laboratory CBR test results for untreated and stabilized surface aggregate	77
Table 19. Summary of laboratory mix design results for existing surface aggregate (AGG), subgrade (SG), and subgrade-surface aggregate (SG+AGG) mixture	80
Table 20. Rigid-wall compaction mold permeameter results for subgrade	83
Table 21. DCP test results of as-constructed first mile demonstration Sections 1–9.....	88
Table 22. Number of freeze-thaw or wet-dry cycles to failure for fly ash-and cement-stabilized specimens.....	106
Table 23. 2014 Post-thawing DCP test results of Vail Avenue demonstration sections	129
Table 24. Comparison between pre-freezing (as-constructed) and 2014 post-thawing average DCP test results for Sections 1–9	131
Table 25. Soil index properties of surface aggregate from dirty macadam Section 1A and dirty macadam with bentonite Section 1B	151
Table 26. Chemical composition of typical Iowa limestone and dolomite (Bergeson et al. 1995).....	154
Table 27. Breakdown of construction costs for the Vail Avenue demonstration sections (\$/sq. yd.)	158
Table 28. Unit costs for materials, labor and equipment	159
Table 29. Estimated annual maintenance costs for years prior to stabilization in 2013, and for stabilization demonstration sections in 2013-2015.....	161

ACKNOWLEDGMENTS

The authors would like to thank the Iowa Department of Transportation (DOT) and the Iowa Highway Research Board (IHRB) for sponsoring this project. The cooperation and assistance of the Hamilton County and Greene County secondary roads departments is greatly appreciated. The authors would like to acknowledge the support of Hamilton County Engineer Dan Waid for overseeing the construction and maintenance of the demonstration sections and providing construction and maintenance cost records. The assistance of Greene County Engineer Wade Weiss is also appreciated in providing equipment and personnel for installation of the aggregate columns.

EXECUTIVE SUMMARY

The goal of this project was to implement several stabilization methods for preventing or mitigating freeze-thaw damage to granular surfaced roads, and identify the most effective and economical methods for the soil and climate conditions of Iowa. Several methods and technologies identified as potentially suitable for Iowa were selected from an extensive analysis of existing literature provided in Iowa Highway Research Board (IHRB) Project TR-632. Using the selected methods, demonstration sections were constructed in Hamilton County on a heavily traveled two-mile section of granular surfaced road that required frequent maintenance during previous thawing periods.

Construction procedures and costs of the demonstration sections were documented and subsequent maintenance requirements were tabulated through two seasonal freeze-thaw periods. Extensive laboratory and field tests were performed prior to construction, as well as before and after the two seasonal freeze-thaw periods, to monitor the performance of the demonstration sections. A weather station was installed at the project site and temperature sensors were embedded in the subgrade to monitor ground temperatures up to a depth of 5 ft and determine the duration and depths of ground freezing and thawing. An economic analysis was performed using the documented construction and maintenance costs, and the estimated cumulative costs per square yard were projected over a 20-year timeframe to determine break-even periods relative to the cost of continuing current maintenance practices.

The post-thawing field tests showed that the composite moduli of the macadam sections were about five times higher than the control sections. However, the macadam sections with non-woven- (NW-) geotextile had lower moduli than the corresponding sections without the NW-geotextile. The chemically and geosynthetically stabilized sections also had significantly increased moduli. The moduli of the aggregate column and geocomposite sections were similar to the control sections. However, these two methods are aimed at improving freeze-thaw resilience by improving drainage, not by increasing stiffness. Based on survey photos taken on 11 different dates during the two freeze-thaw periods, most of the stabilization methods examined can minimize frost boils and potholes and improve the surface conditions of granular surfaced roads to varying degrees. Even the roadway surface treated with bentonite was much drier and tighter than the other sections during the thawing period. However, the sections with chloride surface treatments showed more ice lenses during freezing, and were more prone to potholes and washboarding during the thawing period. Additionally, the geocomposite drain section suffered significant rutting during the 2015 thawing period, which may require further study. The subgrade under the macadam sections also exhibited improved strength, stiffness, and frost-susceptibility ratings compared to the control and other demonstration sections.

Some recommendations for future research activities and implementation are provided below:

- Continue monitoring and comparing the long-term performance of the various demonstration sections to better assess the maintenance requirements, estimate service lifespans, and more clearly identify the most effective and economical solutions for preventing and mitigating seasonal freeze-thaw damage.

- Install additional strings of thermocouples and sensors to monitor the ground temperature profiles and moisture contents under the different stabilization sections.
- Study the physics and mechanisms involved to understand why the chloride surface treatment caused more ice lenses on the roadway surface during freezing and was more prone to potholes and washboarding during thawing.
- Evaluate the feasibility of using multi-channel analysis of surface waves (MASW) testing as a more economical alternative to falling weight deflectometer (FWD) testing for measuring and monitoring the stiffness of the different layers of granular surfaced road systems.

Counties could benefit by immediately implementing some of the research project findings. First, the aggregate columns were very inexpensive to install, and appeared to reduce the occurrence of frost-boils and related washboarding and ice lenses on the surface. Minor rutting was observed near the shoulders, which could be improved by installing more aggregate columns near the shoulders, as well as installing a denser grid of columns. The columns are believed to function primarily as drainage basins, so their effectiveness in any year may be a function of their depth, the depth of the water table, and the amount of seasonal precipitation. The aggregate columns had a break even period of 1 year (2 years with geocomposite linings), after which the cumulative construction and estimated maintenance costs would be less than continuation of existing maintenance practices.

After the aggregate columns, the biaxial (BX) geogrid sections had the next shortest break-even periods of 8 years without a geotextile layer, or 9 years with the geotextile, followed by cement (9 years), recycled Portland cement concrete (RPCC) macadam (10 years), bentonite stabilization and dirty macadam (11 years), dirty macadam with chloride, clean macadam, and geocomposite (12 years), and RPCC macadam with NW-geotextile (13 years). Due to higher construction costs, the clean and dirty macadam sections with bentonite and/or NW-geotextile would have very long break-even periods (>20 years). For the dirty and clean macadam sections with NW-geotextile, virgin aggregates were dumped to cover spots where the geotextile was exposed, which led to higher projected annual maintenance costs. The recorded maintenance cost of the fly ash section was greater than the previous maintenance practices, so no break-even period exists for this section.

Overall, the BX geogrid and macadam-based sections had the best observed freeze-thaw performance in this study. They have larger initial costs and longer break-even periods than the aggregate columns, but counties should also weigh the benefits of improved ride quality and savings that these solutions can provide as excellent foundations for future paving or surface upgrades.

The actual long-term performance of the various sections may be different from those predicted based upon the maintenance costs documented in this two-year project. Additional long-term monitoring is recommended to more accurately determine the life-cycle costs of each section and better identify the most economical and effective stabilization methods.

CHAPTER 1. INTRODUCTION

This chapter introduces the research problem related to freeze-thaw performance of granular surfaced roads and describes the research goals and objectives. The final section of this chapter describes the organization of the report.

1.1 Problem Statement

Granular surfaced roads in seasonally cold regions are frequently subjected to freeze-thaw cycles, which lead to damage such as frost heave, frost boils, thaw weakening, rutting, and potholes. The damage significantly increases maintenance costs, adversely affects public safety, and inconveniences both agricultural traffic and the traveling public. The most unfavorable scenarios usually occur during spring thaws, when granular surfaced roads are most vulnerable and also heavily used by agricultural traffic. Thawing water cannot drain efficiently and becomes trapped above the zone of frozen soil, causing the saturated unbound granular materials to lose strength, especially under heavy traffic loads.

Current maintenance practice typically involves covering the entire damaged road surface with virgin aggregate then blading without compaction, and lowering or cleaning drainage ditches. However, since virgin aggregate is becoming more scarce and continually increasing in price, this is not the most sustainable or economical solution. Additionally, current practice is focused on repairing freeze-thaw damage rather than minimizing or preventing its occurrence in the first place. Many studies have evaluated various methods to improve the freeze-thaw performance of granular surfaced roads such as chemical, mechanical, and biological stabilization, but most of these studies focused on only one or two technologies, without comprehensive long-term performance monitoring. To address the perceived deficiencies, White and Vennapusa (2013) reviewed more than 150 journal articles and research reports from the domestic and international literature. Based on their recommendation that “demonstration research projects be established to examine a range of construction methods and materials for treating granular surfaced roadways to mitigate frost-heave and thaw-weakening problems,” a field demonstration project was conducted in this study to compare the relative performance, durability, and costs of several stabilization technologies under the same set of geological, climate, and traffic conditions.

1.2 Goal and Objectives of the Research

The main goal of this project was to identify the most effective and economical stabilization methods for preventing or mitigating freeze-thaw damage on granular surfaced roads. The specific objectives of the research project were as follows:

- Construct demonstration test sections using several of the stabilization methods recommended in IHRB Project TR-632 (White and Vennapusa 2013)
- Perform comprehensive laboratory tests to compare the relative performance of the various stabilization methods

- Conduct comprehensive field tests to compare the relative performance of the demonstration sections before, during, and after seasonal freeze/thaw cycles
- Assess the construction costs, relative performance, maintenance costs, and long-term life-cycle costs of the different stabilization methods
- Identify the most effective and economical methods for minimizing or eliminating freeze-thaw issues before they occur
- Translate the research results into practice

1.3 Site Selection

A two-mile stretch of granular surfaced road (Vail Avenue between 310th and 330th Streets) was selected for the demonstration sections. This granular surfaced road is one of the most heavily used in Hamilton County, Iowa, requiring constant year-round maintenance with up to four grader passes per week during the 2013 thawing season. The Hamilton County Engineer reported that approximately 350 tons of virgin aggregate was dumped per mile in each year to repair the damage. The County Engineer also prefers to avoid reclaiming ditch material back into the roadway, because the ditch material typically contains a significant amount of fines washed from the adjacent agricultural fields. This section of roadway was chosen for the demonstration project because it experiences the most significant freeze-thaw damage in Hamilton County, and methods that prove effective for this stretch of road should therefore be effective for less damage-prone roads.

1.4 Significance of the Research

This research project aims to generate a better understanding of the relative effectiveness, durability, and life-cycle costs of a range of stabilization methods documented in IHRB TR-632. From this research, best practices for economical mitigation of freeze-thaw related damage to granular surfaced roads will be identified and recommended. The long-term benefits of this project will be to improve the quality, longevity, and state of good repair of granular surfaced roads, which constitute a vital component of Iowa's infrastructure. For the benefit of the public, the results of the research project can be easily implemented by the Iowa Department of Transportation (DOT) and local secondary roads departments.

1.5 Organization of the Report

Chapter 2 provides background information on previous studies, the stabilization technologies used in this study, and the multi-channel analysis of surface waves (MASW) and falling weight deflectometer (FWD) field test methods. Chapter 3 summarizes the laboratory and field test methods used to evaluate and compare the various stabilization methods. Chapter 4 provides details on the sources and properties of geomaterials, chemical stabilizers, and geosynthetics used in this project. Chapter 5 describes the timelines, procedures, and equipment used for constructing the various demonstration sections. Chapter 6 contains discussion of the laboratory and field test results of the preconstruction roadway conditions, as-constructed performance, and post-thawing performance of the various demonstration and control sections, as well as

economic analysis of the various stabilization methods. Chapter 7 presents the conclusions and outcomes derived from this project, and offers recommendations for further research and implementation of the research results into practice. Supporting materials are included as appendices.

CHAPTER 2. BACKGROUND

The Iowa Highway Research Board (IHRB) Project TR-632 “Low-Cost Rural Surface Alternatives: Literature Review and Recommendations” (White and Vennapusa 2013) reviewed more than 150 domestic and international publications to assess technologies for improving the freeze-thaw performances of low-volume roads. Based on the literature review results, the most suitable and economical technologies for constructing and maintaining unpaved roads in seasonally cold regions were recommended. The present project is focused on comparing the relative performance, durability, and life-cycle costs of demonstration sections constructed using several of the recommended technologies under the same set of geological, climate, and traffic conditions.

The following literature review summarizes the construction methods, performance, and key findings related to the recommended technologies. In this project, the multi-channel analysis of surface waves (MASW) test method was used to measure the multi-layered stiffness of the unpaved road systems and compared to falling weight deflectometer (FWD) tests. The MASW test method and differences between the MASW and FWD methods are also discussed in this chapter.

2.1 Freeze-Thaw Damage of Unpaved Roads

The physical mechanisms leading to freeze-thaw damage of road systems have been examined in many previous studies (e.g., Alzubaidi 1999, Saarenketo and Aho 2005, Aho and Saarenketo 2006, Johnson 2012). Freeze-thaw damage is usually caused by a combination of several factors including frost-susceptible soils, a high ground water table, poor subsurface drainage, heavy traffic loading, and frequent freeze-thaw cycling (Hoover et al. 1981, Kestler 2003, Henry et al. 2005, Saarenketo and Aho 2005, White and Vennapusa 2013). During spring thaws when unpaved roads experience heavy loading from agriculture traffic, the melt water and capillary water trapped in the surface course and top of the subgrade of unpaved roads cannot drain efficiently, causing saturation of the materials which consequently lose strength and stiffness. Current practices, such as dumping and blading virgin aggregate, are typically aimed at repairing freeze-thaw damage rather than minimizing or preventing it in the first place (White and Vennapusa 2013). In contrast, one of the goals of this study is to identify methods which can effectively prevent or minimize the occurrence of such damage.

Many previous studies have evaluated various methods such as mechanical and chemical stabilization and the use of geosynthetics to improve the freeze-thaw performance of unpaved roads (e.g., Hoover et al. 1981, Berthelot and Carpentier 2003, Henry et al. 2005, Azadegan et al. 2013), but most of these studies focused on only one or two technologies. Based on the results of the previous studies, it can generally be concluded that technologies which permanently increase strength or improve drainage of surface courses of unpaved roads can also significantly improve their freeze-thaw performance. However, due to the different subgrade, climate, and traffic conditions of the separate studies, it is difficult to accurately compare the true effectiveness of the various stabilization methods. As mentioned above, the present project employs demonstration sections using several technologies on the same 2-mile stretch of granular

surfaced road to directly compare their performance under the same set of subgrade, climate, and traffic conditions.

2.2 Macadam Stone Base Course

The constructability, performance, and durability of both paved and unpaved roads with macadam stone base layers have been evaluated in previous field projects in Iowa (Less and Paulson 1977, Lynam and Jones 1979, Hoover et al. 1981, Jobgen et al. 1994). Macadam stone base layers with large (i.e., maximum of 3 or 4 in.) particle sizes were reported in these studies to improve both drainage and stability of the road systems. Details from several of these projects are summarized in Table 1. The Iowa DOT Standard Specifications for crushed stone base material (Section 4122.02 of Iowa DOT 2012) state that the macadam stone should have a nominal maximum size of 3 in. and be screened over either a 0.75 in. sieve, or a 1 in. sieve if specified in the contract documents. However, some of the previous projects had macadam stone with a maximum size of 4 in. or particles finer than the 0.75 in sieve.

According to the previous studies (Less and Paulson 1977, Lynam and Jones 1979, Jobgen et al. 1994), construction of the macadam stone base layers was simple and fast. The materials were placed either on a prepared subgrade or on an existing unpaved road surface using a Jersey Spreader and compacted using a vibratory drum roller. As shown in Table 1, the macadam base layer thickness varied between 4 and 10 in. for the different projects. A choke stone layer with double seal asphalt coat (Jobgen et al. 1994, Less and Paulson 1977) or Portland cement concrete (PCC) and asphalt concrete (AC) overlays (Lynam and Jones 1979) were built upon the base layer as surface courses. Procedures and equipment for constructing macadam base course are also specified in Section 2210.03 of the Iowa DOT Standard Specifications (2012). According to the specifications, the macadam stone base shall not be constructed on a natural soil subgrade, and the subgrade should first be corrected, with provision for a filter course if required by contract documents.

Performance and durability of the test sections in the previous projects were evaluated by annual field tests or visual inspections and comparison with other chemical stabilization methods. The test results showed that the macadam base layers improved drainage and minimized freeze-thaw damage and other subsurface drainage issues (Less and Paulson 1977, Lynam and Jones 1979). Compared to other stabilization methods, the use of macadam base layers resulted in the best overall performance and durability (Jobgen et al. 1994). Less and Paulson (1977) also evaluated the effects of macadam base layer thickness, and determined that an 8 in. thick macadam stone base layer is the most cost-effective design for Iowa. The effects of nonwoven geotextile layers between the macadam stone base and subgrade were also evaluated (Hoover et al. 1981, Jobgen et al. 1994). The nonwoven geotextile did not show a noticeable improvement in several measures of performance and also decreased the composite stiffness of the road systems. However, permanent deformations of the sections were reduced when the nonwoven geotextile was used. More details about the previous projects in Table 1 are detailed below.

Table 1. Summary of previous field research projects involving macadam stone base layers

Project Number	Location	Construction Year	Gradation of Macadam Stone	Thickness of Macadam Base (in.)	Subgrade	Fabric	Surface Course Material	Reference
IHRB HR-175	Road X-31, Des Moines County, Iowa	October 1975	100% < 4 in. and 12% to 26% < 1 in.	4, 6, 8, and 10	Silty Clay loam and silt loam	No	3 in. thick choke stone with double seal coat	(Less and Paulson 1977)
ISU-ERI-AMES-80211	Fairfax, Linn County, Iowa	October 1976	100% < 4 in. and 14% < #4 sieve	8	A-4(1) and A-6(6)	Yes	4 in. choke stone with seal coat	(Hoover et al. 1981)
IHRB HR-209	Road G-61, Adair County, Iowa	September 1979	100% < 3 in. and 4.1% < 0.75 in.	5 and 6	Unknown	No	PCC and AC	(Lynam and Jones 1979)
IHRB HR-312	Horseshoe Road, Dubuque County, Iowa	November 1988	100% < 3 in. and 100% > 0.75 in.	5	A-6 (4) Glacial clay loam	Yes	3 in. thick choke stone with double seal coat	(Jobgen et al. 1994)

Less and Paulson (1977) evaluated the feasibility and economics of constructing unpaved roads using macadam stone base layers. A total of 8 miles of granular surfaced roads in Des Moines County, Iowa were constructed using macadam base layer thickness of 4, 6, 8, and 10 in. Visual inspections and deflection tests (i.e., Benkelman Beam and Road Rater tests) were conducted annually from 1975 to 1977 to compare performance of the different sections. The results showed breakups and deteriorations of the double-seal coated surface on sections with 4 to 6 in. thick macadam bases layers, but the 8 and 10 in. sections performed well. Based on the test results, the authors recommended an 8 to 10 in. macadam stone base with 2 in. choke stone and earth shoulders, and concluded that quality of the macadam stone is not critical, with marginal crushed limestone (<50% abrasion loss) considered adequate. Based on the construction costs, however, hauling aggregate further than 20 miles to a project site would make the method uneconomical.

Lynam and Jones (1979) evaluated the feasibility, economics, and performance of using macadam stone base layers under PCC and AC pavements, with poor quality aggregate containing fines (Class 1 aggregate). One control and seven test sections with combinations of different base layer thicknesses (5 or 6 in.) and surface courses (2 to 6 in. for PCC and 2 or 3 in. for AC pavement) were constructed in Adair County, Iowa. Pavement cracks and rutting depth were measured, and joint faulting surveys and Road Rater tests were conducted from 1979 to 1984. The 6 in. thick macadam bases with less than 3 in. PCC or 2 in. AC pavements had cracking, breakup, and rutting after the first winter. Based on the Road Rater tests, the authors concluded that 5 in. of macadam base was equivalent to an additional 0.5 or 0.75 in. PCC in terms of structural rating. However, the main function of the macadam base was to drain water from the subgrade and serve as a capillary barrier for the surface course, so the thickness could be reduced to 3.5 to 4 in. The authors also recommended that the quarry be within 10 to 20 miles of the project site for the method to be economically competitive.

Hoover et al. (1981) evaluated the effect of a nonwoven geotextile (Mirafi™ 140) between the macadam base and subgrade on the performance and durability of granular-surfaced roads built on frost-susceptible silty soils. A total of eleven test sections were constructed using conventional granular backfill base and macadam stone base methods in Linn County, Iowa. Field performance tests including spherical bearing value, plate bearing, and Benkelman beam tests were conducted on the sections over three winter-spring freeze-thaw cycles from 1976 to 1979. The nonwoven geotextile did not give a noticeable improvement in performance and decreased the stiffness of the road system, particularly at the most critical stage of frost boil development. However, permanent deformations were decreased when the geotextile was used.

Jobgen et al. (1994) constructed an unpaved road in Dubuque County, Iowa using four stabilization methods: (1) high float emulsion (HFE-300) to treat the top 3 in. of base stone, (2) a bio-chemical formula (BIO CAT 300-1) to treat 6, 8, and 10 in. thick layers of base stone, (3) the Consolid System method in the top 10 in. of subgrade, wherein a combination of two inverted emulsions are used for dry soil, or an inverted emulsion and a lime hydrated base powder are used to treat the base stone for wet soil, and (4) a 5 in. macadam base with 3 in. of choke stone along with Tensar fabric under one of the sections. Annual visual inspections, Roughometer, and Road Rater tests were conducted from 1988 to 1992 to compare the relative performance of the sections. The Road Rater results showed that the BIO CAT and Consolid bases yielded higher

structural ratings and soil K factors, but their visual performance was rated as poor due to alligator cracking, rutting, and chuck holes. The macadam stone-based sections showed the best overall performance and cost-effectiveness, with only a few locations showing minor rutting or needing patching three years after construction. The effect of Tensar fabric placed underneath the macadam base was not noticeable, and caused lower structural ratings and soil K values.

2.3 Chemical Stabilization

Chemical soil stabilization has long been recognized as an effective method to improve engineering properties of soils such as shear strength, stiffness, compressibility, water sensitivity, and frost susceptibility (Winterkorn and Pamukcu 1991). However, selection of appropriate chemical stabilizers to ensure the performance of different soil types requires laboratory mix design tests and an understanding of the chemical reactions. Winterkorn and Pamukcu (1991) discussed the chemical reactions and recommended laboratory mix design procedures for using cement, fly ash, lime, and bitumen to stabilize soils. Many previous studies have also evaluated different chemical stabilizers for improving freeze-thaw performance of unpaved roads (e.g., Hoover 1973, Jones 2003, Shoop et al. 2003, Bushman et al. 2005, Jones and Surdahl 2014). Jones and Surdahl (2014) also developed a web-based tool to select appropriate chemical treatment methods for unpaved road surfaces based on survey results from practitioners.

In the present project, three types of commonly used chemical stabilizers were selected to build the test sections: cement, class C fly ash (ASTM C 618-12a), and bentonite. The laboratory and field performance of these three stabilizers have been evaluated in many previous studies (e.g., Bergeson and Wahbeh 1990, Bergeson et al. 1995, Berg 1998, Bergeson and Barnes 1998, Parsons and Milburn 2003, White et al. 2005b, White et al. 2005a, Johnson 2012, Solanki et al. 2013). Based on the studies, these chemical stabilization technologies can improve the shear strength, stiffness, and freeze-thaw performance of soils, while reducing their wet-dry sensitivity. However, certain issues specific to chemical stabilization need to be carefully considered. For example, characteristics of the class C fly ash can vary significantly between different plants due to different chemical components of the coal used (White et al. 2005a).

Bergeson and Wahbeh (1990) and Bergeson et al. (1995) evaluated the use of bentonite (sodium montmorillonite clay) for dust reduction on limestone-surfaced roads in Iowa. Comprehensive lab and field evaluations were conducted, showing that the negatively charged surfaces of the clay particles interact with positively charged limestone surfaces to effectively bond the fine particles to the large limestone particles. The laboratory tests also indicated that the bentonite can significantly increase compressive strength and improve slaking characteristics. Based on the field evaluations, Bergeson et al. (1995) concluded that 8% bentonite by dry weight of aggregate was the most cost effective mixing percentage. Dust reduction using bentonite was also compared to calcium and magnesium chloride treatments. The authors concluded that calcium chloride treatments are 2 to 3 times more effective in the short term, but bentonite is more cost-effective, because the bonding capability of bentonite can last much longer (2–3 seasons) than chloride treatments (3–4 months). Bergeson and Wahbeh (1990) also observed that chloride treatments leave the surface prone to washboarding and potholes due to maintenance restrictions.

2.4 Geotextiles and Geogrids

Geotextiles and geogrids have been evaluated for mitigating freeze-thaw damage of unpaved roads in many previous studies (Henry 1990, Henry 1996, Hoover et al. 1981, Lai et al. 2012). The geosynthetics were typically placed at the aggregate-subgrade layer interface to provide subsurface drainage, reinforcement, separation, and a capillary barrier. The mechanisms, benefits, and designs for using geogrids and geotextiles to stabilize road materials were discussed in Giroud and Han (2004a, 2004b), and a reference manual on design and construction of highway works using geosynthetics was developed by Holtz (2008).

Henry (1990) conducted lab investigations using geotextiles to mitigate frost heave, and reported that geotextiles used as capillary barrier can reduce the occurrence of frost heaves by about 60%. Henry (1996) also reviewed previous studies employing geotextiles as capillary barriers, reinforcement, or filters between subgrade and base layers to reduce frost damage. He concluded that geotextiles can reduce the rate of frost heave, but the performance depends upon the geotextile's pore size distribution, wettability, and thickness. Geotextiles that exhibited high capillary rise when inserted in water were found to exacerbate frost heave. Henry et al. (2005) also conducted a demonstration project to compare several techniques including geogrid, geotextile, geowrap, geocell, and a patented geosynthetic capillary barrier for improving freeze-thaw performance of unpaved roads in Vermont. Field tests and monitoring over a two-year period showed that the geogrid or geotextile between subgrade and surface course (12 in. below the road surface) did not provide observable benefits.

Hoover et al. (1981) evaluated effects of a commonly used nonwoven-geotextile (Mirafi 140) for improving frost heave and thaw weakening of granular surfaced roads built on frost-susceptible silty soils in Iowa. Laboratory freeze-thaw tests showed that specimens with embedded geotextile discs had lower frost-heave rates and higher values of cohesion and friction angle than control specimens, but lower stiffnesses. However, field tests showed that the geotextile did not significantly influence the performance of roads with stiffer bases (i.e., granular backfill or macadam stone), but did improve freeze-thaw durability of roads with soft subgrades.

Freeman (2006) quantitatively evaluated effects of nonwoven geotextile on dust reduction for granular surfaced roads. Control sections were found to contain more fines than geotextile sections, and it was concluded that the geotextile can effectively prevent fines migrating from the subbase to the surface course. The results showed that the geotextile layer reduced dust content by 70 to 80%.

2.5 Geocomposite Drainage Layers

Geocomposite materials are typically used as drainage layers and capillary barriers for improving hydraulic conductivity and freeze-thaw performance of road systems. They usually consist of two geotextile layers serving as filters, which sandwich a drainage net or geogrid that functions as a conduit for water (Holtz et al. 2008). Several previous studies have assessed the performance of geocomposite drainage layers for paved and unpaved roads using lab, field, and

numerical evaluations (e.g., Christopher et al. 2000, Henry and Holtz 2001, Stormont et al. 2001, Henry et al. 2005, Bahador et al. 2013).

Christopher et al.(2000) studied geocomposite drainage layers at three different locations within a pavement system: (1) under the asphalt concrete pavement, (2) under the base course aggregate, and (3) within the subgrade to create a capillary break to reduce frost action. The geocomposite drainage layer placed on or within the subgrade was found to be the quickest at removing water during spring thaws. However, FWD tests showed that the control section had a higher stiffness (structural number) than sections with the geocomposite, and sections with geocomposite in the subgrade showed higher stiffness than those with geocomposite at higher locations.

Henry and Holtz (2001) conducted a laboratory investigation of geotextile and geocomposite drainage layers to mitigate frost heave. The test results showed that when the geotextiles were moistened and impregnated with soil fines to simulate field conditions, they did not reduce frost heave. A significant reduction in frost heave was observed when the overlying soil had a degree of saturation below 75%. When the degree of saturation exceeded 80%, however, the geocomposite permitted significant heave due to water mitigating from one geotextile layer to the other through films adhered to the middle geonet layer. The authors therefore recommend that *“research is needed to determine the soil moisture retention characteristics of the geocomposite. This would help identify the soil-moisture conditions that must exist to prevent flow across the geocomposites and to study the influence of the geocomposites on frost heave using numerical models.”*

Henry et al. (2005) also conducted a field investigation on technologies for mitigating freeze-thaw damage to unpaved roads. Field DCP test results and rutting measurements showed that a patented Geosynthetic Capillary Barrier Drain provided the greatest benefit by keeping the upper layers of the soil relatively dry. However, geogrid and geotextile separators placed 12 in. deep did not produce observable benefits.

Bahador et al. (2013) evaluated numerically the effects of geocomposite drainage layers on moisture distribution and plastic deformation of paved and unpaved road systems. They found that the geocomposite layer can decrease plastic deformation through combined mechanistic and hydraulic actions, but increasing the surface course thickness reduced the reinforcement effect of the geotextile on either side of the geocomposite material.

2.6 MASW and FWD Tests

The MASW test is a nondestructive geophysical method that has also been applied for assessing the elastic modulus of multi-layered pavement systems (Park et al. 1999, Park et al. 2001). In the test, an impact is applied on the ground surface and the surface wave motion is measured using an array of geophones or accelerometers. Through an inversion procedure, the shear wave velocity, or alternatively, the small-strain shear modulus (G_{max}), can be back-calculated as a function of depth. The MASW test is commonly assumed to measure the surface velocities of “far-field” seismic waves at low strain levels, which is in contrast to the commonly used falling

weight deflectometer (FWD) test that measures road surface deflections at higher strain levels from the “near-field” deflection basin (Lytton 1989). Figure 1 shows a schematic that illustrates the differences between the near field and far field characteristics under a load applied on the road surface.

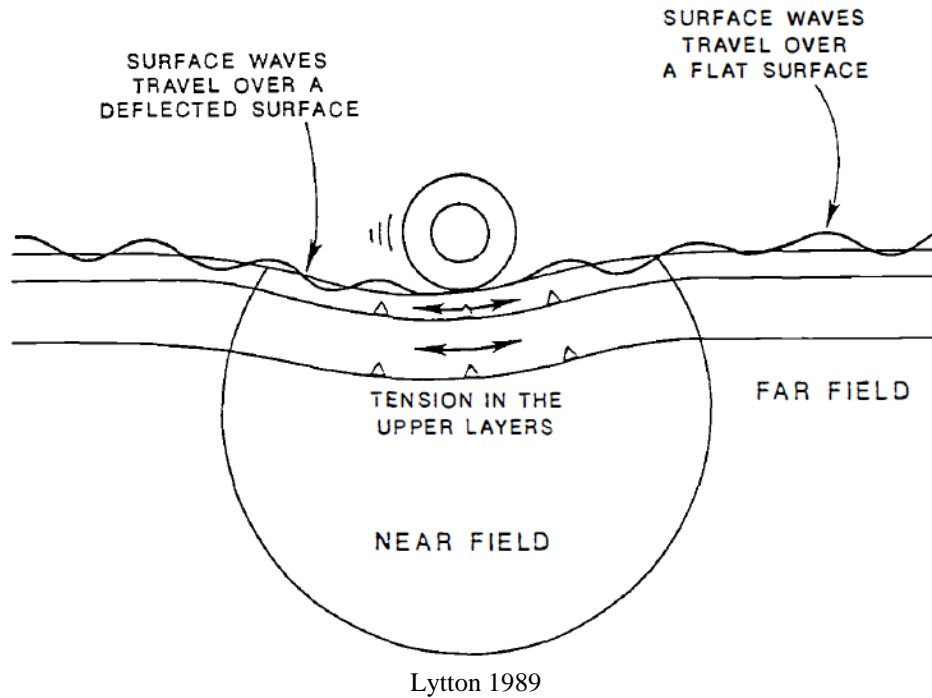


Figure 1. Schematic of near field and far field characteristics

Lytton (1989) also discussed that if far-field measurement methods are used, they “...*must first be able to provide corrections from their high frequencies (above about 2000 Hz) and low stress levels to the low frequencies (below about 200 Hz) and high stress levels,*” because the properties of the pavement layer materials in the near field and at higher strain levels are of interest to pavement engineers.

Surface wave methods have traditionally been used for seismic exploration surveys to determine soil stiffness profiles, which gradually increase with depth when considered on large length scales. For road systems, however, the stiffness of each layer significantly decreases with depth over the first few feet. This can create a few challenges when applying traditional surface wave analysis methods to pavement systems, such as numerical instability when using the transfer matrix method to calculate theoretical dispersion curves at high frequencies, or convergence to a local minimum when using the Levenberg-Marquardt method for inversion (Lin and Ashlock 2011). To address these issues, Lin (2014) developed several improvements to MASW methods that can improve their use for testing pavement systems. A new phase-velocity and intercept-time scanning (PIS) method was developed to improve the resolution and sharpness of experimental dispersion images by minimizing side lobes and aliasing that can be generated by conventional MASW wavefield transformation methods. A new hybrid genetic-simulated annealing (GSA) optimization algorithm was also developed to improve surface wave inversion

procedures by reducing the risk of becoming trapped in a local minimum, thus improving global searching efficiency. These improved methods were used to process MASW test data for the granular surfaced road demonstration sections in this study.

The FWD test measures pavement surface deflections, from which the elastic modulus of each material layer can be calculated based on the applied load, surface deflection data, and assumed layer thicknesses. Many forward- and back-calculation methods have been developed, but each method carries its own assumptions and uncertainties (Lytton 1989). A commonly used equivalent layer method for analyzing FWD data, the AASHTO Guide for the Design of Pavement Structures approach (AASHTO 1993), is a quasi-static approach for calculating layer moduli of a two layered system. This approach was proposed by Ullidtz (1987) and combines Boussinesq theory (Boussinesq 1885) with Odemark's method of equivalent layer thickness (MET) assumption (Odemark 1949). Boussinesq theory is used for calculating stresses, strains, and deformations at a given radius and depth in a homogeneous linear elastic half-space caused by a point load applied on the surface. Odemark's assumption is used to convert the thickness of the top layer to an equivalent thickness of additional subgrade material, and then match the measured surface deflection with the calculated deflection of the equivalent single layer. By combining these two methods, the elastic modulus of a top and bottom layer can be estimated. A detailed derivation of the equivalent layer method is described in Section 3.2.2 of the report.

CHAPTER 3. METHODS

This chapter consists of two parts: (1) presentation of laboratory testing methods used to determine soil index properties, aggregate abrasion characteristics, compaction behavior, shear strength, durability, hydraulic conductivity, chemical composition, and microstructural features of the geomaterials, and (2) field testing methods used to measure in-situ shear strength, stiffness, hydraulic conductivity, and temperature profiles of the granular surfaced road system.

3.1 Laboratory Tests

Laboratory tests were conducted to determine soil index properties, aggregate abrasion characteristics, compaction behavior, shear strength, durability, and hydraulic conductivity of the geomaterials used in this project. Procedures for these tests are described in detail below. The chemical composition, mineralogy, and microstructural features of chemical stabilizers and stabilized materials used in this project were also determined by laboratory x-ray analyses and scanning electron microscopy (SEM).

3.1.1 Soil Index Properties

Particle size analyses, liquid limit tests, plastic limit tests, and soil classifications were conducted in accordance with American Society for Testing and Materials (ASTM) standards to determine soil index properties and classify geomaterials.

3.1.1.1 Particle Size Analysis

Particle-size analysis for geomaterials followed ASTM D 422-63(2007)e2 “*Standard test method for particle-size analysis of soils.*” Representative samples of air-dried coarse grained materials were obtained using a riffle sample splitter in accordance with ASTM D 75-13 “*Standard practice for sampling aggregates.*” Particle size analysis consists of two main parts: sieve analysis and hydrometer tests. Sieve analyses were performed on material retained on the No. 200 (75 μm) sieve and hydrometer tests were used on representative specimens of material passing the No. 10 (2.00 mm) sieve for determining proportions of silt and clay particles size smaller than the No. 200 sieve (Note that 0.002 mm was used as the boundary between silt and clay sizes). After completing the hydrometer test, the material was washed through the No. 200 sieve. The material retained on the No. 200 sieve was then oven dried to complete the sieve analysis for particle sizes between the No. 10 (2.00 mm) and No. 200 sieves. The equipment used for sieve analysis and hydrometer tests is shown in Figure 2.

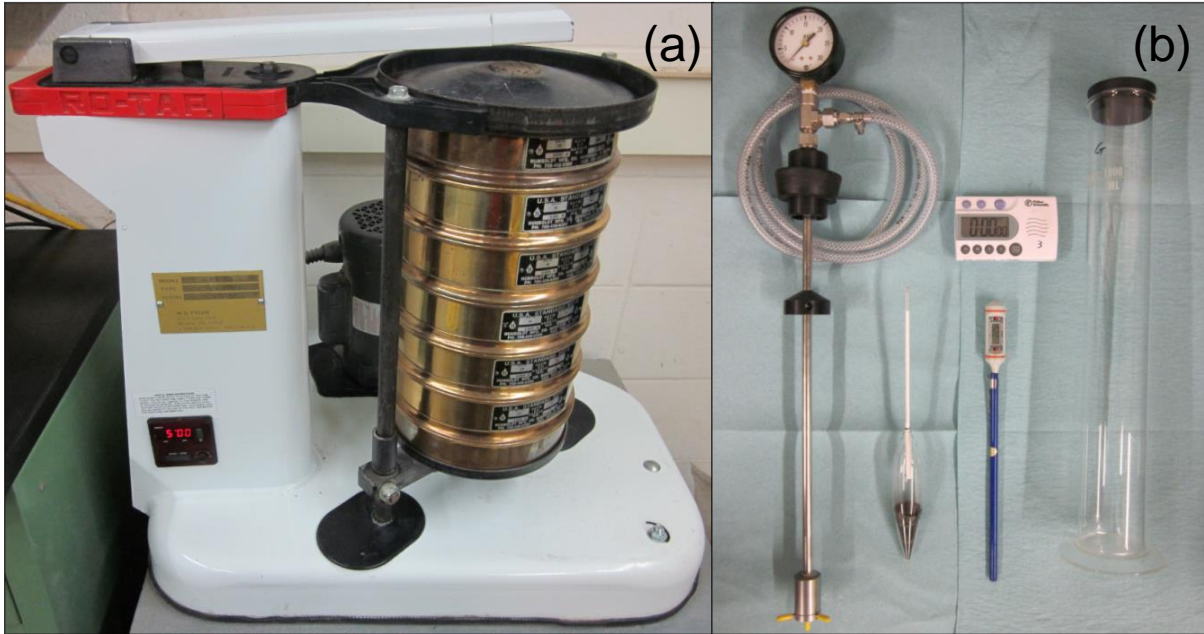


Figure 2. (a) Sieve analysis and (b) hydrometer test devices used in this study

3.1.1.2 Liquid Limit, Plastic Limit, and Plasticity Index (Atterberg Limits)

The liquid limit (LL), plastic limit (PL), and plasticity index (PI) of geomaterials passing the No. 40 (425 μm) sieve were determined in accordance with ASTM D 4318-10e1 “*Standard Test Methods for Liquid Limit, Plastic Limit, and Plasticity Index of Soils.*” The wet preparation method was followed for preparing representative samples for the tests. Liquid limit tests were performed using the multi-point liquid limit test method, and at least three points were determined for each sample. Plastic limit tests were conducted using the hand method. Both LL and PL were rounded to the nearest integers for calculating the PI. According to the Standard, if either the LL or PL could not be determined, or if the PL was equal to or greater than the LL, the material was reported as nonplastic (NP). The liquid limit device used in this study is shown in Figure 3. A ground glass plate was used for the plastic limit test.



Figure 3. Liquid limit test device used in this study

3.1.1.3 Soil Classification

The particle size analysis and Atterberg limits test results were used to classify materials in accordance with ASTM D 2487-11 “*Standard Practice for Classification of Soils for Engineering Purposes (Unified Soil Classification System (USCS))*” and ASTM D 3282-09 “*Standard Practice for Classification of Soils and Soil-Aggregate Mixtures for Highway Construction Purposes (AASHTO classification system)*.”

3.1.2 Aggregate Abrasion Characteristics

Two ASTM-standardized aggregate abrasion tests were used to evaluate the degradation resistance of geomaterials having different maximum grain sizes. Both test methods measure degradation of aggregate resulting from the interaction of aggregate, steel balls, and water in a rotating cylindrical jar or drum which causes crushing, grinding, and impacts on the aggregates. Changes in mass of the specimens measured before and after the tests were used to evaluate and compare abrasion characteristics of geomaterials used in this project, to determine their relative resistance to crushing, degradation and disintegration in the field.

3.1.2.1 Los Angeles Abrasion Test

Los Angeles (L.A.) abrasion tests were conducted on three types of macadam materials from the demonstration project site, in accordance with ASTM C 535-12 “*Standard test method for resistance to degradation of large-size coarse aggregate by abrasion and impact in the Los Angeles machine*.” For each macadam type, triplicate test specimens containing particle sizes between 1.5 and 3 in. were prepared to determine average degradation properties of the material. The abrasion tests were conducted by the Iowa DOT Central Materials Aggregates Lab, as they possessed the necessary equipment.

3.1.2.2 Micro-Deval Abrasion Test

Micro-Deval tests were conducted on surface course materials from the project site in accordance with ASTM D 6928-10 “*Standard test method for resistance of coarse aggregate to degradation by abrasion in the Micro-Deval apparatus.*” The surface course materials used in Micro-Deval tests had smaller maximum particle sizes than the macadam materials used in the LA abrasion tests. Triplicate test specimens containing particles between 3/8 and 0.75 in. were tested to determine their abrasion resistance and durability under abrasion and grinding action of the Micro-Deval machine (Figure 4).



Figure 4. Micro-Deval testing machine used in this study

3.1.3 Compaction Behavior

Standard Proctor compaction tests were performed to determine the relationship between water content and dry unit weight of geomaterials according to ASTM D 698-12e1 “*Standard test methods for laboratory compaction characteristics of soil using standard effort (12 400 ft-lbf/ft³ (600 kN-m/m³)).*” A Hobart mixer was used to prepare fine-grained geomaterials to predetermined moisture contents (Figure 5a), and an automated mechanical rammer was used to compact the specimens (Figure 5b).



Figure 5. (a) Hobart mixer and (b) automated mechanical rammer used in this study

The ASTM compaction test standard specifies the mold size and methods for preparing the specimens based on the gradation of the geomaterial. Corrections were made to the unit weight and water content in accordance with ASTM D 4718-87(2007) “*Standard Practice for Correction of Unit Weight and Water Content for Soils Containing Oversize Particles*” for geomaterials that contained 5% by mass of oversize fraction.

3.1.4 Shear Strength

Unconfined compressive strength (UCS) and California bearing ratio (CBR) tests were conducted to evaluate and compare the undrained shear strength properties of compacted geomaterials.

3.1.4.1 Unconfined Compressive Strength Test

The unconfined compressive strength (UCS) of compacted untreated and chemically stabilized soil specimens was measured in accordance with ASTM D 1633-00(2007) “*Standard Test Methods for Compressive Strength of Molded Soil-Cement Cylinders.*” As specified in Method A of the standard, a specimen diameter of 4 in. and height of 4.6 in was used. The chemically stabilized specimens were extruded from the four inch diameter Proctor mold and wrapped with plastic film and aluminum foil to retain moisture during curing. The specimens were cured in a 38°C (100°F) controlled temperature environment for seven days. The compression device used in this study is shown in Figure 6.



Figure 6. Unconfined compressive strength test on a fly ash-treated soil specimen

The unconfined compressive strength, σ_c , can be calculated as:

$$\sigma_c = \frac{P}{A} \quad (1)$$

where P is the peak vertical load and A is the cross-sectional area of the specimen.

3.1.4.2 California Bearing Ratio Test

California bearing ratio (CBR) tests were used to evaluate the undrained shear strength of untreated and chemically stabilized subgrade and surface aggregate materials in accordance with ASTM D 1883-07e2 “*Standard Test Method for CBR (California Bearing Ratio) of Laboratory-Compacted Soils.*” CBR specimens were prepared and compacted at their optimum moisture content (OMC) according to ASTM D 698-12e1. Both as-compacted and soaked specimens were tested to determine how shear strength changes after soaking. The CBR test setup is shown in Figure 7.



Figure 7. CBR tests conducted on (a) OMC and (b) saturated specimens

The Statewide Urban Design and Specifications manual (SUDAS 2015) provides a relative rating system to evaluate the support conditions for subbase and subgrade layers of rigid and flexible pavement systems based on CBR (Table 2). A frost susceptibility classification system for soils based on post-thawing CBR values is also provided in ASTM D 5918-13 “*Standard Test Methods for Frost Heave and Thaw Weakening Susceptibility of Soils*” (Table 3). In this study, both laboratory CBR test results and in situ CBR values calculated using the DCP test data (See Section 3.2.1 of the report) will be used to rate the materials according to the criteria in these two tables.

Table 2. Relative ratings of subbase and subgrade layers based on CBR values (SUDAS 2015)

CBR (%)	Layer	Rating
> 80	Subbase	Excellent (E)
50 to 80	Subbase	Very Good (VG)
30 to 50	Subbase	Good (G)
<30	Subbase	Below Good (<G)*
>30	Subgrade	Excellent (E) ^a
20 to 30	Subgrade	Very Good (VG)
10 to 20	Subgrade	Fair to Good (F to G)
5 to 10	Subgrade	Poor to Fair (P to F)
< 5	Subgrade	Very Poor (VP)

* Rating was added by authors and is not present in SUDAS table.

Table 3. Frost susceptibility classification system (ASTM D 5918-13)

Frost-Susceptibility Classification	Symbol	8-h Heave Rate (mm/day)	CBR After Thaw (%)
Negligible	NFS	<1	>20
Very low	VL	1 to 2	15 to 20
Low	L	2 to 4	10 to 15
Medium	M	4 to 8	5 to 10
High	H	8 to 16	2 to 5
Very high	VH	>16	<2

3.1.5 Durability

Three durability tests, (1) vacuum saturation, (2) freezing and thawing, and (3) wetting and drying tests, were performed to evaluate freezing-thawing and wetting and drying durability of chemically stabilized geomaterials.

3.1.5.1 Vacuum Saturation Test

The vacuum saturation test is a rapid method to predict freeze-thaw and post-saturation durability of chemically stabilized soil specimens (Dempsey and Thompson 1973). In this project, the vacuum saturation test was also conducted on untreated subgrade specimens to assess the improvement in shear strength and durability imparted by the chemical stabilizers. The vacuum saturation test procedure consisted of the following steps:

1. Chemically stabilized specimens were removed from a curing oven and allowed to equilibrate to room temperature for 30 minutes,
2. Specimens were placed on a perforated plate in a vacuum desiccation chamber,
3. A vacuum pressure of 28 in. of mercury was applied for at least 30 minutes,
4. The chamber was flooded with tap water until the specimens were submerged,
5. Specimens were soaked for one hour at atmospheric pressure,
6. Broken specimens were discarded and their post-saturation shear strengths were assumed to be zero,
7. Unconfined compressive strength of intact specimens was measured in accordance with ASTM D 1633-00(2007).

Figure 8 shows the untreated Vail Avenue subgrade specimens before, during, and after the vacuum saturation process.

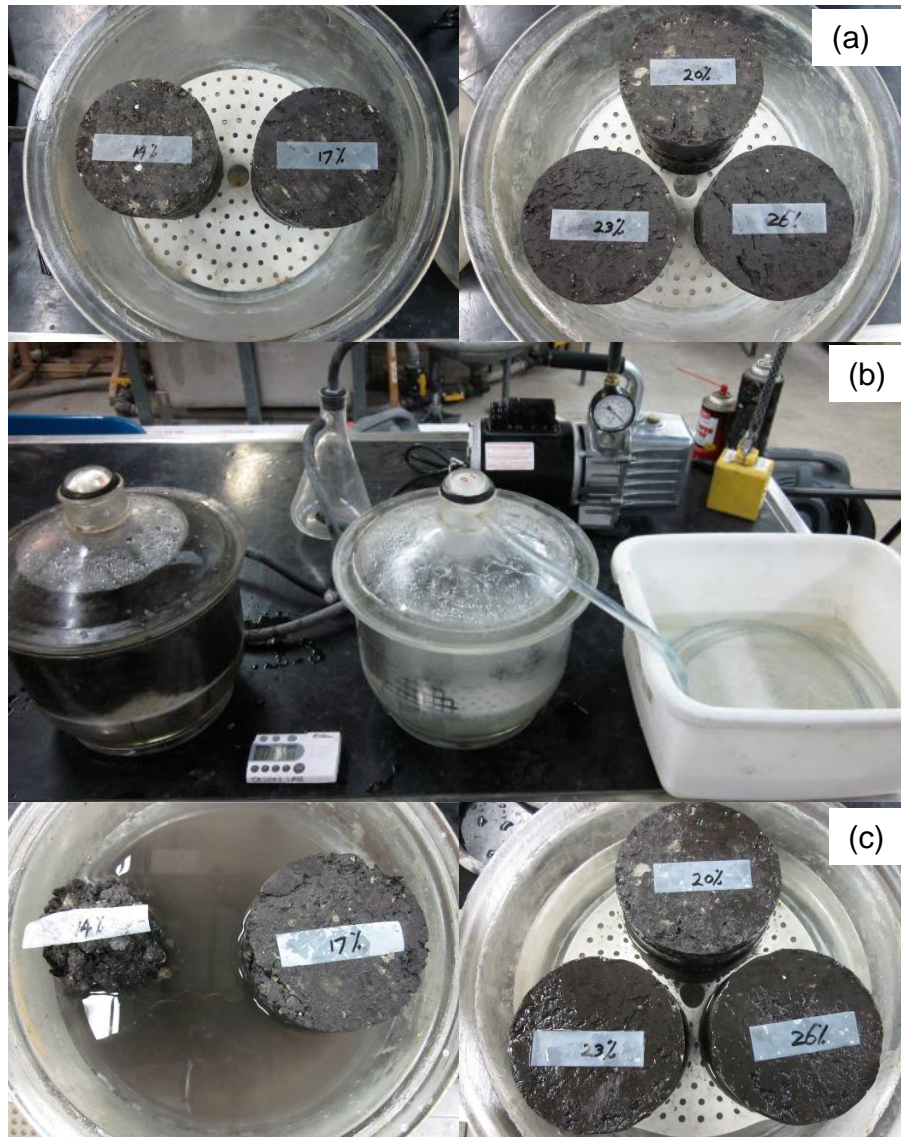


Figure 8. Vail Avenue subgrade specimens (a) before, (b) during, and (c) after vacuum saturation (compacted moisture contents are indicated on specimens)

3.1.5.2 Freezing and Thawing Test

The freezing and thawing test can determine mass loss, water content changes, and volume changes of chemically stabilized soil specimens induced by repeated freezing and thawing cycles. The testing procedures essentially followed ASTM D 560-03 “*Standard test methods for freezing and thawing compacted soil-cement mixtures,*” with some slight modifications. The Standard specified that specimens be compacted to maximum dry unit weight and optimum moisture content. However, in this study, the cement- and fly ash-treated specimens were compacted in the field during construction, so the moisture contents of the specimens corresponded to the as-built field compaction moisture contents. Also, volume changes of the specimens cannot be measured precisely, because the specimens typically do not maintain a cylindrical geometry after repeated freeze-thaw cycles.

3.1.5.3 Wetting and Drying Test

The wetting and drying test can determine mass loss, water content changes, and volume changes of chemically stabilized soil specimens induced by repeated wetting and drying cycles. The testing procedures essentially followed ASTM D 559-03 “*Standard test methods for wetting and drying compacted soil-cement mixtures*,” but specimens were also prepared in the field and volume changes of the specimens were not recorded during the tests.

3.1.6 Hydraulic Conductivity

In this project, two types of laboratory permeability tests were conducted to determine hydraulic conductivity of the Vail Avenue geomaterials. The rigid-wall compaction mold permeameter test was used for the subgrade material, and large-scale horizontal permeameter tests were used to measure permeability of the surface course materials with and without an embedded geocomposite drainage layer.

3.1.6.1 Rigid-Wall Compaction Mold Permeameter Test

The laboratory rigid-wall compaction mold permeameter test was conducted to estimate hydraulic conductivity of the Vail Avenue subgrade material. The falling head test method was used, following Method B of ASTM D 5856-95(2007) “*Standard test method for measurement of hydraulic conductivity of porous material using a rigid-wall, compaction-mold permeameter*.” Because the Vail Avenue subgrade has a high clay content (~29%), water channeling through the interface between the rigid mold and soil specimen was prevented by expansion of the specimen after saturation. Prior to the tests, specimens were saturated for 4 days under 14 psi vacuum pressure, then soaked for 7 days without vacuum pressure. Figure 9 shows the rigid-wall permeameter device and test setup.

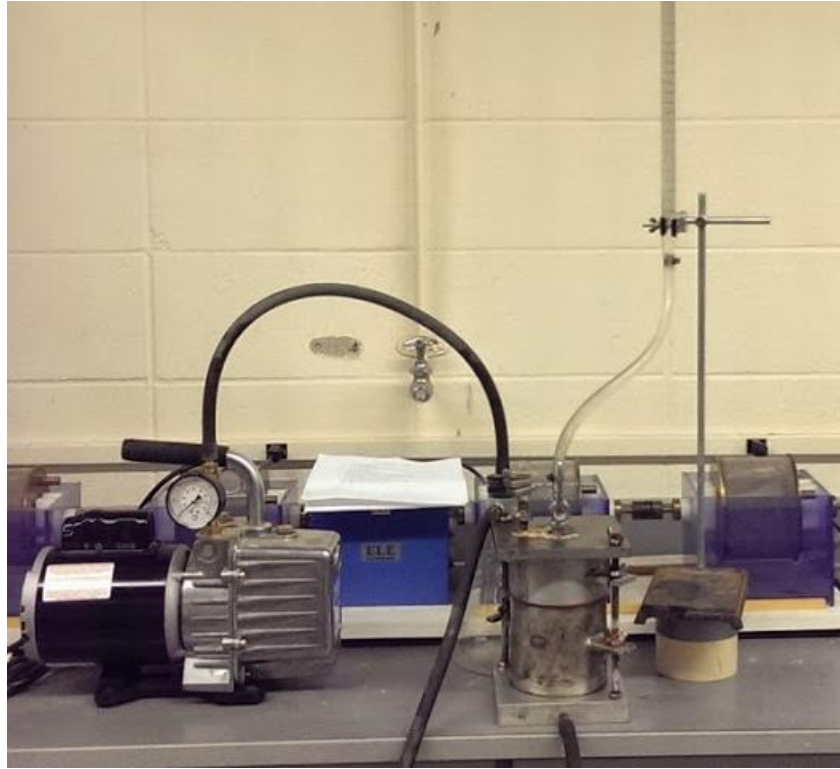


Figure 9. Rigid-wall compaction mold permeameter test device used in this study

3.1.6.2 Large-Scale Horizontal Permeameter Test

The large-scale horizontal permeameter test (HPT) was developed by Iowa State University's Center for Earthworks Engineering Research (CEER). This test was developed because most permeability tests are conducted using vertical flow, which does not accurately represent how water typically drains or flows through the soil horizontally in the field. The unique HPT device was therefore designed to measure the permeability of soils under horizontal flow conditions. The device can simulate direct horizontal flow situations under different initial hydraulic gradients, and is large enough to effectively test multiple material layers. Representative aggregate materials were collected from the field and compacted in the HPT soil tank with or without a layer of geocomposite at the middle of the test specimen. The horizontal hydraulic conductivity was measured under four different constant water heads (50, 100, 150, 200 mm). The test data can be used to determine relationships between hydraulic conductivity and hydraulic gradient for different materials. The HPT testing device is shown in Figure 10.

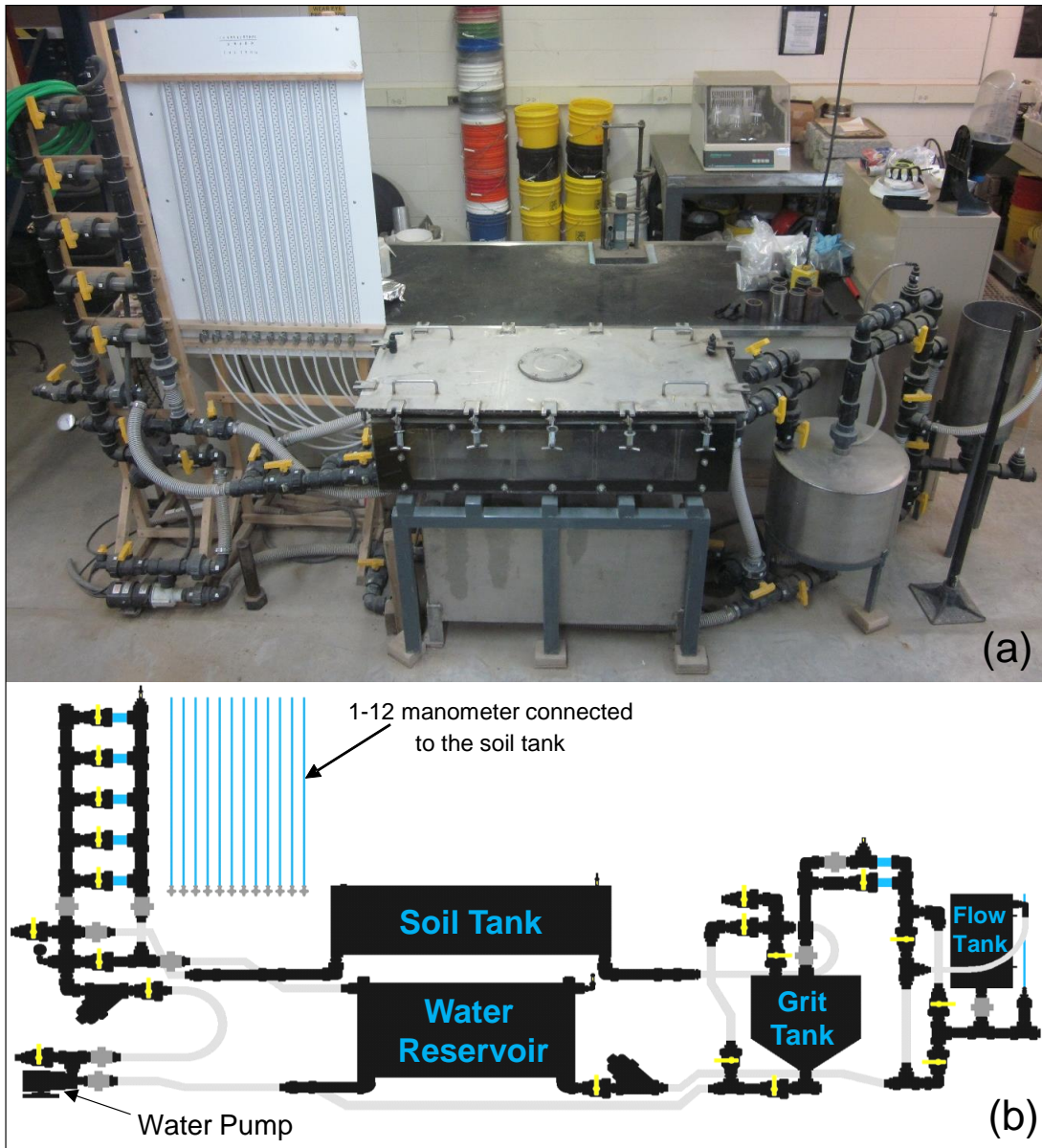


Figure 10. (a) Photo and (b) schematic of the large-scale HPT device used in this study

3.1.7 Chemical Composition, Mineralogy, and Microstructure

X-ray fluorescence (XRF) and x-ray diffraction (XRD) analyses were performed on the bentonite and fly ash stabilizers to determine their chemical composition and mineralogy, respectively. From these results, the type and quality of the chemical stabilizers can also be determined. Scanning electron microscopy (SEM) was used to analyze microstructural features of the chemically stabilized surface course materials collected from the demonstration sections. All of the tests were conducted by the Materials Analysis and Research Laboratory at Iowa State University.

3.2 Field Tests

Field tests used to determine the shear strength, stiffness, and hydraulic conductivity of various demonstration road sections are presented in the following sections.

3.2.1 Dynamic Cone Penetrometer Test

The dynamic cone penetrometer (DCP) test was performed in accordance with ASTM D 6951-09 “*Standard Test Method for Use of the Dynamic Cone Penetrometer in Shallow Pavement Applications*” for estimating shear strength of surface course and subgrade materials of the Vail Avenue demonstration sections. The test involves driving a conical point with a diameter at the base of 0.79 in., using a 17.6 lb hammer dropped a distance of 22.6 in., and measuring the penetration distance per blow, referred to as the dynamic cone penetration index (DCPI).



Figure 11. Dynamic cone penetrometer (DCP) test

The DCPI with units of inches per blow was measured for the various demonstration sections, and used in the empirical correlations of Equations 2 through 4 to estimate the in situ CBR values:

$$\text{for CBR} > 10, \text{ DCP-CBR} = 292 / (\text{DCPI} \times 25.4)^{1.12} \quad (2)$$

$$\text{for CL soils with CBR} < 10, \text{ DCP-CBR} = 1 / (0.432283 \times \text{DCPI})^2 \quad (3)$$

$$\text{for CH soils with CBR} < 10, \text{ DCP-CBR} = 1 / (0.072923 \times \text{DCPI}) \quad (4)$$

In this project, all of the demonstration sections were analyzed as two-layered systems consisting of a surface course and subgrade. To calculate the average DCP-CBR of each layer, the boundary between the two layers was identified by a sudden change in slope of the cumulative blows versus depth profile or a sudden drop in DCP-CBR, as shown in Figure 12.

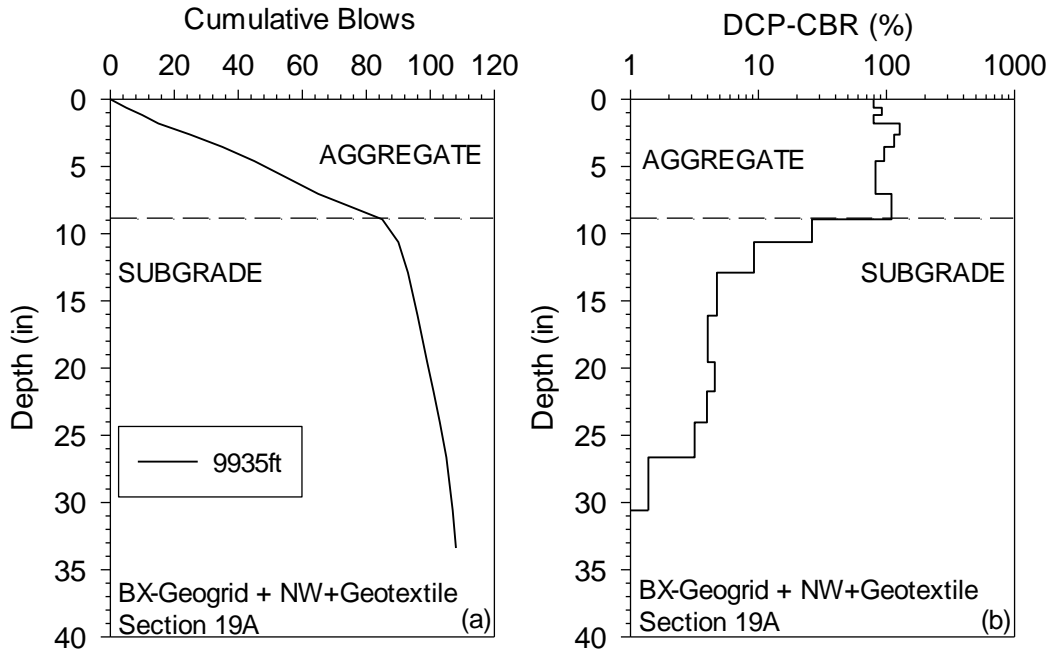


Figure 12. Example of DCP depth profiles: (a) cumulative blows and (b) DCP-CBR

The notation $DCP-CBR_{AGG}$ will be used to denote the average DCP-CBR of the surface course (aggregate) layer, and $DCP-CBR_{SG}$ will represent the average DCP-CBR of the subgrade up to the maximum depth measured. The average DCPI of each layer can be calculated using Equations 5 and 6, then substituted into Equations 2 through 4 to obtain the average DCP-CBR of each layer.

$$DCPI_{AGG} = \frac{\text{Cumulative blows in the surface course}}{\text{Thickness of the surface course}} \quad (5)$$

$$DCPI_{SG} = \frac{\text{Cumulative blows of the test} - \text{Cumulative blows in the surface course}}{\text{Total measurement depth} - \text{Thickness of the surface course}} \quad (6)$$

3.2.2 Falling Weight Deflectometer (FWD) Test

Falling weight deflectometer (FWD) tests were conducted using a Kuab Model 150 2m FWD (Figure 13) with an 11.81 in. diameter loading plate. A static seating load was applied, followed by four weight drops with measured loads normalized to 6,000, 9,000, 12,000, and 16,000 lb. A load cell recorded the actual applied forces while geophones recorded deflections of the roadway surface. A segmented loading plate was used to ensure a uniform stress distribution over the plate (Crovetti et al. 1989).



Figure 13. Kuab falling weight deflectometer setup

To directly compare the FWD tests results from different test locations at the same applied dynamic contact stress, deflection values at each test location were normalized to a 12,000 lb load using the Engineering Research International Data Analysis (ERIDA) program (ERI 2009). Because the actual measured loads were not exactly equal to the target loads during testing, linear adjustments were applied to the measured deflections to calculate the deflections at the target load levels. For each test location, a single equivalent composite elastic modulus of the granular surfaced road and subgrade system was determined from the FWD tests using Equation 7.

$$E_{FWD-Composite} = \frac{(1-\nu^2)\sigma_0 A}{d_0} \times f \quad (7)$$

where,

$E_{FWD-Composite}$ = Composite elastic modulus (psi)

d_0 = measured deflection under the center of the loading plate (in.),

ν = Poisson's ratio (assumed as 0.4),

σ_0 = normalized applied peak stress (psi),

A = radius of the plate (in.), and

f = shape factor was assumed to be 2, because the segmented loading plate provides uniform stress distribution.

The FWD test data were also used to calculate separate elastic moduli of the surface course and subgrade layers using the AASHTO Guide for the Design of Pavement Structures approach (AASHTO 1993). The AASHTO approach for calculating moduli of a two-layered system is based on the equivalent layer theory. This approach combines the Boussinesq theory (Boussinesq 1885) and Odemark's method of equivalent layer thickness (MET) assumption (Odemark 1949). The Boussinesq theory is used for calculating stresses, strains, and deformations at a given radius and depth in a homogeneous linear elastic half-space, caused by a point load applied on the surface (Equation 8). Because the FWD test applies a dynamic load on a circular plate, the surface deflection of a homogeneous layer material underneath the loading plate is calculated by integrating Boussinesq's solution (Equation 9).

$$d_{r,z} = \frac{(1+\nu)F_{max}}{2\pi E\sqrt{z^2+r^2}} \left[2(1-\nu) + \frac{z^2}{z^2+r^2} \right] \quad (8)$$

$$d_{0,z} = \frac{(1-\nu^2)F_{max}f}{\pi AE} \frac{1}{\sqrt{1+(\frac{z}{R})^2}} \quad (9)$$

where,

r = radius from the point load,

z = vertical depth from the point load,

$d_{r,z}$ = vertical deflection at radius r and depth z,

ν = Poisson's ratio,

E = elastic modulus,

F_{max} = maximum vertical force,

f = shape factor, and

A = radius of the loading plate.

For pavement systems, according to AASHTO (1993), deflections measured a sufficiently large distance from the load are considered to be independent of the size of the loading plate and caused only by subgrade deformation. Therefore, the elastic modulus of the subgrade (E_{FWD-SG}) can be calculated using a single deflection measurement as shown in Equation 10.

$$E_{FWD-SG} \text{ or } E_2 = \frac{(1-\nu^2)F_{max}}{\pi r d_{r,0}} \quad (10)$$

To determine the elastic modulus of the surface course layer (E_1 or E_{FWD-GR}), Odemark's assumption is first used to determine the deflection of a two layer system under an applied load by converting the thickness of the top layer into an equivalent thickness (h_e) of additional subgrade material by Equation 11.

$$h_e = h \sqrt[3]{\frac{E_1}{E_2}} \quad (11)$$

where,

h_e = equivalent single thickness of the two-layered system

h = thickness of top layer,

E_1 = modulus of top layer, and

E_2 = converted single modulus of the two-layered system.

According to AASHTO (1993), the surface deflection should be measured at a distance greater than the effective radius (a_e) of the stress bulb at the interface of the top and bottom layers given by Equation 12.

$$a_e = \sqrt{[A^2 + (h^3 \sqrt{\frac{E_1}{E_2}})^2]} \quad (12)$$

However, as the measurement distance increases, the magnitude of the deflection decreases, which may increase measurement error for calculating subgrade modulus. Based on a series of numerical analyses, AASHTO (1993) recommended that the deflection ($d_{r,0}$) used for calculating the subgrade modulus in Equation 10 be greater than or equal to $0.7a_e$.

Combining the Boussinesq theory and Odemark's assumption, the total surface deflection directly beneath the FWD loading plate caused by the deformation of both the top and bottom layers can be calculated using Equation 13.

$$d_{0,0} = \frac{(1-\nu^2)F_{max}f}{\pi A} \left\{ \frac{1}{E_2 \sqrt{1 + \left(\frac{h^3 \sqrt{\frac{E_1}{E_2}}}{A}\right)^2}} + \frac{\left[1 - \frac{1}{\sqrt{1 + \left(\frac{h}{A}\right)^2}}\right]}{E_1} \right\} \quad (13)$$

By matching the calculated deflection to the measured deflection underneath the loading plate, the elastic modulus of the surface course ($E_{FWD-AGG}$ or E_1) can then be determined.

3.2.3 Multi-Channel Analysis of Surface Waves (MASW) Test

The multi-channel analysis of surface waves (MASW) test was used to measure and compare stiffness of various road sections at relatively lower strain levels compared to the FWD test. Compared to the FWD test, a lower energy source and close receiver spacing was used to focus the measurements on the surface aggregate layer and top few inches of subgrade. The MASW test measures the seismic Rayleigh wave velocity as a function of frequency, from which the shear wave velocity, or alternatively, the small-strain shear modulus (G_{max}) can be determined as a function of depth for the surface course and subgrade (Lin and Ashlock 2011, Park et al. 1999). A triggered ball-peen hammer source was used to impact a 6 in. square by 1 in. thick aluminum plate resting on the road surface to generate the surface waves. The vertical velocity of the surface was measured by an array of twenty-four 4.5-Hz geophone receivers with 6 in. spacing using a custom-built land streamer. Data was recorded using a Geometrics Geode seismograph. The MASW test setup is shown in Figure 14. The MASW test configuration is summarized in Table 4.



Figure 14. MASW test setup with landstreamer

Table 4. Configuration used for MASW tests

Test setup parameters	Values
Source-to-first-receiver offset (x_1)	12 in.
Receiver spacing (d_x)	6 in.
Total number of channels (N)	24
Total length of receiver spread (X_T)	11.5 ft

Data from the MASW tests was used to back-calculate the shear-wave velocity (V_s) profile based on an inversion procedure that uses the measured dispersion characteristics of the surface (Rayleigh) wave velocity (V_R) as input. Figure 15 shows an example of the experimental

dispersion image generated using the phase-velocity and intercept-time scanning (PIS) data processing method (Lin 2014).

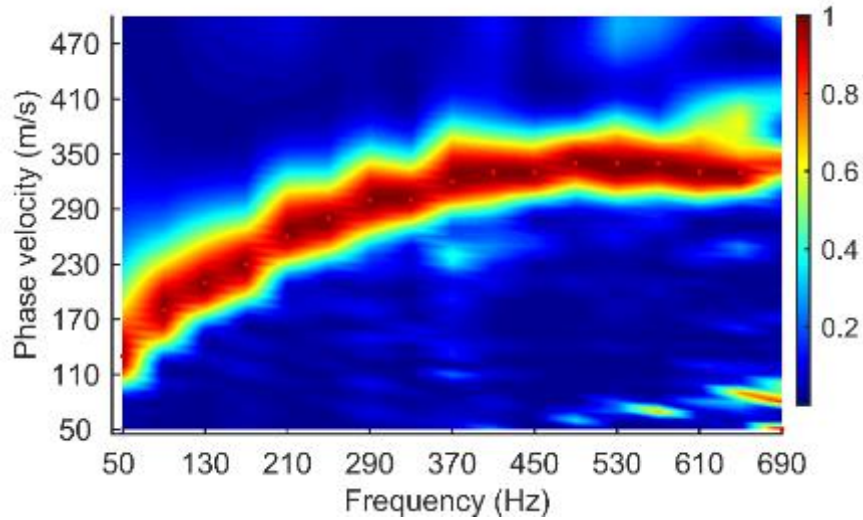


Figure 15. Example of experimental dispersion image from MASW test on granular surfaced road

The peaks of the dispersion image are picked to obtain the experimental dispersion curve. Figure 16 shows the corresponding experimental dispersion curve and a matched or back-calculated theoretical dispersion curve obtained using a new hybrid genetic-simulated annealing (GSA) inversion procedure (Lin 2014).

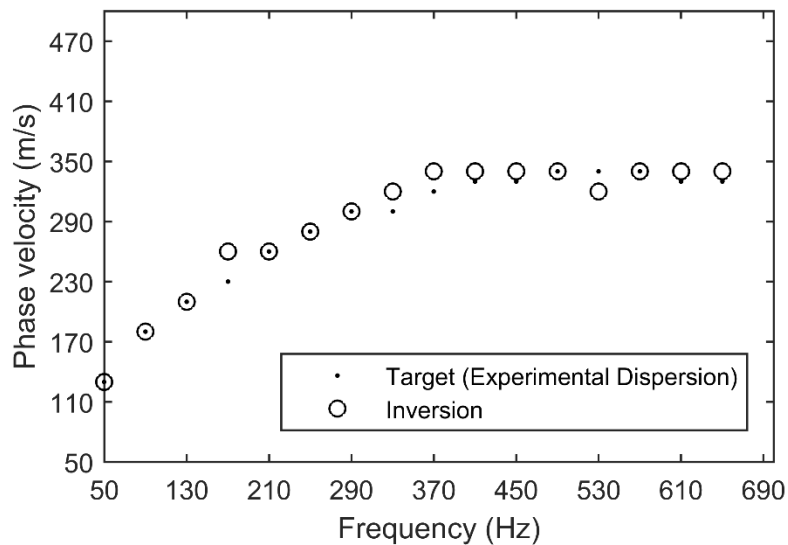


Figure 16. Example of experimental dispersion curve (target) and theoretical dispersion curve from inversion procedure

The shear wave velocity V_s is directly related to the layer stiffness and can be used to calculate the elastic modulus (E_{MASW}) of each layer using Equations 14–16.

$$V_s = V_R \times (1.13 - 0.16\nu) \quad (14)$$

$$G = V_s^2 \times \rho \quad (15)$$

$$E_{MASW} = 2(1 + \nu)G \quad (16)$$

where,

V_R = Surface (Rayleigh) wave velocity,

ν = Poisson's ratio,

V_s = Shear wave velocity

G = Shear modulus, and

E_{MASW} = Elastic (Young's) modulus.

In this project, MASW tests were conducted at three to five uniformly distributed locations per demonstration section and compared with the FWD tests. MASW tests were also conducted on the fly ash- and cement-stabilized sections during curing (at 1, 7, 22, and 28 days) and after thawing to monitor the stiffness changes of the sections with time.

3.2.4 Air Permeameter Test

The air permeameter test (APT) was used to measure in situ saturated hydraulic conductivity as a function of depth for the surface course of the geocomposite drain section and a nearby control section. For the geocomposite section, after the last APT test, a piece of geocomposite was cut to examine whether it was damaged due to traffic loading. Figure 17 shows the APT test procedures used for this study.



Figure 17. Air permeameter test

Saturated hydraulic conductivity of the testing materials can be calculated using the APT test data by Equation 17 (White et al. 2014, White et al. 2007):

$$K_{\text{sat}} = \left[\frac{2\mu_{\text{gas}}QP_{2a}}{rG_0(P_{2a}^2 - P_{\text{atm}}^2)} \right] \times \frac{\rho g}{\mu_{\text{water}}(1 - S_e)^2(1 - S_e^{((2+\lambda)\lambda)})} \quad (17)$$

where,

K_{sat} = saturated hydraulic conductivity (cm/s),

μ_{gas} = kinematic viscosity of the gas (Pa-s),

Q = flow rate (cm³/s),

P_{2a} = absolute gas pressure on the surface (Pa),

r = radius at the outlet (cm),

G_0 = geometric factor determined from test layer thickness,

P_a = atmospheric pressure (Pa),

ρ = density of water (g/cm³),

g = acceleration due to gravity (cm/s²),

μ_{water} = kinematic viscosity of water,

S_e = effective saturation, and

λ = Brooks-Corey pore size distribution index.

3.2.5 Ground Temperature Monitoring

To monitor the local weather conditions, ground temperature, and frost depth of a representative section of Vail Avenue, a weather station (Figure 18a) and six thermocouples (Figure 18b) were installed on November, 2013. The weather station (Novalynx model 110-WS-16) was installed to recorded average ambient air temperature, relative humidity, wind speed and direction, and precipitation at 15 minute intervals. Each of the type T thermocouples were connected to a separate battery-powered data logger that recorded ground temperature with 0.5 °F precision at 5 minute intervals. The locations of the thermocouples are shown in Figure 18c. The top sensor is at the boundary between the surface aggregate and subgrade, and the bottom sensor is 5 ft below the roadway surface

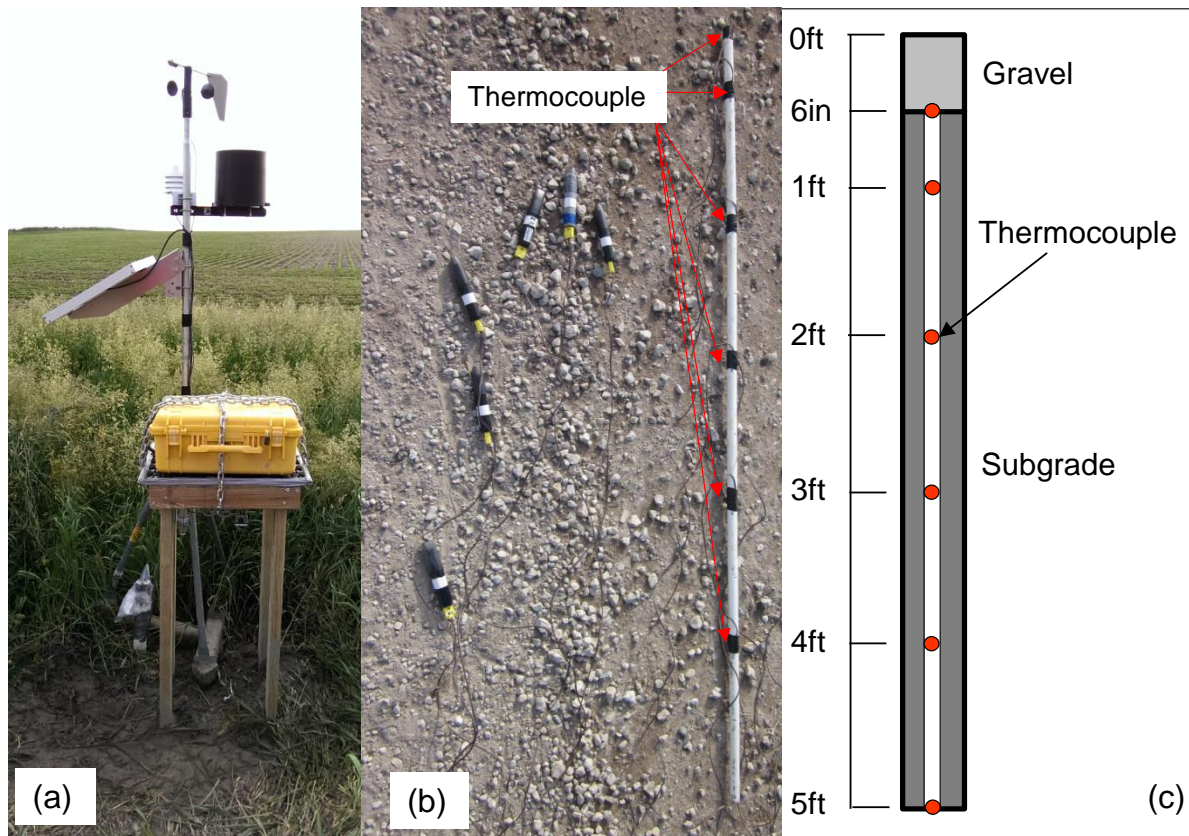


Figure 18. (a) Weather station, (b) thermocouples and data loggers, and (c) layout of thermocouples

Based on the ground temperature data, the number of freeze-thaw cycles was estimated at each measurement depth by counting the number of times the temperature decreased to 31.5 °F or lower then increased to 32.5 °F or higher. Figure 19 shows an example in which nine freeze-thaw cycles were counted at 1 ft depth during the 2014–2015 seasonal freeze-thaw period.

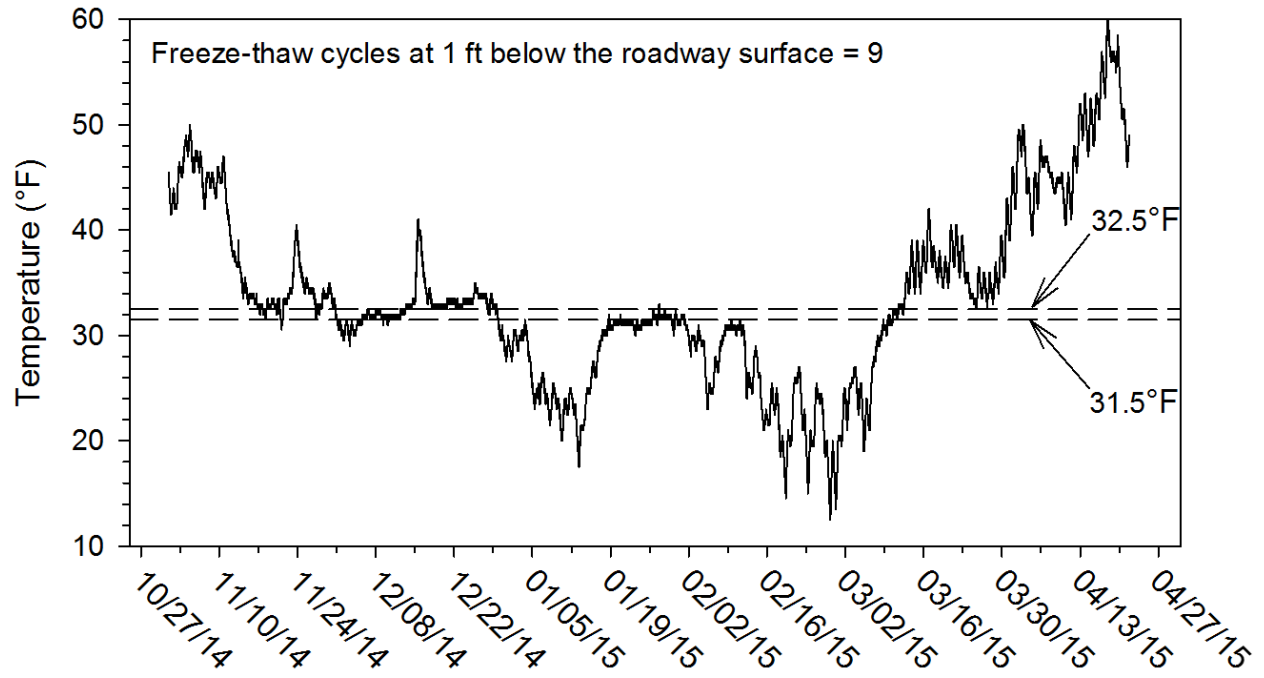


Figure 19. Example of estimating field freeze-thaw cycles from ground temperature data

CHAPTER 4. MATERIALS

This chapter presents the soil index properties, laboratory abrasion test results, and compaction test results of the geomaterials used in the project. The types and sources of chemical stabilizers and geosynthetics used are also discussed.

4.1 Geomaterials

A total of nine types of geomaterials including dirty and clean macadam stone, recycled Portland cement concrete (RPCC) macadam, choke stone, road stone, aggregate column fill, existing surface aggregate, subgrade, and a mixture of subgrade with existing surface aggregate (SG+AGG) were used in the project. Table 5 summarizes the experimentally determined soil index properties and classifications of the geomaterials.

Table 5. Soil index properties of the nine geomaterials used in this project

Parameter	Dirty Macadam	Clean Macadam	RPCC Macadam	Choke Stone	Road Stone	Aggregate Column Fill	Existing Aggregate	Subgrade	SG+AGG Mixture
Particle-size analysis results (ASTM D 422-03)									
Gravel content (%)	56.2	96.4	63.3	60.7	57.9	99.7	25.7	0.9	10.6
Sand content (%)	28.3	3.6	15.4	31.7	30.3	0.3	57.1	39.8	44.9
Silt content (%)	10.7			6.4	9.2			30.6	24.9
Clay content (%)	4.8	0.0	3.7 ^a	1.2	2.6	0.0	17.2 ^a	28.7	19.6
D ₁₀ (mm)	0.028	20.829	0.772	0.140	0.049	19.045	–	–	–
D ₃₀ (mm)	0.680	32.599	12.319	3.053	1.731	20.992	0.282	0.003	0.0096
D ₆₀ (mm)	14.750	42.457	26.704	9.207	9.720	23.488	2.489	0.081	0.3115
Coefficient of uniformity, c _u	524.46	2.04	34.57	65.87	198.96	1.23	–	–	–
Coefficient of curvature, c _c	1.11	1.20	7.36	7.24	6.31	0.99	–	–	–
Atterberg limits test results (ASTM D 4318-10e1)									
Liquid limit (%)	NP	NP	NP	NP	NP	NP	NP	43	30
Plastic limit (%)								22	14
AASHTO and USCS soil classification (ASTM D 2487-11 & D3282-09)									
AASHTO classification	A-1-b	A-1-a	A-1-a	A-1-a	A-1-a	A-1-b	A-1-a	A-7-6(10)	A-6(3)
USCS classification	GM	GP	GP	GP-GM	GP-GM	SM	GP	CL	SC
USCS group name	Silty gravel with sand	Poorly graded gravel	Poorly graded gravel with sand	Poorly graded gravel with silt and sand	Poorly graded gravel with silt and sand	Silty sand	Poorly graded gravel with sand	Sandy lean clay	Clayey sand with gravel

^a Percentage shown includes both silt and clay content.

The following sections consist of scaled photographs of the geomaterials, grain-size distribution curves, Proctor compaction curves, and laboratory abrasion test results.

4.1.1 Choke Stone, Road Stone, Existing Surface Aggregate, and Clean Aggregate Fill

Representative samples of the existing surface aggregate were collected from the Vail Avenue in August, 2013. One-inch road stone, 0.75 in. choke stone, and clean aggregate column fill materials were obtained from the Martin Marietta Aggregates Alden Quarry, which is approximately 26 miles from the Vail Avenue project site. Figure 20 shows these four material types.

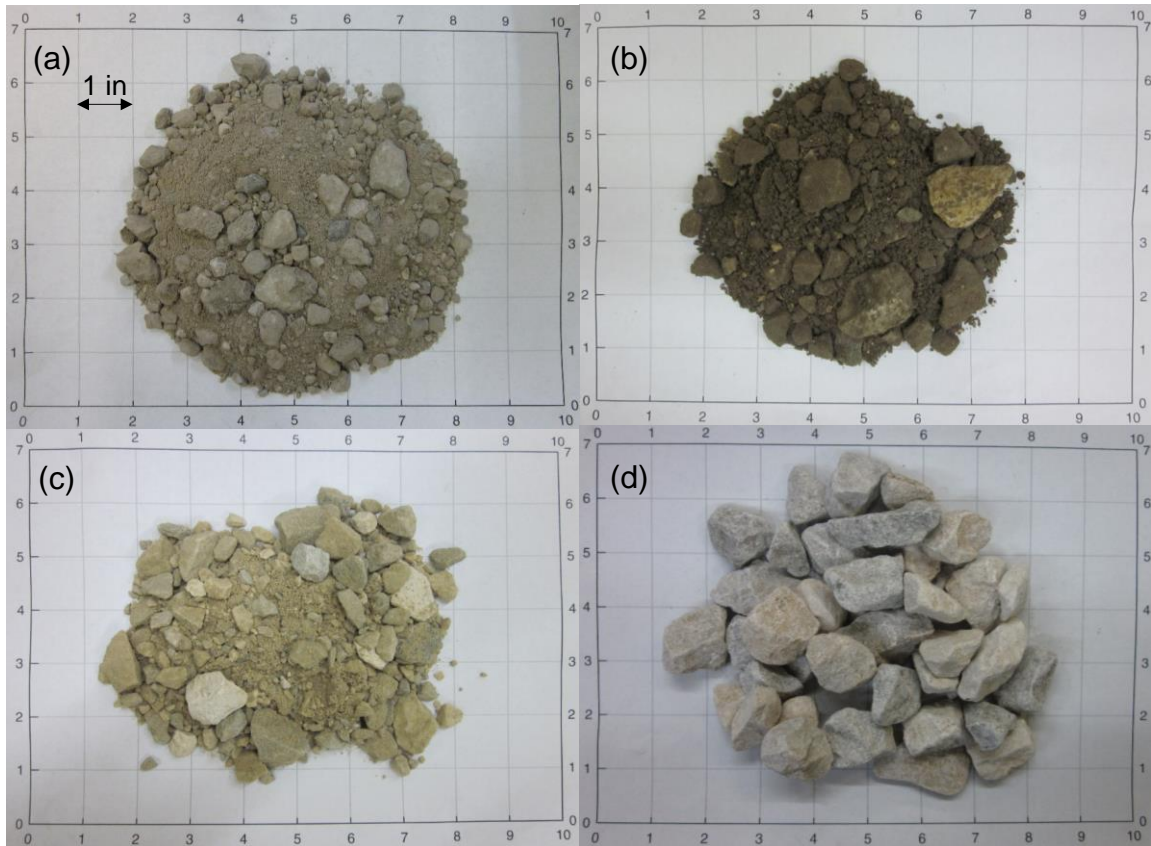


Figure 20. (a) Air-dried existing surface aggregate, (b) 1 in. road stone, (c) 0.75 in. choke stone, and (d) clean aggregate-column fill

Particle size analysis and Atterberg limits tests were conducted on the four types of aggregates to determine the material index properties. Particle size distribution curves of the four materials are shown in Figure 21. The gradation of the 1 in. road stone met the Iowa DOT specifications for Class A granular surfacing material (Gradation No.11 of the aggregate gradation table of Iowa DOT 2012). The gradation of the 0.75 in. choke stone met the Iowa DOT specifications for crushed stone base materials (Section 4122.02 of Iowa DOT 2012), which require 100% passing 3/4 in. or 1 in. and between 6% and 16% fines passing the #200 sieve.

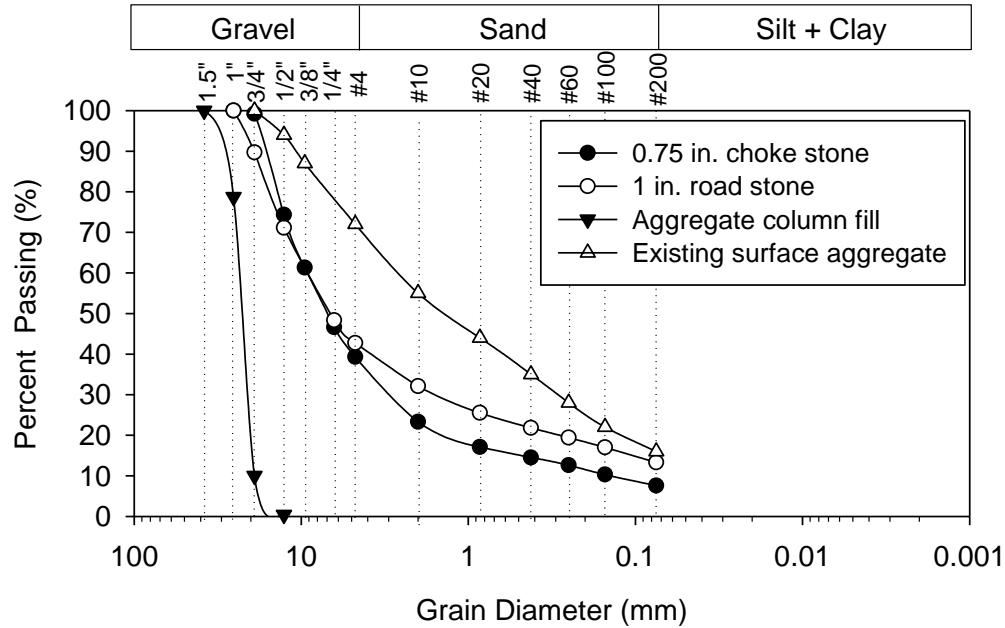


Figure 21. Particle size distribution curves of the four aggregate materials

The moisture-density relationships, optimum moisture contents, and maximum dry unit weights of the existing surface aggregate were determined using standard Proctor compaction tests with 6 in. diameter molds in accordance ASTM D 698-12e1. The bulking moisture content was determined to be 2.2% for this material, which corresponds to the lowest dry unit weight of the compaction curve. The optimum moisture content of the existing surface aggregate is approximately 6.2%, and the corresponding maximum dry unit weight is 140.8 pcf (Figure 22).

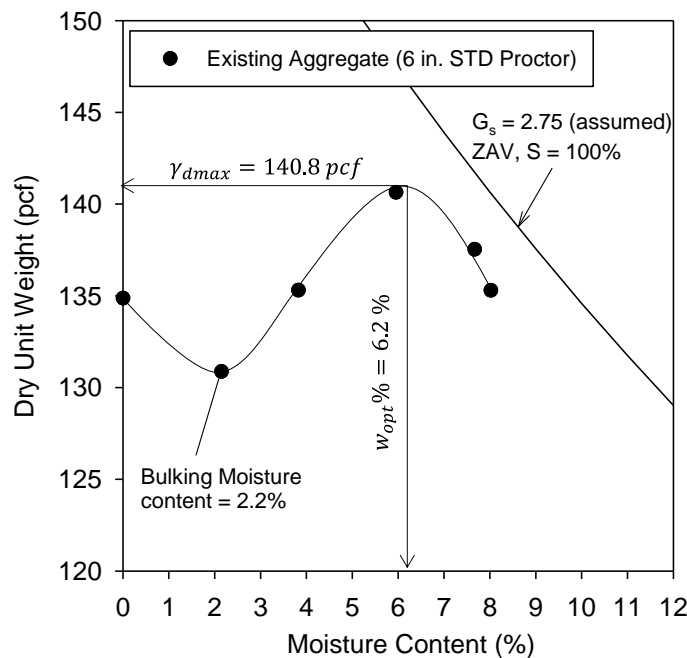


Figure 22. Proctor compaction curve for existing surface aggregate

The abrasion loss of the choke stone and road stone were determined using Micro-Deval tests in accordance with ASTM D 6928-10. Three specimens were tested for each material to determine the average abrasion resistance and durability under abrasion and grinding induced by the Micro-Deval testing machine. The initial gradations and mass of each test specimen are provided in Table 6.

Table 6. Initial gradations and masses of Micro-Deval test specimens

Material	Specimen Number	Material between 3/4 in. and 5/8 in. (g)	Material between 5/8 in. and 1/2 in. (g)	Material between 1/2 in. and 3/8 in. (g)	Total Mass (g)
0.75 in. choke stone	1	375.1	374.9	750.1	1500.1
	2	375.9	375.6	750.1	1501.6
	3	374.7	375.1	749.7	1499.5
1 in. road stone	1	374.5	375.4	750.8	1500.7
	2	375.5	375.8	749.7	1501.0
	3	375.0	374.8	750.2	1500.0

The Micro-Deval test results are summarized in Table 7. The average abrasion losses of both choke stone and road stone were below 30%. These materials therefore met the Iowa DOT specifications, which require that the abrasion loss for granular surfacing materials and choke stone should be less than 45%. However, Iowa DOT specifications state that the abrasion loss should be measured using Los Angeles (L.A.) abrasion tests.

Table 7. Laboratory Micro-Deval abrasion test results for choke stone and road stone

Material Type	Sample Number	Abrasion Loss (%)	Average Abrasion Loss (%)
0.75 in. choke stone	1	20.9	22.4
	2	25.2	
	3	21.2	
1 in. road stone	1	28.1	27.8
	2	26.3	
	3	28.9	

Figure 23 shows pictures of choke stone and road stone before and after the Micro-Deval tests. The particle shapes of both these materials were changed from angular to rounded during the abrasion tests.

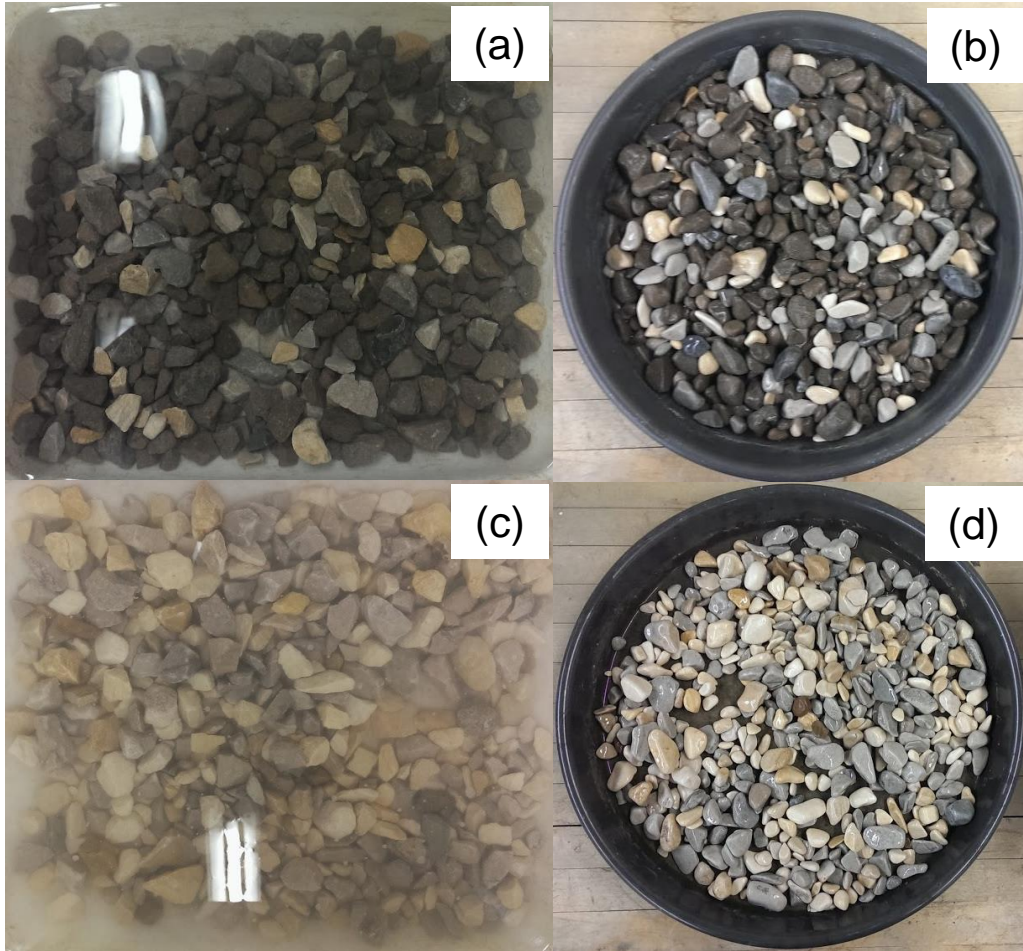


Figure 23. Samples of road stone (a) before and (b) after Micro-Deval tests, and choke stone (c) before and (d) after Micro-Deval tests

4.1.2 Dirty, Clean, and RPCC Macadam Materials

The dirty and clean macadam used as base materials for several demonstration sections were obtained from the Martin Marietta Aggregates Alden Quarry. The recycled Portland cement concrete (RPCC) macadam material was obtained from a concrete recycle pile owned by the Hamilton County Secondary Roads Department. The recycle pile has mixed sources, including recycled pavements, demolitions, and leftover materials from ready-mix concrete trucks. Figure 24 shows scaled photographs of samples of the three types of macadam materials used.

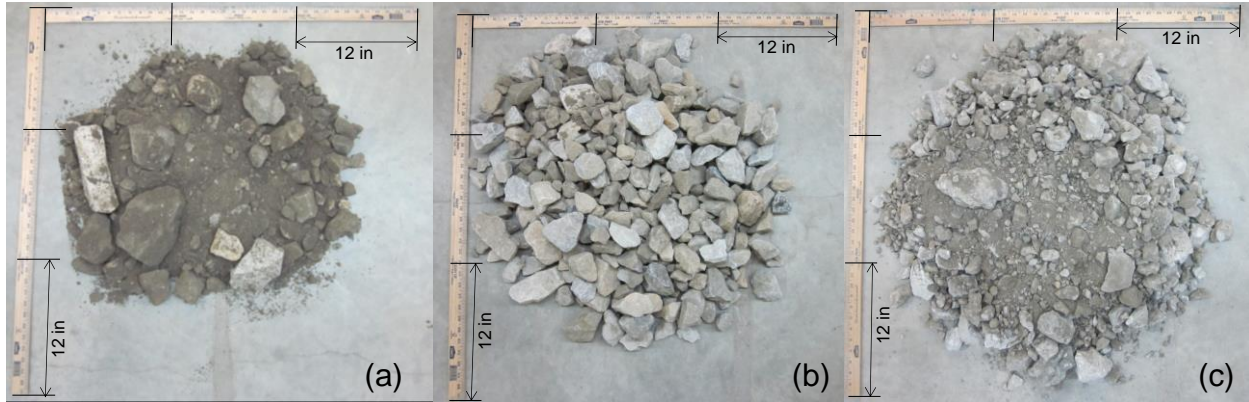


Figure 24. Air-dried samples of (a) dirty, (b) clean, and (c) RPCC macadam materials

The particle size distribution curves of three materials are shown in Figure 25.

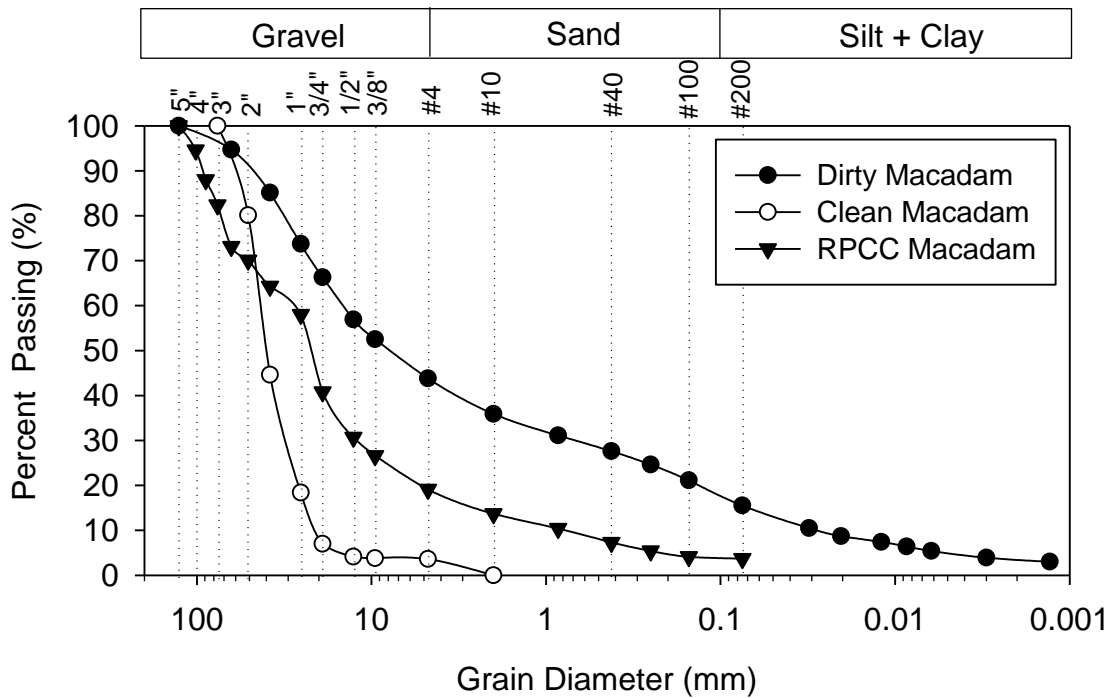


Figure 25. Particle size distribution curves of the three macadam types

A hydrometer test was performed on the dirty macadam stone to determine percentage of silt and clay size particles. Iowa DOT specifications state that the nominal maximum size of macadam stone should be 3 in., and the materials should be screened over a 3/4 in. or 1 in sieve (Section 4122.02 of Iowa DOT 2012). However, of the materials shown in Figure 4, only the clean macadam met this specification. The dirty macadam contained 67% passing the 3/4 in. sieve and 21.7% fines, while the RPCC had a maximum size of 5 in. with 40% passing the 3/4 in. sieve and 3.7% fines.

Laboratory L.A. abrasion tests were also conducted on the three macadam stone samples by the Iowa DOT Central Materials Aggregates Lab, in accordance with ASTM C 535-12. Three specimens were tested for each material to determine the average degradation of aggregates under impact-crushing effects induced by steel spheres in the L.A. abrasion machine. Table 8 shows the gradation and mass of the specimens used.

Table 8. Initial gradations and masses of L.A. abrasion test specimens

Material	Sample #	Material between 3 in. and 2.5 in. (g)	Material between 2.5 in. and 2 in. (g)	Material between 2 in. and 1.5 in. (g)	Total Mass (g)
Dirty Macadam	1	2507.9	2546.3	5028.3	10082.5
	2	2541.8	2548.0	4993.9	10083.7
	3	2509.8	2531.2	4986.7	10027.7
Clean Macadam	1	2545.1	2537.3	5035.4	10117.8
	2	2505.1	2509.4	5043.7	10058.2
	3	2498.3	2512.2	4999.3	10009.8
RPCC Macadam	1	2496.0	2495.1	5017.4	10008.5
	2	2503.8	2497.4	5039.1	10040.3
	3	2499.1	2487.9	5035.4	10022.4

The L.A. abrasion test results are summarized in Table 9.

Table 9. L.A. abrasion test results for the three macadam types

Material Type	Sample Number	Abrasion Loss (%)	Average Abrasion Loss (%)
Dirty Macadam	1	40.01	38.5
	2	37.23	
	3	38.17	
Clean Macadam	1	34.15	34.8
	2	34.55	
	3	35.61	
RPCC Macadam	1	48.29	48.0
	2	48.12	
	3	47.64	

The average abrasion loss of the RPCC macadam was higher than those of the dirty and clean macadam. The average abrasion losses of all three macadam types were below 50%, which is the upper limit specified by Iowa DOT for macadam stone (Table 4122.03-1 of Iowa DOT 2012).

Figure 26 shows dirty, clean, and RPCC macadam specimens after the L.A. abrasion tests. Degradation of the RPCC macadam specimen was more severe than the clean and dirty macadam specimens.



Figure 26. Dirty, clean, and RPCC macadam specimens after L.A. abrasion tests

4.1.3 Subgrade and Mixture of Subgrade with Existing Surface Aggregate (SG+AGG)

Representative samples of the subgrade and existing surface aggregate materials were collected from Vail Avenue. In this project, the subgrade (SG) was also mixed with the existing surface aggregate (AGG) for construction of the cement- and fly ash-stabilized sections. The SG+AGG mixture consisted of 63% SG (5 in.) and 37% AGG (3 in.) by volume. Figure 27 shows the two types of materials.

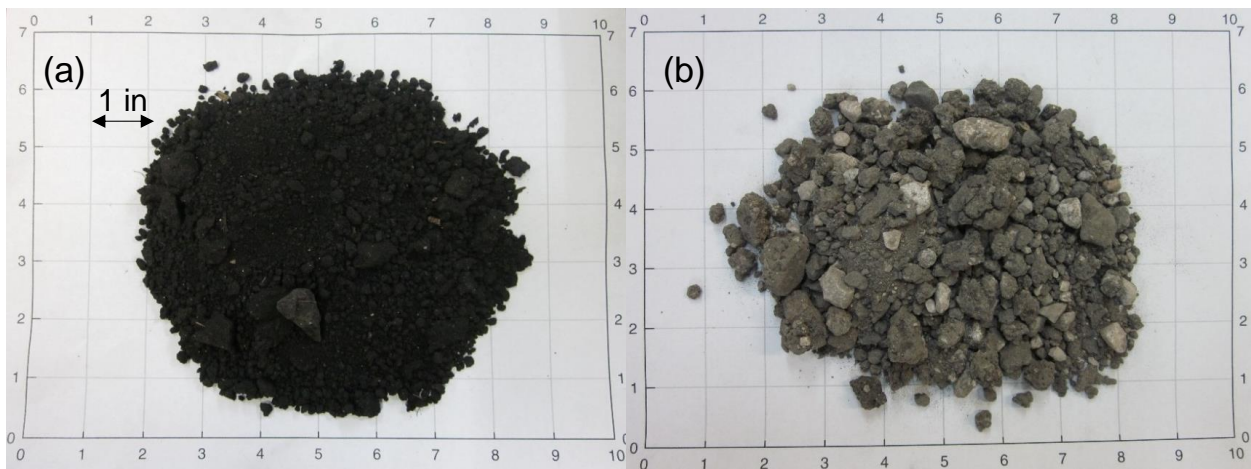
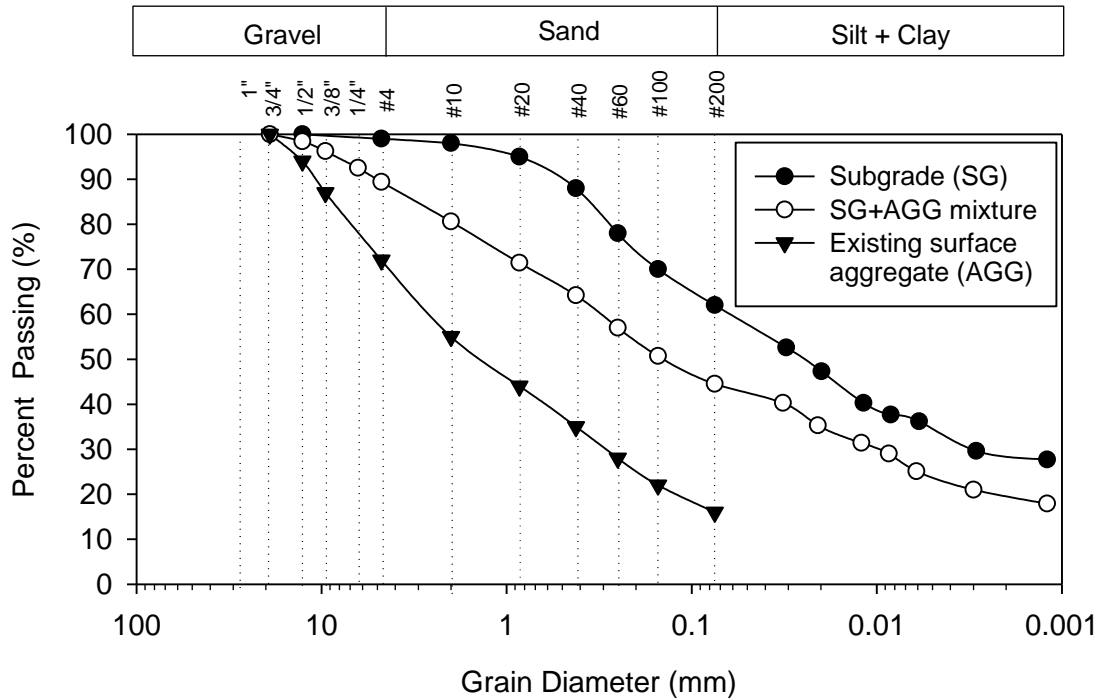


Figure 27. (a) Existing subgrade with 9.0% moisture content and (b) SG+AGG mixture with 1.0% moisture content

Table 5 summarizes the soil index properties of the subgrade. Hydrometer test were performed to determine the silt and clay content of the subgrade and SG+AGG mixture. The particle size distribution curves of the two materials are shown in Figure 28. The subgrade material contains 29% clay and 31% silt. The clay and silt contents of the SG+AGG mixture were 19.6% and 24.9%, respectively.



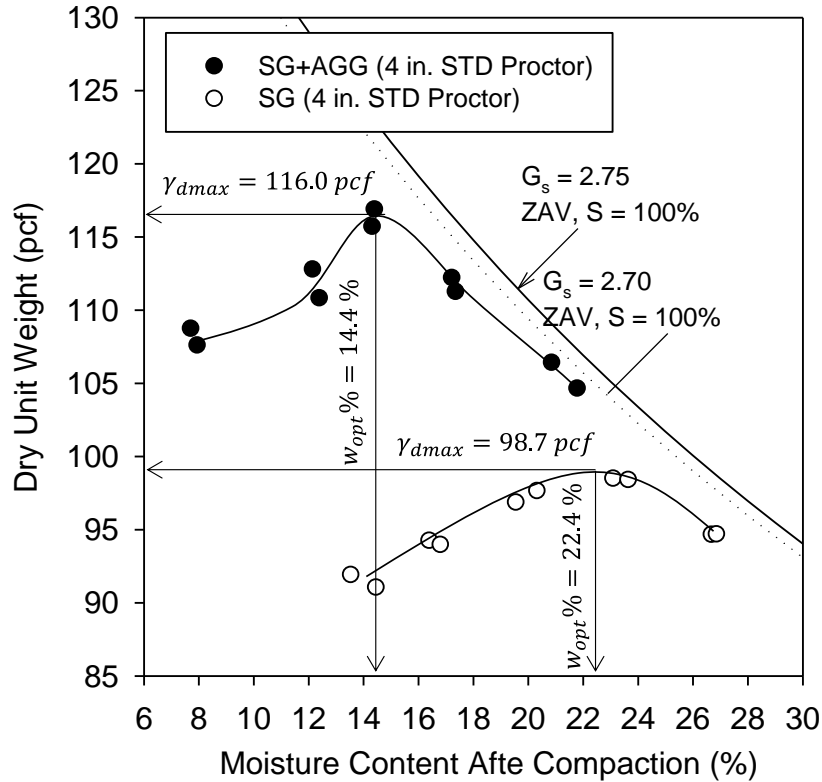


Figure 29. Proctor compaction curves for subgrade and subgrade-aggregate mixture.

4.2 Chemical Stabilizers

Type I/II Portland cement, self-cementing fly ash, and bentonite were used to improve performance and durability of the surface course materials in three of the demonstration sections of the Vail Avenue project. All chemical stabilizers were purchased and applied by Manatts, Inc. The sources of the three chemical stabilizers are provided in Table 10.

Table 10. Sources of chemical stabilizers used in this study

Chemical Stabilizer Type	Manufacturer	Source
Type I/II cement	Lafarge North America, Inc.	Buffalo, Iowa
Class C fly ash	Headwaters Resources, Inc.	Council Bluffs, Iowa
Bentonite	American Colloid Company	Colony East, Wyoming

Based on the product datasheets provided by the manufactures (Appendix A), the self-cementing fly ash is classified as class C per ASTM D 618-12a. Both the fly ash and type I/II cement were found to comply with the applicable Iowa DOT specification requirements. For demonstration Section 17, 6% cement by dry mass was mixed with 8 inches of the in situ SG+AGG material in the field. For Section 16, 15% class C fly ash (ASTM C 618-12a) was mixed with 8 inches of the in situ SG+AGG material. For Sections 1B, 3, and 15, bentonite was mixed with the top 5 in. of the surface course.

According to White et al. (2005a), the fly ash set time can significantly influence the compaction behavior and strength gain of the soil-fly ash mixture. White et al. (2005a) also found that class C fly ash is a highly variable material, with significant variation in set time between different fly ash sources. Representative fly ash samples were collected during construction of the demonstration sections and their set time was measured using the method of White et al. (2005a). Specimens were mixed to 27.5% moisture content in a shallow dish, and a pocket penetrometer was used to measure penetration resistance versus time as shown in Figure 30.



Figure 30. Fly ash set-time test

The measurement range of the pocket penetrometer was 4.5 tsf, so the final set time was recorded when the penetration resistance reached 4.5 tsf. Three replicate tests were conducted on representative fly ash specimens collected during construction of Section 16. The average initial and final set times were 5 and 9 minutes, respectively (Figure 31), which are quick relative to class C fly ash specimens from 13 different Iowa generation stations tested by White et al. (2005a).

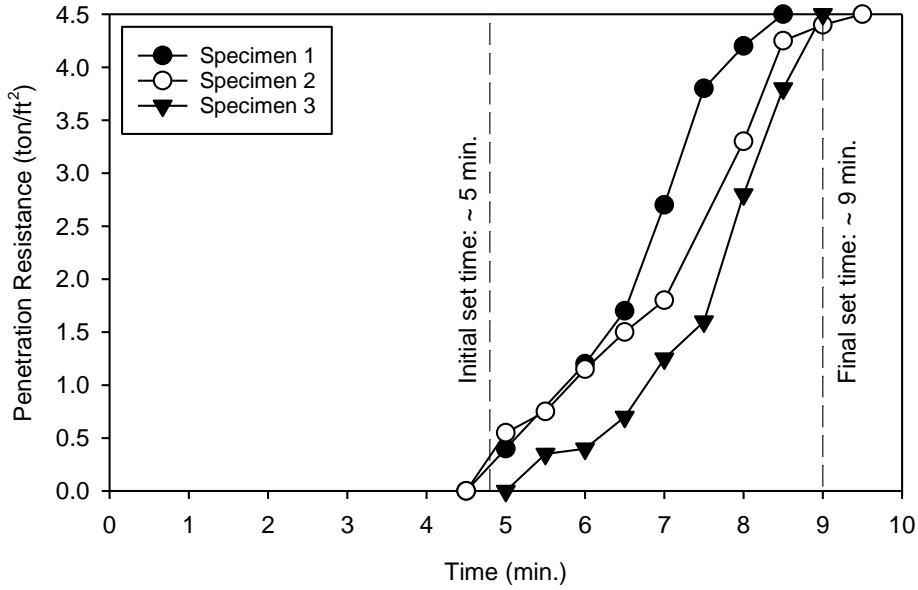


Figure 31. Set time of fly ash used for construction of Section 16

Based on the set-time test results, a compaction delay time of less than 5 minutes is recommended for construction, and the delay time should not exceed 10 minutes.

The chemical composition and mineralogy of the chemical stabilizers were determined using x-ray fluorescence (XRF) and x-ray diffraction (XRD) analyses, respectively. The chemical composition of the fly ash used for Section 16 met the requirements for Class C fly ash designated in ASTM C618-12a (2012), and the sulfur content (SO_3) was about 1.5% (Table 11).

Table 11. Chemical composition of fly ash for Section 16 compared to typical Iowa self-cementing fly ash (Barnes 1997), 13 Iowa self-cementing fly ash samples from seven sources (White et al. 2005a), and ASTM C618 requirements for Class C fly ash

Chemical Composition	Fly Ash for Section 16	Typical Iowa Self-Cementing Fly Ash (Barnes 1997)	Iowa Self-Cementing Fly Ash (White et al. 2005a)	ASTM C618 for Class C Fly Ash
SiO ₂	38.08	20–40	26.10–37.78	–
Al ₂ O ₃	21.42	10–30	16.15–21.22	–
Fe ₂ O ₃	4.96	3–10	4.92–8.74	–
Sum of Oxides	64.46	–	50.98–63.52	50 min.
SO ₃	1.50	1–8	1.71–3.48	5 max.
CaO	23.04	10–32	22.23–28.47	–
MgO	4.30	0.5–8	4.08–5.93	–
Na ₂ O	1.57	0.5–6	1.51–3.42	–
K ₂ O	0.56	0.5–4	0.30–0.63	–
P ₂ O ₅	0.90	–	1.04–1.63	–
TiO ₂	1.56	0.5–2	1.36–1.65	–
SrO	0.37	–	0.30–0.46	–
BaO	0.61	–	0.64–0.83	–
Total	98.87	–	–	–
LOI	0.71	0–3	0.36–9.20	6 max.
Bulk Moisture	0.05	–	0.12–0.46	3 max.

According to White et al. (2005a), sulfur contents greater than 5% may cause formation of ettringite in soil-fly ash mixtures, which can cause long-term volume expansion and reduce strength and durability. The fly ash used in this study had a similar chemical composition to the typical Iowa self-cementing fly ash reported in Barnes (1997), but had higher SiO₂ and Al₂O₃ and lower SO₃ contents than the fly ash reported in White et al. (2005a). The quick set time measured for the fly ash of Section 16 may be due to the high Al₂O₃ and low SO₃ contents, because the initial formation of cementitious reaction is due to hydration of tricalcium aluminate (Ca₃Al₂O₆), while sulfates tend to retard the initial setting of fly ash.

The XRD results showed that the primary minerals in the fly ash are quartz (SiO₂), tricalcium aluminate (Ca₃Al₂O₆), anhydrite (CaSO₄), and lime (CaO), which are common minerals in self-cementing fly ash (Figure 32).

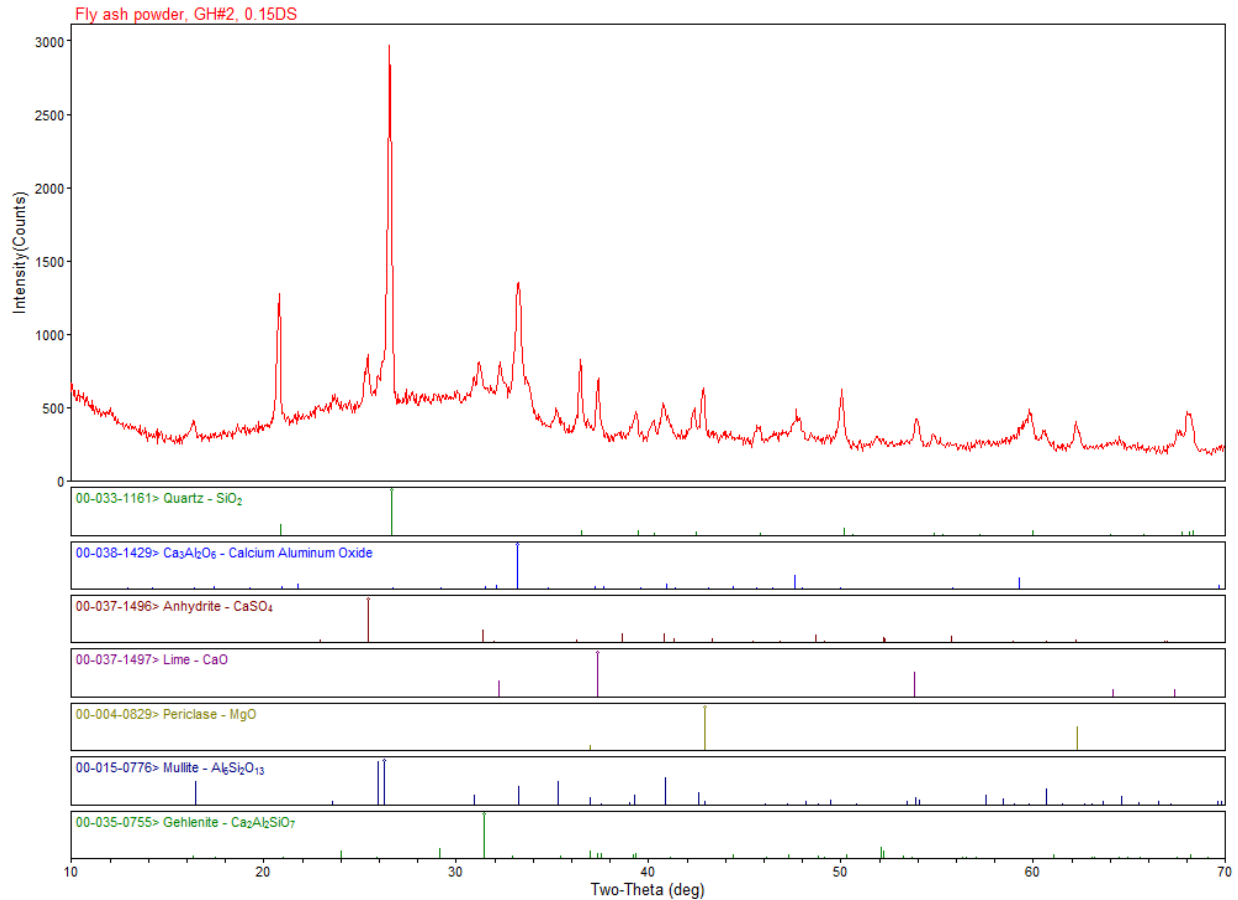


Figure 32. XRD results for fly ash of Section 16

White et al. (2005) also explained that “*tricalcium aluminate is important because it contributes to initial hardening when hydrated. The free lime also contributes to the formation of cementitious reaction products in combination with silicon and aluminum in the fly ash and clay minerals. Anhydrite is a precursor to ettringite formation.*” However, the ettringite could be minimal due to low sulfur content of the fly ash material as shown in Table 11.

The XRD results showed that the bentonite used in this project was sodium montmorillonite ($\text{Na}_{0.3}(\text{Al},\text{Mg})_2\text{Si}_4\text{O}_{10}(\text{OH})_2 \cdot 4\text{H}_2\text{O}$) with calcite (CaCO_3) and quartz (SiO_2) (Figure 33). The XRF results showed that the main chemical components of the bentonite were SiO_2 and Al_2O_3 (Table 12).

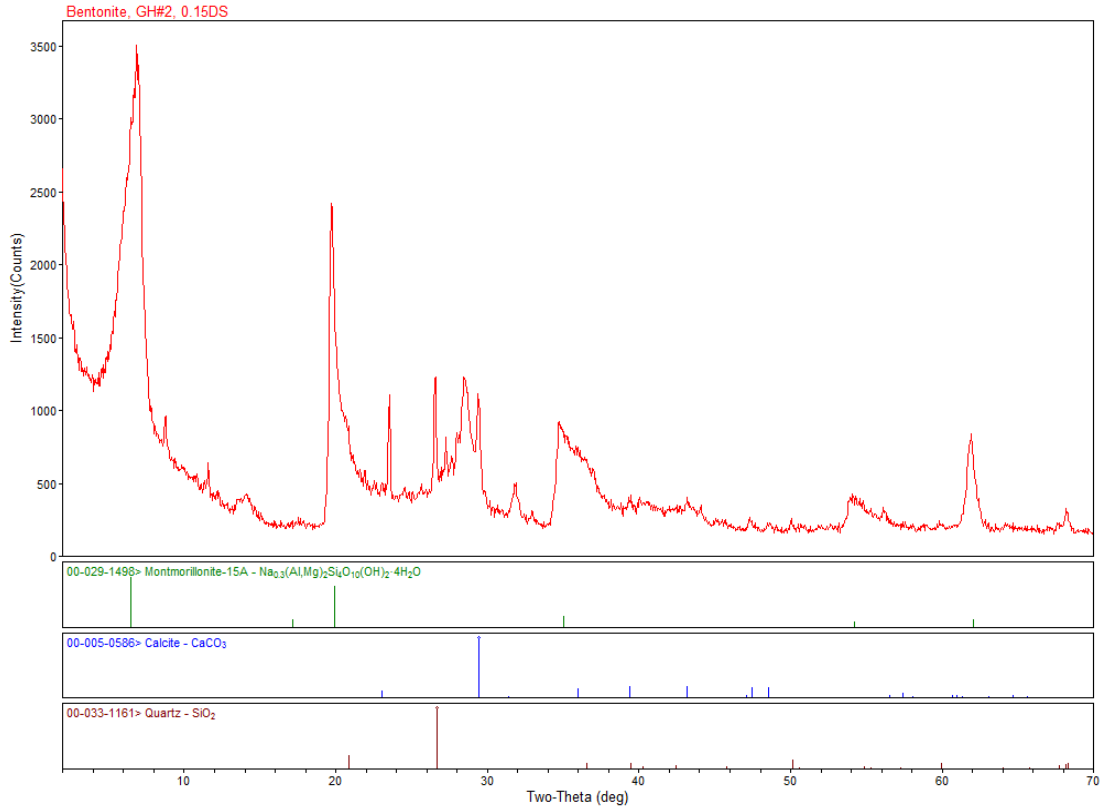


Figure 33. XRD results for bentonite of Section 15

Table 12. Chemical composition of bentonite used for Sections 1B, 4, and 15

Chemical Composition	Percent
SiO_2	58.77
Al_2O_3	20.66
Fe_2O_3	3.81
Sum of Oxides	83.24
SO_3	0.86
CaO	2.42
MgO	3.61
Na_2O	2.45
K_2O	0.62
P_2O_5	0.08
TiO_2	0.18
SrO	0.03
BaO	0.02
Total	93.50
LOI	6.15
Bulk Moisture	7.60

4.3 Geosynthetics

Non-woven geotextile, biaxial geogrid, and three different types of geocomposite materials were used to provide separation, planar subsurface drainage, or reinforcement for the surface course and subgrade of several demonstration sections of the Vail Avenue project. The sources and mechanical properties of the geosynthetics are presented in the following sections.

4.3.1 Non-woven Geotextile

Mirafi 160N non-woven geotextile (NW-geotextile) was purchased from the Northern Iowa Construction Products Inc. The material is composed of polypropylene fibers and can be used to provide planar subsurface drainage and separate soil layers. The properties of the NW-geotextile meet the AASHTO specification for Class II geotextile for elongation greater than 50% (AASHTO M288-06). Also, the material meets the Iowa DOT specifications for engineering fabrics used for subsurface drainage (Section 4916 of Iowa DOT 2012). A full product datasheet is provided in Appendix A.

4.3.2 Biaxial Geogrid

Mirafi BXG110 biaxial geogrid was obtained from Northern Iowa Construction Products Inc. to provide reinforcement for both the surface course and subgrade material. The BX geogrid is composed of polypropylene resin with rectangular-shaped aperture openings with a size of 1 in. According to the FHWA geosynthetic manual (Holtz et al. 2008), the aperture size of a BX-geogrid should be greater than D_{50} but smaller than 2 times D_{85} of the aggregate above the geogrid. As shown in Table 13, these criteria were met for the 1 in. road stone, but not for the existing surface aggregate. A detailed product datasheet for this geogrid is also provided in Appendix A.

Table 13. D_{50} and 2 times D_{85} of existing surface aggregate and 1 in. road stone

Parameters	Existing Surface Aggregate	1 in. Road Stone
D_{50} , in.	0.054	0.273
$2 \times D_{85}$, in.	0.702	1.368

4.3.3 Macdrain Geocomposite

Two types of Macdrain (MD) geocomposite planar drainage materials (W1051 and W1091) were donated by Maccaferri's parent company in Italy. The materials are designed to provide three-dimensional subsurface drainage, soil separation, and filtration. They consist of two layers of non-woven geotextile surrounding a flexible core made of synthetic polymers. Figure 34a shows the W1051 geocomposite with the upper layer of non-woven geotextile peeled back. Compared to W1051, the W1091 product has a heavier flexible core and a higher compressive strength. Both of the materials meet the Iowa DOT specifications for engineering fabrics for subsurface drainage (Section 4916 of Iowa DOT 2012). Detailed product datasheets for these materials are provided in Appendix A.

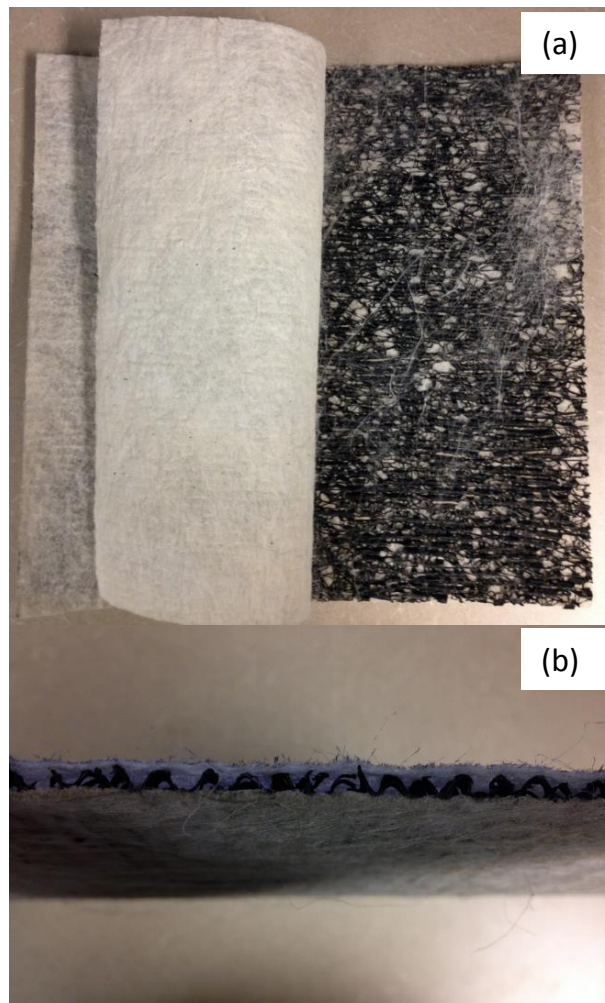


Figure 34. Macdrain W1051 geocomposite material: (a) top view and (b) side view

4.3.4 Roadrain Geocomposite

Roadrain geocomposite drainage material (RD-5) from Tensar International was used as a lining for half of the aggregate columns to improve drainage and prevent contamination of the clean aggregate fill by subgrade material. The geocomposite consists of two layers of non-woven geotextile and a geonet core made of synthetic polymers. Figure 35a shows a sample of the RD-5 geocomposite material with the upper layer peeled back to expose the core. The product datasheet is attached in Appendix A.

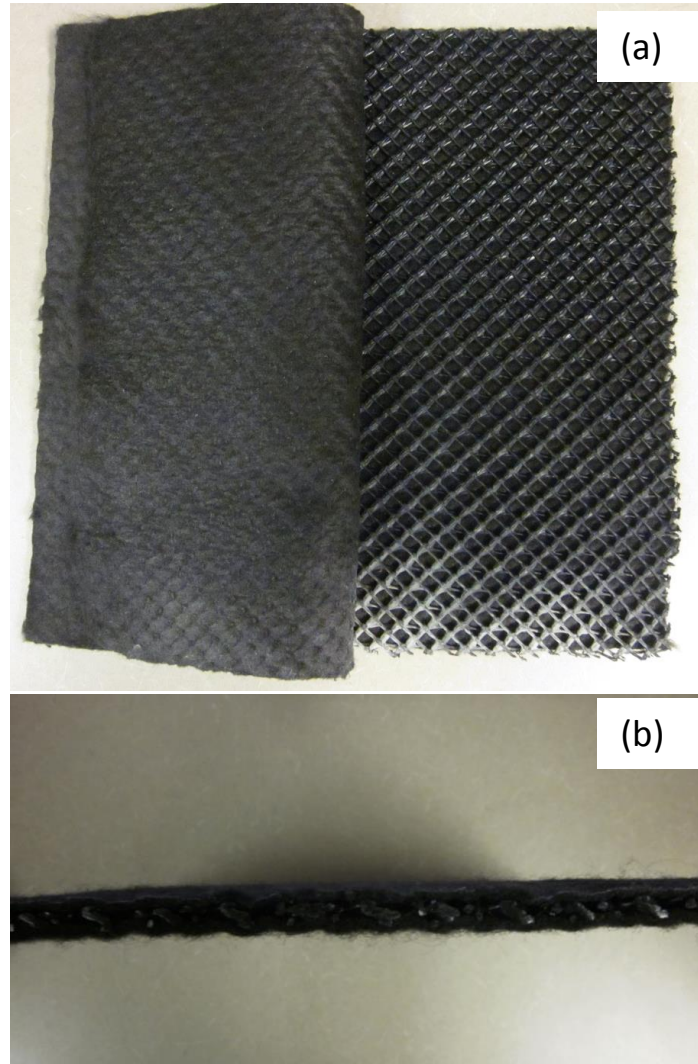


Figure 35. Tensar Roadrain RD-5 geocomposite: (a) top view and (b) side view

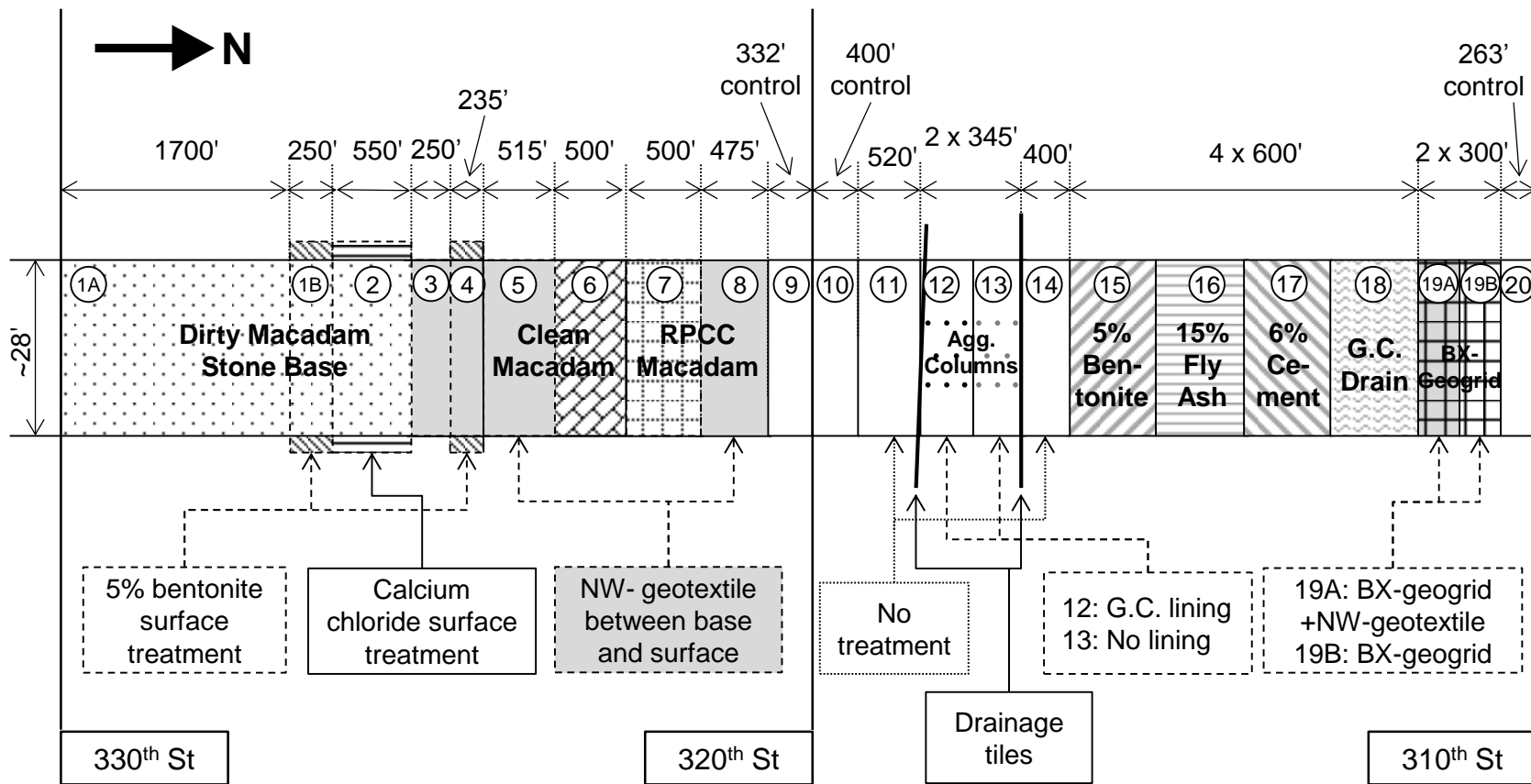
CHAPTER 5. CONSTRUCTION METHODS

The construction procedures, equipment, and dates for the various sections of the demonstration project are detailed in the following sections. A two-mile stretch of Vail Avenue between 330th and 310th streets was divided into a total of twenty-two demonstration sections, including five untreated control sections (Figure 36). Several of the most promising stabilization and construction technologies identified in the previous IHRB project “Low Cost Rural Surface Alternatives” (IHRB 10-05) were selected by the research team in consultation with the project technical advisory committee (TAC) for use in the present project. Construction of the demonstration sections was performed by the Hamilton County secondary roads department, with the exception of the chemical stabilization Sections 15–17 (bentonite, cement, and fly ash) and bentonite mixing for Sections 1B and 4, which were constructed by Manatts, Inc.

5.1 Macadam Stone Base: Sections 1 through 8

The first mile of Vail Avenue between 330th and 320th street was constructed using the three macadam types described in Chapter 4 as base layers. The macadam stone in this project was not bound with tar or bitumen. Various combinations of macadam stone base layers, a nonwoven geotextile interlayer, bentonite, and a calcium chloride surface treatment were used, giving a total of eight different section designs in the first mile, along with a ninth control section. The dirty macadam stone base was used for the first 2,985 ft of roadway (Sections 1–4), followed by 1,000 ft of clean macadam stone base (Sections 5 and 6), 975 ft of RPCC macadam base materials (Sections 7 and 8), and a 332 ft control section (Section 9).

The construction procedures and equipment used for these macadam base sections are shown in Figure 37. The macadam materials were placed in one lift on top of the existing road surface using a Jersey Spreader (Caterpillar 102) and compacted by a smooth drum vibratory roller compactor (Bomag BW211-D40) as shown in Figure 37a. The thickness of the macadam base layer was approximately 6 in. after compaction. For Sections 3, 4, 5, and 8, the non-woven geotextile was placed on top of the macadam base layer to provide planar subsurface drainage and maintain separation between the macadam and choke stone layers (Figure 37b). The average thickness the choke stone layers in each section varied between 2 and 3 in. (Figure 37c). Above the choke stone layer, a road stone layer approximately 2 to 3 in. thick was built as a surface course for these sections. During construction, where the aggregate materials were very dry, a water truck was used to increase the water content and reach a greater degree of compaction. After compaction of the surface course, the road was shaped to a 4% crown using a motor grader (Caterpillar 12M2) as shown in Figure 37d. The construction speed for the macadam base sections depended highly on the availability of trucks for hauling materials from the quarry, which is 26 miles from the project site. For future projects, access to a quarry closer to the construction site can potentially provide significant savings on construction costs.



Not to scale

Figure 36. Plan view of demonstration sections on Vail Avenue in Ellsworth, Iowa



Figure 37. Construction procedures and equipment for Sections 1-8 with macadam base courses: (a) placing macadam with Jersey spreader, (b) non-woven geotextile interlayer, (c) spreading choke stone with Jersey spreader, and (d) shaping with motor grader

Typical cross-sections of the base and surface course of Sections 1–9 between 330th and 320th Streets are shown in Figure 38. For Section 2, liquid calcium chloride was sprayed on the road surface by a local resident for dust control purposes in summer 2014. Construction of the first mile (Sections 1 through 8) was completed in 9 days, September 5 to 19, 2013 except for the bentonite for Sections 1B and 4, which were mixed by Manatts, Inc. September 20, 2014.

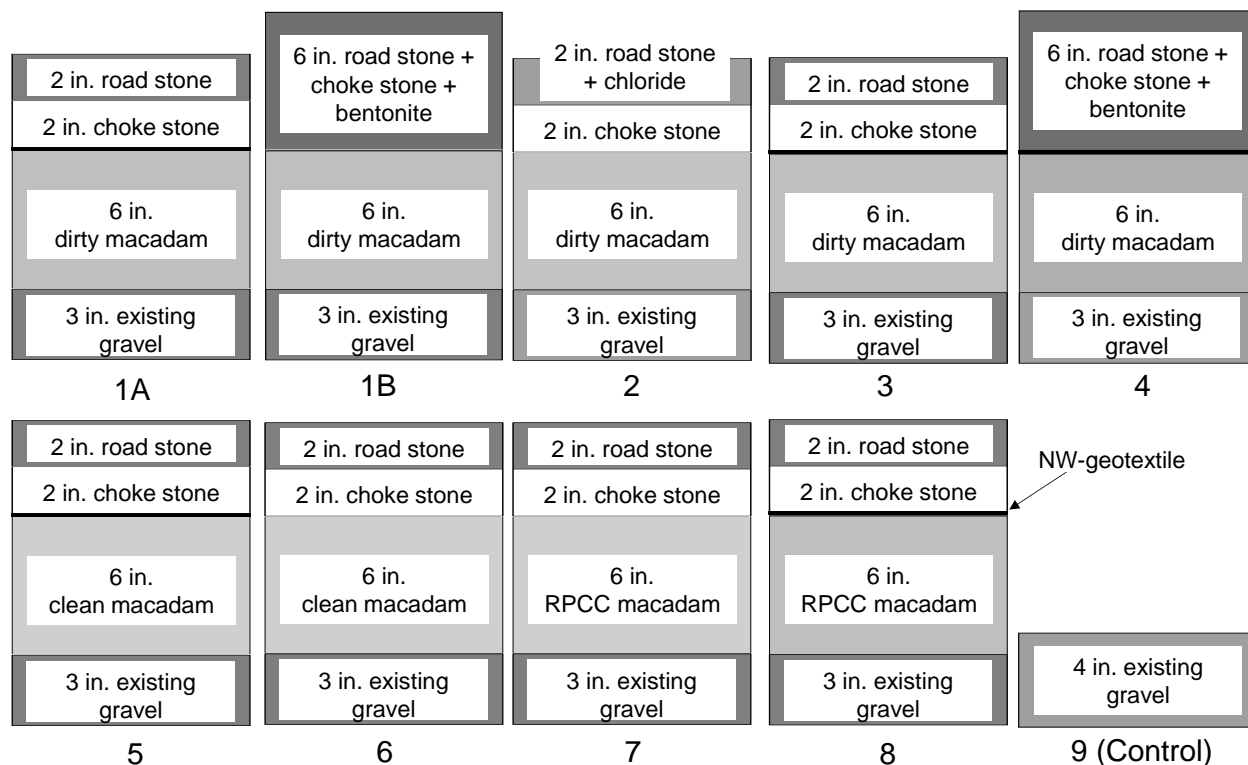


Figure 38. Cross-sectional profiles with nominal thicknesses for Sections 1A through 9

5.2 Aggregate Column Drains: Sections 12 and 13

The first 280 ft of the second mile was used as control (Section 10 in Figure 36). Two drainage tiles ran beneath the roadway from west to east as shown in Figure 1, with the first tile slightly skewed and the second perpendicular to the road alignment. Since frost boils were often observed to occur near these tile crossings, aggregate column drains were installed on one side of each tile crossing (Sections 12 and 13), with the other sides used as controls (Sections 11 and 14). This allowed the effectiveness of the aggregate columns next to the drainage tiles as well as in general cross sections away from the tile crossings to be assessed for mitigating freeze-thaw damage. In Section 12, the bottom 48 in. of the aggregate column drains were lined around the perimeter with the Tensar Roadrain™ RD-5 geocomposite detailed in Chapter 4. This was done to study whether use of the geocomposite offers a measurable performance advantage by preventing contamination of the clean aggregate fill by the subgrade soil and thus improving drainage.

The construction procedures, equipment, and layout of the aggregate column drains are shown in Figure 39. Construction equipment and labor for installing the columns was provided by the Greene County Engineer’s Office. Holes for the aggregate columns were drilled to a depth of 6 ft using a Bobcat skid-steer loader with an 8 in. auger (Figure 39a). The RD-5 geocomposite material lining the bottom 48 in. of the columns in Section 12 are shown in Figure 39b. For comparison, no geocomposite linings were installed in the aggregate columns in Section 13. Clean aggregate was backfilled in the augured holes using a dump truck (Figure 39c). The

aggregate column layout is shown in Figure 39d, with approximately 1 column per 25 square yards of surface area. Both sections were constructed September 26, 2013, requiring seven hours labor for installation of a total of 83 columns (41 columns in Section 12 and 42 in Section 13).

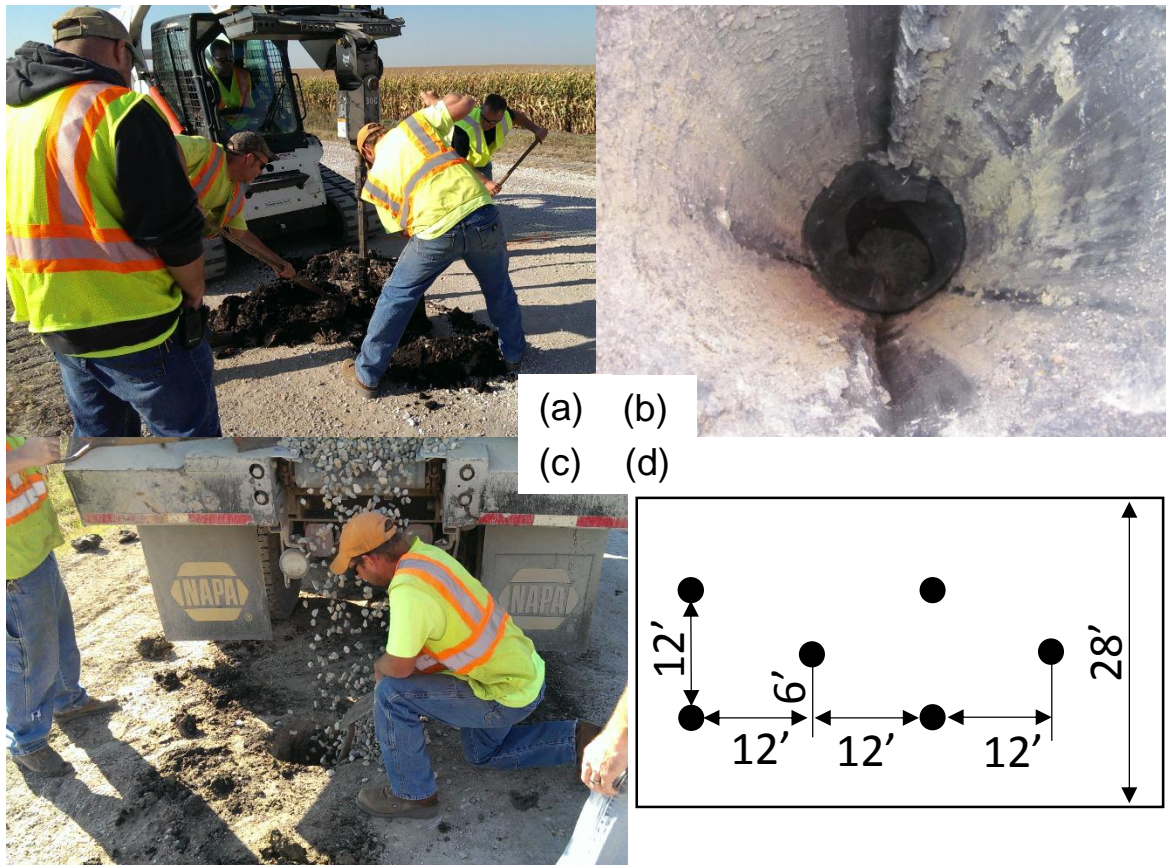


Figure 39. Construction procedures and equipment for aggregate columns in Sections 12 and 13: (a) drilling columns, (b) placing geocomposite lining, (c) filling with clean aggregate, and (d) column layout pattern

5.3 Chemical Stabilization: Sections 15 through 17

The bentonite-, fly ash-, and cement-stabilized sections were constructed by Manatts, Inc. using a full-depth reclamation (FDR) machine September 30 (Sections 15 and 17) and October 2, 2014 (Section 16). For Section 15, 5% bentonite by dry mass was mixed with the top 5 in. of surface aggregate. For Sections 16 and 17, 15% by dry mass class C fly ash and 6% type I/II cement were mixed with the nominal 3 in. thick existing surface course and 5 in. of the subgrade material. The chemical stabilizers were first spread on the existing road surface using a powder truck (Figure 40a), then a full depth reclaimer (Wirtgen WR-2500S) connected to a water truck was used to mill the chemical stabilizers to the specified depth and water content (Figure 40b). The field moisture contents of the mixtures were close to the optimum moisture contents determined by laboratory standard Proctor tests. A vibratory pad-foot roller (HAMM 3412P) following the FDR machine (Figure 40c) was used to compact the mixtures immediately after milling to reduce compaction delay time, because the chemical stabilizers can setup quickly

(under 30 minutes) which would adversely affect final performance. After compaction of the fly ash and cement sections, the road surface was covered by a nominal 1 in.-thick layer of road stone to prevent wearing and retain moisture during curing of the chemically stabilized material (Figure 40d).



Figure 40. Construction procedures and equipment for chemically stabilized Sections 15, 16, and 17: (a) powder truck for spreading bentonite, fly ash, and cement, (b) full depth reclaimer connected to water truck milling chemical stabilizers to the specified depth and water content, (c) vibratory pad-foot roller following the full depth reclaimer, and (d) 1 in.-thick road-stone wearing surface

Typical cross-sectional profiles of the chemical stabilization sections are shown in Figure 41. For future chemical stabilization projects, the forecasted wind speed should be carefully considered when selecting the construction date and time, because a portion of the chemical stabilizers can be easily blown from the road surface prior to mixing and compaction.

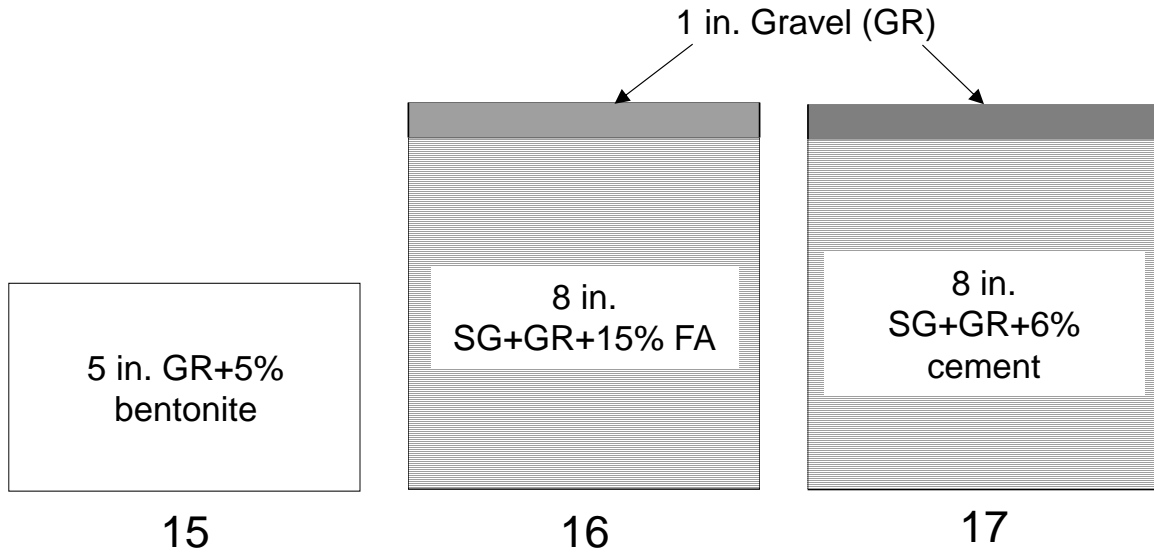


Figure 41. Typical surface course cross-sectional profiles of chemically-stabilized Sections 15, 16, and 17

5.4 Geosynthetic Interlayers: Sections 18, 19A, and 19B

Three types of geosynthetic materials were placed between the subgrade and surface course to provide subsurface drainage, separation, and reinforcement for three demonstration sections. Sections 19A and 19B were constructed October 1 and 2, 2013, and Section 18 was constructed June 5 and 6, 2014. Construction procedures for the three sections were the same (Figure 42). First, the existing surface course material was removed using a Caterpillar motor grader (Figure 42a). The Macdrain (MD) W1051 and W1091 geocomposite, non-woven geotextile with biaxial (BX) geogrid, and the BX geogrid alone were installed for Sections 18, 19A, and 19B, respectively (Figure 42b, 42c, and 42d). For the geocomposite Section 18, the W1091 material was installed for approximately 450 ft starting at the south end, and the W1051 was installed for the remaining 150 ft. After laying down the geocomposite in Section 18, an earth mover was used to replace the surface course material (Figure 42c) because a motor grader could easily roll-up and damage the geocomposite. A motor grader was used to replace the surface course in Sections 19A and 19B. The surface courses of the three sections were approximately 8 in. thick after compaction by a rubber-tire compactor (Figure 42f) and shaping by a motor grader. Typical cross-section profiles of the geosynthetically stabilized sections are shown in Figure 43.



Figure 42. Construction procedures and equipment for geosynthetically stabilized sections: (a) removal of existing surface, (b) geocomposite in Section 18, (c) replacement of surface course by earth mover for geocomposite Section 18, (d) BX geogrid in Section 19B on left with added non-woven geotextile in Section 19A on right, (e) replacement of surface course by motor grader for Sections 19A and 19B, and (f) compaction by rubber-tire compactor

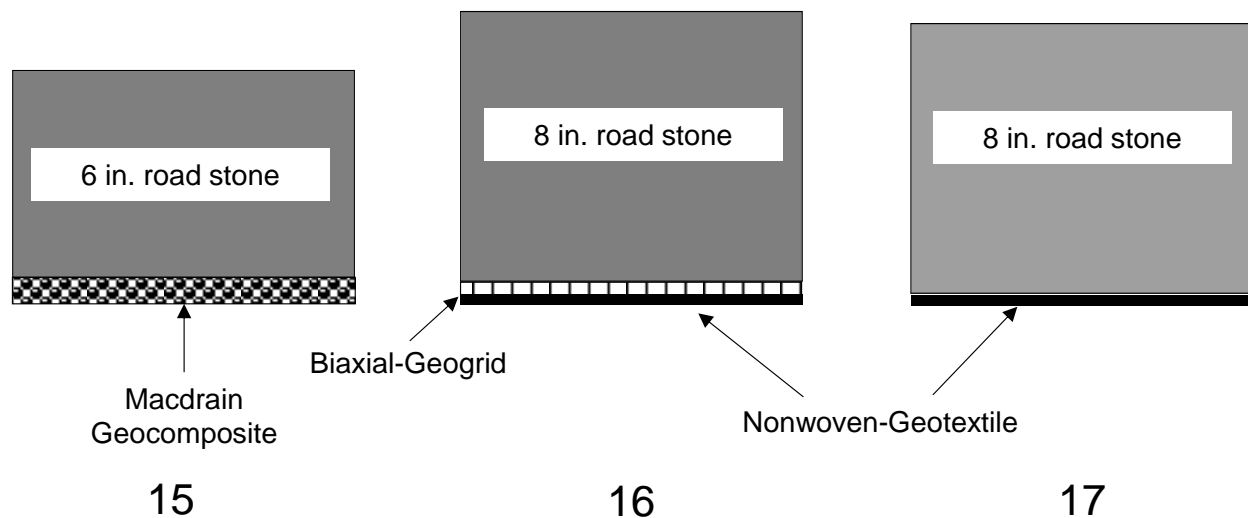


Figure 43. Typical surface course cross-sectional profiles of geosynthetically stabilized Sections 18, 19A, and 19B

5.5 QC/QA Methods

Quality control and quality assurance (QC/QA) for construction of the demonstration sections primarily consisted of visual observations and experience of the construction crew and county engineer.

For the macadam sections, the thickness of each layer before compaction was controlled by the Jersey spreader set at fixed heights determined from several trials of placement and compaction. An average of six to eight vibratory roller compactor passes were conducted on each layer. The moisture contents of the macadam materials were not adjusted, but the moisture contents of the choke stone and road stone were increased using a water truck when the materials were observed to be very dry (i.e., fine particles were seen blowing from the road surface). However, to avoid compacting the granular materials at their bulking moisture contents, which can significantly decrease compatibility of the materials, high compaction moisture contents are recommended. The road surface crown was shaped by the motor grader with the moldboard board set at a 4% angle.

For each of the chemical stabilization sections, the average thickness of the existing surface course was measured before construction. If the existing surface course was thinner than the design thicknesses, virgin 1 in. road stone was added. During construction, the mixing depths were controlled by the FDR machine set at the specified depths. For the fly ash and cement stabilization sections, the target compaction moisture contents were determined by laboratory mix design tests. The target moisture contents were found to be close to the optimum moisture contents determined by standard Proctor tests. The hand-feel for the materials at their target moisture contents were then described to the construction crew. During mixing, a construction supervisor followed the FDR to check the moisture contents of the mixed materials at 20 ft intervals, and moisture content was adjusted if necessary. Another critical factor that can

significantly influence the performance of fly ash- and cement-stabilized materials is the compaction delay time. In this project, the compactor followed the FDR, and the compaction delay time was controlled to be less than 5 minutes after mixing.

For the geosynthetically stabilized sections, the existing surface course was removed to expose the subgrade. The geosynthetic was then laid down by a crew of 5 as shown in Figure 42b. If the geosynthetic tended to roll up during replacement of the surface course, the rolled-up portions were cut to maintain contact between the geosynthetic and subgrade. To meet the design thickness of surface course layers, the amount of additional virgin materials needed was calculated assuming that the virgin aggregate could be placed at 95% Proctor density. An average of six to eight passes was made using a rubber tire compactor on the surface course materials. For the geocomposite and NW-geotextile sections, however, a vibratory roller compactor is recommended. The roadway surfaces of the geosynthetically stabilized sections were shaped using the same equipment and procedures used for the macadam sections.

CHAPTER 6. RESULTS AND DISCUSSION

This chapter consists of the following parts:

1. Results of field and laboratory tests on the existing roadway materials prior to stabilization
2. Laboratory mix-design test results for the chemically stabilized sections
3. Laboratory permeameter test results for the geocomposite drain section
4. As-constructed performance data for all stabilized demonstration sections prior to a freeze/thaw cycle
5. Post-thawing performance and durability data for all sections
6. Economic analysis including construction and maintenance costs of the various demonstration sections

6.1 Pre-Construction Conditions of Existing Roadway

Field and lab tests were conducted to evaluate the in situ support conditions and materials present at the project site. Dynamic cone penetrometer (DCP) and falling weight deflectometer (FWD) tests were conducted to measure the penetration resistance profiles and elastic modulus values of the existing roadway. Laboratory California bearing ratio (CBR) and unconfined compressive strength (UCS) tests were also performed to determine and compare strength parameter values of the materials.

6.1.1 DCP and FWD Tests

The initial DCP and FWD tests were performed on August 7, 2013 within three representative sections (Sections 10, 18 and 19 – See Figure 36). For each section, three DCP tests were performed to determine nominal thickness of the surface aggregate layer and estimate the in situ CBR of the aggregate layer and underlying subgrade to a depth of about 36 inches. Figure 44 shows DCP test results. The thickness of the surface aggregate layer ranged from 3.7 to 6.3 in. based on interpretation of the cumulative blows plot and DCP-CBR versus depth profiles. DCP-CBR values were above 100% within the surface aggregate layer and decreased with depth in the subgrade.

The average thickness and DCP-CBR values for the surface aggregate layer (DCP-CBR_{AGG}) and subgrade (DCP-CBR_{SG}) are summarized in Table 14. The overall average thickness of the surface course of the three sections was 4.8 in., and the overall average values of DCP-CBR_{AGG} and DCP-CBR_{SG} were 161% and 12.5%, respectively. Support ratings based on SUDAS (2015) are also provided in Table 14 for the aggregate and subgrade layers. Field observations during the in-situ testing included that test sections were relatively dry and stable with no significant rutting issues.

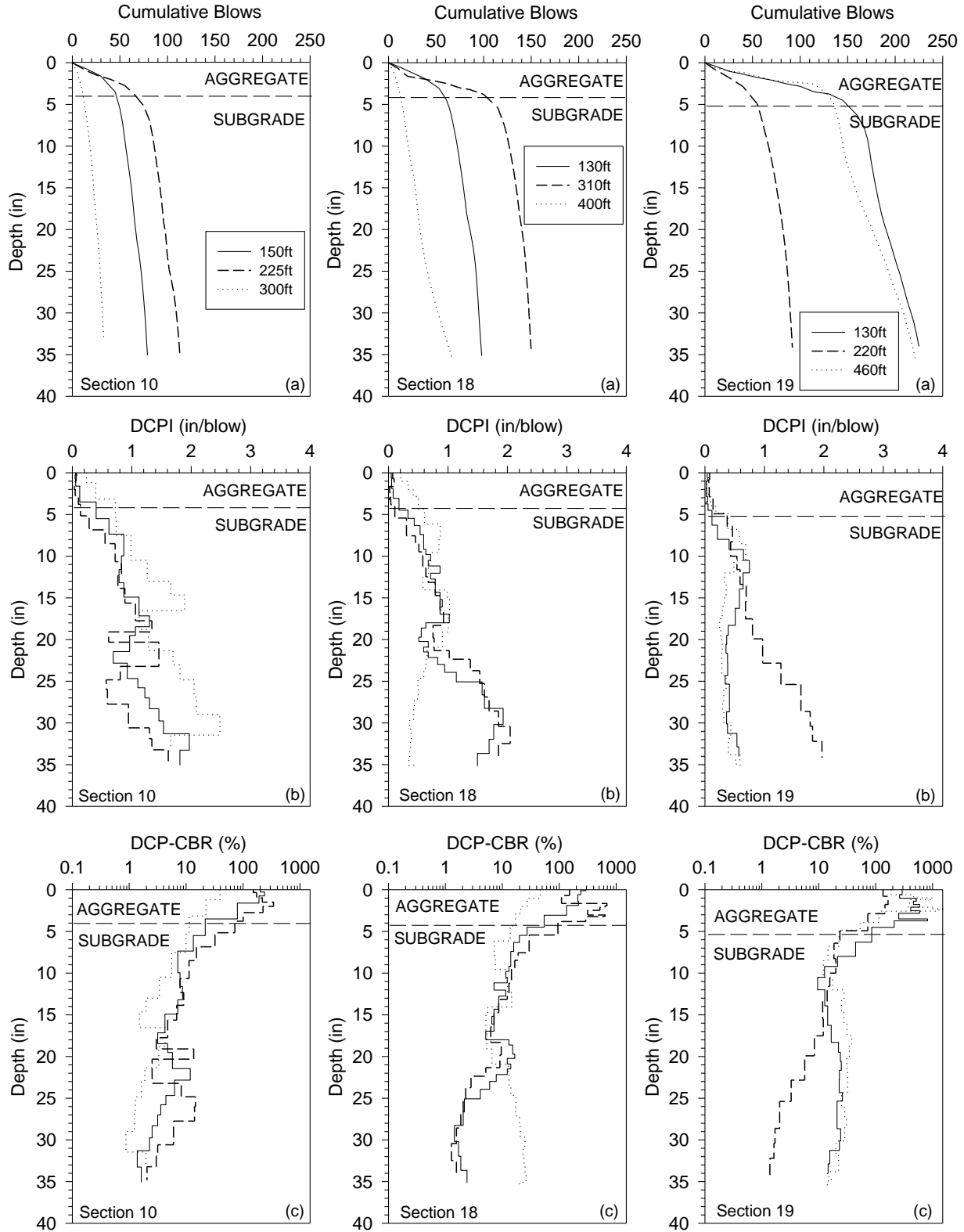


Figure 44. Pre-construction DCP test results for the three representative road sections (Sections 10, 18, and 19): (a) cumulative blows, (b) DCPI, and (c) DCP-CBR versus depth

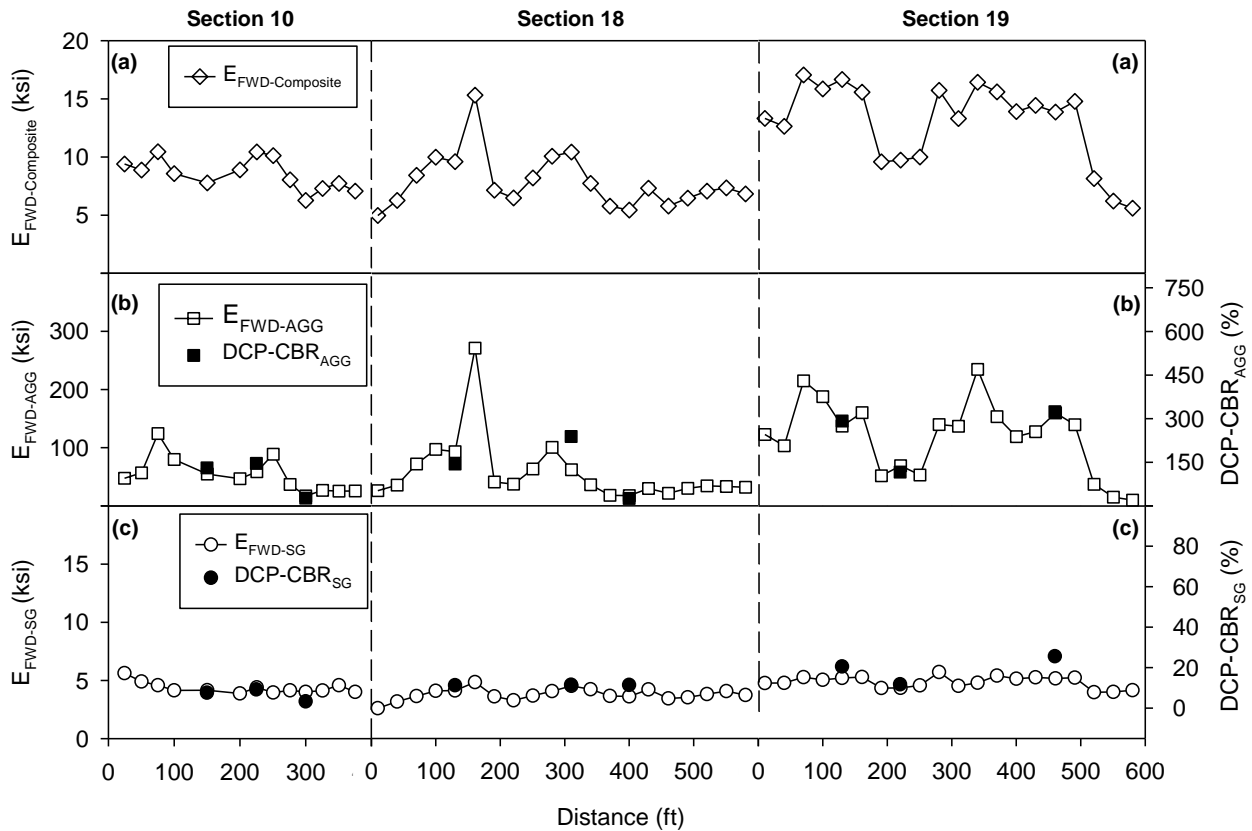
Table 14. Summary of preconstruction DCP test results

Testing Point (Distance from South End of Each Section)	Thickness of Surface Course (in.)	DCP-CBR_{AGG} (%) / Rating^a	Avg. DCP-CBR_{SG} (%) / Rating^b
Section 10 (150ft)	3.7	130.3 / E	7.7 / P-F
Section 10 (225ft)	5.7	146.0 / E	9.3 / P-F
Section 10 (300ft)	3.7	26.4 / <G	3.4 / VP
Section 18 (130ft)	4.5	145.0 / E	11.3 / F-G
Section 18 (310ft)	5.4	239.3 / E	11.5 / F-G
Section 18 (400ft)	4.3	26.6 / <G	11.4 / F-G
Section 19 (130ft)	6.3	292.0 / E	20.5 / VG
Section 19 (220ft)	4.9	116.4 / E	11.7 / F-G
Section 19 (460ft)	4.8	324.1 / E	25.6 / VG
Overall average (Coefficient of Variation)	4.8 (17.2%)	160.7 / E (62.1%)	12.5 / F-G (50.5%)

^a SUDAS relative support condition rating for subbase (Table 2): E=Excellent, VG=Very Good, G=Good, <G=below Good

^b SUDAS relative support condition rating for subgrade (Table 2): E=Excellent, VG=Very Good, F-G=Fair to Good, P-F=Poor to Fair, VP=Very Poor

FWD tests were performed to determine the composite elastic modulus ($E_{\text{FWD-Composite}}$) and layer modulus values of the surface aggregate layer ($E_{\text{FWD-AGG}}$) and subgrade ($E_{\text{FWD-SG}}$). Layer modulus values were calculated in accordance AASHTO (1993) as described in Section 3.2.2 of the report. The FWD modulus values are plotted together with the DCP-CBR values in Figure 45. The $E_{\text{FWD-Composite}}$, $E_{\text{FWD-AGG}}$, and $E_{\text{FWD-SG}}$ values of Section 19 were higher than those of Sections 10 and 18. Figure 45 also shows that the trends of the DCP tests agreed well with those of the FWD tests.



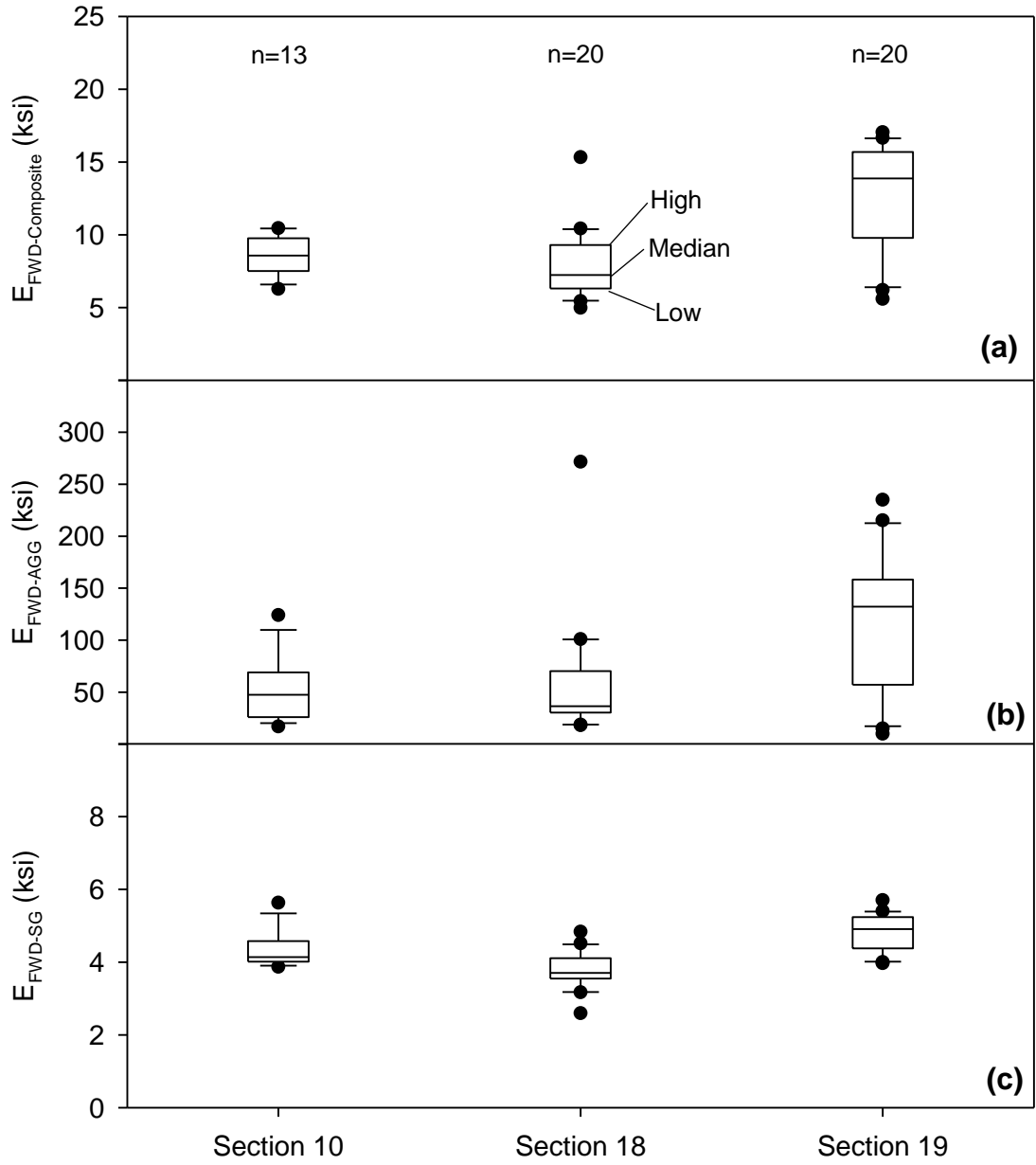
Note: The elastic moduli are calculated under 12000 lb applied load

Figure 45. Pre-construction FWD and DCP test results of the three representative sections: (a) $E_{FWD-Composite}$, (b) $E_{FWD-AGG}$ and $DCP-CBR_{AGG}$ of surface aggregate, and (c) E_{FWD-SG} and $DCP-CBR_{SG}$ of subgrade

Results of a statistical analysis of the FWD test results are summarized in Table 15 and Figure 46. The average $E_{FWD-Composite}$ and $E_{FWD-AGG}$ of Section 19 were approximately 50 to 100% higher, respectively, than those of Sections 10 and 18. However, the subgrade material of the three sections was similar in terms of the average E_{FWD-SG} values.

Table 15. Summary of pre-construction FWD test results for three representative sections

Parameters	Section 10	Section 18	Section 19
Average $E_{FWD-Composite}$, ksi (COV)	8.5 (15.5%)	7.8 (30.3%)	12.9 (27.2%)
Average $E_{FWD-AGG}$, ksi (COV)	52.9 (57.1%)	58.1 (97.5%)	118.7 (62.6%)
Average E_{FWD-SG} , ksi (COV)	4.3 (11.2%)	3.8 (13.2%)	4.8 (10.3%)



Middle line of box is median, box edges are 25th and 75th percentiles, dots are outliers, and whiskers extend to most extreme data not considered outliers

Figure 46. Summary boxplots of pre-construction FWD test results for the three representative sections: (a) $E_{FWD-Composite}$, (b) $E_{FWD-AGG}$, and (c) E_{FWD-SG}

6.1.2 Laboratory CBR and UCS Tests

Laboratory CBR and UCS tests were performed using representative surface aggregate and subgrade materials. CBR specimens were compacted at their optimum moisture contents (OMC) as determined by the laboratory standard Proctor tests. In this study, the CBR tests were conducted on both as-compacted and soaked specimens for comparison. Figure 47 shows the piston stress versus penetration depth for the CBR tests on the surface aggregate and subgrade specimens. At low penetration the penetration resistance is low and similar between materials, while at high penetration, the penetration resistance is 15 to 20 times higher for the aggregate.

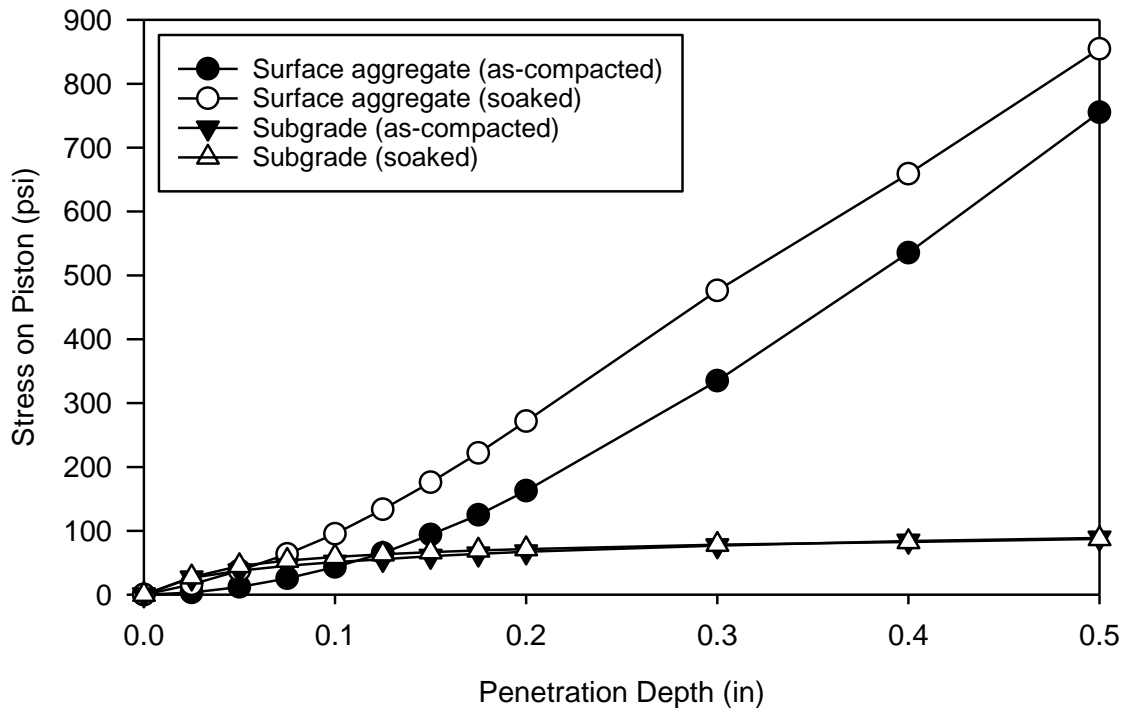


Figure 47. Uncorrected stress on piston versus penetration depth from CBR tests on surface aggregate and subgrade

For each specimen, the laboratory CBR value, dry unit weight, and moisture content before and after CBR testing are summarized and compared with the in situ DCP-CBR values in Table 16. The moisture contents and lab CBR of both the surface aggregate and subgrade were similar after soaking. The laboratory CBR values were lower than the average in situ DCP-CBR values, but were similar to the minimum values of the in situ CBR ranges. The in situ tests were performed at what was observed to be “dry” field conditions.

Table 16. Laboratory CBR test results for as-compacted and soaked surface aggregate and subgrade

Material	Dry Unit Weight (pcf)	As-Compacted w (%)	w (%) after CBR Test	Lab CBR (%) / Rating ^{a, b}	Range and (Average) in-situ DCP-CBR (%) / Rating ^{a, b}
Surface aggregate (as-compacted)	139.5	7.1	7.5	27.0 / <G	26 to 324 (160.7) / E
Surface aggregate (soaked)	138.4	7.6	7.8 ^c	26.1 / <G	
Subgrade (as-compacted)	103.6	21.1	20.7	5.1 / P-F	3.4 to 25.6 (12.5) / F-G
Subgrade (soaked)	102.2	21.6	22.6 ^c	5.9 / P-F	

^a SUDAS relative support condition rating for subbase (Table 2): E=Excellent, VG=Very Good, G=Good, <G=below Good

^b SUDAS relative support condition rating for subgrade (Table 2): E=Excellent, VG=Very Good, F-G=Fair to Good, P-F=Poor to Fair, VP=Very Poor

^c The specimen was soaked for 96 hours prior to the CBR test in accordance with ASTM D 1883-07e2.

UCS tests were performed to measure the shear strength of as-compacted and vacuum-saturated subgrade specimens for a range of compaction moisture contents. The UCS test specimens were prepared using the standard Proctor compaction test, and the resulting relationships between compaction moisture content, dry unit weight, and UCS are shown in Figure 48. The moisture contents of the specimens after vacuum-saturation are also plotted in Figure 48a. The UCS for subgrade compacted dry of optimum reduced significantly after vacuum saturation, and the specimens at the two lowest moisture contents slaked and collapsed. The as-compacted specimens reached a peak UCS of 36 psi at a compaction moisture content of 16.4%, while the vacuum saturated specimens reached a peak UCS of 9.2 psi at a compaction moisture content of 23.6% (Figure 48b). The optimum compaction moisture content in terms of peak saturated UCS is denoted $w_{opt(UCS)}$, which in this case was practically the same as the OMC for maximum dry density (unit weight $w_{opt(DD)}$).

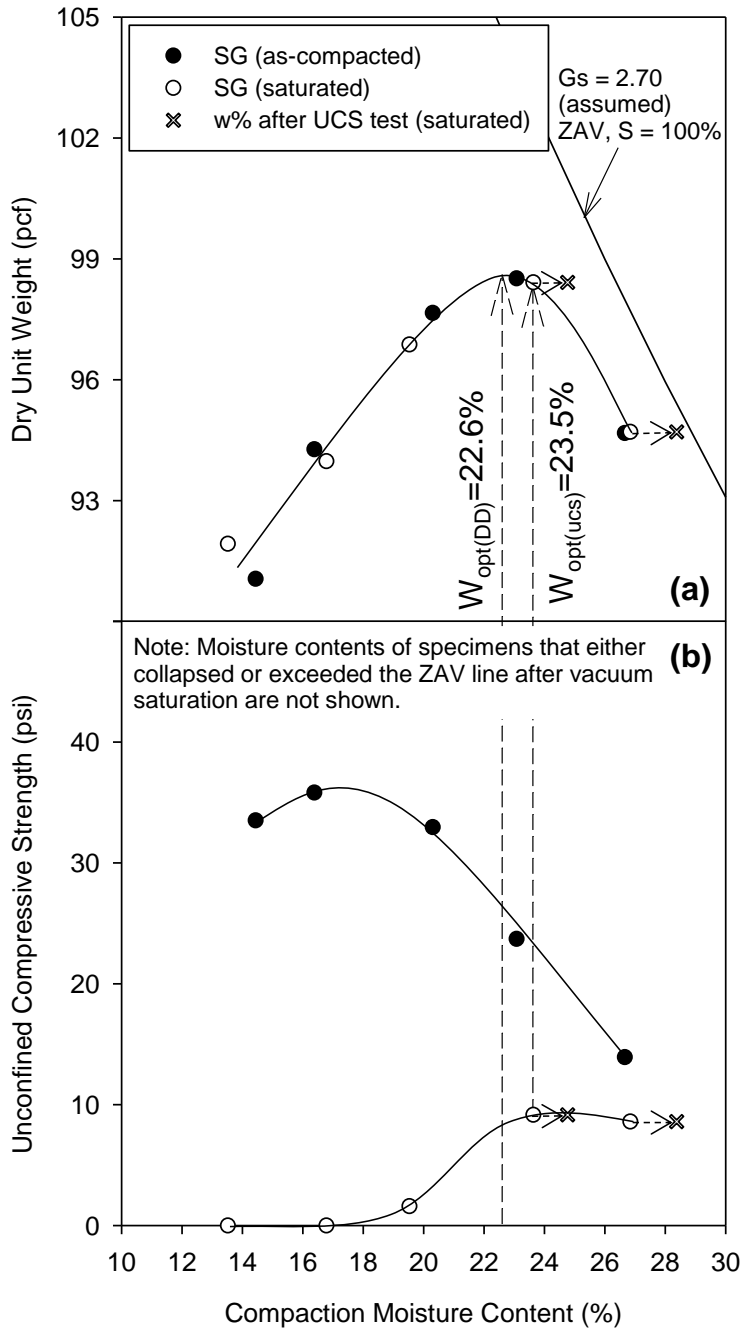


Figure 48. (a) Standard Proctor compaction and (b) UCS test results for the as-compacted and vacuum-saturated subgrade

6.2 Laboratory Mix Design for Chemical Stabilization Sections (Sections 16 and 17)

A range of laboratory mix designs were evaluated for existing subgrade (SG) materials, surface aggregate (AGG) materials, and subgrade plus surface aggregate (SG+AGG) mixtures. For each material type, fly ash (15% by dry soil weight) or type I/II cement (6% by dry soil weight) was added to further study the influence of chemical stabilization. Standard Proctor compaction, CBR, and UCS tests were conducted on as-compacted and vacuum-saturated specimens to determine moisture-density-unconfined compressive strength relationships. Compaction of the chemically stabilized laboratory specimens was performed within 30 minutes of mixing, and all specimens were cured at a temperature of 100 °F for seven days before performing CBR and UCS tests.

6.2.1 Subgrade

Figure 49 shows piston stress versus penetration depth for the as-compacted and soaked CBR tests. The fly ash and cement stabilized specimens increased the penetration resistance for both as-compacted and soaked specimens. The stresses at 0.1 in. penetration for the fly ash and cement stabilized specimens were about 11 and 17 times higher, respectively, than those of the untreated specimens. After soaking, the penetration resistance of the fly ash and cement stabilized specimens dropped by about 10% and 14%, respectively.

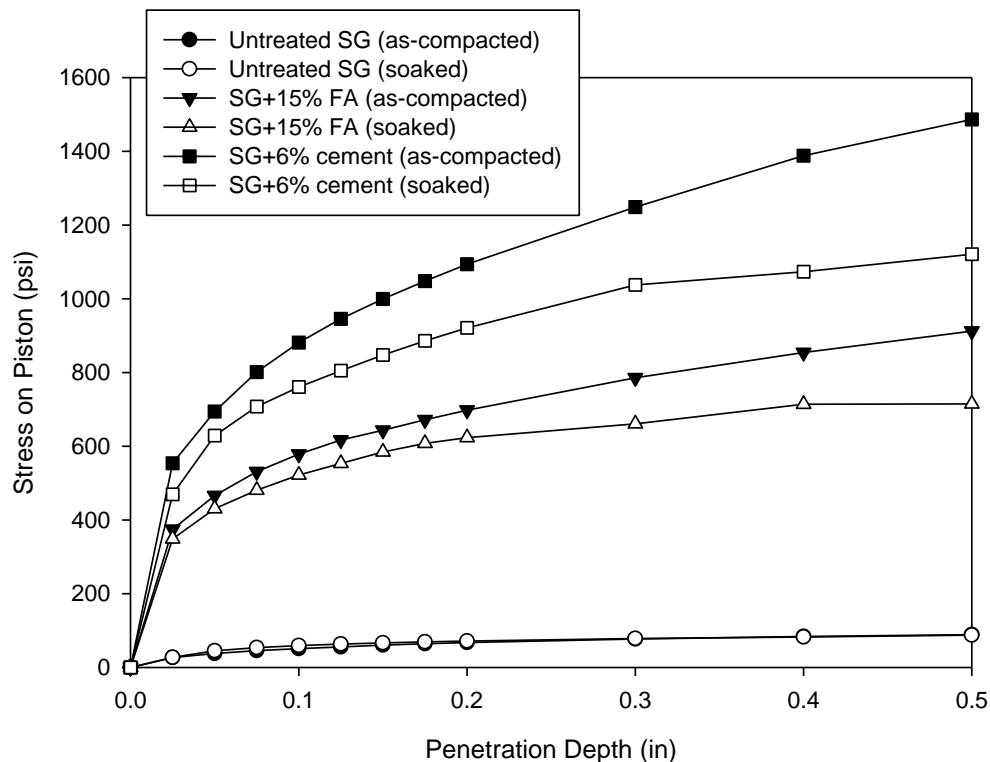


Figure 49. Uncorrected stress on piston versus penetration depth for CBR tests on untreated, fly ash-stabilized, and cement-stabilized subgrade

The CBR values, as-compacted dry unit weights, and moisture contents before and after the CBR tests are summarized in Table 17. The CBR specimens were compacted close to their optimum moisture contents as determined by standard Proctor tests (Figure 50). Both the fly ash- and cement-stabilization increased the CBR values of the subgrade specimens by more than 10 times compared to the untreated specimens.

Table 17. Laboratory CBR test results for untreated and stabilized subgrade

Material	Dry Unit Weight (pcf)	As-Compacted w (%)	w (%) After CBR Test	CBR (%) / Rating^a
Untreated SG (as-compacted)	102.2	21.6	20.7	5.1 / P-F
Untreated SG (soaked)	103.6	21.1	22.6 ^b	5.9 / P-F
SG+15% FA (as-compacted)	106.1	17.0	16.9	57.9 / E
SG+15% FA (soaked)	107.1	17.6	19.3 ^b	52.2 / E
SG+6% cement (as-compacted)	101.9	20.2	19.6	88.1 / E
SG+6% cement (soaked)	102.2	21.4	21.3 ^b	76.0 / E

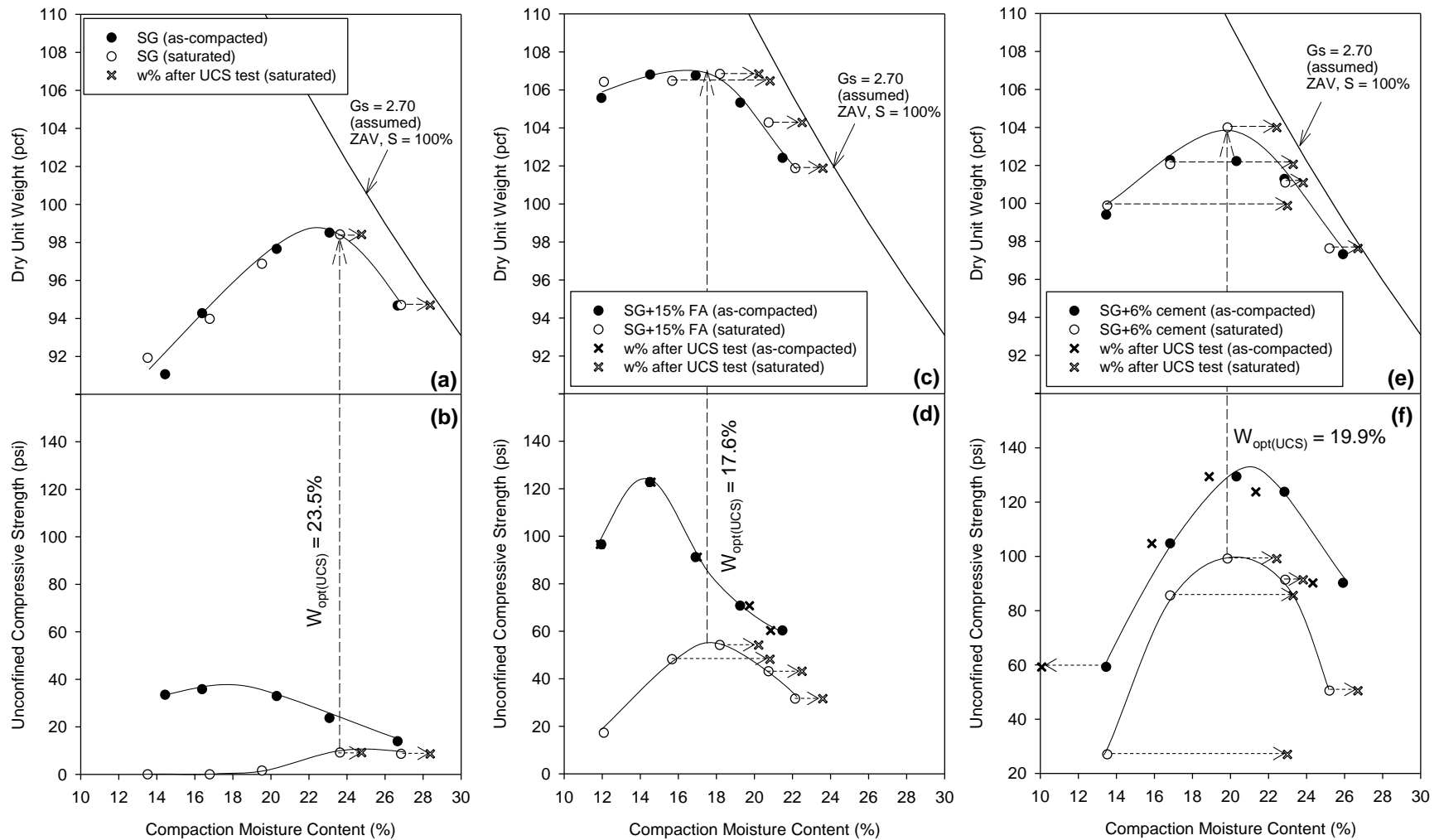
^a SUDAS relative support condition rating for subgrade (Table 2): E=Excellent, VG=Very Good, F-G=Fair to Good, P-F=Poor to Fair, VP=Very Poor

^b Specimen soaked for 96 hours prior to the CBR test in accordance with ASTM D 1883-07e2.

Standard Proctor tests were also conducted on as-compacted and vacuum-saturated specimens to determine the moisture-density relationships for the untreated and chemically stabilized subgrade materials (Figure 50a, 50c, and 50e). Results show that the maximum dry unit weights of the fly ash- and cement-stabilized specimens were higher than the untreated specimens, while the optimum moisture contents of chemically stabilized specimens were lower.

Following the Proctor tests, UCS tests were also conducted on as-compacted and vacuum-saturated specimens. Similar to the CBR test results for subgrade materials in the previous section, the vacuum-saturation technique was more effective than soaking, giving a greater increase in moisture content and a greater relative reduction in strength. Stabilization by fly ash and cement increased the peak UCS of the as-compacted specimens by about 3 times, (Figure 50b, 50d, and 50f). In contrast, the peak saturated UCS of the subgrade was increased for the fly ash and cement by 6 and 10 times, respectively.

For all tests, compaction moisture content was found to be an important factor in terms of UCS. Based on the vacuum-saturated results shown in Figure 50b, 50d, and 50f, the untreated subgrade should be compacted between +1 to +3% OMC for peak strength, while the fly ash- or cement-stabilized subgrade could be compacted between $\pm 2\%$ OMC. The latter range could be adjusted depending on the design strength criteria. Overall, the test results showed that both fly ash and cement stabilization can significantly improve the UCS of the existing subgrade material. Depending on the design requirements, the chemical stabilizer addition rate may need to be adjusted, and would require a new Proctor to establish suitable moisture content limits.



Note: Moisture contents of specimens that either collapsed or exceeded the ZAV line after vacuum saturation are not shown.

Figure 50. Moisture-density-UCS relationships of as-compacted and saturated subgrade specimens: (a and b) untreated, (c and d) fly ash-stabilized, and (e and f) cement-stabilized (optimum moisture content $w_{opt(UCS)}$ for peak saturated UCS shown)

6.2.2 Surface Aggregate

The laboratory mix design tests detailed in the previous section were also conducted on the untreated, fly ash-stabilized, and cement-stabilized surface aggregate. Figure 51 shows the piston stress versus penetration depth for the CBR tests. Results show that the stresses at 0.1 in. penetration for the fly ash-stabilized specimens were about 30 times higher than those of the untreated specimens. The cement-stabilized specimens were also prepared and tested after 7 days of curing, but the specimen strength exceeded the 10,000 lb-capacity of the load cell at about 0.03 in. penetration.

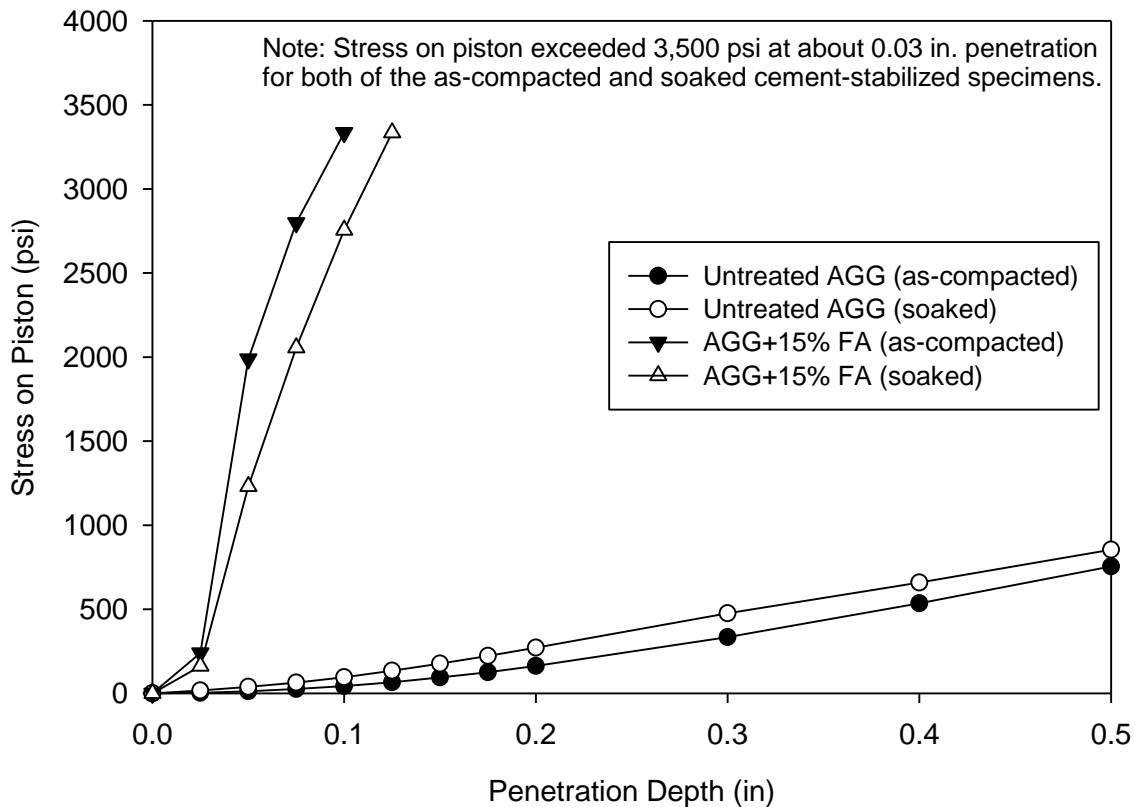


Figure 51. Uncorrected stress on Piston versus penetration depth for CBR tests on untreated and fly ash-stabilized surface aggregate specimens

The as-compacted dry unit weights, moisture contents before and after testing, and CBR values of the untreated and fly ash-stabilized specimens are summarized in Table 18. The CBR values of the fly ash-stabilized specimens were more than 10 times those of the untreated specimens.

Table 18. Laboratory CBR test results for untreated and stabilized surface aggregate

Material	Dry Unit Weight (pcf)	As-Compacted w%	w% after CBR Test	CBR (%) / Rating^a
Untreated AGG (as-compacted)	138.4	7.6	7.5	27.0 / <G
Untreated AGG (soaked)	139.5	7.1	7.8 ^b	26.1 / <G
AGG+15% FA (as-compacted)	138.9	7.2	6.5	333.5 / E
AGG+15% FA (soaked)	138.6	7.5	7.5 ^b	275.5 / E
AGG+6% cement (as-compacted)	135.8	7.6	–	>333.5 / E
AGG+6% cement (soaked)	136.2	7.4	–	>333.5 / E

^a SUDAS relative support condition rating for subbase (Table 2): E=Excellent, VG=Very Good, G=Good, <G=below Good

^b Specimen soaked for 96 hours prior to the CBR test in accordance with ASTM D 1883-07e2.

Laboratory Proctor and UCS tests were also conducted on the fly ash- and cement-stabilized surface aggregate specimens. Because the surface aggregate is an unbound material, vacuum saturation and UCS tests were not performed. Compared to the cement-stabilized specimens, the fly ash-stabilized specimens had higher maximum dry unit weights and lower optimum moisture contents (Figure 52). A bulking moisture content yielding the lowest dry unit weight was observed for the cement-stabilized specimens.

The maximum as-compacted and saturated UCS of cement-stabilized specimens (~500 psi) were higher than the fly ash-stabilized specimens (~450 psi), as shown in Figure 52. The UCS decreased by approximately 10% after vacuum saturation for both types of stabilized specimens. Similar to the subgrade materials, the UCS of stabilized surface aggregate was significantly influenced by compaction moisture content. The optimum moisture contents $w_{opt(UCS)}$ in terms of the peak saturated UCS are identified in Figure 52. For the cement-stabilized specimens, the strength increased significantly with increasing moisture content dry of optimum, and did not drop as severely as the fly ash wet of optimum.

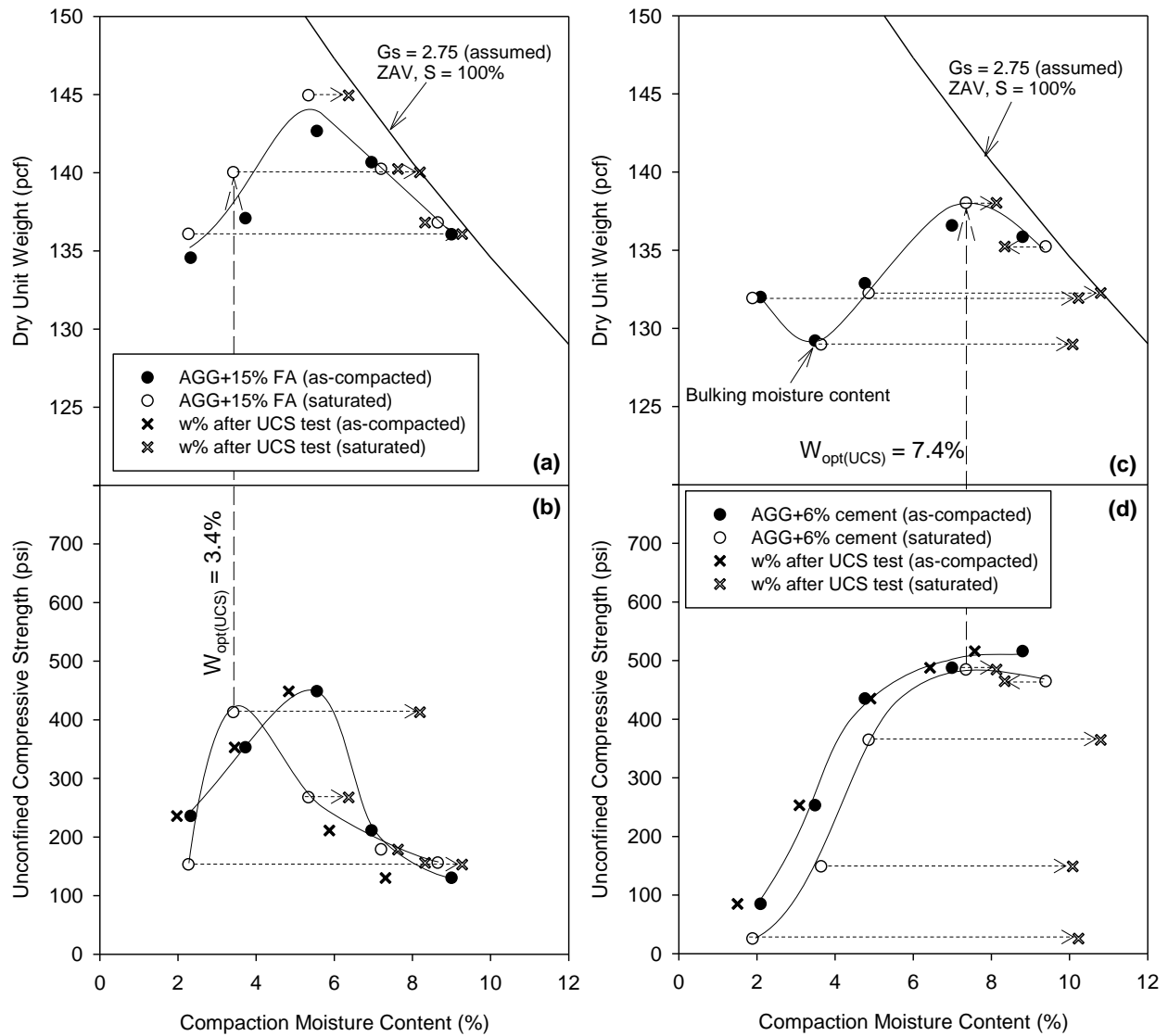


Figure 52. Moisture-density-UCS relationships of as-compacted and saturated surface aggregate: (a and b) fly ash-stabilized and (c and d) cement-stabilized

6.2.3 Mixture of Subgrade and Surface Aggregate

The laboratory mix design tests detailed in the previous sections were also conducted on a mixture of existing subgrade and surface aggregate (SG+AGG). Based upon practical and economic considerations in consultation with the project Technical Advisory Committee (TAC), the surface aggregate for the fly ash-stabilized Section 16 and cement-stabilized Section 17 were constructed by mixing fly ash or cement with the existing 3 in. aggregate layer and 5 in. of the subgrade. The SG+AGG mixtures tested in the laboratory were therefore comprised of 62.5% subgrade and 37.5% surface aggregate by volume. Fly ash and cement addition rates were based on the SG+AGG dry mass.

The moisture-density-UCS relationships of the untreated, fly ash-stabilized, and cement-stabilized SG+AGG mixtures are shown in Figure 53. The maximum dry unit weight increased and optimum moisture content decreased after mixing in the chemical stabilizers, while the UCS was increased but significantly influenced by the compaction moisture content. The optimum compaction moisture contents ($w_{opt(UCS)}$) that resulted in the highest saturated UCS are shown in Figure 53 for the three types of materials.

To compare the performance of the chemically stabilized SG+AGG mixture to the stabilized subgrade material alone, the mix design test results of Figure 50 and Figure 53 are plotted together in Figure 54. The Proctor curves of the untreated and fly ash- and cement-stabilized SG+AGG specimens are similar to the corresponding curves of the subgrade specimens. However, the maximum dry unit weights of the SG+AGG mixtures were higher, and the optimum moisture contents were about 6% lower than the SG specimens without aggregate. These phenomena indicate that the compaction behavior of the SG+AGG mixtures were still governed primarily by the shear strength properties of the SG material.

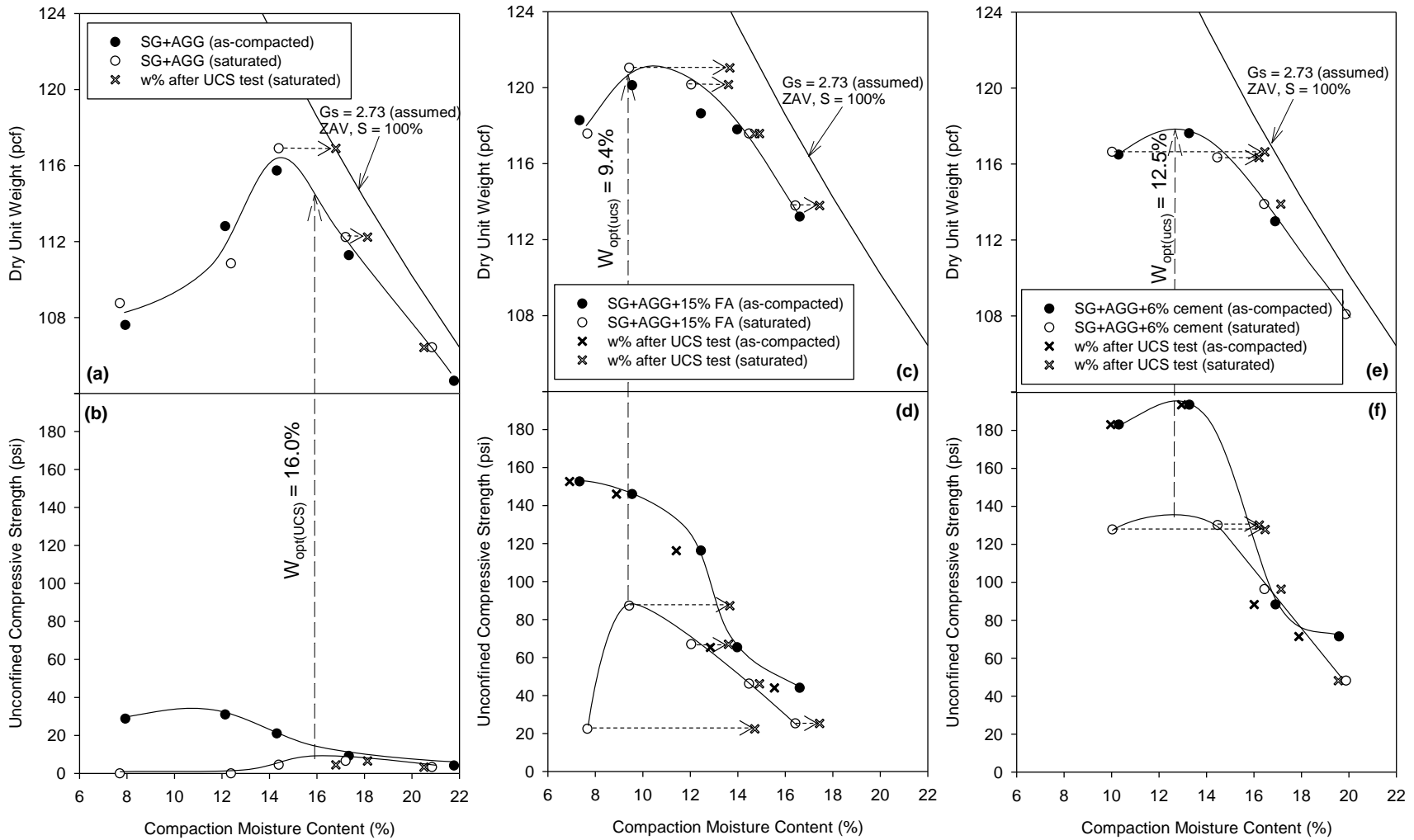
The peak UCS of the untreated SG+AGG was nearly the same as that of the untreated SG, for both the as-compacted and saturated cases (Figure 54b). This further indicates that the shear strength of the SG+AGG mixture was still governed by the SG matrix, and adding the 37.5% aggregate to the subgrade did not result in a strength gain. However, the chemically stabilized SG+AGG mixtures resulted in higher UCS than the chemically stabilized SG alone (Figure 54d and 54f). This may be because the aggregate particles in the SG+AGG mixture reduced the volume of the fine SG particle matrix, so the same percentage of stabilizers on a volume basis resulted in a higher concentration within the fine SG particle matrix of the SG+AGG mixture than in the SG-only specimens.

The laboratory mix design results for the existing surface aggregate (AGG), subgrade (SG), and subgrade and surface aggregate (SG+AGG) mixtures are summarized in Table 19. Stabilization of the AGG by 15% fly ash or 6% cement resulted in peak UCS exceeding 400 psi for both as-compacted and saturated conditions. For the SG with 15% fly ash, the as-compacted and saturated peak UCS increased by factors of 3.4 and 5.9, respectively. For the SG with 6% cement, the as-compacted and saturated peak UCS increased by factors of 3.6 and 10.8, respectively. The chemically stabilized SG+AGG mixtures showed even greater improvement in peak UCS than the stabilized SG, with the as-compacted and saturated fly ash-stabilized UCS

increasing by 4.9 and 8.6 times, respectively, and cement-stabilized UCS increasing by 6.2 and 17.4 times, respectively. Compared to the untreated materials, the materials stabilized with 15% fly ash or 6% cement yielded higher standard Proctor maximum dry unit weights ($\gamma_{d \max}$) and lower optimum moisture contents (w_{opt}), with the exception of the AGG-cement mixture. Also, for most of the materials, the optimum compaction moisture contents that produced the peak saturated UCS ($w_{\text{opt(UCS)}}$) were within 1.5% of their standard Proctor optimum moisture contents (w_{opt}).

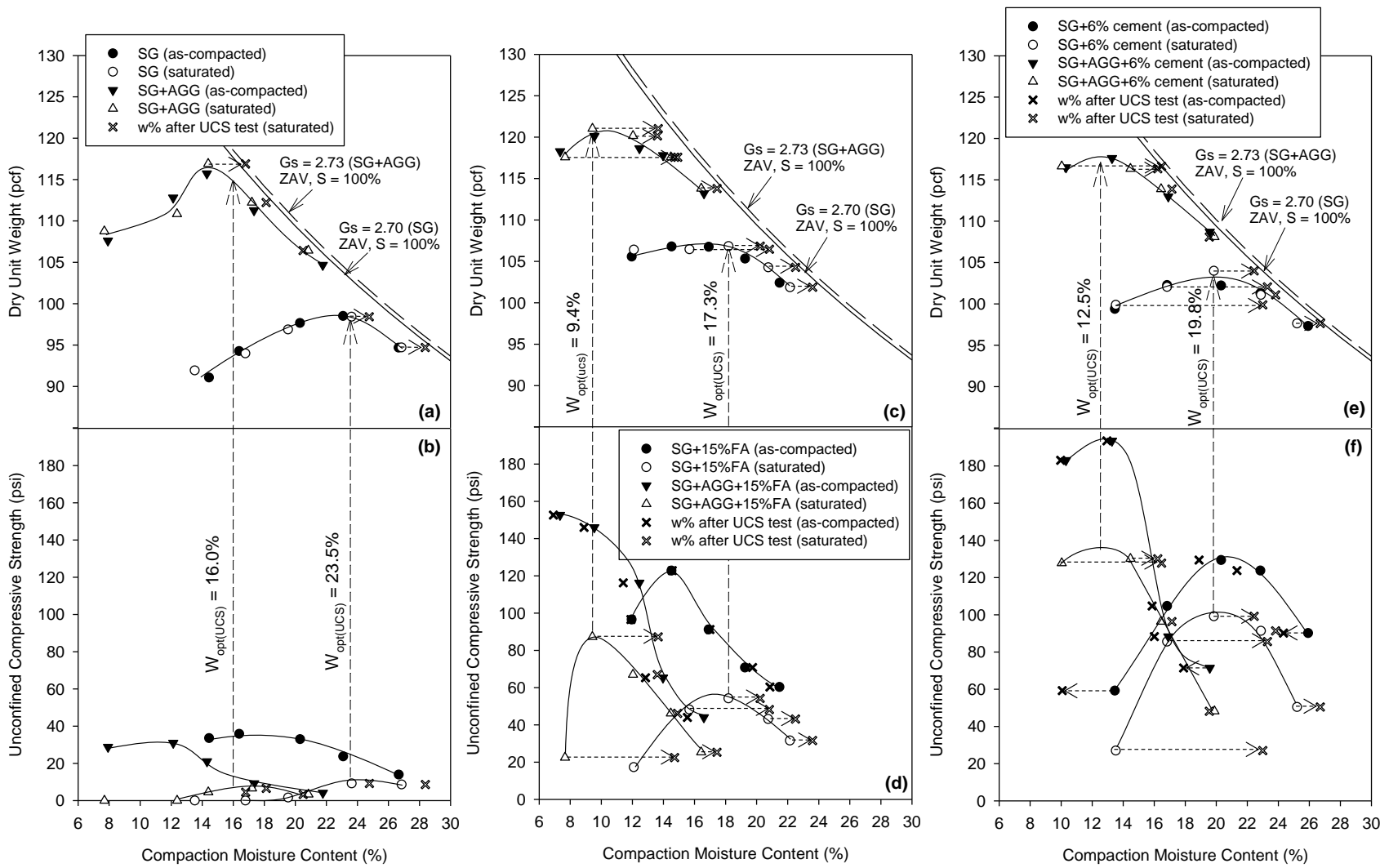
Table 19. Summary of laboratory mix design results for existing surface aggregate (AGG), subgrade (SG), and subgrade-surface aggregate (SG+AGG) mixture

Materials	Peak UCS, psi (as-compacted)	Peak UCS, psi (saturated)	$w_{\text{opt(UCS)}}$ %	w_{opt} %	$\gamma_{d \max}$, pcf
AGG	–	–	–	6.2	140.8
AGG+15% FA	448.5	413.0	3.4	5.5	143.8
AGG+6% Cement	516.0	487.7	7.4	7.4	138.1
SG	36.3	9.2	23.5	22.4	98.7
SG+15% FA	122.7	54.2	17.6	16.5	107.0
SG+6% Cement	131.4	99.1	19.9	19.9	103.2
SG+AGG	31.0	7.8	16.0	14.4	116.9
SG+AGG+15% FA	152.6	66.9	9.4	10.9	121.2
SG+AGG+6% Cement	190.7	136.0	12.5	12.5	118.1



Note: Moisture contents of specimens that either collapsed or exceeded the ZAV line after vacuum saturation are not shown.

Figure 53. Moisture-density-UCS relationships of as-compacted and saturated SG+AGG mixtures: (a and b) untreated, (c and d) fly ash-stabilized, and (e and f) cement-stabilized



Note: Moisture contents of specimens that either collapsed or exceeded the ZAV line after vacuum saturation are not shown.

Figure 54. Moisture-density-UCS relationships of as-compacted and saturated subgrade and SG+AGG mixtures: (a and b) untreated, (c and d) fly ash-stabilized, and (e and f) cement-stabilized

6.3 Laboratory Permeameter Tests for Geocomposite Drain Section (Section 18)

Damage to granular surfaced roads, such as surface water erosion, rutting, and potholes are attributed to insufficient drainage during spring-thawing periods, when ice lenses in the soil create a barrier to downward flow of water. As one method to address this problem, a geocomposite drainage layer was installed in Section 18 to improve horizontal drainage and provide a capillary barrier at the aggregate-subgrade layer interface. To quantify the effectiveness of the geocomposite drainage layer, the hydraulic conductivity of the existing subgrade and surface aggregate materials was measured in the laboratory using rigid-wall compaction mold permeameter tests and large-scale horizontal permeameter tests (HPTs). HPTs were also performed on surface aggregate with an embedded geocomposite drainage layer.

The rigid-wall compaction mold permeameter test was conducted on subgrade specimens in accordance with ASTM D 5856-95(2007). The dry unit weights, moisture contents before and after testing, and measured saturated hydraulic conductivities are detailed in Table 20. The results show that the subgrade material, which has 28.7% clay content and an AASHTO classification of A-7-6(10), can be considered as an impermeable material.

Table 20. Rigid-wall compaction mold permeameter results for subgrade

Parameters	As-Compacted	After the Test
Water content (%)	23.7	26.4
Dry unit weight (lb/ft ³)	96.8	96.8 ^a
Degree of saturation (%)	86.6	96.4
Hydraulic conductivity (ft/day)	5.06×10^{-05}	

^a Dry unit weight of specimen was assumed unchanged after test, because volume of specimen did not change during test.

Three HPTs were conducted on the surface aggregate: one specimen consisted of aggregate only, and the other two had one of the two types of geocomposite drainage materials embedded (i.e., Macdrain™ drainage W1051 and Roadrain™ RD-5). As described in Chapters 4 and 5, the Macdrain™ drainage W1051 was installed as a geocomposite drainage layer in Section 18, and the Roadrain™ RD-5 was installed as a lining around the perimeter of the bottom of the aggregate columns in Section 13.

For the first HPT, the surface aggregate was compacted to a dry unit weight of 139.4 pcf, which is close to the standard Proctor maximum dry unit weight of 140.8 pcf. After completing the HPT, the top half the material was removed, the geocomposite layer placed at the mid-depth of the specimen, and the top half of the aggregate replaced. Photos of specimen preparation are provided in Appendix B.

The saturated horizontal hydraulic conductivities of the three specimens were each measured under four different constant water heads (2, 4, 6, and 8 in.), giving the relationships between hydraulic conductivity and hydraulic gradient shown in Figure 55. The horizontal saturated hydraulic conductivity at 68 °F (K_{68 °F}) of the existing surface aggregate specimen was between 2

and 3 ft/day, and remained relatively constant as hydraulic gradient increased. The geocomposite drainage layer effectively increased the $K_{68^{\circ}\text{F}}$ by more than three orders of magnitude, and the W1051 geocomposite had a higher permeability (~4,000 ft/day) than the RD-5 geocomposite (~1,000 ft/day).

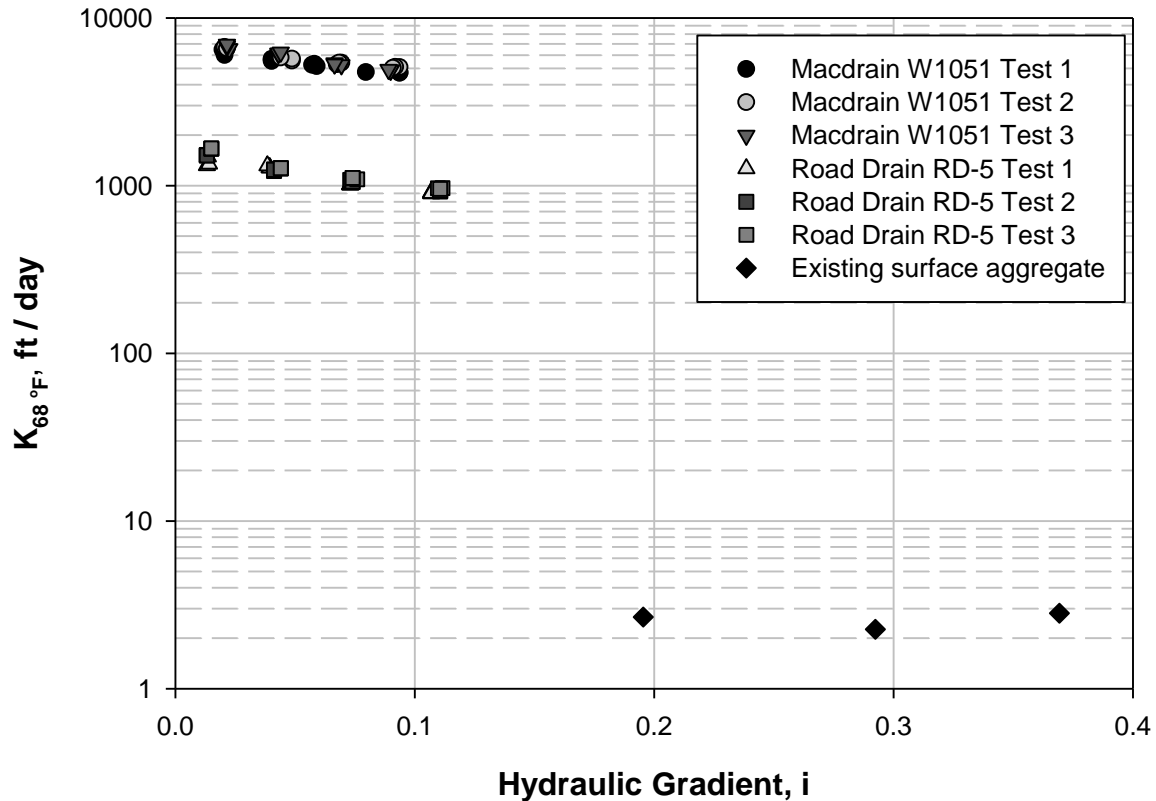


Figure 55. Large-scale horizontal permeameter test (HPT) results of existing surface aggregate and surface aggregate with embedded geocomposite drainage layer

6.4 Performance of As-Constructed Demonstration Sections

The performance of the as-constructed demonstration sections covering the two-mile stretch of Vail Avenue was monitored through the 2013-2014 and 2014-2015 seasonal free-thaw cycles. Several series of field tests including DCP, FWD, and multi-channel analysis of surface wave (MASW) tests were conducted to determine the thickness of the surface course layer and the shear strength and stiffness of the surface course and subgrade materials. To evaluate the effectiveness of the geocomposite drainage layer in improving the hydraulic conductivity and drainage, in situ air permeameter tests (APT) were also conducted on the geocomposite drain Section 18 as well as one nearby control section.

6.4.1 DCP and FWD Tests

Construction of demonstration Sections 1–8, 12, 13, and 19A and 19B was completed on September 19, 2013, except for the calcium chloride for Section 2 and the bentonite for Sections 1B and 4, which were completed in summer 2014. Construction of Sections 15–18 was not completed until the following year, on October 2, 2014. Therefore, two groups of as-constructed field tests were conducted in both 2013 and 2014. For the first group of field tests in 2013, DCP and FWD tests were performed on demonstration Sections 1–9 of the first mile. At that time, Sections 1A, 1B, and 2 were the same (dirty macadam) and Sections 3 and 4 were the same (dirty macadam with nonwoven geotextile), because the calcium chloride and bentonite had not yet been applied. For the second group of field tests in 2014, FWD and MASW tests were performed for the entire two mile stretch, covering demonstration Sections 1A–20.

DCP tests were performed on the macadam Sections 1–9 on October 31, 2013 and November 7, 2013, which was after construction but before the first freeze-thaw cycle. From the test results, the thickness of the surface course layer and shear strength of the surface course and subgrade materials were estimated. The cumulative blows, DCPI, and DCP-CBR values versus depth for these tests are shown in Figure 56 and Figure 57. According to ASTM D 6951-09, the DCP tests should not be used for testing granular materials containing a large percentage of aggregates greater than 2 in., so the DCP-CBR values shown for the macadam stone base layers do not fully reflect the shear strength of the materials. However, they do clearly indicate the depth to the surface of the subgrade layer. The estimated DCP-CBR values of the subgrade decreased with depth (Figure 56 and Figure 57), which may be due to an increasing moisture content with depth. Also, the DCP results do not clearly delineate the interfaces of the macadam stone base layer with the aggregate layers above and below. Therefore, the embedded macadam stone base layer and aggregate layers were treated as a single combined (aggregate+macadam+aggregate) surface course layer in the plots.

The thickness of the combined surface layer was then calculated for each test, along with the average DCP-CBR values of the combined surface course layer ($DCP-CBR_{AGG}$) and subgrade ($DCP-CBR_{SG}$), as summarized in Table 21. The average thickness of the combined surface course layer for Sections 1–8 ranged between 13.3 and 15.8 in., and the depth-averaged $DCP-CBR_{SG}$ of the subgrade ranged between 12.8% and 25.9%, which classifies as fair to very good according to the SUDAS rating system in Table 2. However, the average $DCP-CBR_{SG}$ of the control Section 9 subgrade was 10.6%, which is lower than the corresponding values for the macadam base Sections 1–8. Since the subgrade material for all sections was the same type of backfill, the lower $DCP-CBR_{SG}$ in Section 9 was assumed to result from deeper and softer subgrade materials being included for this section due to its thinner surface course consisting only of aggregate (see Figure 57). To verify this assumption, the average $DCP-CBR_{SG}$ of Section 9 was re-calculated over the same depth range within the subgrade as Sections 1–8 (i.e., to a depth of 20 rather than 34 in. below the subgrade surface), giving a slightly higher value of 14.6% which is comparable to that of the macadam sections. To simulate the same total influence depth of traffic loads, however, the average $DCP-CBR_{SG}$ calculated using the full measurement depth of 35 in. from the roadway surface will be used for all sections.

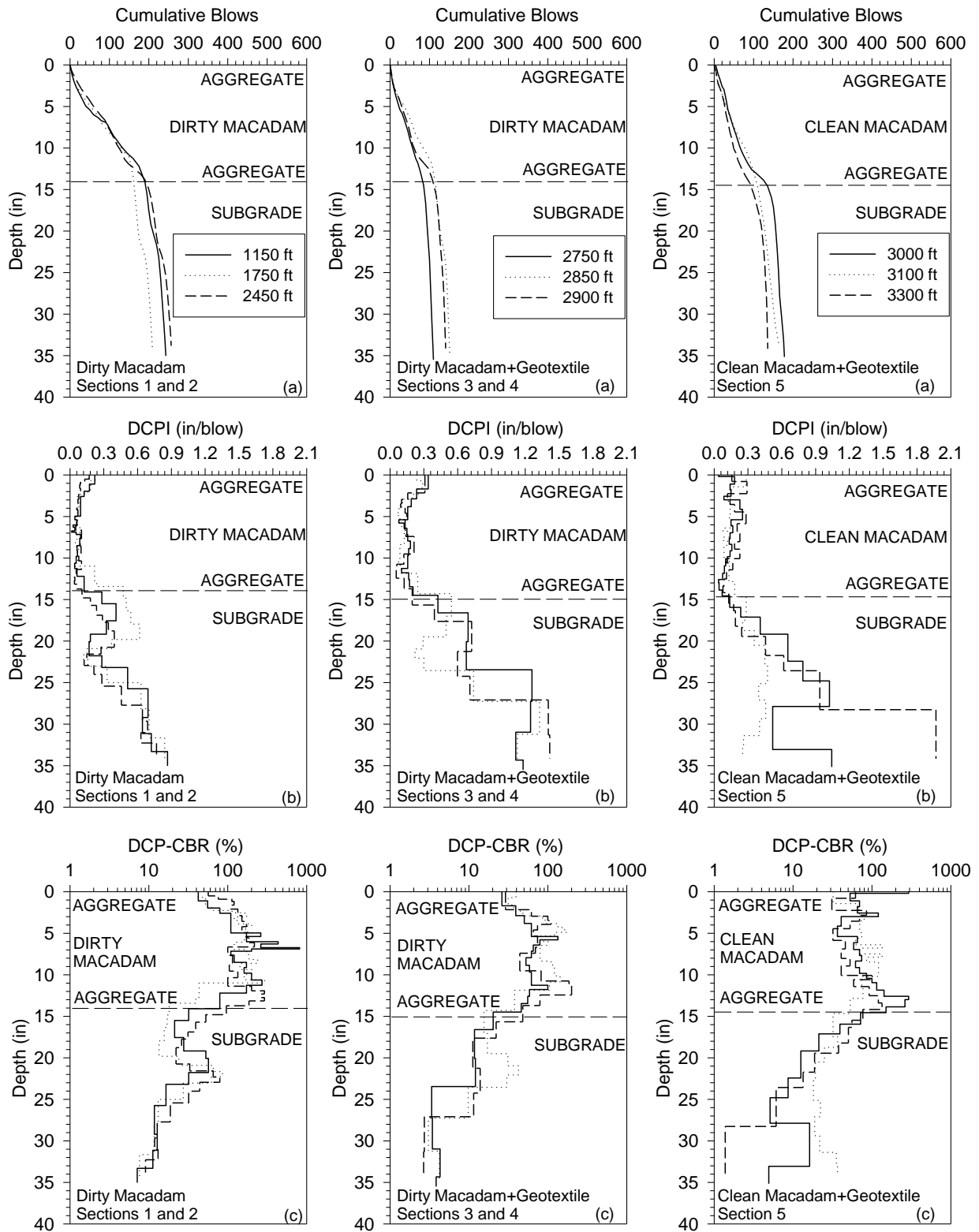


Figure 56. DCP test results for as-constructed Sections 1 through 5: (a) cumulative blows, (b) DCPI, and (c) DCP-CBR versus depth

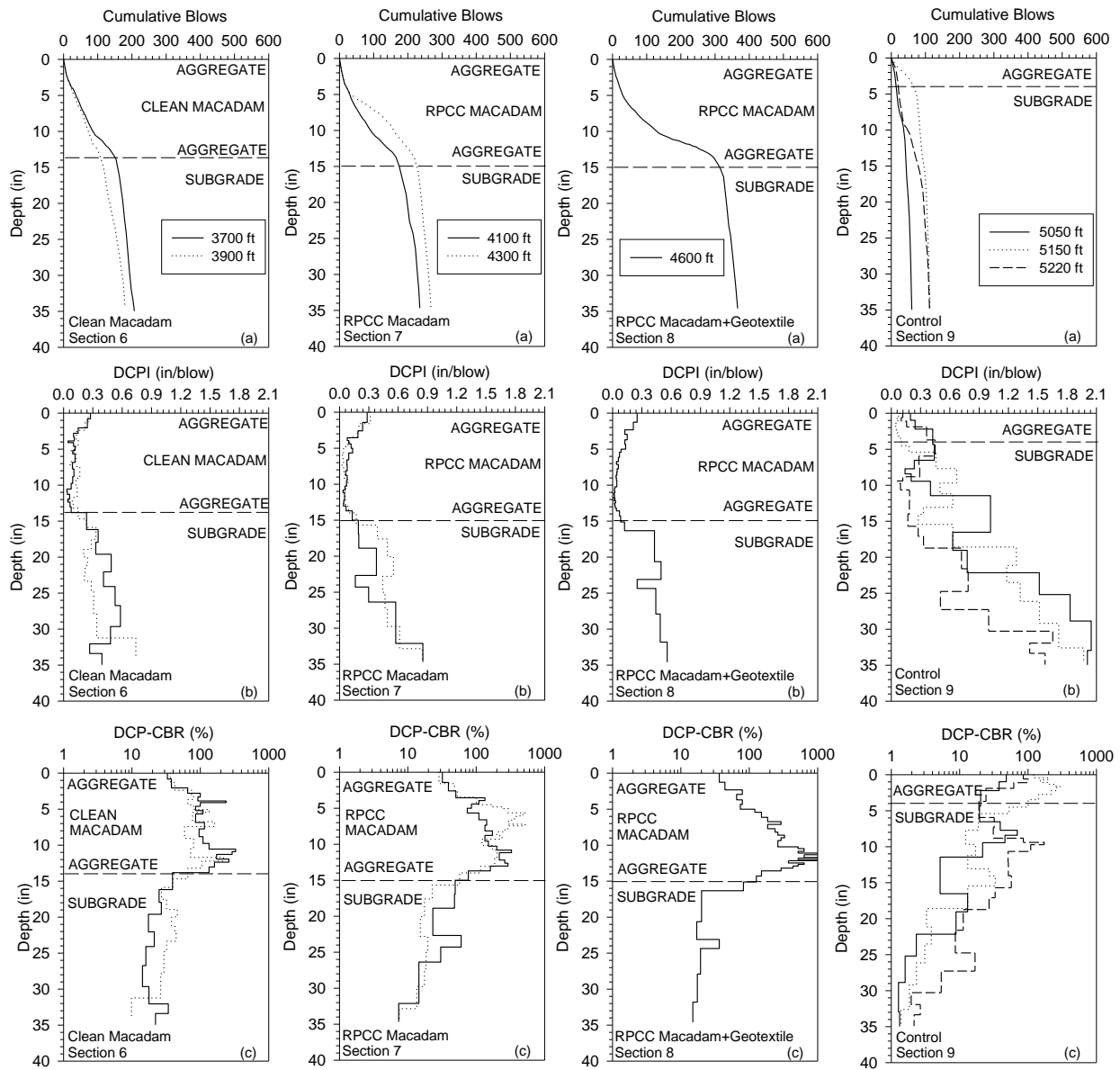


Figure 57. DCP test results for as-constructed Sections 6 through 9: (a) cumulative blows, (b) DCPI, and (c) DCP-CBR versus depth

Table 21. DCP test results of as-constructed first mile demonstration Sections 1–9

Description (Section Number)	Distance (ft)	Thickness of Combined Surface Course (in.)	Average Thickness (in.)	DCP- CBR_{AGG} (%)	Average DCP- CBR_{AGG} (%) / Rating^a	DCP- CBR_{SG} (%)	Average DCP- CBR_{SG} (%) / Rating^b
Dirty Macadam (1 and 2)	1150	14.1		143.6		22.1	
	1750	11.0	13.3	144.6	143.8 / E	22.6	24.0 / VG
	2450	14.8		143.2		27.2	
Dirty Macadam + NW-Geotextile (3 and 4)	2750	14.5		56.6		7.6	
	2850	11.9	13.3	89.8	74.8 / VG	17.2	12.8 / F–G
	2900	13.7		77.9		13.8	
Clean Macadam + NW-Geotextile (5)	3000	14.6		94.4		17.8	
	3100	14.6	15.8	74.6	76.8 / VG	25.2	17.4 / F–G
	3300	18.2		61.4		9.3	
Clean Macadam (6)	3700	13.8		115.2		22.3	
	3900	14.7	14.3	78.2	96.7 / E	29.5	25.9 / VG
RPCC Macadam (7)	4100	13.7		126.6		30.1	
	4300	14.0	13.8	170.9	148.7 / E	19.7	24.9 / VG
RPCC Macadam + NW-Geotextile (8)	4600	15.1	15.1	233.9	233.9 / E	22.9	22.9 / VG
Control (9)	5050	4.3		31.4		12.0	
	5150	5.4	4.9	148.7	90.0 / E	9.1	10.6 / F–G

^a SUDAS relative support condition rating for subbase (Table 2): E=Excellent, VG=Very Good, G=Good, <G=below Good

^b SUDAS relative support condition rating for subgrade (Table 2): E=Excellent, VG=Very Good, F–G=Fair to Good, P–F=Poor to Fair, VP=Very Poor

The first group of FWD tests on the as-constructed Sections 1–9 were conducted on October 17, 2013, approximately one month after construction. The resulting elastic modulus of the combined (aggregate+macadam+aggregate) surface course layer ($E_{FWD-AGG}$) and the subgrade (E_{FWD-SG}), as well as the composite elastic modulus of the surface-and-subgrade system ($E_{FWD-Composite}$) are shown in Figure 58. The $E_{FWD-Composite}$ of the macadam stone base Sections 1–8 ranged between 21 and 46 ksi, with the clean macadam Section 6 producing the highest modulus values, while the average $E_{FWD-Composite}$ of control Section 9 was only about 9 ksi. The DCP-CBR values of the combined surface course layer and subgrade are also plotted in Figure 58. As explained above, according to ASTM D 6951-09, the DCP tests do not fully reflect the shear strength of the macadam materials. However, the DCP-CBR trends for most of the sections generally agreed with the E_{FWD} trends for both the combined surface course layer and subgrade.

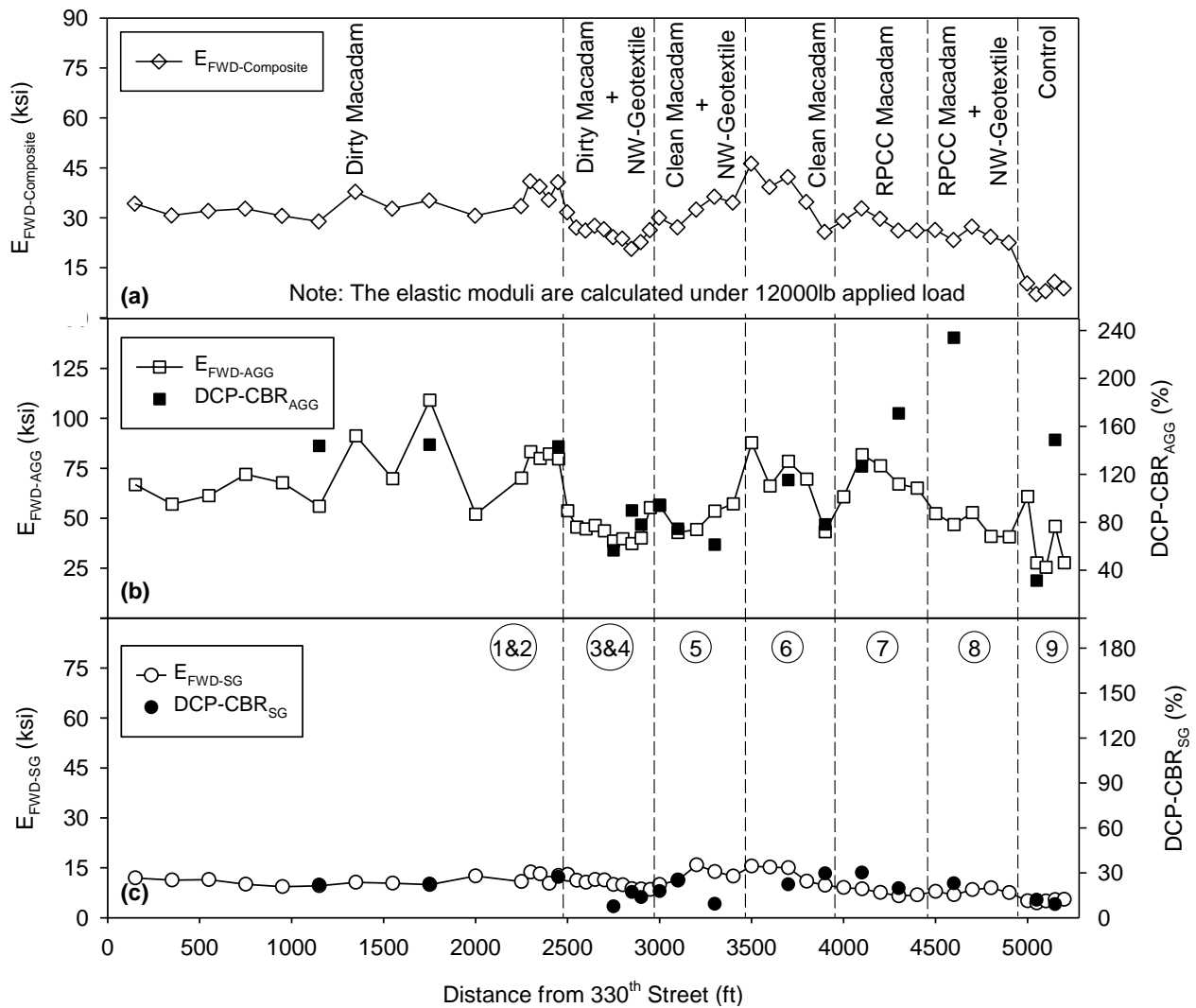


Figure 58. 2013 FWD and DCP test results for as-constructed first-mile Sections 1–9: (a) $E_{FWD-Composite}$, (b) $E_{FWD-AGG}$ and $DCP-CBR_{AGG}$ of combined surface course, and (c) E_{FWD-SG} and $DCP-CBR_{SG}$ of subgrade

Construction of the second mile demonstration sections was completed on October 1, 2014, approximately one year after completion of the first mile demonstration sections. A second group of as-constructed FWD tests was then performed on all demonstration sections on October 20, 2014. The FWD test results from 2013 and 2014 are compared in Figure 59. As mentioned above, Sections 1A, 1B, and 2 were the same (dirty macadam), and Sections 3 and 4 were the same (dirty macadam with nonwoven geotextile) during the first group of tests, because the calcium chloride and bentonite had not yet been applied. Also, ground temperature profiles were not measured during the first group of tests in 2013, because the weather station and ground temperature sensors had not yet been installed. However, both air and road surface temperatures were measured by the FWD at each testing point in 2013 and 2014, and their average values in each year differed by 12 °F for air and 8 °F for the road surface. Based on visual observation, the weather and road conditions were similar for the two test periods.

The $E_{\text{FWD-Composite}}$ values (Figure 59) decreased slightly from 2013 to 2014 for most of the sections, with the exception of the dirty macadam with bentonite and NW-geotextile (Section 4), RPCC macadam (Section 7), and RPCC macadam with NW-geotextile (Section 8). For Section 4, approximately 2 in. of aggregate was added for bentonite mixing after the 2013 FWD tests, which increased the $E_{\text{FWD-Composite}}$ values for 2014. For Sections 7 and 8, the increase in $E_{\text{FWD-Composite}}$ might be attributable to a beneficial further hydration of the RPCC macadam base material. Figure 59b shows the $E_{\text{FWD-AGG}}$ of the combined (aggregate+macadam+aggregate) surface course layers, which more clearly indicates that the modulus increases of the RPCC macadam sections may be due to further hydration of the RPCC. This hypothesis is also supported by the fact that the $E_{\text{FWD-SG}}$ for Sections 7 and 8 were similar or slightly decreased from 2013 to 2014 (Figure 59c).

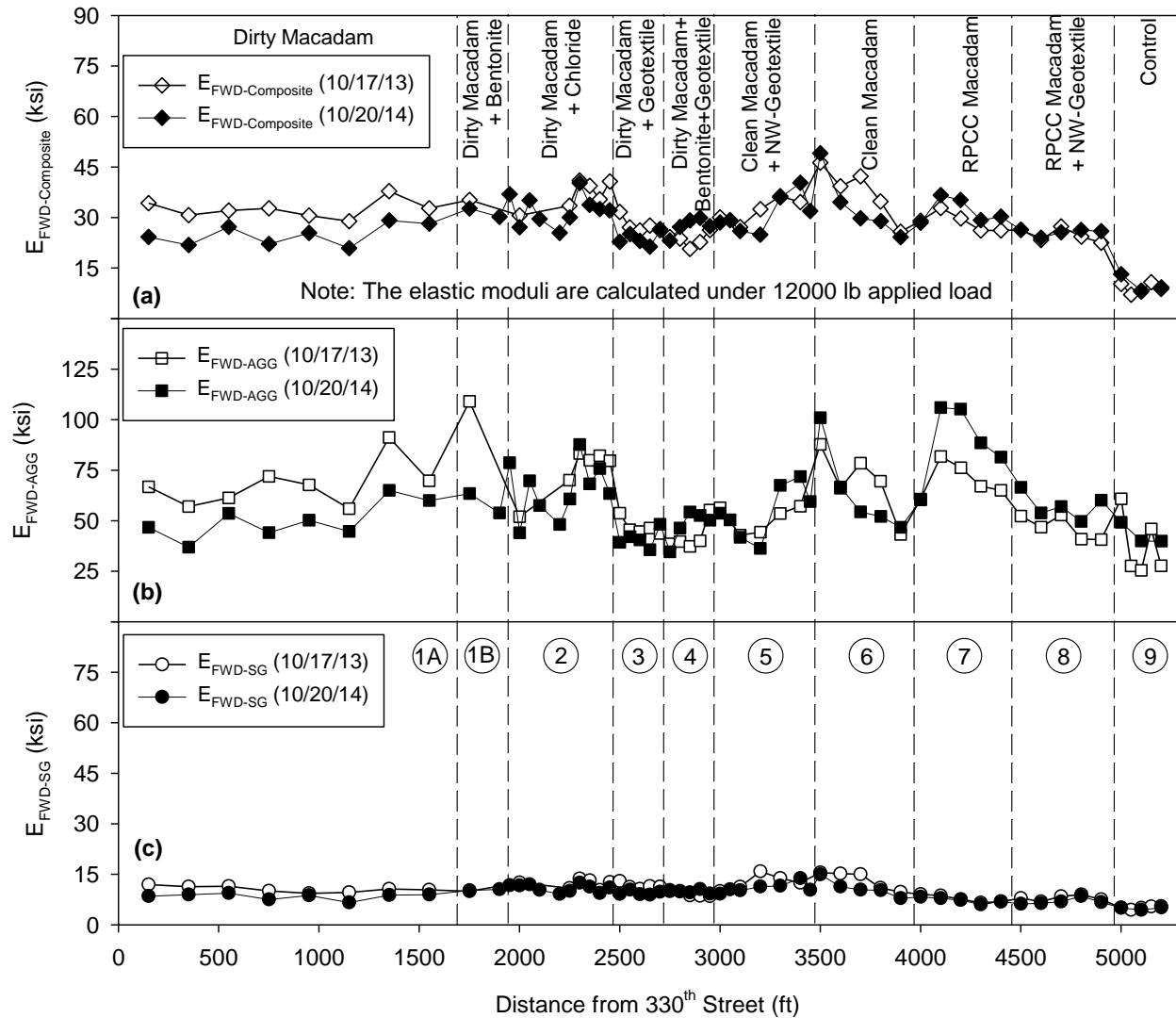
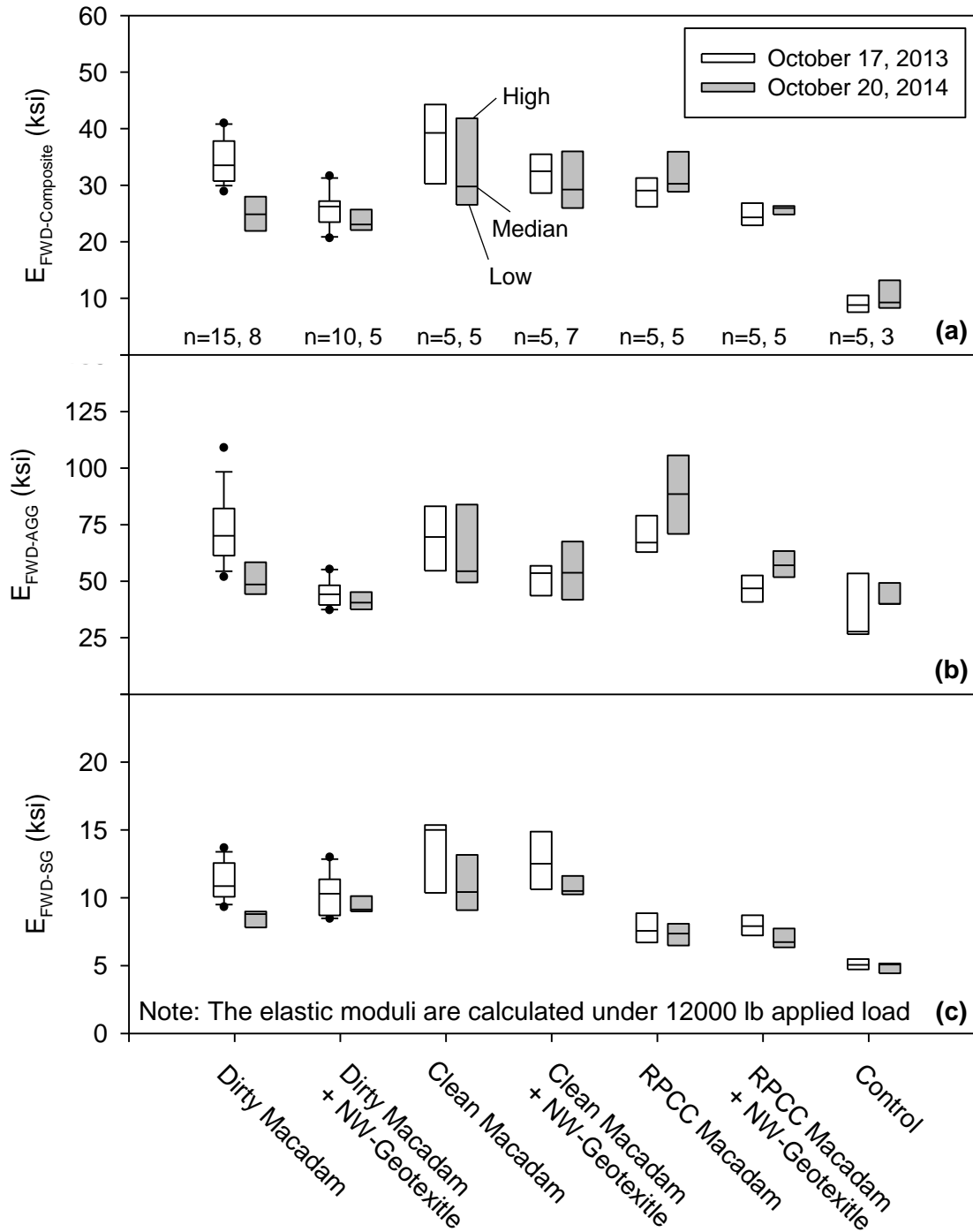


Figure 59. Comparison of 2013 and 2014 FWD test results for first-mile Sections 1A–9:
(a) $E_{FWD-Composite}$, (b) $E_{FWD-AGG}$, and (c) E_{FWD-SG}

Statistical boxplots of the 2013 and 2014 FWD test results for the first-mile sections are presented in Figure 60. The sections with the NW-geotextile exhibited lower $E_{FWD-Composite}$ values than the corresponding sections without NW-geotextile, but also experienced smaller reductions in $E_{FWD-Composite}$ and $E_{FWD-AGG}$ from 2013 to 2014. This suggests that the NW-geotextile between the macadam stone base and surface aggregate can enhance long-term stability, possibly due to improved subsurface drainage and reduced contamination of the clean macadam material by fines migrating from the surface course. On the other hand, the smaller reduction could be a result of the initial modulus values being lower for the sections with NW-geotextile compared to the same material without the geotextile. The improvement in modulus discussed above for the RPCC sections from 2013 to 2014 is also evident in Figure 60a and 58b. For the subgrade, the modulus E_{FWD-SG} decreased from 2013 to 2014 for all of the test sections (Figure 60c).



Middle line of box is median, box edges are 25th and 75th percentiles, dots are outliers, and whiskers extend to most extreme data not considered outliers

Figure 60. Summary boxplots of 2013 and 2014 FWD test results for first-mile sections:
(a) $E_{FWD-Composite}$, (b) $E_{FWD-AGG}$, and (c) E_{FWD-SG}

The 2014 FWD test results for the as-constructed second mile Sections 10–20 are shown in Figure 61. These tests were conducted 20 days after construction of the chemically stabilized Sections 15–17. Both $E_{FWD-Composite}$ and $E_{FWD-AGG}$ of the chemically stabilized Sections 15–17 and the mechanically stabilized Sections 19A–19B were higher than the rest of the sections. Compared to the variations of $E_{FWD-Composite}$ and $E_{FWD-AGG}$ across all sections, the E_{FWD-SG} of the subgrade was relatively uniform. The FWD moduli of the fly ash-stabilized Section 16 were much more uniform than the cement-stabilized Section 17 in terms of $E_{FWD-Composite}$ and $E_{FWD-AGG}$ (Figure 61a and Figure 61b). The greater variability in the moduli of the cement section may be due to a more variable surface aggregate course thickness in this section, because the cement-stabilized UCS was found to be more sensitive to the aggregate content of the SG+AGG mixture than the fly ash-stabilized UCS. This hypothesis is also supported by the good agreement between the trends of the FWD and UCS test results across Section 17, as well as the fact that the UCS specimen at 100 ft in Section 17 gave the highest UCS and FWD modulus and was comprised mainly of aggregate with little to no subgrade mixed in (see section 6.4.3).

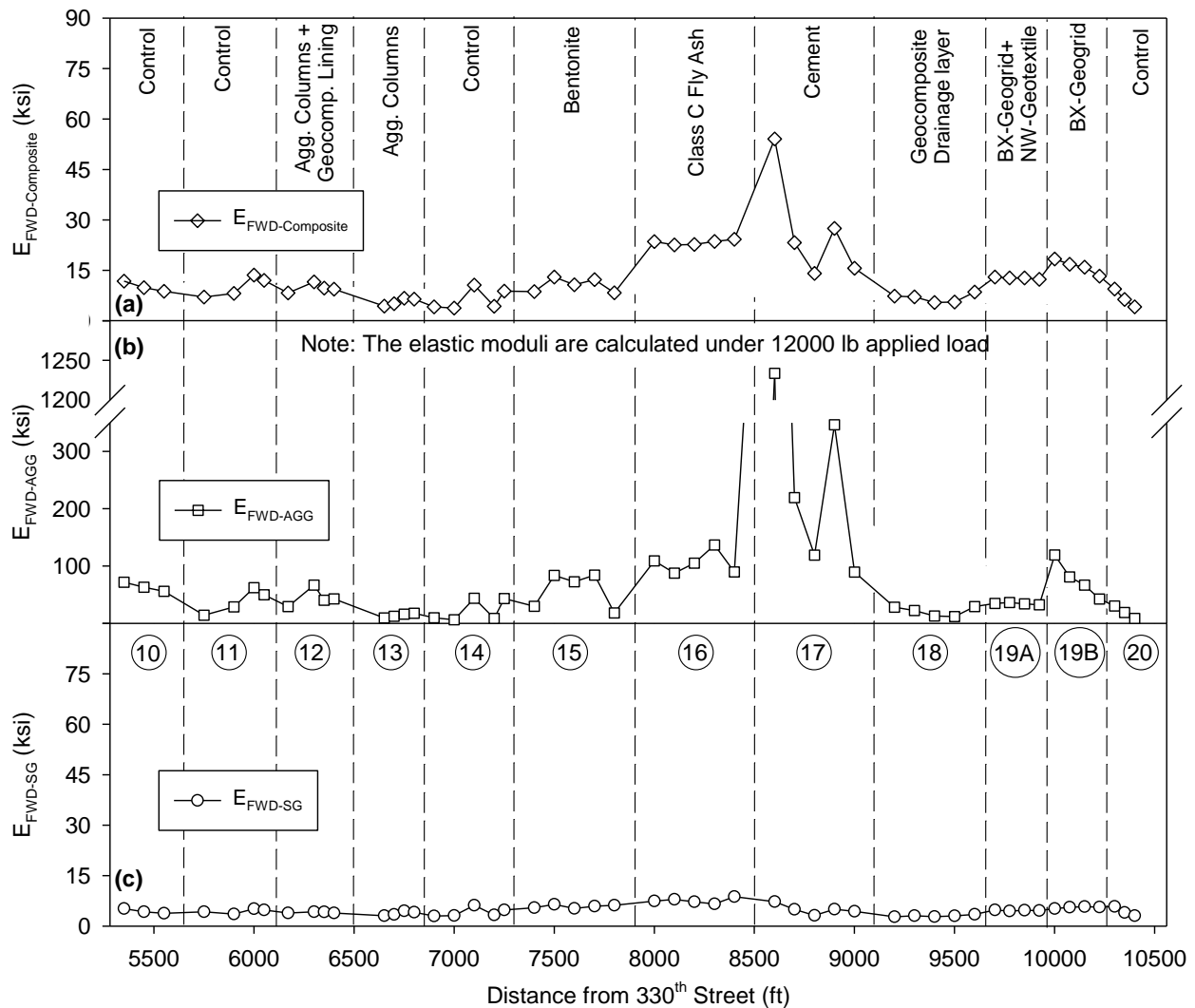
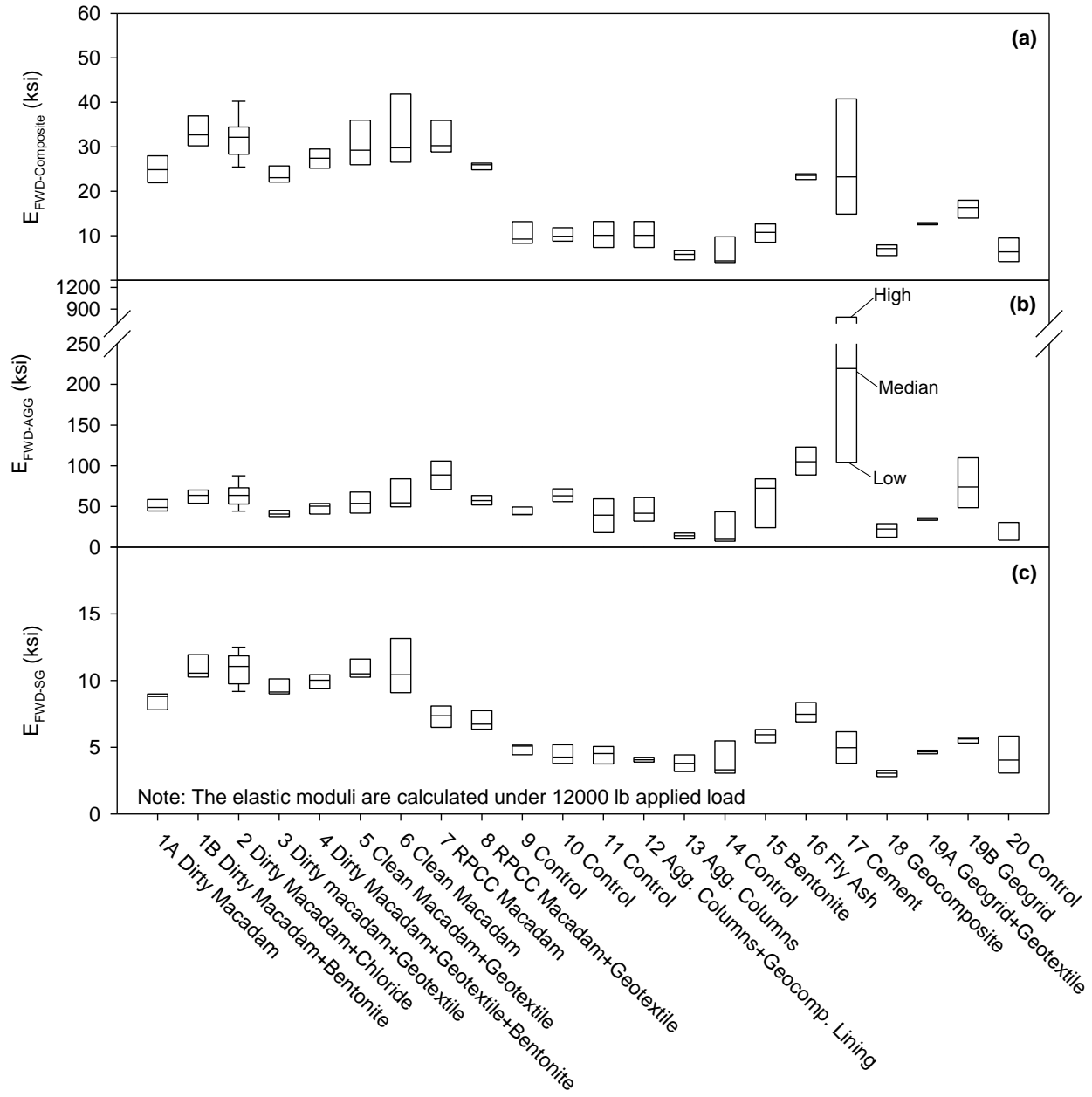


Figure 61. 2014 FWD test results for second-mile Sections 10–20: (a) $E_{FWD-Composite}$, (b) $E_{FWD-AGG}$, and (c) E_{FWD-SG}

Statistical boxplots of the second group of FWD tests in 2014 are presented in Figure 62. The $E_{\text{FWD-Composite}}$ values of the macadam Sections 1A–8 and fly ash- and cement-stabilized Sections 16 and 17 were about three times higher than the control Sections 9–11, 14, and 20 (Figure 62a). As noted above, however, the cement-stabilized Section 17 produced significant variation in $E_{\text{FWD-Composite}}$ over its length, with some values falling below those of the fly ash-stabilized Section 16. The $E_{\text{FWD-Composite}}$ values for the BX geogrid with NW-geotextile (Section 19A) and BX-geogrid (Section 19B) were also higher than the control sections. The composite modulus $E_{\text{FWD-Composite}}$ was not significantly increased relative to the nearest control section for the aggregate column Sections 12 and 13, the bentonite Section 15, or the geocomposite drain Section 18.

The median $E_{\text{FWD-AGG}}$ values ranged between 10 to 50 ksi for most of the sections, but were significantly higher for the RPCC macadam Section 7, fly ash Section 16, cement Section 17, and BX-geogrid Section 19B (Figure 62b).

The subgrade material for the entire two miles of demonstration sections is the same type of backfill. However, the $E_{\text{FWD-SG}}$ values for the macadam Sections 1–8 in Figure 62c were higher than those of the other sections. This phenomenon may have two causes: (1) due to the thicker surface course of the macadam sections, the measurement influence depth of the FWD into the subgrade layer was shallower, similar to the DCP- CBR_{SG} test results discussed above, and (2) the additional surcharge of the extra macadam and aggregate layers increased the effective stress and therefore the modulus of the underlying subgrade.



Middle line of box is median, box edges are 25th and 75th percentiles, and whiskers extend to most extreme data not considered outliers

Figure 62. Summary boxplots of 2014 FWD tests on all demonstration sections: (a) $E_{FWD-Composite}$, (b) $E_{FWD-AGG}$, and (c) E_{FWD-SG}

6.4.2 MASW Tests

Multichannel Analysis of Surface Waves (MASW) geophysical tests were conducted at the same time and locations as the 2014 FWD tests. MASW tests were performed to assess the feasibility of using this type of non-destructive testing (NDT) method on granular surfaced roads, the resolution in terms of the smallest layer thickness that could be resolved, and to compare the agreement of back-calculated moduli with the FWD method.

The MASW and FWD NDT methods employ different theoretical solutions to back-calculate layer stiffnesses (moduli) of an assumed multi-layered system. Since the aggregate surface course and underlying near-surface subgrade were of interest in this study, all of the demonstration sections were analyzed as simple two-layer systems. The notation $E_{\text{MASW-AGG}}$ and $E_{\text{MASW-SG}}$ will be used to denote the elastic modulus of the surface course and subgrade material, respectively, as determined by MASW tests. To reduce the number of unknowns in the back-calculation (inversion) procedures of the MASW tests, the average thickness of the surface course layer of each section as determined from the DCP tests was used for both the FWD and MASW back-calculations. Also, layer densities are inputs for the MASW inversion, but the influence of density is much smaller than that of modulus. Therefore, the standard Proctor maximum dry unit weights of the surface aggregate (140 pcf) and subgrade (98 pcf) were used for all of the sections. The Poisson's ratios of the surface course and subgrade material were assumed to be 0.3 and 0.4, respectively.

The back-calculated MASW and FWD moduli are compared in Figure 63 and Figure 64. For the surface course layer, the two test methods showed very similar trends, but the MASW moduli of the surface courses were much higher than the FWD moduli. This behavior is expected, because dynamic strain levels imposed in MASW tests employing a small hammer source were much lower than those of FWD tests employing large weight drops of several thousand pounds (see Sections 3.2.2 and 3.2.3 of the report). It is well-known that the elastic modulus of granular materials decreases nonlinearly with increasing strain.

For the subgrade, the values of MASW and FWD moduli were in closer agreement, but $E_{\text{MASW-SG}}$ showed significantly more variation (Figure 63b and Figure 64b). The greater variation may be a result of using a small ball-peen hammer as the impact source, which results in very small strains in the subgrade. However, the small hammer was chosen because the goal was to focus the MASW measurement resolution on the thin aggregate layer. A smaller hammer creates higher frequency content in the seismic surface waves and enables a closer source-to-first-receiver impact distance without overloading the geophones. If measurements of the subgrade stiffness are desired by MASW, a larger source such as the traditionally used sledge hammer could easily be employed with a larger impact offset, to generate greater impact energy and therefore larger strains in the subgrade. For the second mile sections, the surface course layers were much thinner than the first mile, but most of the MASW trends still followed the FWD trends (Figure 64a). Again, the MASW results for the subgrade showed much more variation than the FWD tests, and the MASW moduli of the control Sections 10 and 11, geocomposite drain Section 18, and BX-geogrid with NW-geotextile Section 19A were lower than the corresponding FWD moduli.

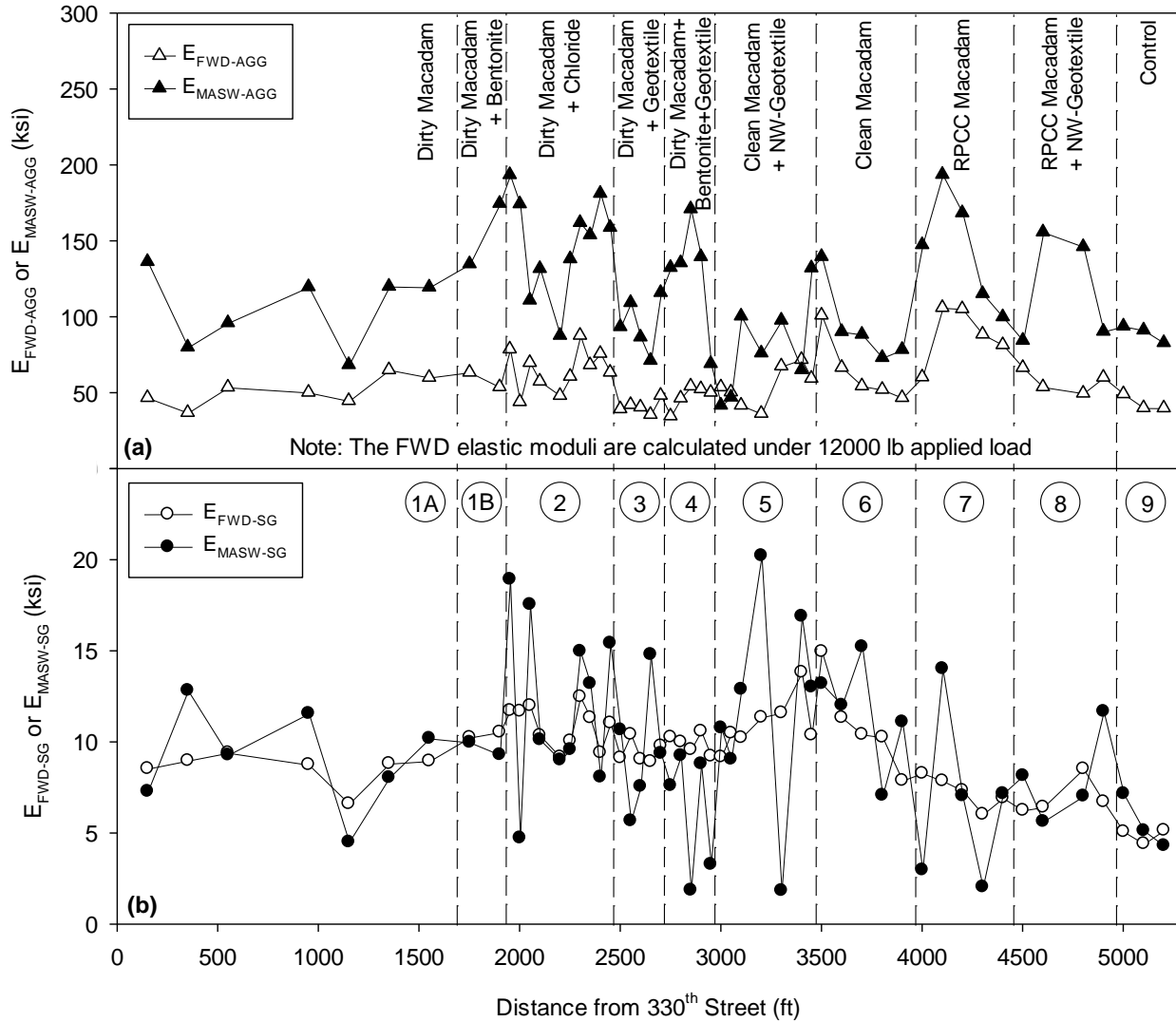


**Figure 63. FWD and MASW back-calculated moduli for first-mile Sections 1A–9:
(a) surface course modulus and (b) subgrade modulus**

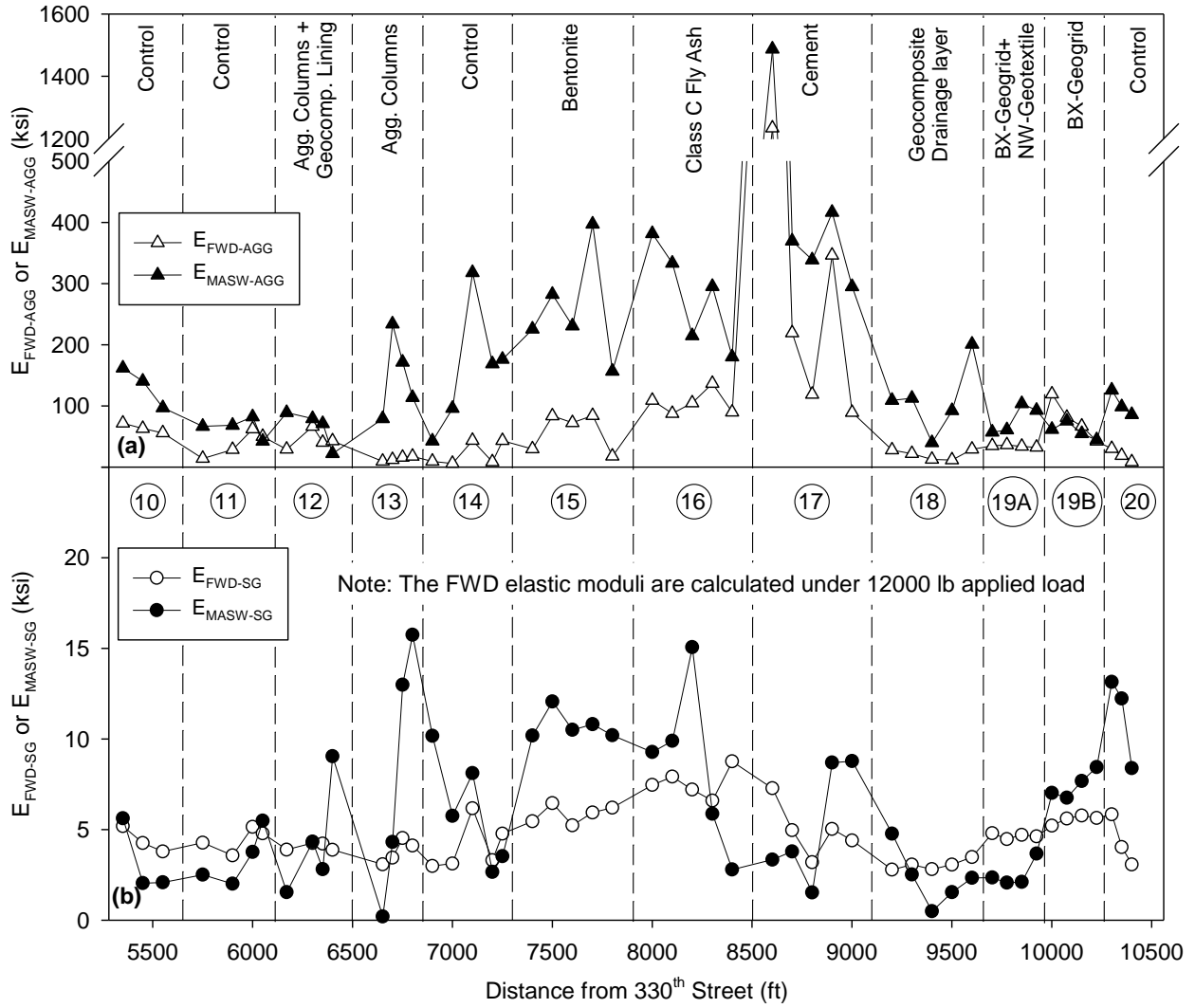
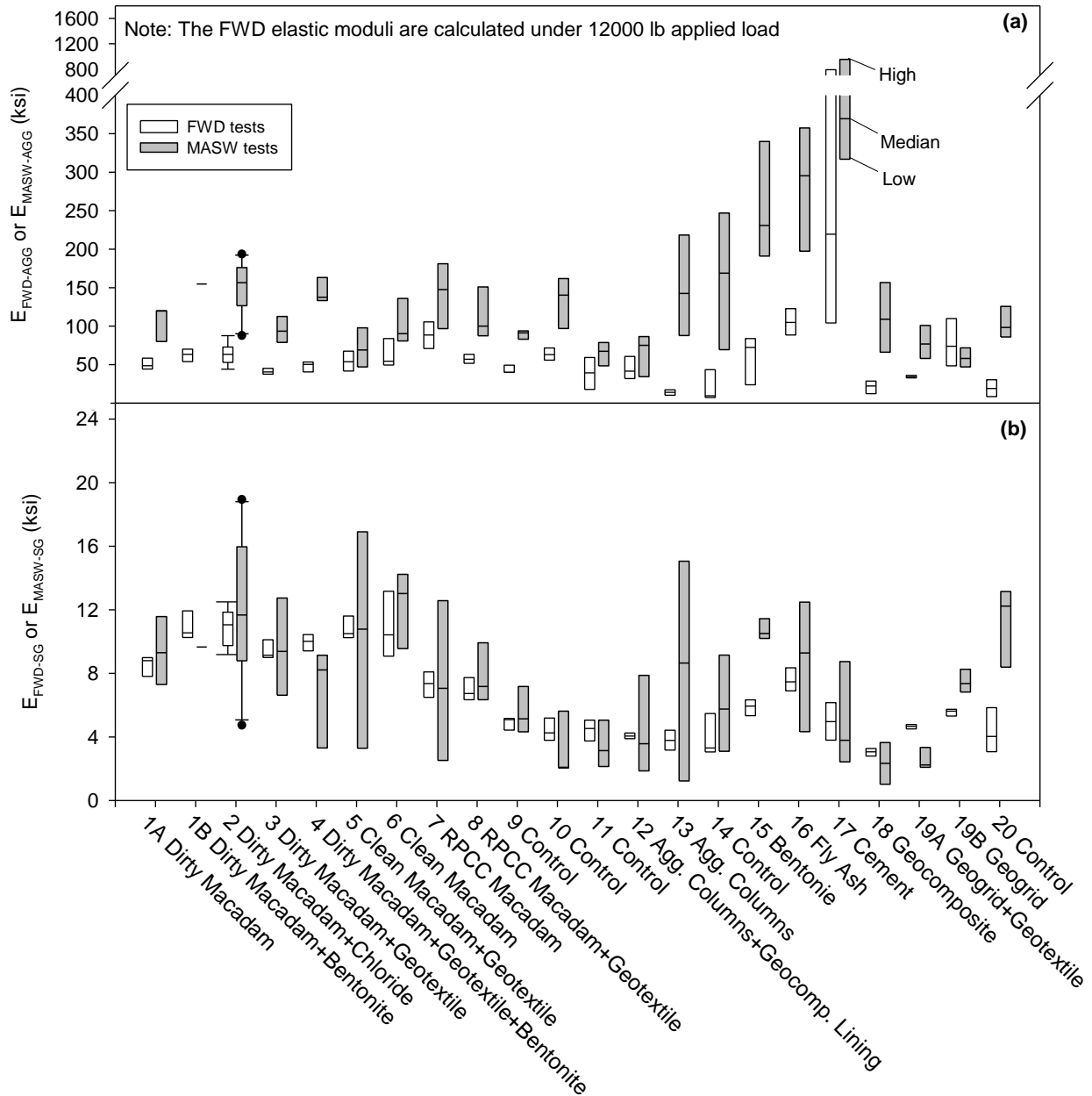


**Figure 64. FWD and MASW back-calculated moduli for second-mile Sections 10–20:
(a) surface course modulus, (b) subgrade modulus**

Statistical boxplots of all the FWD and MASW back-calculated moduli are shown in Figure 65. The two tests methods showed similar trends among the different sections, but the MASW test results showed greater variation, especially for the $E_{\text{MASW-SG}}$ values. As mentioned above, a larger impact source could reduce the variability of the MASW method for the subgrade.



Middle line of box is median, box edges are 25th and 75th percentiles, dots are outliers, and whiskers extend to most extreme data not considered outliers

Figure 65. Summary boxplots of back-calculated FWD and MASW moduli: (a) first mile Sections 1A–9, (b) second mile Sections 10–20

Statistical correlations between the mean MASW and FWD moduli were generated for both the surface course and subgrade materials of all sections. The correlation for the surface course materials is shown in Figure 66a. The coefficients of determination (R^2) of the linear regression models are below 0.5. To develop a meaningful physics-based relationship between the low-strain MASW and higher-strain FWD results, the different strain levels induced in the two tests should be accounted for.

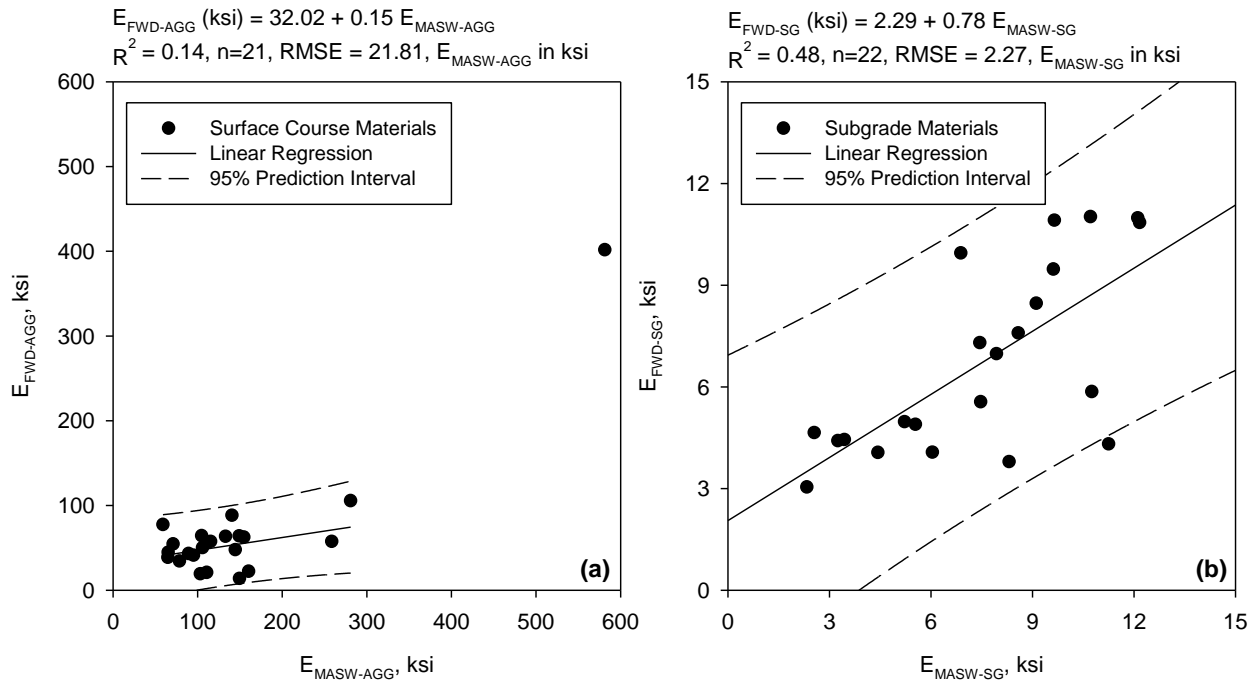


Figure 66. Statistical correlations between mean MASW and FWD back-calculated moduli: (a) for surface course materials, (b) for subgrade

Additional MASW tests were also conducted to monitor the elastic modulus of the fly ash- and cement-stabilized surface course materials during their curing periods. The test results (Figure 67) show that the modulus of the fly ash-stabilized surface course materials in Section 16 did not significantly increase up to 28 days after construction, except for one test location at 18 days. The moduli of the cement-stabilized surface course for four out of the five test locations increased after 20 days, but then decreased by 30 days. The $E_{MASW-AGG}$ values between the two sections were similar except for one point of the cement-stabilization section, which had a much higher stiffness than all others. The $E_{MASW-SG}$ values showed more variation for reasons discussed previously, and did not exhibit any significant trends.

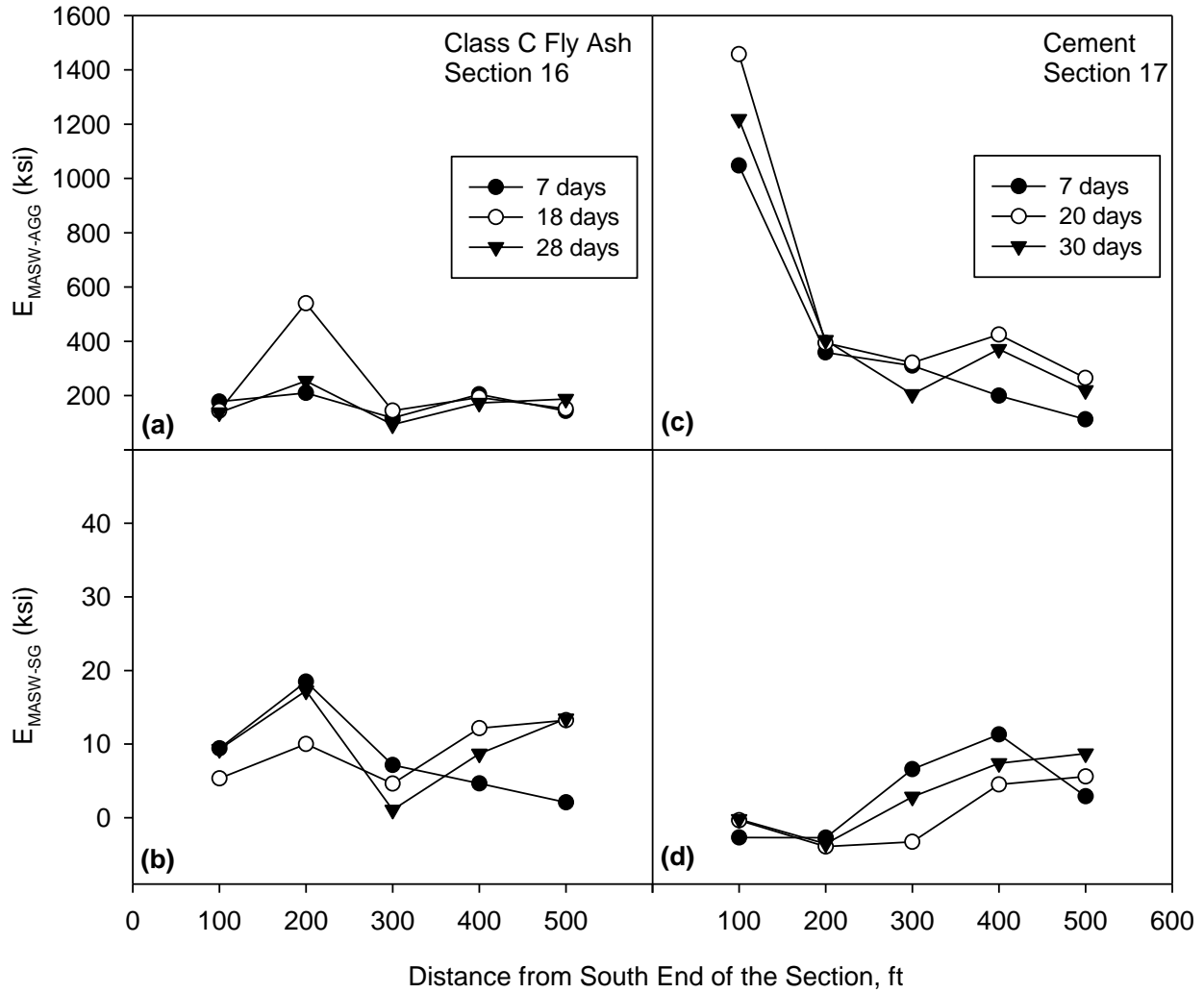


Figure 67. Back-calculated moduli of surface course and subgrade from MASW tests during curing of chemically stabilized sections: (a and b) fly ash Section 16 and (c and d) cement Section 17

6.4.3 Laboratory Proctor and UCS Tests for Surface Course Materials of Chemical Stabilization Sections

During construction of the fly ash- and cement-stabilized Sections 16 and 17, standard Proctor tests were conducted on the as-constructed chemically stabilized surface course materials in the field. The representative surface course materials were collected from five locations of each section: 100, 200, 300, 400, and 500 ft from the south end. The field Proctor test results are plotted with the laboratory standard Proctor test results of the chemically stabilized subgrade (SG), surface aggregate (AGG), and subgrade plus surface aggregate mixture (SG+AGG) specimens in Figure 68. The results show that moisture contents of the field SG+AGG specimens were within $\pm 3\%$ of the optimum moisture contents (w_{opt}) determined by the laboratory standard Proctor tests. However, the dry unit weights of most of the field specimens were lower than those of the laboratory specimens compacted using the same compaction energy. These differences indicate that the field-mixed surface course materials may have contained higher proportions of subgrade materials than the laboratory-prepared specimens. Also, based on visual observations, the field specimens that yielded higher dry unit weights than the laboratory Proctor specimens contained higher proportions of surface aggregate material.

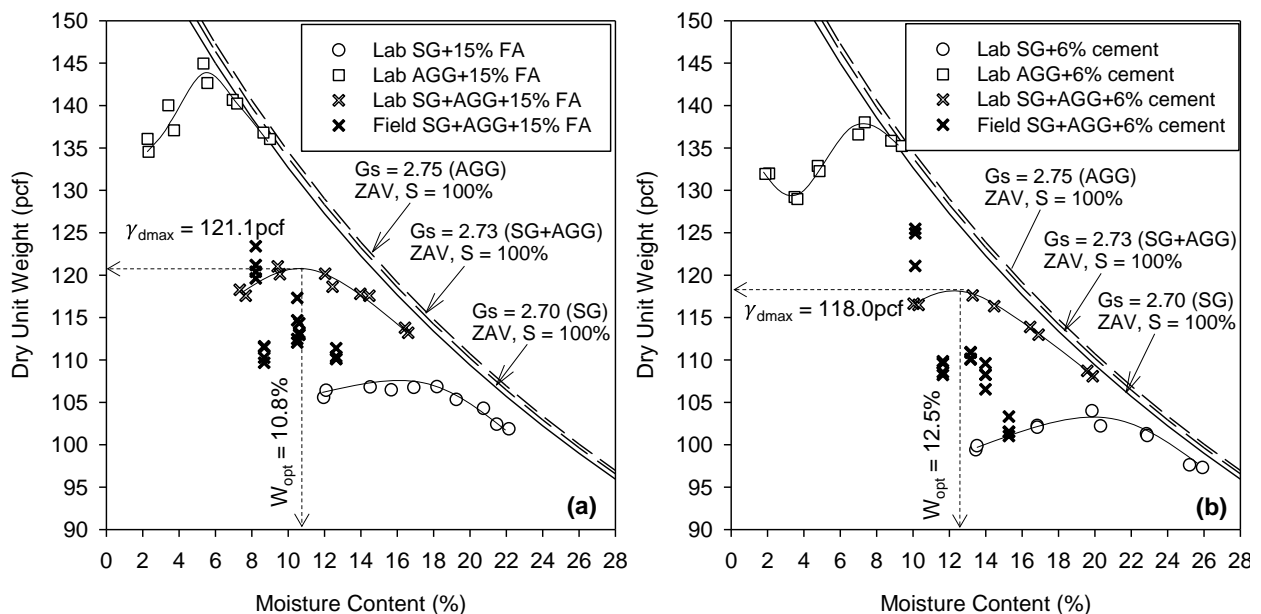


Figure 68. Standard Proctor test results for subgrade, surface aggregate, and lab- and field-compacted subgrade-surface aggregate mixture: (a) fly ash-stabilized and (b) cement-stabilized

UCS tests were also conducted on the field-compacted Proctor specimens to measure as-compacted and vacuum-saturated shear strength at 7 days curing. The as-compacted and saturated UCS of the fly ash-stabilized specimens were generally lower than the cement-stabilized specimens, as shown in Figure 69. As was found for the FWD tests in Figure 61, the fly ash-stabilized specimens yielded a more uniform UCS across the test section than the cement-

stabilized specimens. The cement-stabilized specimens that yielded the highest UCS (at 100 ft in Figure 69) were observed to consist primarily of surface aggregate material with little subgrade.

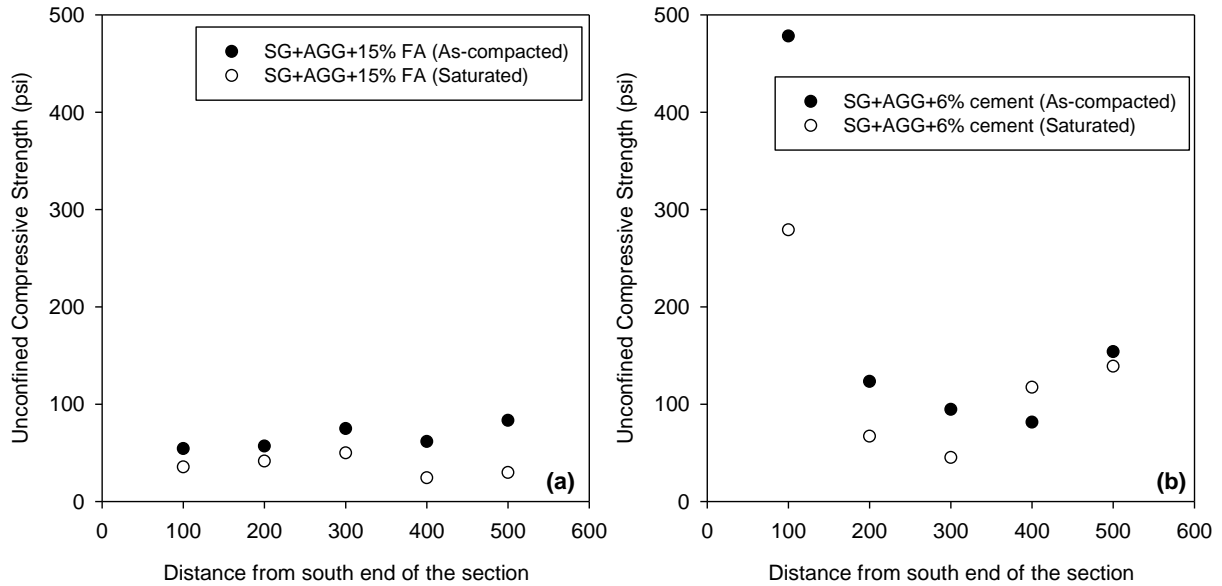


Figure 69. UCS test results of field-compacted (a) fly ash-stabilized and (b) cement-stabilized SG+AGG specimens at 7 days curing

The as-compacted UCS values of the field-compacted surface course specimens shown in Figure 69 are compared with the field MASW surface course moduli ($E_{MASW-AGG}$) in Figure 70. For the fly ash section, the MASW and UCS test results did not follow the same minor trends, but both tests exhibited relatively constant values across the section. For the cement Section 17, the two test methods showed similar trends. The MASW test clearly indicated the high stiffness associated with the high strength of the material at 100 ft from the south end.

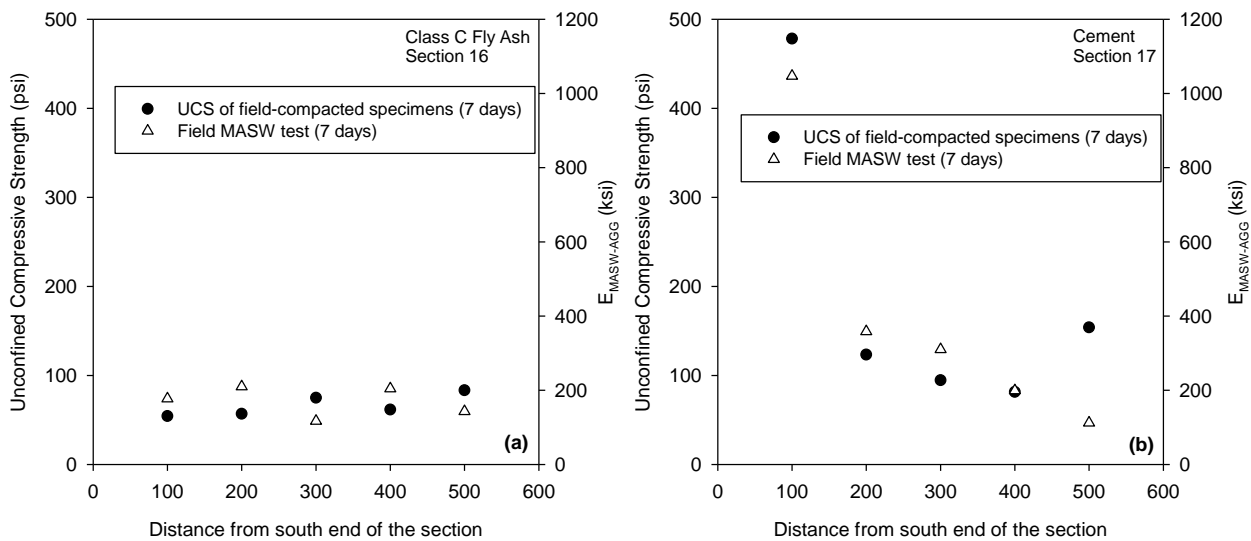


Figure 70. Comparison of UCS and MASW results for (a) fly ash-stabilized Section 16 and (b) cement-stabilized Section 17

6.4.4 Field Air Permeameter Tests for Geocomposite Drain Section

In this study, Air Permeameter Tests (APT) were conducted to quantify the improvement in drainage provided by the geocomposite layer of the granular surfaced road. For the geocomposite drain Section 18, the Macdrain™ (MD) W1051 and W1091 geocomposite materials were installed. APTs were performed at three different locations in the geocomposite drain Section 18 and at three locations in nearby Section 17, which was not stabilized yet and therefore still a control section. At each test location, APTs were performed at different depths within the surface course layer, as shown in Figure 71, to determine how the hydraulic conductivity changes with depth.

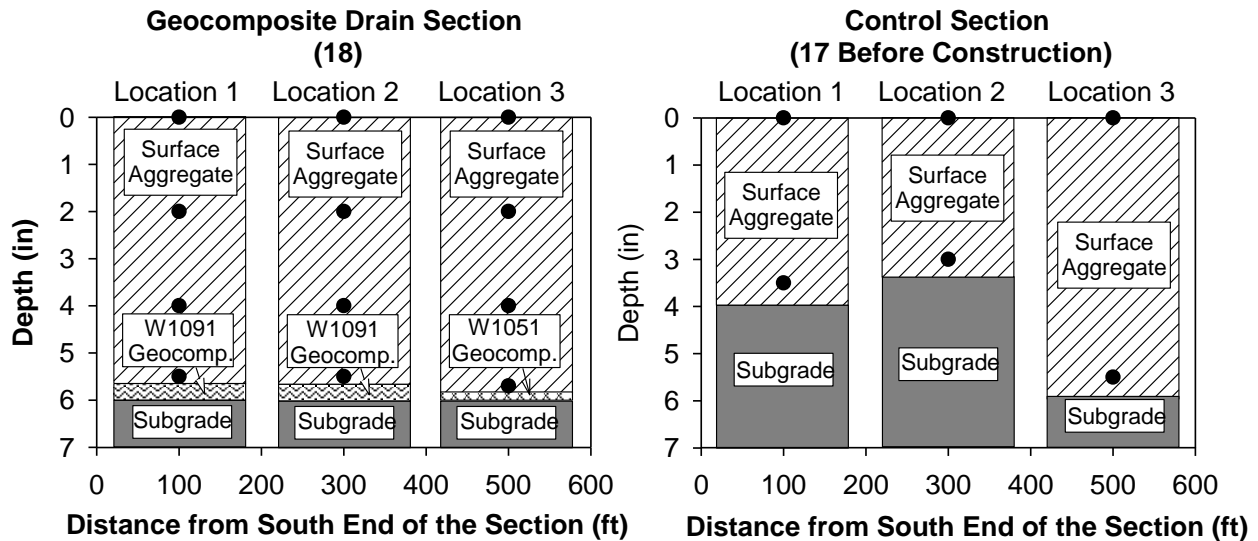


Figure 71. APT locations (indicated by black dots) and cross-section profiles of the geocomposite drain Section 18 and control Section 17

The APT results are shown in Figure 72. For the control section, the saturated hydraulic conductivities (K_{sat}) at the three test locations were very similar (~60 ft/day), and relatively constant with depth. However, for the geocomposite drain at Locations 1 and 2 which have the W1091 geocomposite with a thicker flexible core than the W1051 (see Section 4.3.3 of the report), K_{sat} in the surface aggregate layer increased consistently with depth. For test Location 3 with the W1051 geocomposite, K_{sat} initially decreased with depth for the first 2 in. below the road surface, then increased as the geocomposite was approached. However, because there was only one test conducted on the section with W1051 geocomposite, this trend should be verified by additional tests. Based on the APT data, the saturated hydraulic conductivity was approximately 2,000 ft/day for the W1051 geocomposite and 6,500 ft/day for the W1091 geocomposite.

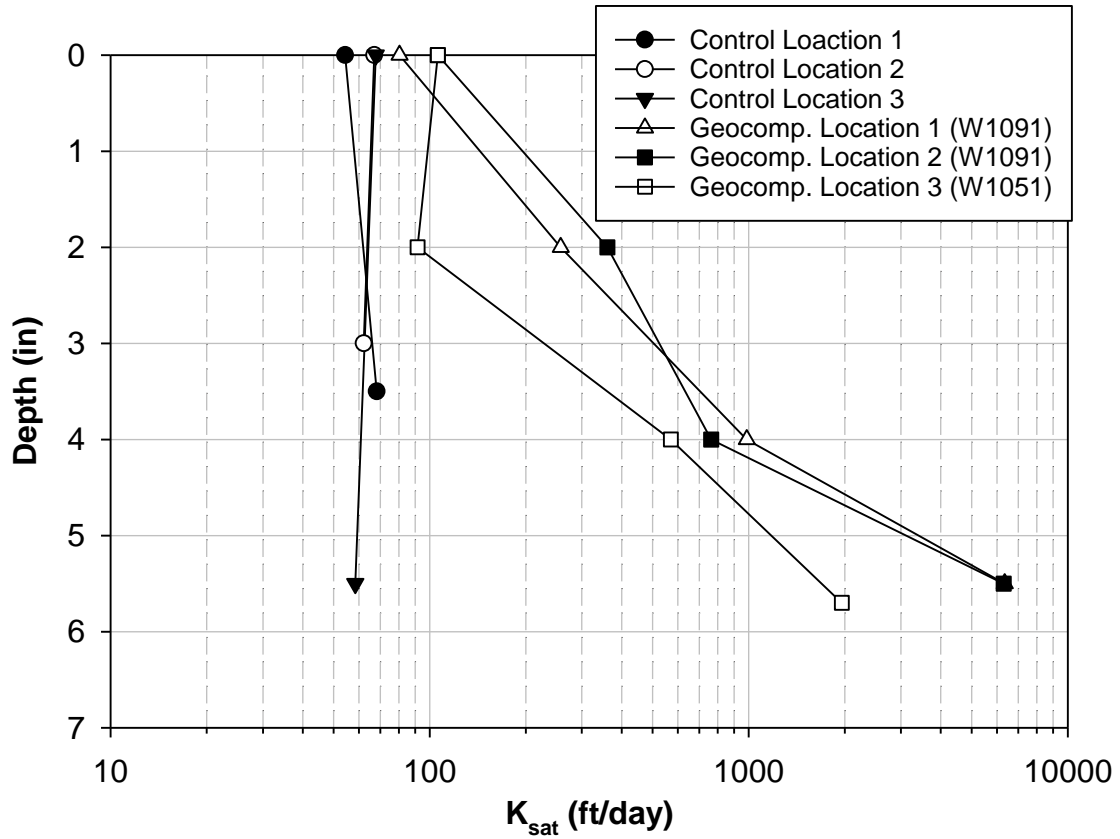


Figure 72. Saturated hydraulic conductivity versus depth for aggregate layers of geocomposite drain Section 18 and control Section 17

6.5 Evaluation of Post-Thawing Durability

Laboratory freezing-thawing and wetting-drying tests were conducted on the surface course materials of the fly ash- and cement-stabilized Sections 16 and 17, which included approximately 3 in. of existing surface aggregate mixed with 5 in. of subgrade as described in Section 5.3 of the report. Two groups of post-thawing field tests were also conducted in spring of 2014 and 2015 to compare the in situ post-thawing performance of the various demonstration sections.

6.5.1 Laboratory Freezing-Thawing and Wetting-drying Tests for Chemical Stabilization Sections

Laboratory freezing-thawing and wetting-drying tests were conducted on field-compacted specimens to evaluate the durability of the fly ash- and cement-stabilized surface course materials. According to ASTM D 559-03 and D560-03, these test methods are intended for cement-stabilized specimens. However, they were also conducted on the fly ash-stabilized specimens for a direct comparison in this study. The ASTM standards specify subjecting each specimen to 12 cycles for both the freezing-thawing and wetting-drying tests.

The number of freeze-thaw or wet-dry cycles until failure of the specimens is reported in Table 22. As anticipated, the cement-stabilized specimens exhibited better freeze-thaw and wet-dry durability than the fly ash-stabilized specimens. Of the cement-stabilized specimens, none failed within 12 wet-dry cycles, but three out of four failed between 9 and 11 freeze-thaw cycles. In contrast, none of the fly ash-stabilized specimens survived more than 9 wet-dry or 6 freeze-thaw cycles. For the cement-stabilized specimen at 500 ft, an intact specimen could not be obtained, because the specimens collapsed when de-molded after compaction in the field.

Table 22. Number of freeze-thaw or wet-dry cycles to failure for fly ash-and cement-stabilized specimens

Fly Ash-Stabilized Specimens			Cement-Stabilized Specimens			
Distance From E. End of Test Section	Wet-Dry Cycles to Failure	Freeze-thaw Cycles to Failure	Distance From E. End of Test Section	Wet-Dry Cycles to Failure	Distance From E. End of Test Section	Freeze-thaw Cycles to Failure
100	4	4	200	>12	100 #1	11
200	2	4	300 #1	>12	100 #2	>12
300	10	6	300 #2	>12	400 #1	10
400	7	4	500	>12	400 #2	9
500	2	3			—	

The percent mass changes during freeze-thaw and wet-dry cycling of the fly ash- and cement-stabilized specimens are shown in Figure 73 and Figure 74, respectively. The results show that the cement-stabilized aggregate-subgrade mixture specimens provide better durability than the fly ash-stabilized specimens as expected. Photographs of each specimen after each freeze-thaw or wet-dry cycle are shown in Figure 75 through Figure 78.

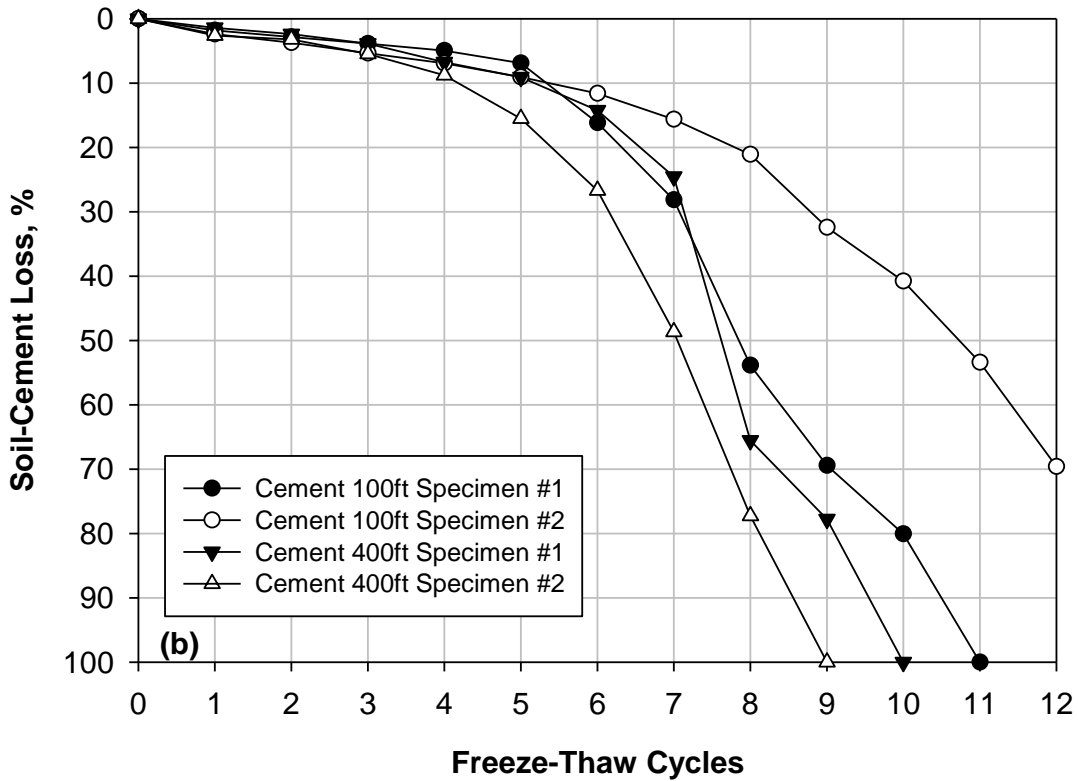
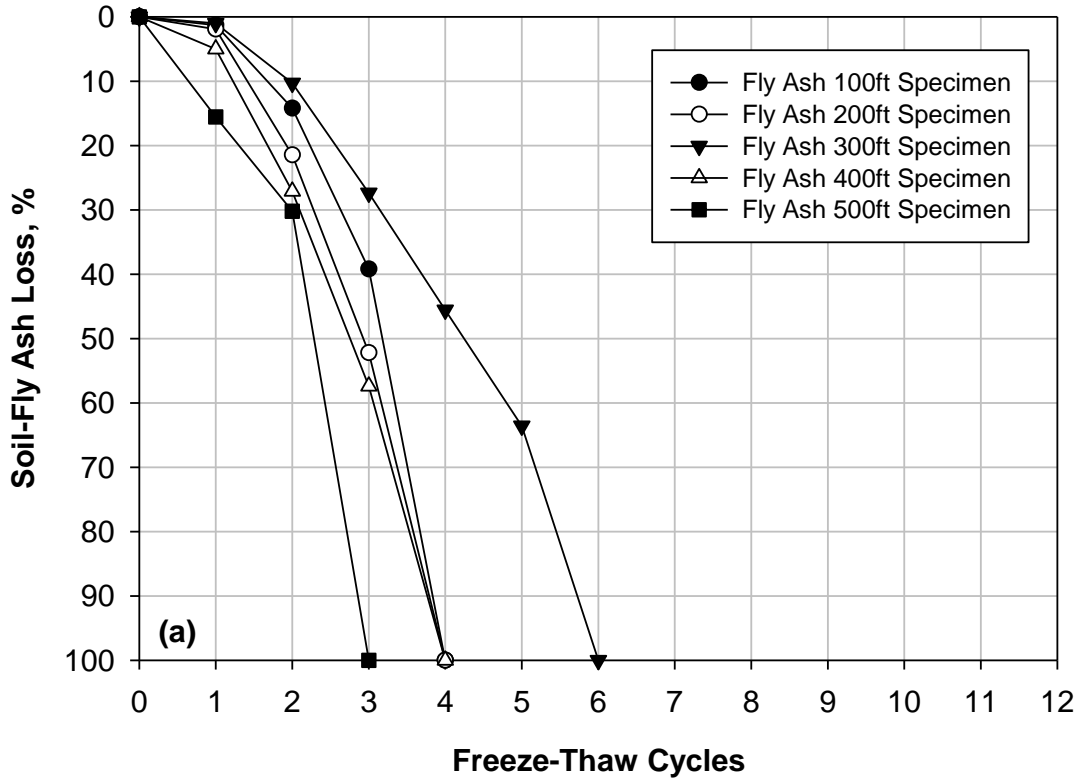


Figure 73. Mass changes of (a) fly ash-stabilized and (b) cement-stabilized aggregate-subgrade mixture specimens during freeze-thaw cycling

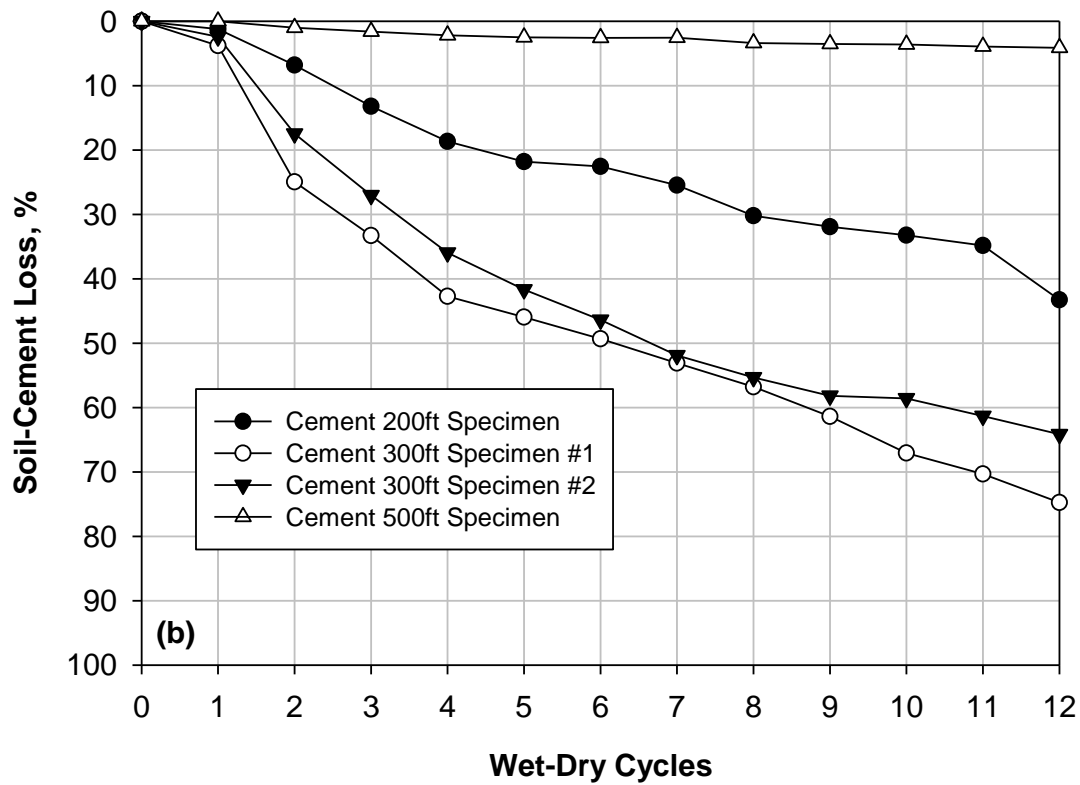
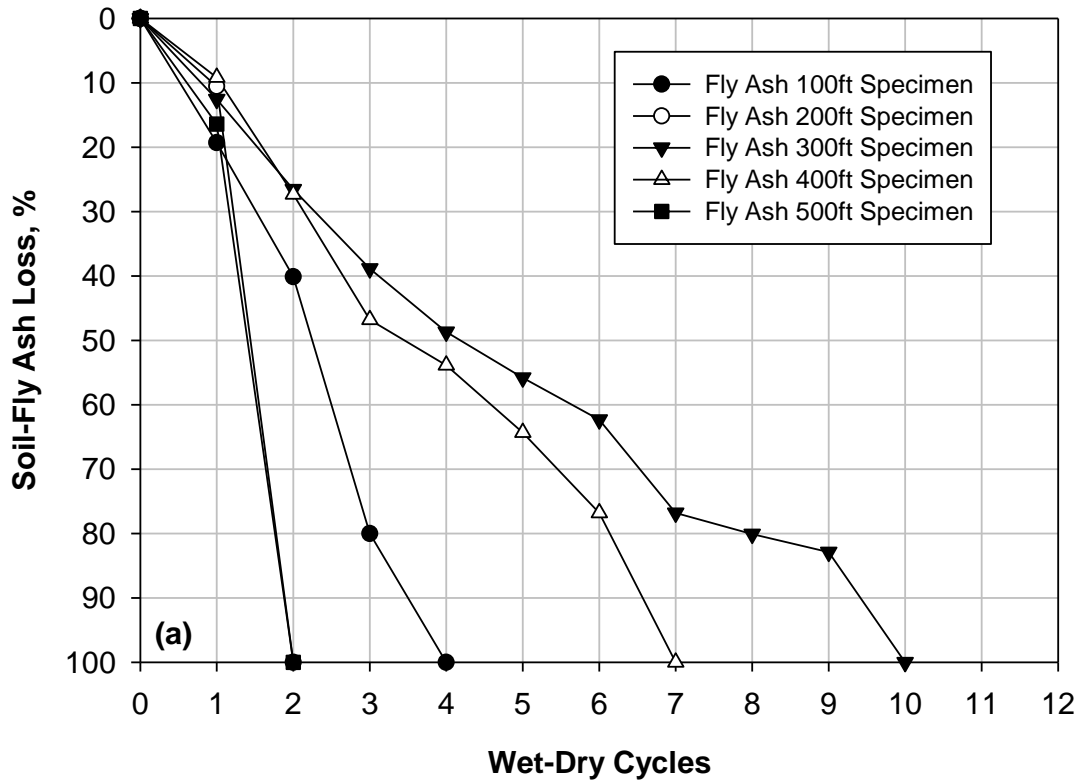


Figure 74. Mass changes of (a) fly ash-stabilized and (b) cement-stabilized aggregate-subgrade mixture specimens during wet-dry cycling



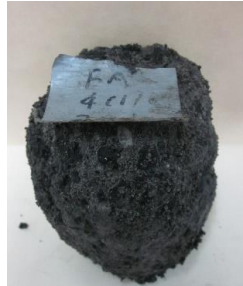
Before Test



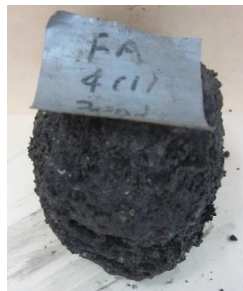
After 1st freeze-thaw cycle



After 3rd freeze-thaw cycle



After 4th freeze-thaw cycle



After 5th freeze-thaw cycle

Figure 75. Photos of fly ash-stabilized specimens after freeze-thaw cycles



Before Test



After 1st freeze-thaw cycle



After 2nd freeze-thaw cycle



After 4th freeze-thaw cycle

Figure 76. Photos of cement-stabilized specimens after freeze-thaw cycles



After 5th freeze-thaw cycle



After 6th freeze-thaw cycle



After 7th freeze-thaw cycle



After 8th freeze-thaw cycle

Figure 76 (continued). Photos of cement-stabilized specimens after freeze-thaw cycles



After 9th freeze-thaw cycle



After 10th freeze-thaw cycle



After 11th freeze-thaw cycle



After 12th freeze-thaw cycle

Figure 76 (continued). Photos of cement-stabilized specimens after freeze-thaw cycles



Before test



After 2nd wet-dry cycle



After 3rd wet-dry cycle



After 4th wet-dry cycle

Figure 77. Photos of fly ash-stabilized specimens after wet-dry cycles



After 5th wet-dry cycle



After 6th wet-dry cycle



After 7th wet-dry cycle



After 8th wet-dry cycle



After 9th wet-dry cycle

Figure 77 (continued). Photos of fly ash-stabilized specimens after wet-dry cycles



After 1st wet-dry cycle



After 3rd wet-dry cycle



After 4th wet-dry cycle



After 5th wet-dry cycle

Figure 78. Photos of cement-stabilized specimens after wet-dry cycles



After 6th wet-dry cycle



After 7th wet-dry cycle



After 8th wet-dry cycle



After 9th wet-dry cycle

Figure 78 (continued). Photos of cement-stabilized specimens after wet-dry cycles



After 10th wet-dry cycle



After 11th wet-dry cycle



After 12th wet-dry cycle

Figure 78 (continued). Photos of cement-stabilized specimens after wet-dry cycles

6.5.2 Post-Thawing Performance in 2014

To evaluate the post-thawing performance of the demonstration sections after the first (2013-2014) freeze-thaw cycle, FWD and DCP tests were conducted on April 25 and May 3, 2014, respectively. The following sections present the weather and ground temperatures at the project site, results of post-thawing field tests, and survey photos taken during the thawing period.

6.5.2.1 Weather and Ground Temperature Profiles

A weather station and five thermocouples at different depths were installed on November 25, 2013 to monitor the air and ground temperatures and precipitation (Figure 18). The complete set of raw air and ground temperature data during the 2013-2014 seasonal freeze-thaw period are shown in Figure 79. The ground temperature profiles (with air temperature at 0 ft depth) are shown in Figure 80 for three different representative dates: the weather station installation date (November 25, 2013), the coldest ground temperature date (February 11, 2014), and the post-thawing FWD test date (April 25, 2014). The number of freeze-thaw (F/T) cycles at each depth were counted as described in Figure 19, and are reported in Figure 80. The number of F/T cycles generally increased with depth. Also, Figure 80 may indicate that the seasonal frost line of the ground was just below 5 ft depth. However, the data loggers stopped working for about two weeks, so the actual numbers of F/T cycles at each depth may be slightly higher than those shown in the figure.

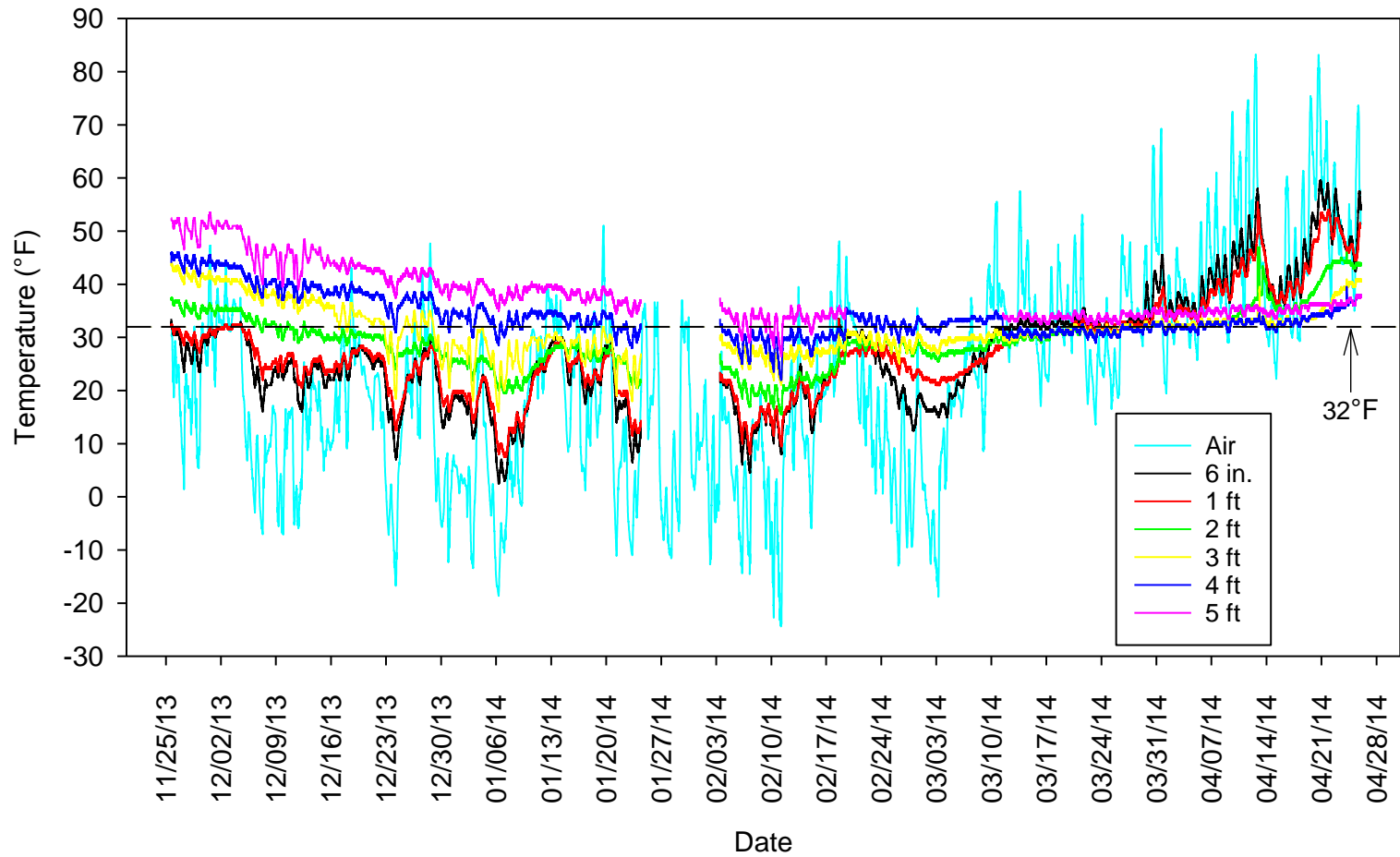


Figure 79. Air and ground temperature data during 2013-2014 seasonal freeze-thaw period

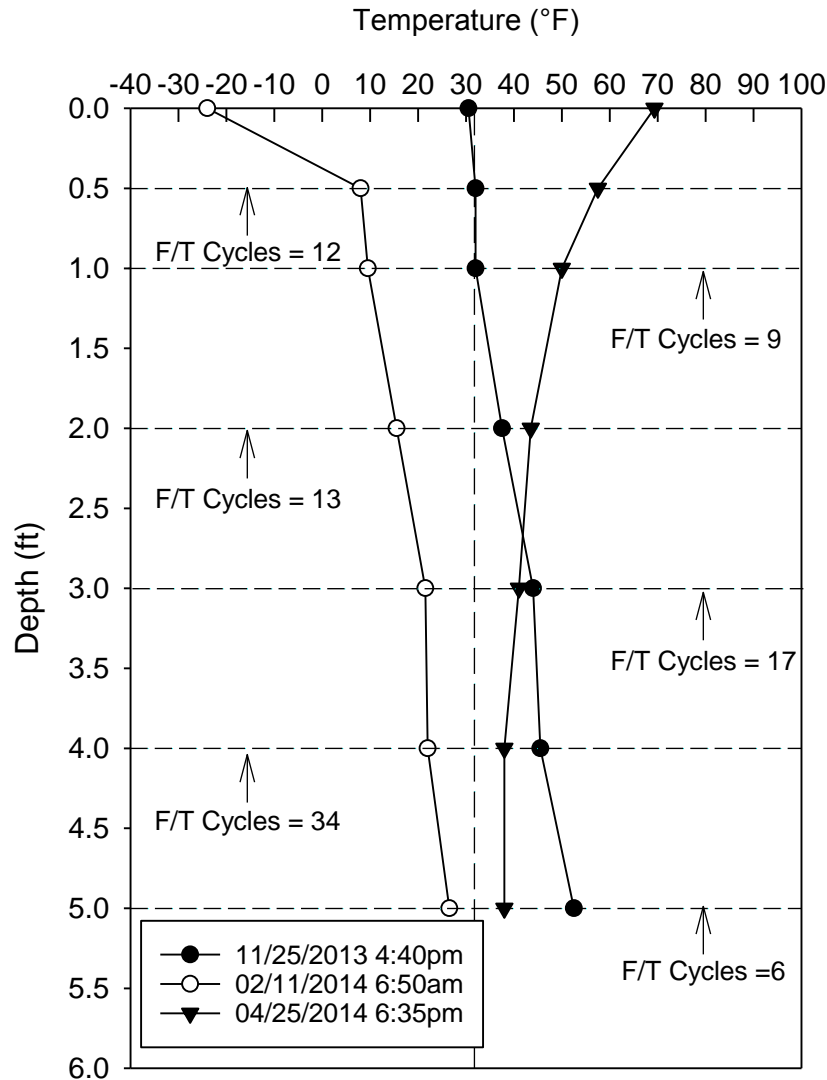


Figure 80. Ground temperature profiles at three different dates during 2013-2014 seasonal freeze-thaw period

Based on the weather station and ground temperature profile data, the freezing and thawing period can be determined for the project site by constructing the 32 °F isotherm from a contour map of temperature vs. time and depth, as shown in Figure 81. Because the weather station and ground temperature sensors were installed on November 25, 2013 when most of the ground was already frozen, the portion of the isotherm above 2 ft depth was estimated in this figure. The isotherm shows that freezing began at the ground surface around November 13, 2013, and progressed to a depth of at least 5 ft by February 5, 2014 (since the maximum depth monitored was 5 ft, the actual maximum depth of freezing could have been greater). The ground started to thaw from the bottom up beginning February 15 and from the top down beginning March 12, and progressed until the last portion of frozen subgrade at approximately 3.75 ft depth thawed around April 21, 2014. As shown in the figure, the freezing period at the surface was approximately 119 days. The thawing period, during which time groundwater above the frozen zone cannot

penetrate or drain downwards through the frozen zone, was approximately 40 days. During this thawing period, the roadway surface is most susceptible to damage because excess water trapped in the melted subgrade above the frozen zone generates high pore-water pressures under heavy traffic loads and cannot drain through the frozen subgrade underneath (Andersland and Ladanyi 2004).

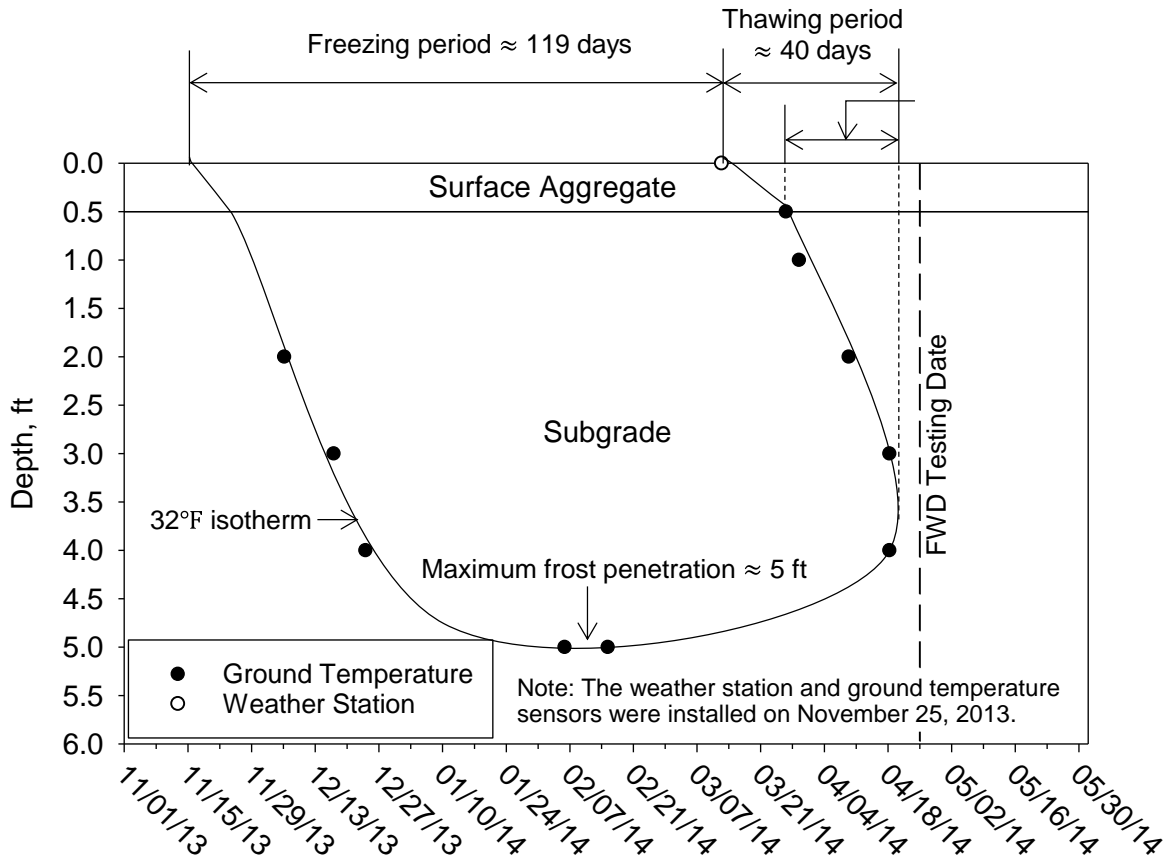


Figure 81. 2013–2014 ground freezing-thawing period of the project site

Rainfall data was also continuously recorded at 15 minute intervals using the weather station. The cumulative precipitation for the month of March 2014 was 2.04 in., which increased significantly in April to 12.88 in. (Figure 82). The maximum rainfall intensities over any 15 minute period of March and April, 2014 were approximately 1.24 and 1.96 in. per hour, respectively.

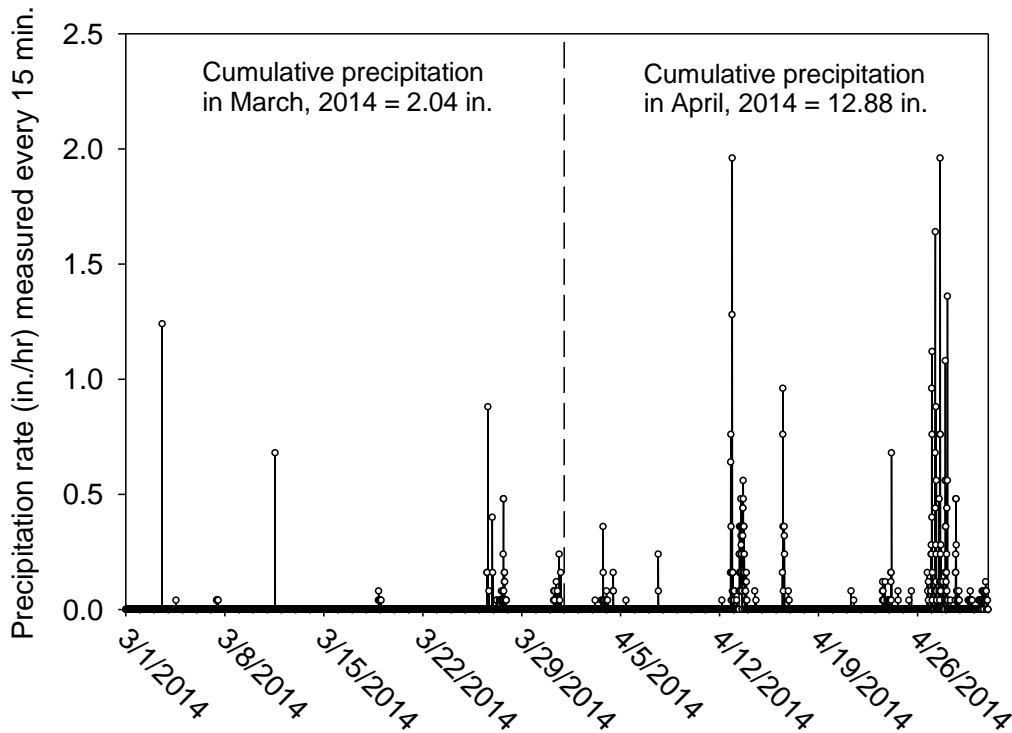


Figure 82. Precipitation rates during 2014 thawing period measured every 15 minutes at the project site

6.5.2.2 DCP and FWD Test Results

DCP tests were conducted on May 3, 2014 to measure the post-thawing shear strength of the surface course and subgrade materials of the demonstration sections. The cumulative blows, dynamic cone penetrometer index (DCPI), and DCP-CBR versus depth are shown in Figure 83 through Figure 87. All DCP tests on the clean macadam with NW-geotextile (Section 5) hit refusal near the surface of the macadam layer between 7 and 12 in. depth, and are therefore not shown in the figures. As previously discussed in Section 6.4.1, the aggregate and macadam layers were combined into one layer (aggregate+macadam+aggregate) for Sections 1–8, and the DCP-CBR_{AGG} of the macadam stone base may not fully reflect the shear strength due to the presence of large aggregates. However, the DCP-CBR values of the surface course layers remained relatively constant with depth, while the values for the subgrade significantly decreased with depth, which is likely due to increasing moisture content.

The thickness of the combined surface course layer, average DCP-CBR_{AGG} of the surface course, and DCP-CBR_{SG} of the subgrade are summarized in Table 23. The average DCP-CBR_{AGG} ranged between 70% and 129% for the macadam stone base Sections 1–8, between 70% and 74% for the geogrid Sections 19A and 19B, and between 26% and 65% for the aggregate column Sections 12 and 13 and the control sections. According to the SUDAS relative ratings of support conditions in Table 2, the combined surface courses of the macadam sections rate as excellent or very good, and the surface course of other sections rate from very good to below good (Table 23). The subgrade of Sections 9–20 rated as very poor, with the exception of the aggregate

column Section 13 which rated as fair to poor. In contrast to these poor subgrade soils, the subgrade of the macadam Sections 1–8 rated as fair to good. Also, according to the frost susceptibility classification system in Table 3, the subgrade of the macadam Sections 1–8 had low susceptibility, but subgrade of the other sections had high to very high susceptibility.

Because the subgrade material for all sections is the same type of backfill, the higher subgrade DCP-CBR values beneath the macadam sections could be attributed to either the different DCP measurement depth for the subgrade, as described in Section 6.4.1, or the improved drainage offered by the macadam stone as well as the increased effective stress due to the surcharge of the additional macadam stone and aggregate layers. To determine if the difference in measurement depth was responsible for the difference, the post-thawing average DCP-CBR_{SG} values for Sections 9–20 were re-calculated using the same smaller 20 in. depth within the subgrade used for Sections 1–8. The resulting values for Sections 9–20 were approximately the same (within 3%). Therefore, the differences in DCP-CBR_{SG} between the macadam and other sections can be attributed to the improved drainage in the macadam layer and increased effective stress due to the surcharge of the additional macadam stone and aggregate layers.

The pre-freezing (as-constructed) and post-thawing DCP test results of the first mile demonstration Sections 1–9 are compared in Table 24. The average thickness of the surface course layers did not change significantly between the two test periods. The DCP-CBR_{AGG} of the reference control Section 9 decreased by 28% after thawing, and the values for Sections 6 and 7 (clean macadam and RPCC macadam) decreased by similar percentages. The DCP-CBR_{AGG} values for Sections 1 and 2 (dirty macadam) decreased by only 10%, while the value for the same dirty macadam base material with added NW-geotextile in Sections 3 and 4 actually increased by 17%. Therefore, it is apparent that the NW-geotextile may result in a more favorable change in DCP-CBR_{AGG} before and after thawing. On the other hand, this may be due to the fact that the DCP-CBR values in Table 24 are typically lower for the layers containing the NW-geotextile compared to the same materials without the geotextile. Additionally, the DCP-CBR_{AGG} value for Section 8 (RPCC macadam with NW-geotextile) actually started out higher than the same material in Section 7 without the geotextile pre-freezing, but then experienced the largest decrease of 55% post-thawing and ended up lower than the value for Section 7, consistent with Sections 3 and 4 versus 1 and 2. However, since only one to three successful DCP tests were conducted for the macadam sections, more data are needed to verify the trends discussed above. Also, it should be noted that despite the decreases in DCP-CBR_{AGG} values after thawing, the surface courses of Sections 1–9 still rated as very good to excellent.

For the subgrade, on the other hand, the pre- to post-thawing DCP-CBR_{SG} value for control Section 9 decreased by 74%, while the value for Sections 3 and 4 (dirty macadam+NW-geotextile) decreased by only 14%. All the other macadam base sections showed decreases between 40% and 44%. Before the winter season, the subgrade materials in all of Sections 1–9 rated fair-to-good or very good, but after thawing they all degraded to very poor for control Section 9, and fair to poor for the macadam sections. The subgrade of Section 5 could not be tested due to refusal of the DCP to advance in the surface course.

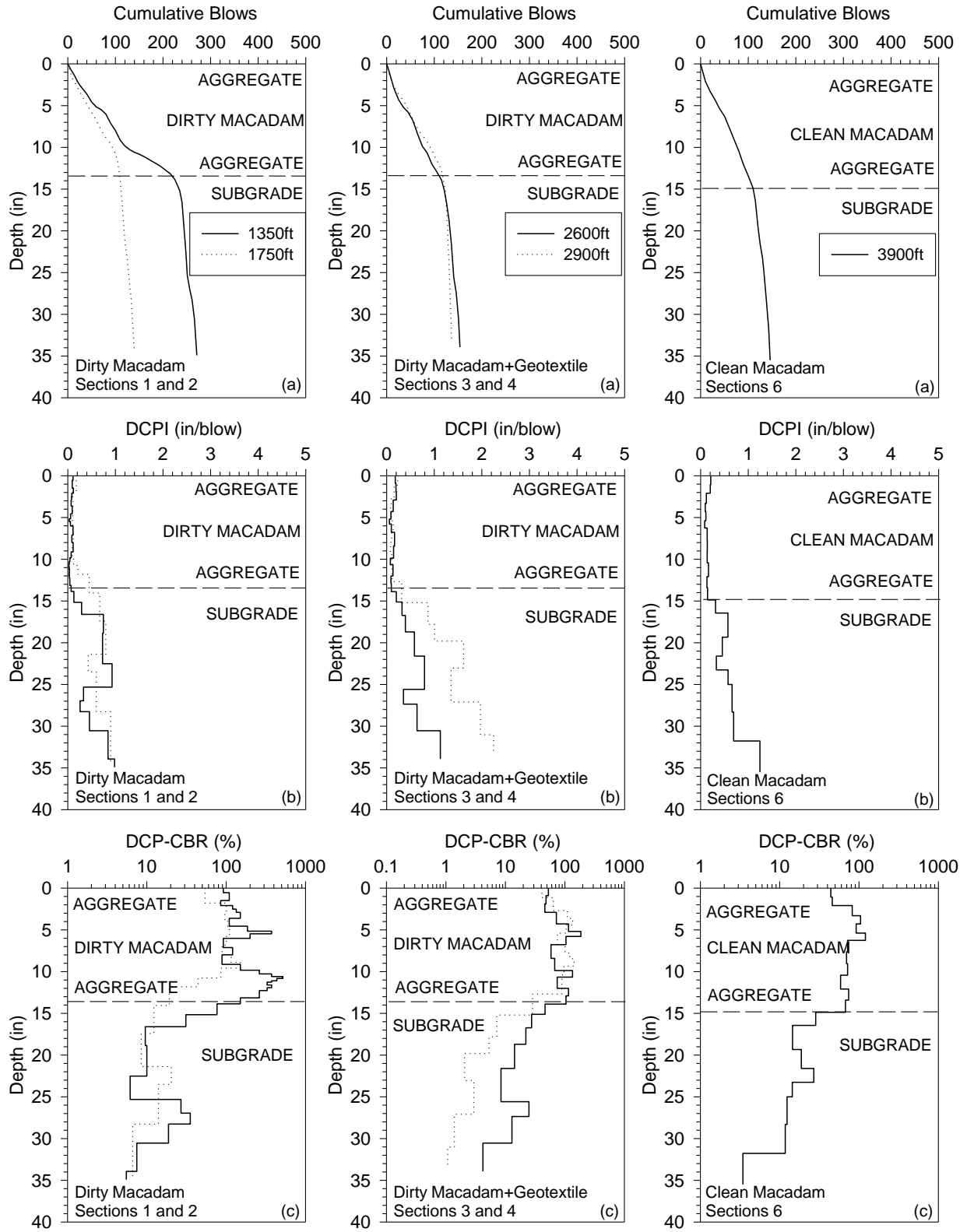


**Figure 83. 2014 Post-thawing DCP test results versus depth for Sections 1-6:
(a) cumulative blows, (b) DCPI, and (c) DCP-CBR**

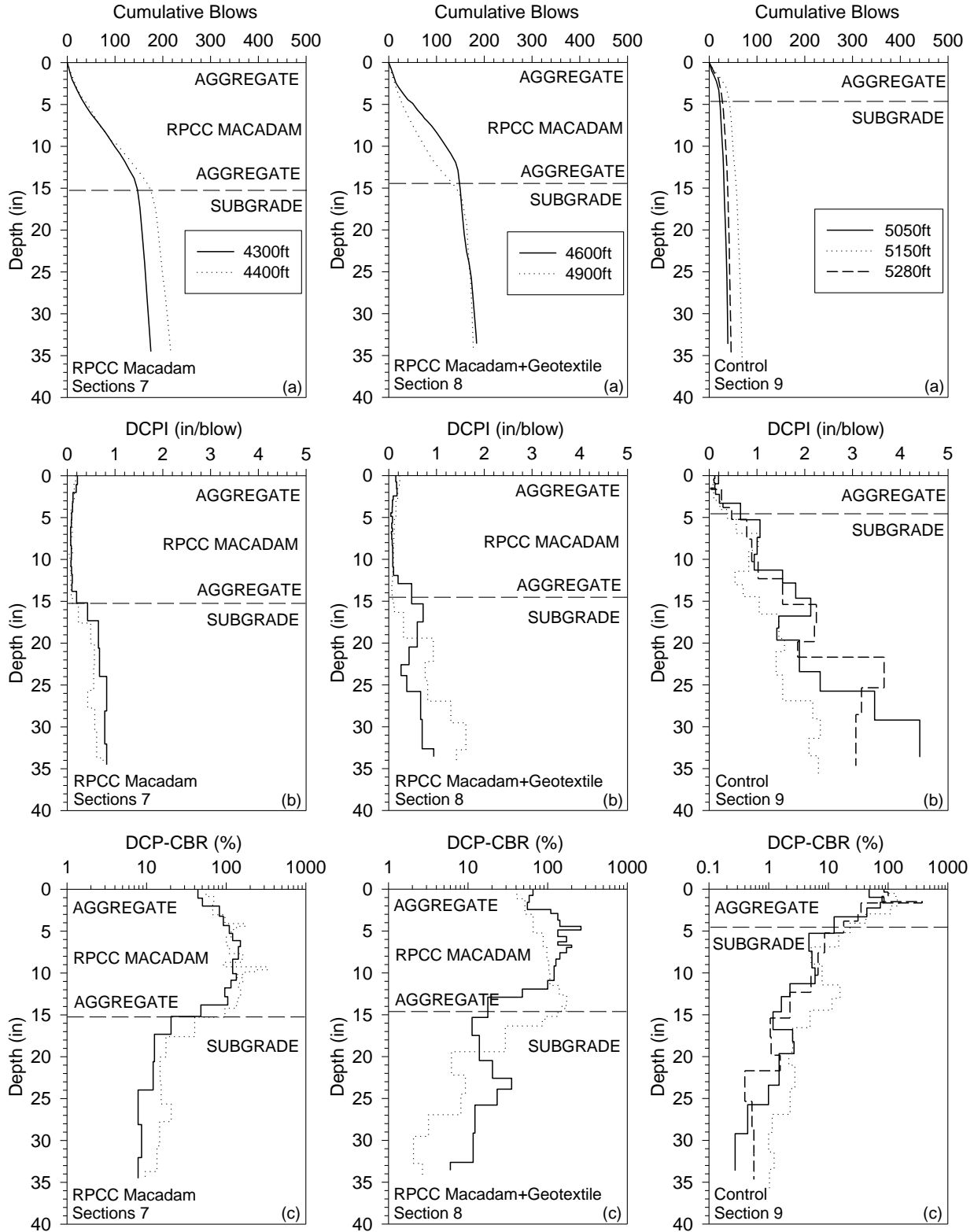


**Figure 84. 2014 Post-thawing DCP test results versus depth for Sections 7-9:
(a) cumulative blows, (b) DCPI, and (c) DCP-CBR**

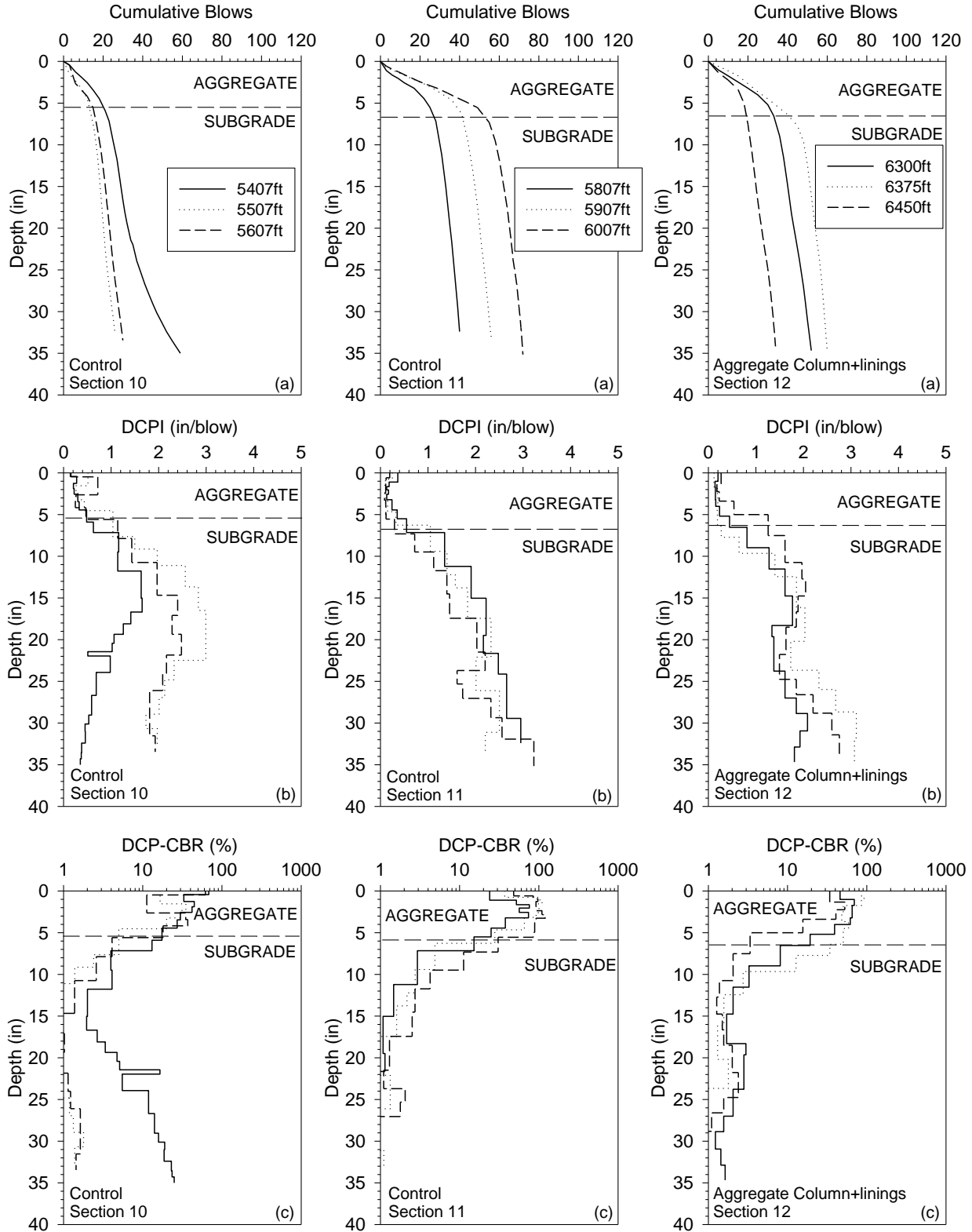


**Figure 85. 2014 Post-thawing DCP test results versus depth for Sections 10–12:
(a) cumulative blows, (b) DCPI, and (c) DCP-CBR**

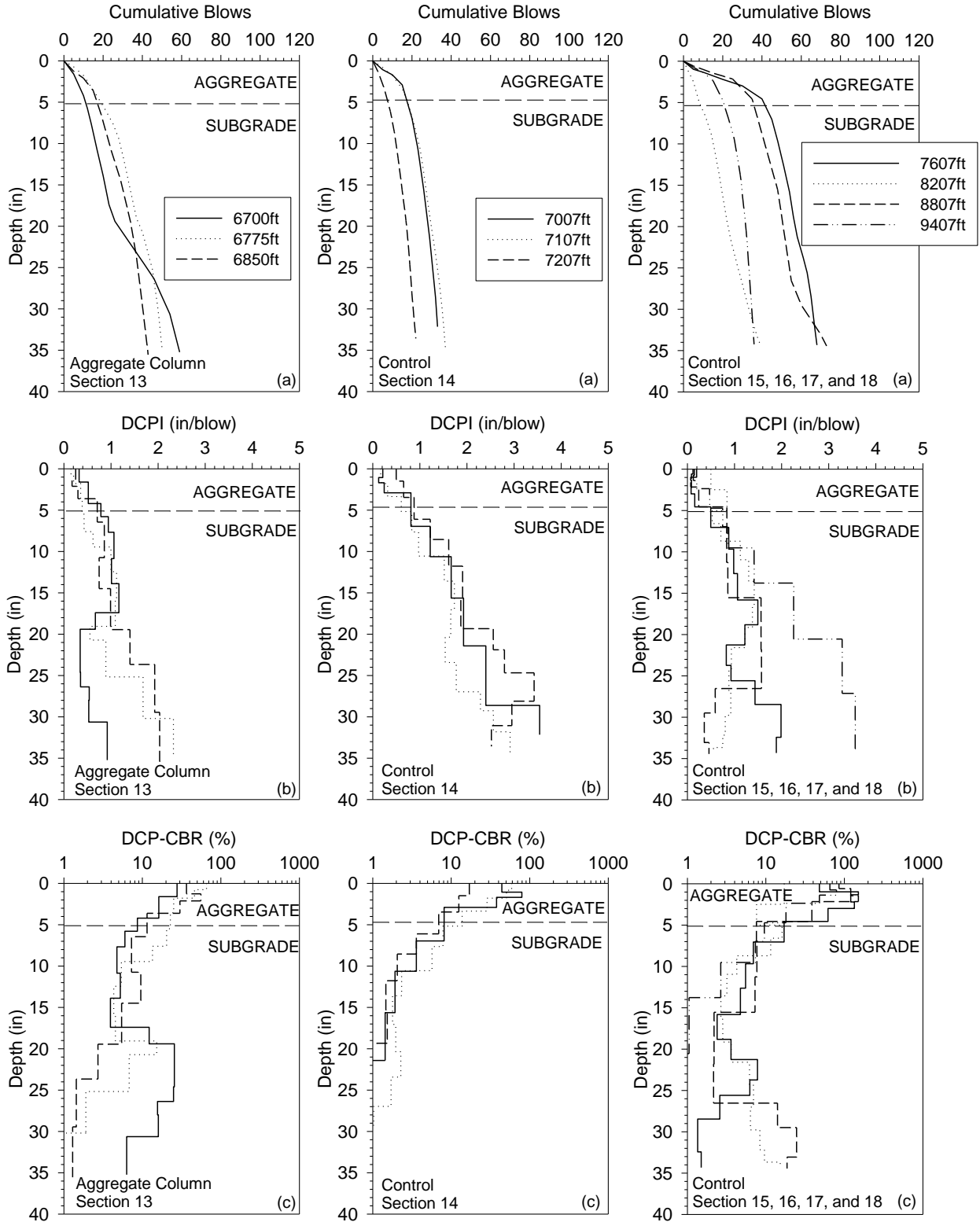


**Figure 86. 2014 Post-thawing DCP test results versus depth for Sections 13–18:
(a) cumulative blows, (b) DCPI, and (c) DCP-CBR**

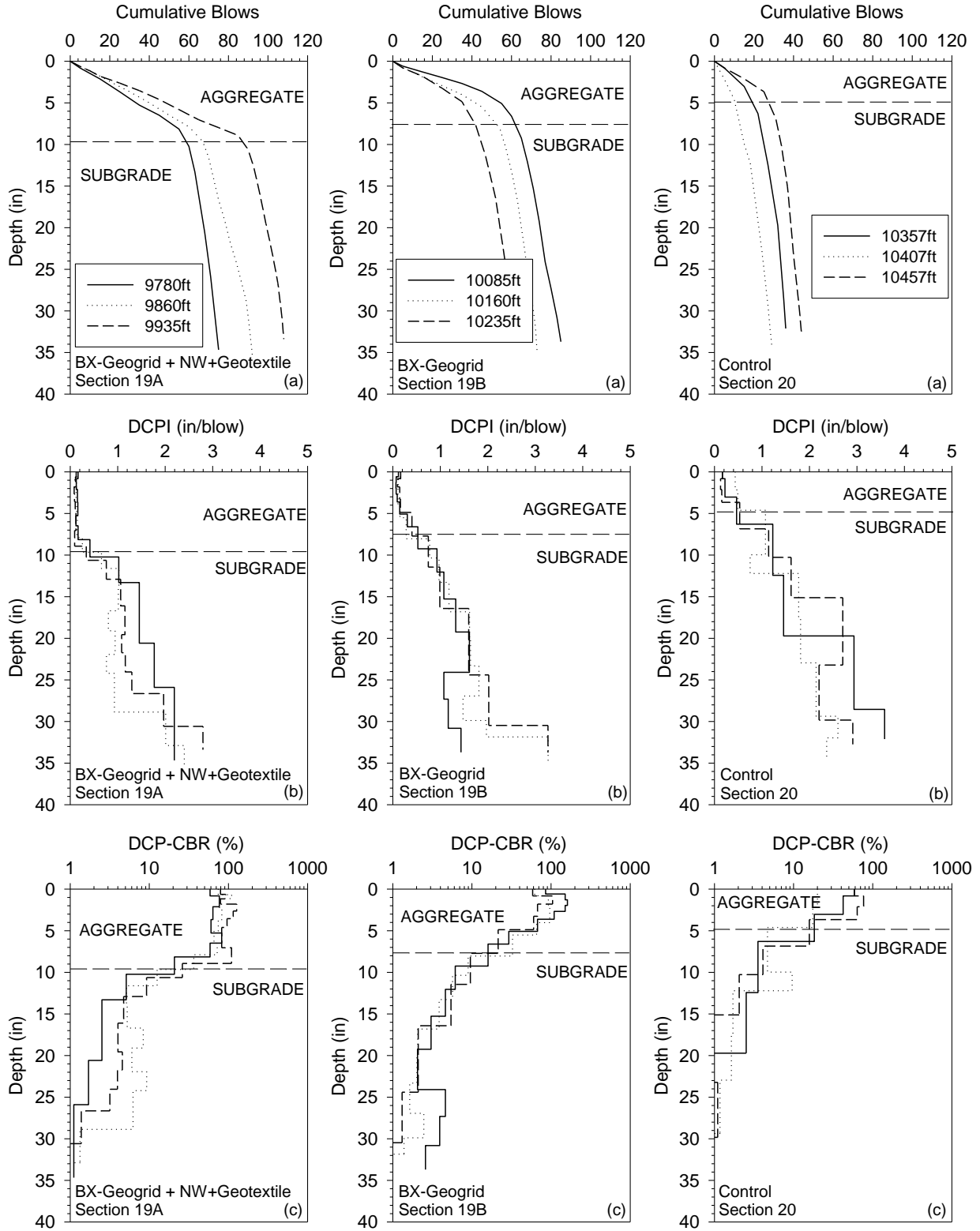


**Figure 87. 2014 Post-thawing DCP test results versus depth for Sections 19A–20:
 (a) cumulative blows, (b) DCPI, and (c) DCP-CBR**

Table 23. 2014 Post-thawing DCP test results of Vail Avenue demonstration sections

Description (Section Number)	Distance (ft)	Surface Course Thickness (in.)	Average Thickness (in.)	DCP- CBR _{AGG} (%)	Average DCP- CBR _{AGG} (%) / Support Rating ^a	DCP- CBR _{SG} (%)	Average DCP-CBR _{SG} (%) / Support Rating ^b / Frost Susceptibility Rating ^c
Dirty Macadam (1 and 2)	1,350	15.2	13.5	168.0	129.0 / E	15.3	13.9 / F-G / L
	1,750	11.8		90.1		12.6	
Dirty Macadam + NW- Geotextile (3 and 4)	2,600	13.9	13.3	83.1	87.7 / E	16.4	11.0 / F-G / L
	2,900	12.7		92.2		5.6	
Clean Macadam (6)	3,900	14.9	14.9	73.3	73.3 / VG	14.5	14.5 / F-G / L
RPCC Macadam (7)	4,300	15.2	15.2	99.0	109.4 / E	11.8	15.0 / F-G / L
	4,400	15.3		119.7		18.3	
RPCC Macadam + NW-Geotextile (8)	4,600	12.9	14.6	117.0	106.3 / E	15.9	12.8 / F-G / L
	4,900	16.3		95.5		9.7	
Control (9)	5,050	3.3	4.6	58.5	64.9 / VG	2.1	2.6 / VP / H
	5,150	5.2		83.1		3.9	
	5,280	5.2		53.0		1.8	
Control (10)	5,407	5.9	5.3	32.3	26.4 / (<G)	9.1	4.0 / VP / H
	5,507	4.5		23.2		1.3	
	5,607	5.6		23.6		1.5	
Control (11)	5,807	7.2	6.9	35.9	58.2 / VG	1.2	1.6 / VP / VH
	5,907	6.3		64.0		1.6	
	6,007	7.3		74.6		2.0	
Aggregate Column + Geocomposite Lining (12)	6,300	6.5	6.4	47.8	45.6 / G	2.4	1.9 / VP / VH
	6,375	7.7		56.2		1.6	
	6,450	5.0		32.7		1.6	

^a SUDAS relative support condition rating for subbase (Table 2): E=Excellent, VG=Very Good, G=Good, <G=below Good

^b SUDAS relative support condition rating for subgrade (Table 2): E=Excellent, VG=Very Good, F-G=Fair to Good, P-F=Poor to Fair, VP=Very Poor

^c ASTM D 5918-13 frost susceptibility rating: NFS=Negligible, VL=Very Low, L=Low, M=Medium, H=High, VH=Very High

Table 23 (continued). 2014 Post-thawing DCP test results of Vail Avenue demonstration sections

Description (Section Number)	Distance (ft)	Surface Course Thickness (in.)	Average Thickness (in.)	DCP- CBR _{AGG} (%)	Average DCP- CBR _{AGG} (%) / Support Rating ^a	DCP- CBR _{SG} (%)	Average DCP-CBR _{SG} (%) / Support Rating ^b / Frost Susceptibility Rating ^c
Aggregate Column (13)	6,700	4.2		20.5		13.0	
	6,775	7.6	5.1	29.6	29.5 / (<G)	4.5	7.2 / P-F / M
	6,850	3.6		38.3		4.1	
Control (14)	7,007	2.9		48.9		2.0	
	7,107	5.2	4.7	31.6	30.8 / G	2.2	1.8 / VP / VH
	7,207	6.1		12.0		1.2	
Control (15–18)	7,607	4.6		88.6		4.7	
	8,207	6.6	5.1	13.9	54.5 / VG	5.3	4.0 / VP / H
	8,807	4.6		76.3		4.4	
	9,407	4.7		39.3		1.6	
BX-Geogrid + NW- Geotextile (19A)	9,780	10.2		56.5		2.0	
	9,860	9.6	9.6	68.3	74.0 / VG	5.1	3.9 / VP / H
	9,935	8.9		97.2		4.7	
BX-Geogrid (19B)	10,085	6.6		92.2		4.6	
	10,160	8.0	7.5	65.9	70.0 / VG	2.6	3.3 / VP / H
	10,235	7.7		52.0		2.9	
Control (20)	10,357	6.3		31.6		1.6	
	10,407	4.6	4.9	18.6	39.1 / G	2.2	2.0 / VP / H
	10,457	3.7		67.0		2.3	

^a SUDAS relative support condition rating for subbase (Table 2): E=Excellent, VG=Very Good, G=Good, <G=below Good

^b SUDAS relative support condition rating for subgrade (Table 2): E=Excellent, VG=Very Good, F–G=Fair to Good, P–F=Poor to Fair, VP=Very Poor

^c ASTM D 5918-13 frost susceptibility rating: NFS=Negligible, VL=Very Low, L=Low, M=Medium, H=High, VH=Very High

Table 24. Comparison between pre-freezing (as-constructed) and 2014 post-thawing average DCP test results for Sections 1–9

Description (Section Number)	Average Thickness of Combined Surface Course (in.)		Average DCP-CBR _{AGG} (%) / Rating ^a		Average DCP-CBR _{SG} (%) / Rating ^b	
	As-Constructed	Post-Thawing	As-Constructed	Post-Thawing	As-Constructed	Post-Thawing
Dirty Macadam (1 and 2)	13.3	13.5	143.8 / E	129.0 / E	24.0 / VG	13.9 / F–G
Dirty Macadam + NW-Geotextile (3 and 4)	13.3	13.3	74.8 / VG	87.7 / VG	12.8 / F–G	11.0 / F–G
Clean Macadam + NW-Geotextile (5)	15.8	–	76.8 / VG	–	17.4 / F–G	–
Clean Macadam (6)	14.3	14.9	96.7 / E	73.3 / VG	25.9 / VG	14.5 / F–G
RPCC Macadam (7)	13.8	15.2	148.7 / E	109.4 / E	24.9 / VG	15.0 / F–G
RPCC Macadam + NW-Geotextile (8)	15.1	14.6	233.9 / E	106.3 / E	22.9 / VG	12.8 / F–G
Control (9)	4.9	4.6	90.0 / E	64.9 / VG	10.5 / F–G	2.6 / VP

^a SUDAS relative support condition rating for subbase (Table 2): E=Excellent, VG=Very Good, G=Good, <G=below Good

^b SUDAS relative support condition rating for subgrade (Table 2): E=Excellent, VG=Very Good, F–G=Fair to Good, P–F=Poor to Fair, VP=Very Poor

– All of the post-thawing DCP tests conducted on this section hit refusal.

FWD tests were also conducted on April 25, 2014 to measure and compare the post-thawing stiffness of the sections. The FWD and DCP test results of the first and second mile sections are compared in Figure 88 and Figure 89, respectively. The $E_{FWD-Composite}$ and $E_{FWD-AGG}$ values of the macadam sections generally exhibited higher post-thawing values than control Section 9 (Figure 88a and Figure 88b), which agrees with the DCP results discussed above. However, the $E_{FWD-Composite}$ and $E_{FWD-AGG}$ of the macadam sections with NW-geotextile (Sections 3 and 4, 5, and 8) were lower than the corresponding sections without the NW-geotextile (Sections 1 and 2, 3, and 7). Thus, the improvement in drainage offered by the NW-geotextile comes with a trade-off of lower composite stiffness of the granular surfaced road systems. For the subgrade, the E_{FWD-SG} values were relatively constant at around 7 ksi except for Sections 5 and 6, which were relatively higher at over 10 ksi (Figure 88c). The trends of DCP-CBR values generally agreed well with the moduli from FWD tests, for both the combined surface course and subgrade materials (Figure 88b and Figure 88c).

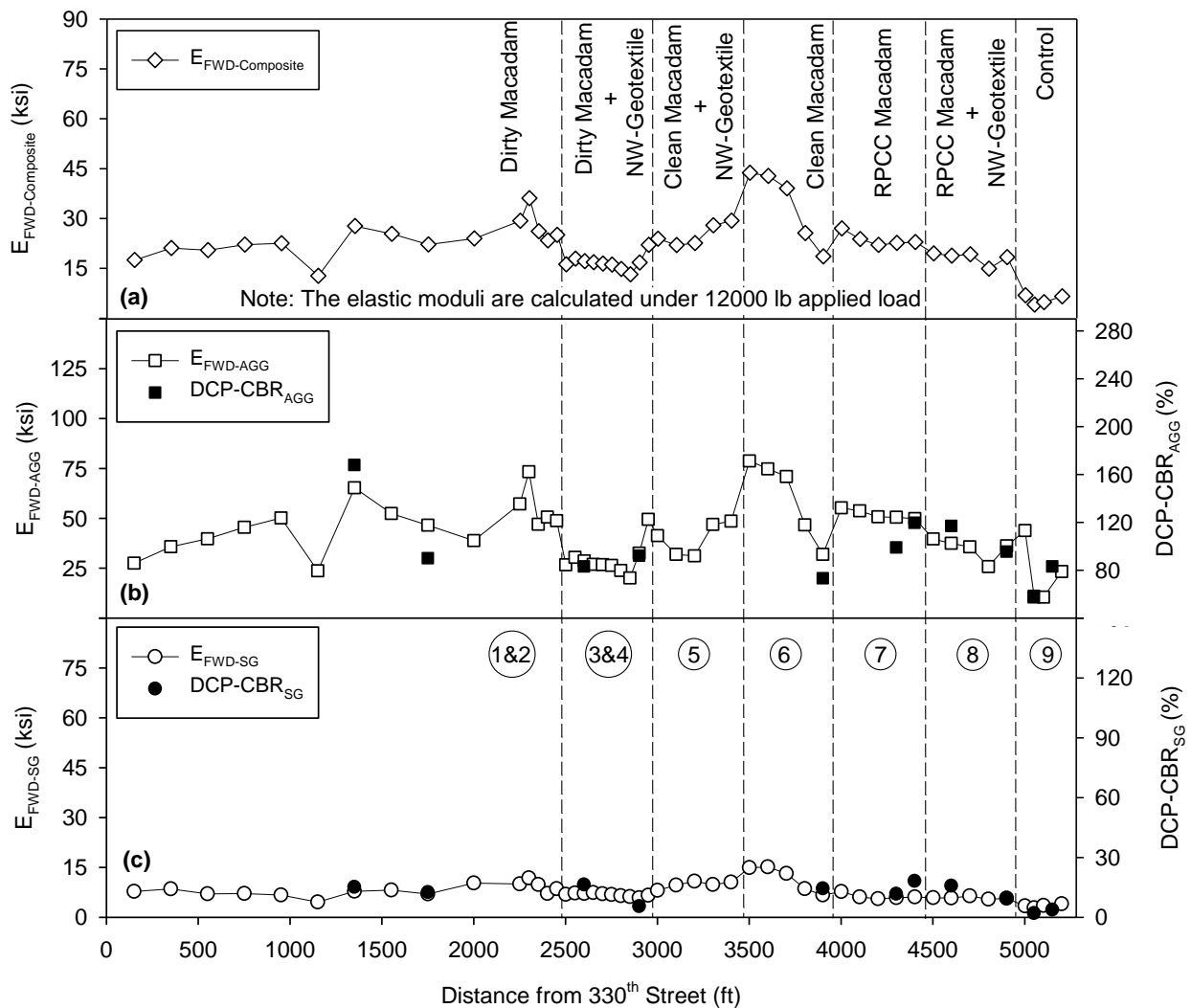


Figure 88. 2014 Post-thawing FWD and DCP results for Sections 1–9: (a) $E_{FWD-Composite}$, (b) $E_{FWD-AGG}$ and $DCP-CBR_{AGG}$ of combined surface course, and (c) E_{FWD-SG} and $DCP-CBR_{SG}$ of subgrade

For the second mile demonstration Sections 10–20, the $E_{FWD-Composite}$, $E_{FWD-AGG}$, and E_{FWD-SG} results are shown in Figure 89. Because the chemical stabilization Sections 15–18 had not yet been constructed at the time of testing in 2014, they were still considered control sections during these tests. Some test points of Sections 13, 14 and 16 were so soft that the road surface deflections under the 12,000 lb FWD load exceeded the measurement capacity of the FWD, so their moduli could not be calculated. The test results in Figure 89 show that the back-calculated $E_{FWD-composite}$ and $E_{FWD-AGG}$ of the BX-geogrid Section 19B were higher than the other sections in the second mile, and the $E_{FWD-AGG}$ values of Section 19B were similar to those of the clean macadam Section 6 (Figure 88b). However, the BX-geogrid with NW-geotextile in Section 19A did not result in significant improvement in $E_{FWD-AGG}$. Also, the aggregate column Sections 12 and 13 did not result in a significant change in DCP or $E_{FWD-AGG}$, which is to be expected as the columns are widely spaced on a 12 ft-offset grid, and the aggregate backfill was not compacted. The purpose of the aggregate columns was not to increase the stiffness or modulus of the surface course or subgrade, but to provide drainage basins to reduce the occurrence of frost boils.

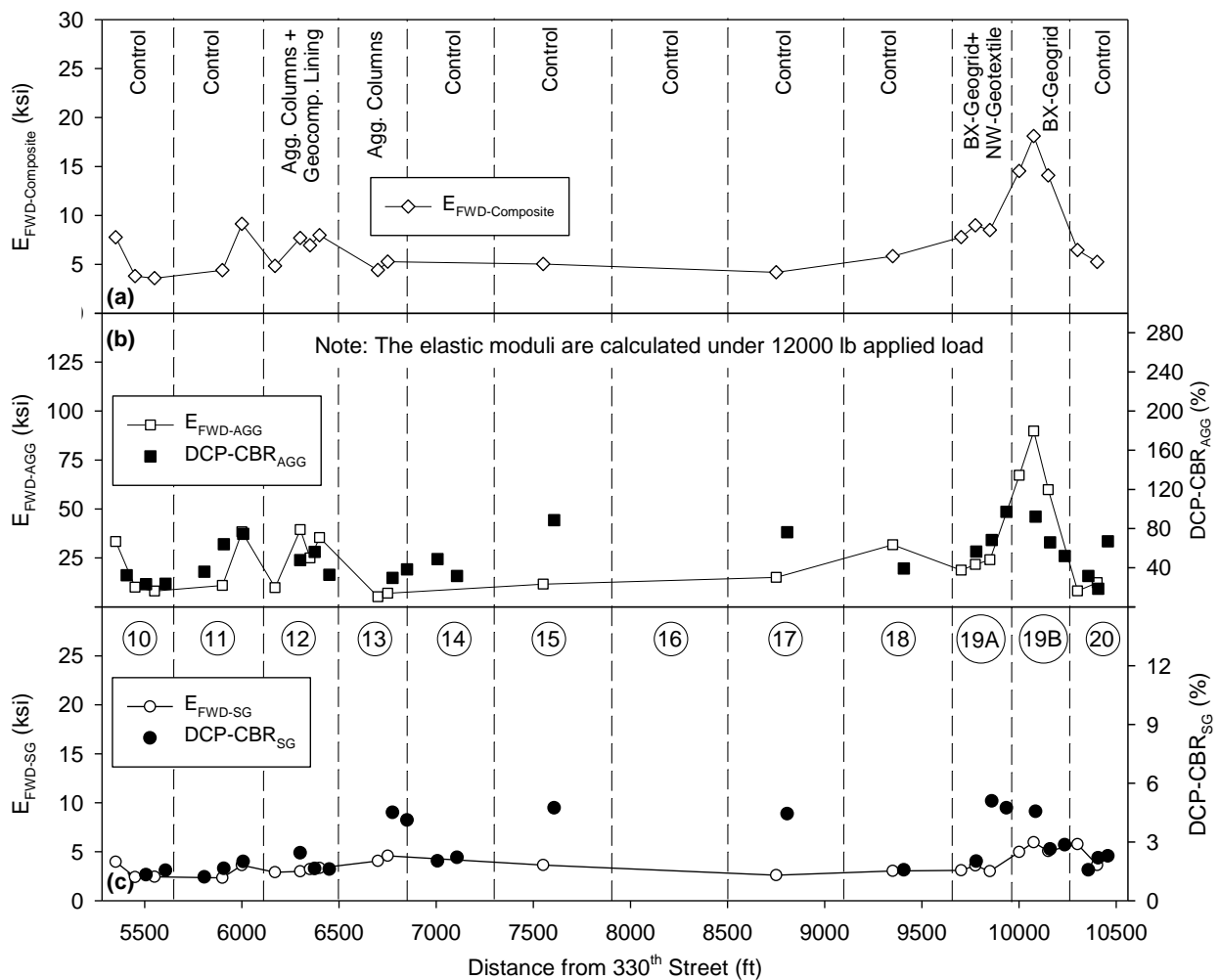


Figure 89. 2014 Post-thawing FWD and DCP results for Sections 10–20: (a) $E_{FWD-Composite}$, (b) $E_{FWD-AGG}$ and $DCP-CBR_{AGG}$ of surface course, and (c) E_{FWD-SG} and $DCP-CBR_{SG}$ of subgrade (Sections 15–18 not yet stabilized at time of tests)

To evaluate the freeze-thaw durability of the first mile sections, the pre-freezing (as-constructed) and post-thawing FWD test results are directly compared in Figure 90. The results show very repeatable trends between the two test periods, and the average modulus of both the surface course and subgrade of each section was reduced by approximately 10%–40%. Based on the $E_{FWD-composite}$ and $E_{FWD-AGG}$ values, the clean macadam Section 6 showed the best freeze-thaw durability among Sections 1–9, and the dirty macadam Sections 1–4 yielded the largest modulus reductions.

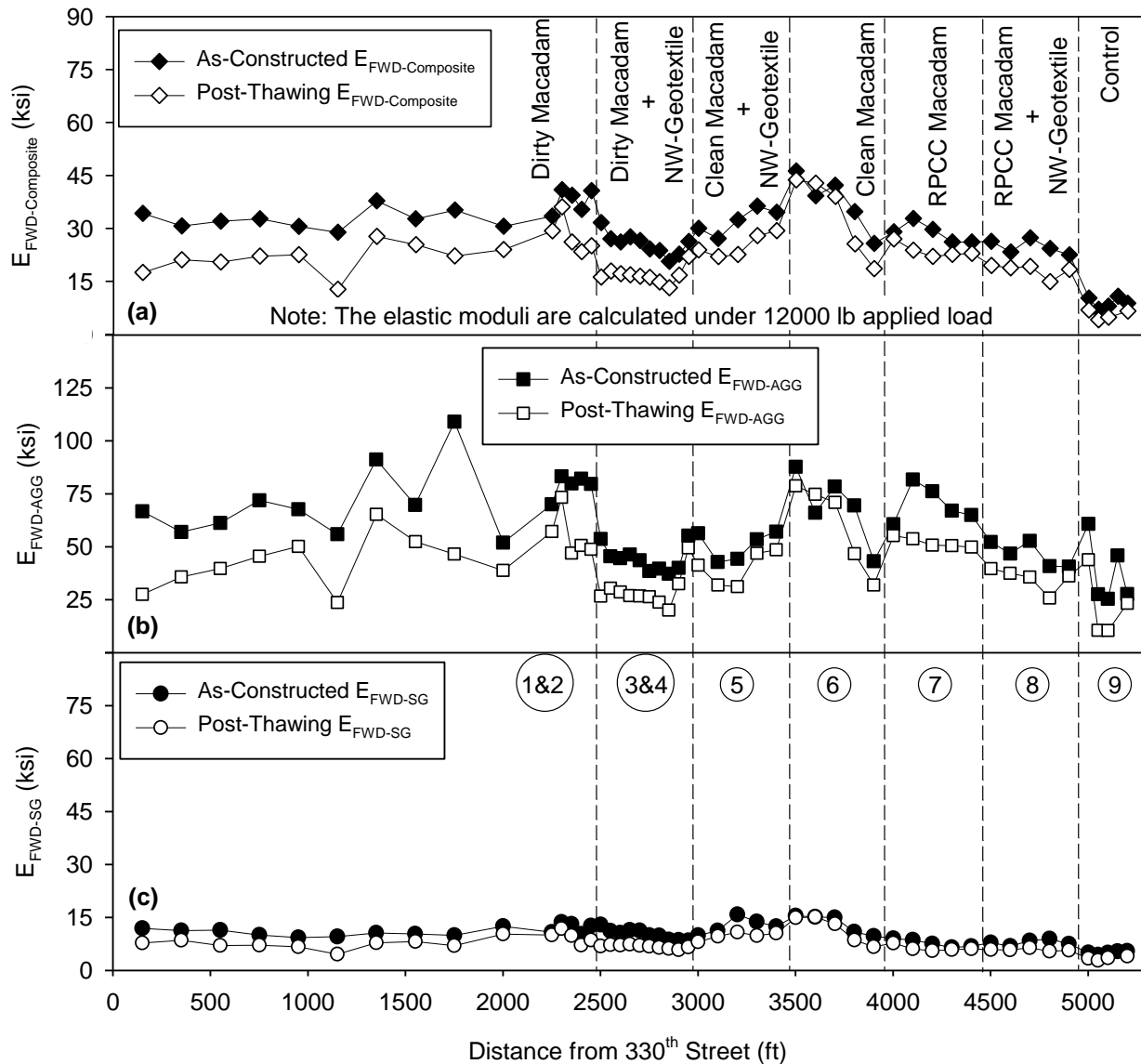


Figure 90. Comparison of 2013 pre-freezing and 2014 post-thawing FWD test results for Sections 1A–9: (a) $E_{FWD-Composite}$, (b) $E_{FWD-AGG}$, and (c) E_{FWD-SG}

Statistical boxplots of the pre-freezing and 2014 post-thawing FWD test results for the first mile sections are shown in Figure 91. For both the 2013 pre-freezing (as-constructed) and 2014 post-thawing FWD tests, it can again be seen that the macadam sections with NW-geotextile yielded lower $E_{FWD-Composite}$ values than the corresponding sections without NW-geotextile. However, the sections with NW-geotextile had smaller $E_{FWD-AGG}$ reductions after thawing, which may imply the NW-geotextile placed between the macadam stone base and surface aggregate can bring long term benefits such as preventing the base macadam stone from being contaminated by fines from the surface course, and improving subsurface drainage. As mentioned above, the smaller reduction could also be a result of the lower starting modulus values for the sections with NW-geotextile.

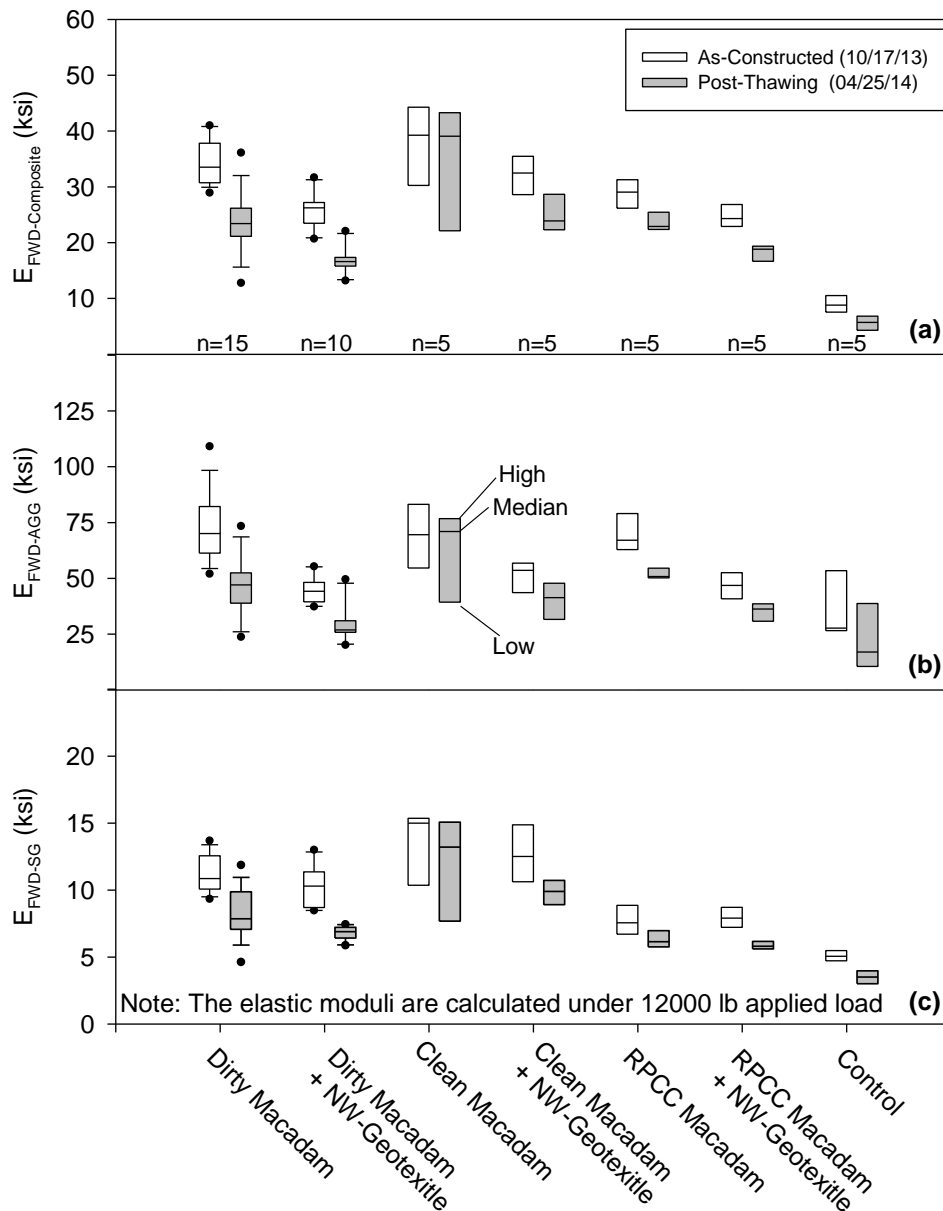


Figure 91. Summary boxplots of 2013 pre-freezing and 2014 post-thawing FWD test results for Sections 1A–9: (a) $E_{FWD-Composite}$, (b) $E_{FWD-AGG}$, and (c) E_{FWD-SG}

6.5.2.3 Survey Photographs

Survey photographs were taken during the 2014 thawing period for a visual comparison of the road surface conditions of the various control and stabilized demonstration sections. A group of survey photos taken on March 11, 2014 are shown in Figure 92. The photos show that the surfaces of the macadam Sections 1–8, BX-geogrid with NW-geotextile (Section 19A), and BX-geogrid (Section 19B) had much less rutting than the control sections. The other groups of survey photos can be found in Appendix C.

Rutting was observed for the control sections and intersections in Figure 92. However, the rutting depth was only about 0.5 in., and the problem was mainly a muddy surface. The Hamilton County Engineer reported observing frost boils in previous years near the drainage tile crossing between the aggregate column Sections 12 and 13. Minor rutting near the shoulders can be seen for the aggregate column sections in Figure 92. However, no frost boils were observed in this area in the 2013-2014 or 2014-2015 freeze-thaw cycles, indicating that the aggregate columns were effective in minimizing the occurrence of frost boils in this area.

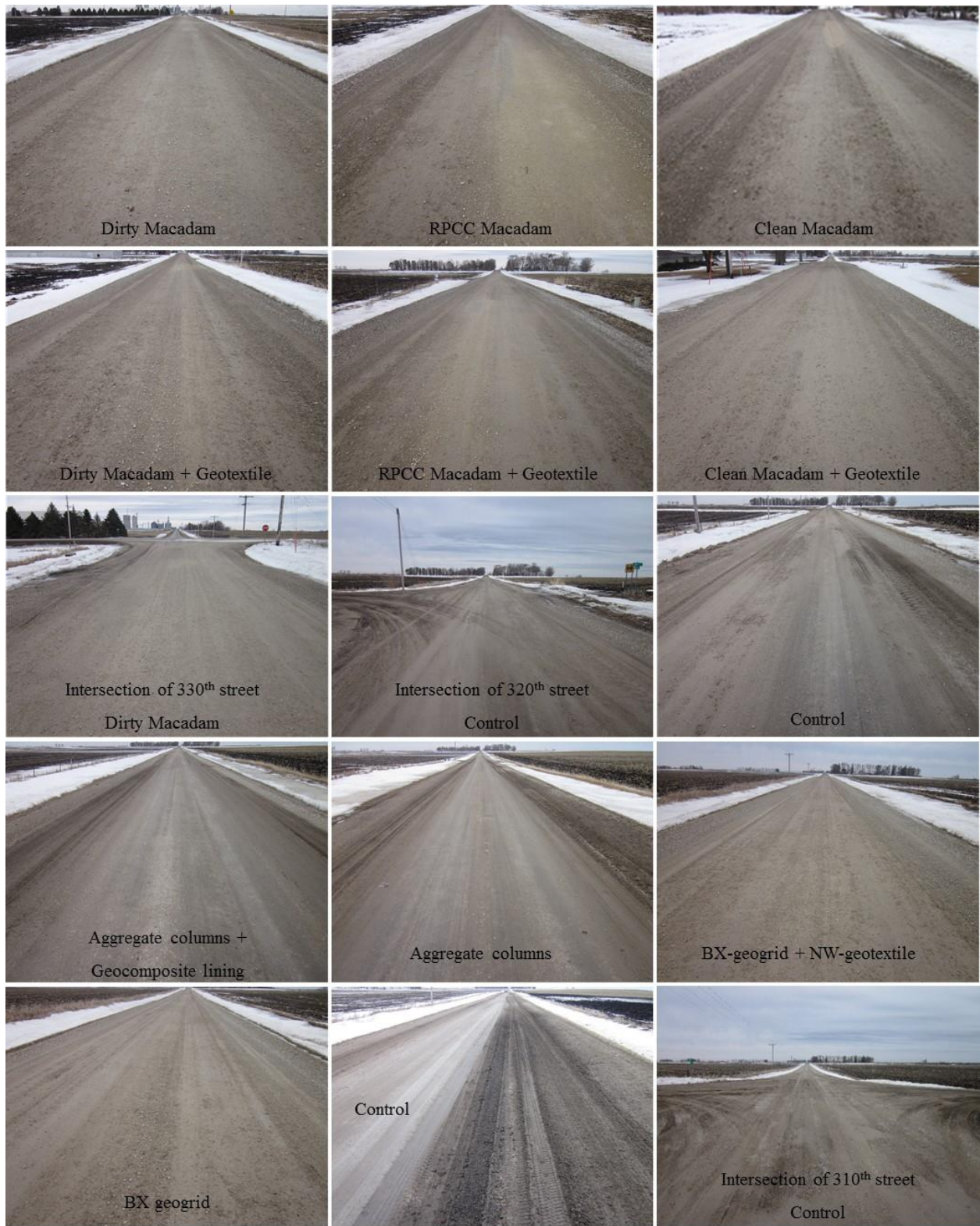


Figure 92. Survey photos of Vail Avenue demonstration sections (March 11, 2014)

6.5.3 Post-Thawing Performance in 2015

To compare the post-thawing performance of the demonstration sections in 2015, MASW tests were conducted on the fly ash and cement Sections 16 and 17 on March 20, and FWD tests were conducted all sections on March 28, 2015. Weather and ground temperature data were also recorded continuously, and survey photos were taken at several times during the second seasonal freeze-thaw cycle.

6.5.3.1 Weather and Ground Temperature Profiles

The air and ground temperatures were recorded continuously during the second (2014-2015) seasonal freeze-thaw period of the project. The raw air and ground temperature data during the freeze-thaw period (November 1, 2014 to March 28, 2015) are shown in Figure 93. Ground temperature profiles are shown in Figure 94 for three different dates: the highest ground temperature date (August 22, 2014), the coldest ground temperature date (February 27, 2015), and the date of the second seasonal post-thawing FWD tests (March 28, 2015). The number of freeze-thaw (F/T) cycles shown in Figure 94 generally decreased from 2 ft to 5 ft depth. Figure 94 also indicates that the seasonal frost line of the ground was between 4 and 5 ft depth.

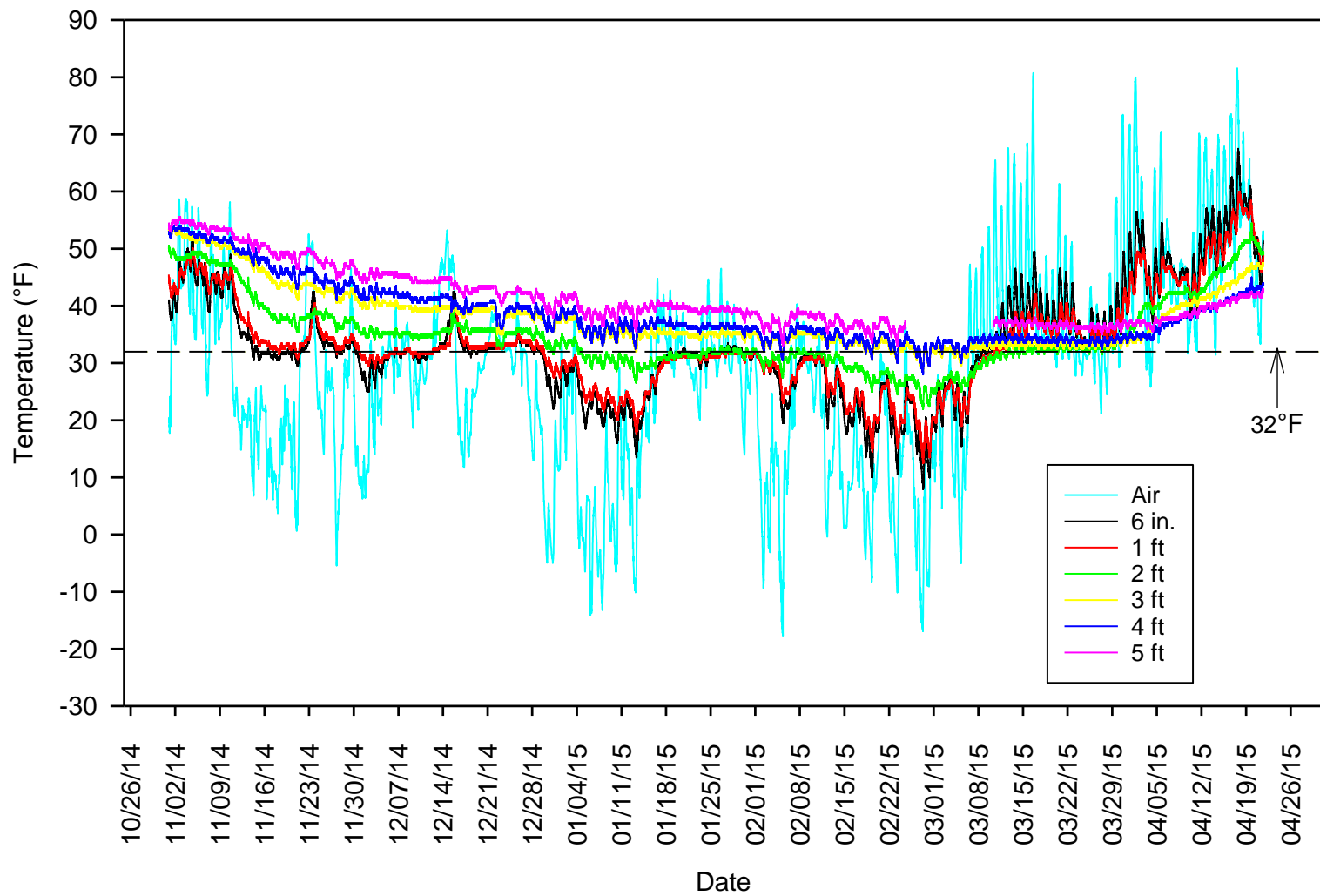


Figure 93. Air and ground temperature data during 2014-2015 seasonal freeze-thaw period

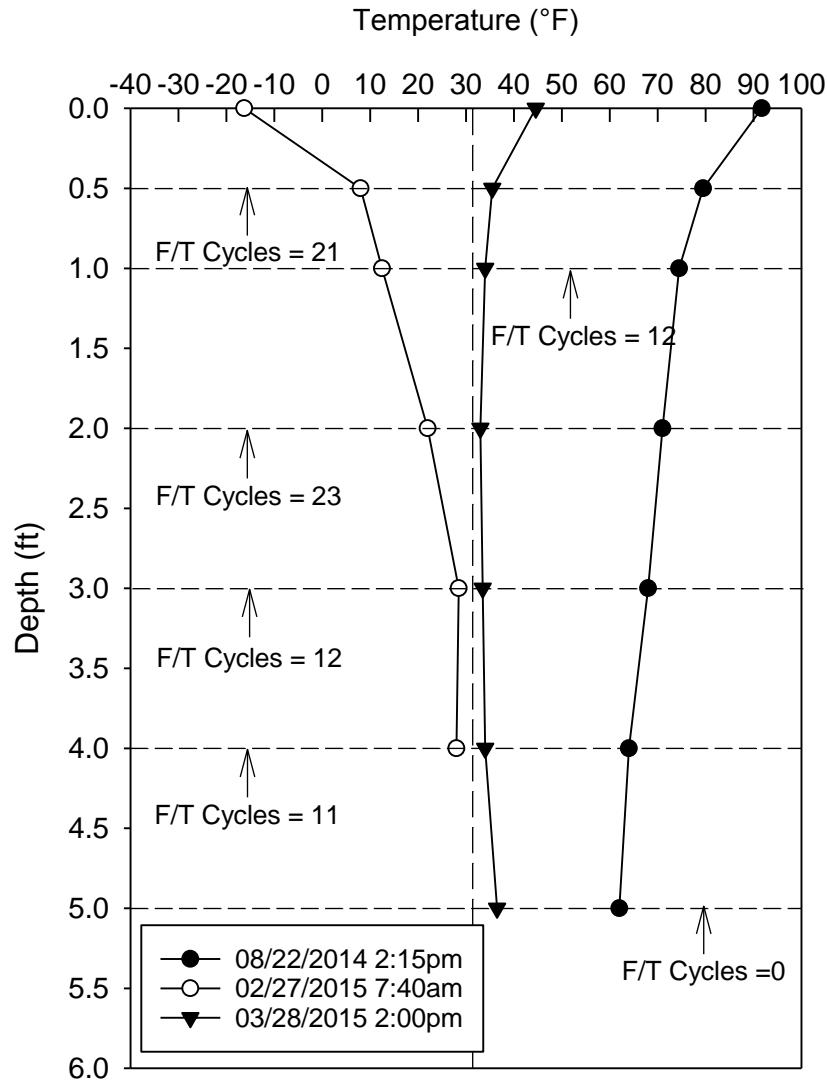


Figure 94. Ground temperature profiles at three different dates during 2014-2015 seasonal freeze-thaw period

The 2014-2015 freezing period, shown by the intersection of the 32 °F isotherm with the ground surface in Figure 95, was approximately the same duration as the 2013-2014 freezing period (also shown in Figure 95 for reference). However, the 2015 thawing period was shorter at only 23 days, the maximum frost penetration depth was only 4 ft, and the last portion of frozen subgrade finally thawed at approximately 2.5 ft depth on or around March 30, 2015.

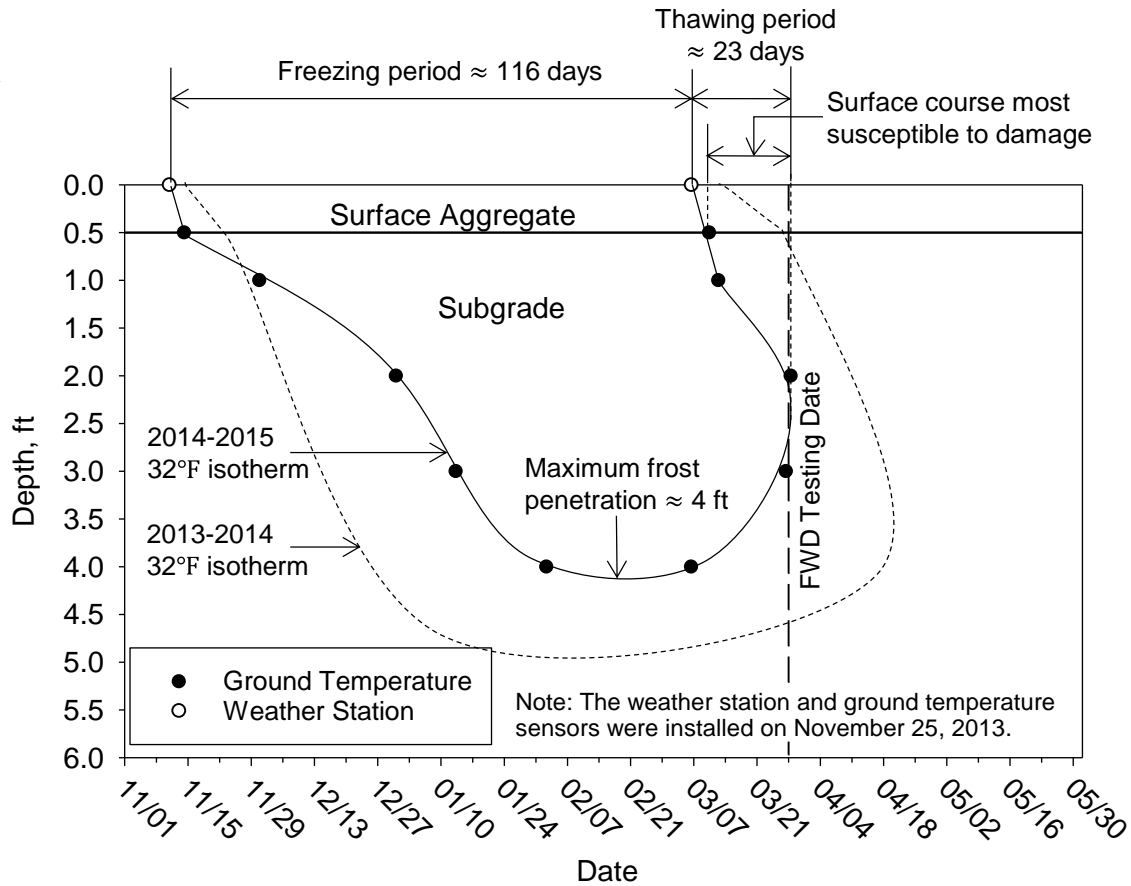


Figure 95. 2014–2015 ground freezing-thawing period of the project site compared with the 2013-2014 period

Rainfall data was also continuously recorded at 15 minute intervals using the weather station. The cumulative precipitation for the month of March 2015 was 0.72 in (compared to 2.04 in. for 2014), which increased in April to 3.22 in. (compared to 12.88 in. for 2014), as shown in Figure 96. The maximum rainfall intensities over any 15 minute period of March and April, 2015 were approximately 0.24 and 1.2 in. per hour, respectively. Overall, the 2015 thawing period was much drier than the 2014 period.

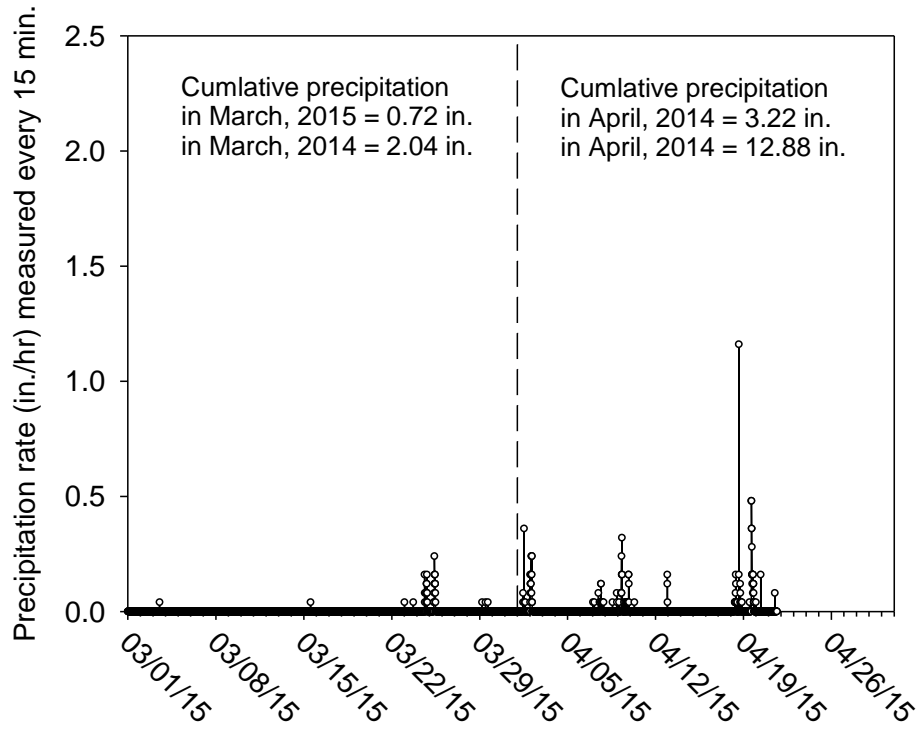


Figure 96. Precipitation rates during 2015 thawing period measured every 15 minutes at the project site

6.5.3.2 FWD Test Results

Results of FWD tests conducted on October 20, 2014 before the winter freeze and on March 28, 2015 after the spring-thaw are shown in Figure 97 and Figure 98 for the first and second mile, respectively.

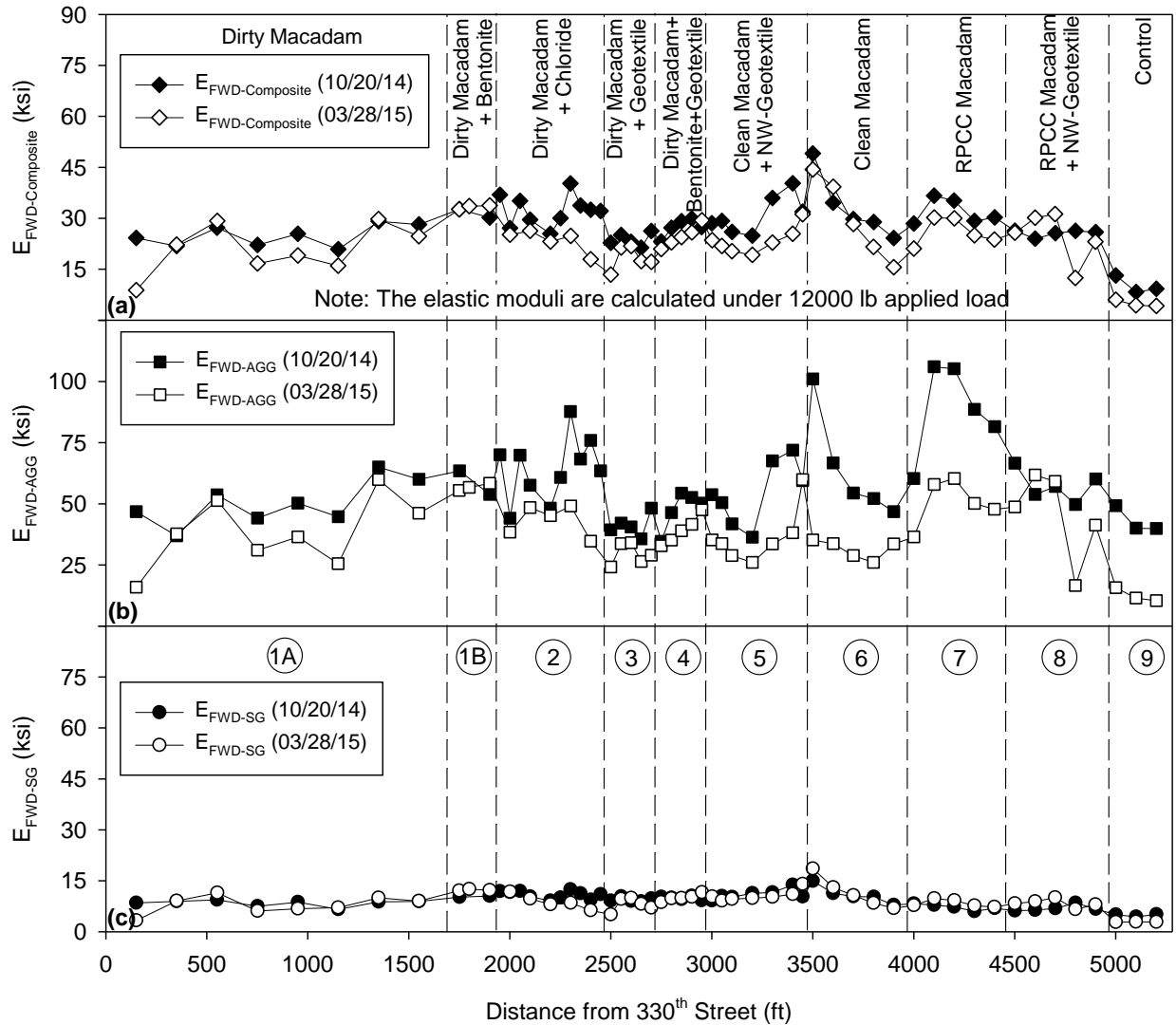


Figure 97. Comparison of 2014 pre-freezing and 2015 post-thawing FWD tests on Sections 1A–9: (a) $E_{FWD-Composite}$, (b) $E_{FWD-AGG}$, and (c) E_{FWD-SG}

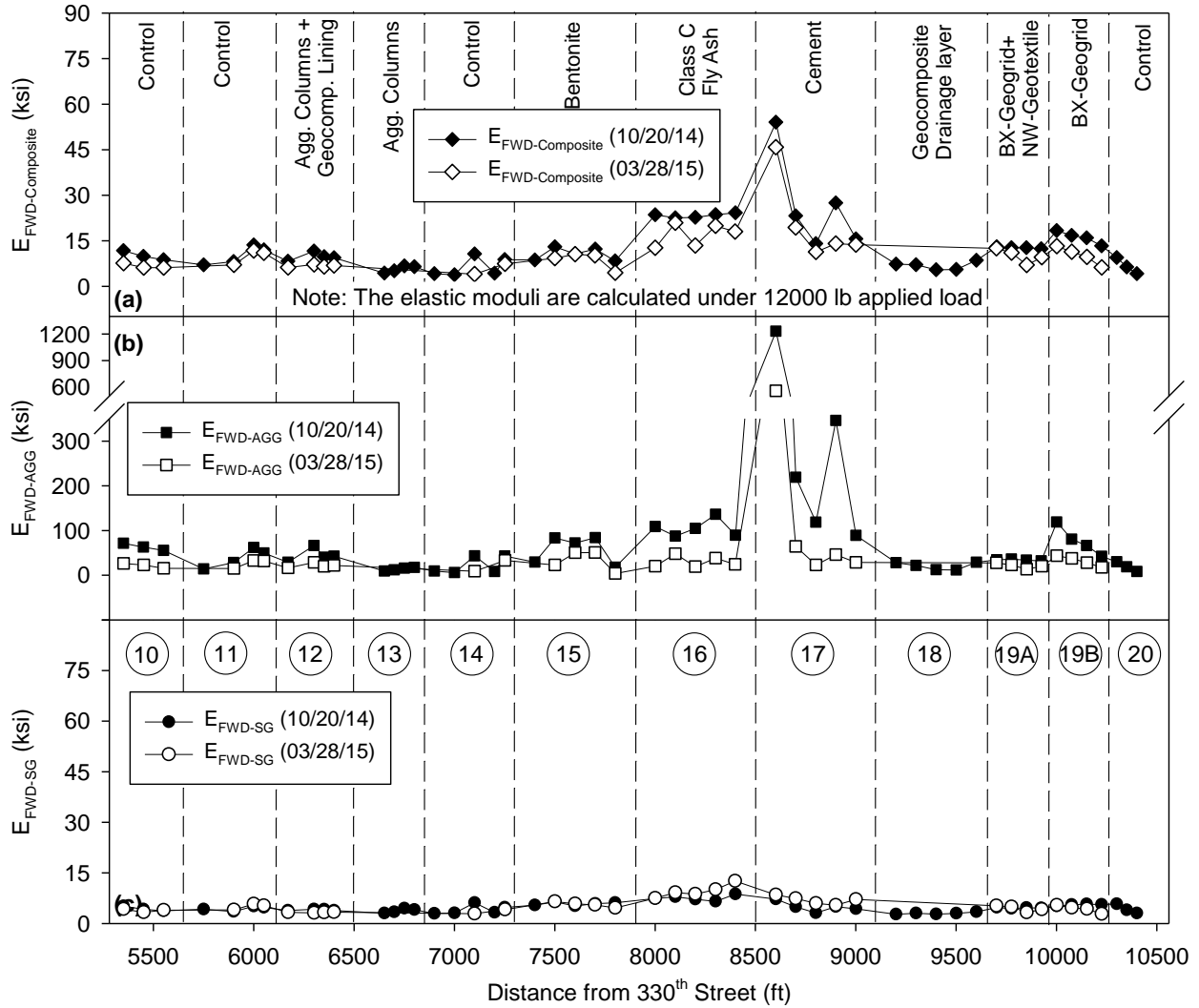


Figure 98. Comparison of 2014 pre-freezing and 2015 post-thawing FWD tests on Sections 10–20: (a) $E_{FWD-Composite}$, (b) $E_{FWD-AGG}$, and (c) E_{FWD-SG}

The results show very repeatable trends between the two test periods. The $E_{FWD-composite}$ and E_{FWD-SG} modulus values did not reduce as significantly as during the 2013-2014 seasonal freeze-thaw cycle. However, the surface course modulus $E_{FWD-AGG}$ of the clean and RPCC macadam Sections 6 and 7 showed greater reductions than the other macadam sections during this freeze-thaw cycle (Figure 97b). For the second mile sections, some test points (especially in Sections 13, 14, 18 and 20) were extremely soft and the surface deflections exceeded the measurement capacity of the FWD, so moduli could not be calculated for these locations. The fly ash- and cement-stabilized sections showed much higher $E_{FWD-composite}$ and $E_{FWD-AGG}$ values than the other sections. This was the first freeze-thaw cycle for the three chemically stabilized sections, and their surface course moduli $E_{FWD-AGG}$ reduced significantly compared to the other sections.

Statistical boxplots of the pre-freezing and post-thawing FWD test results for all sections are shown in Figure 99.

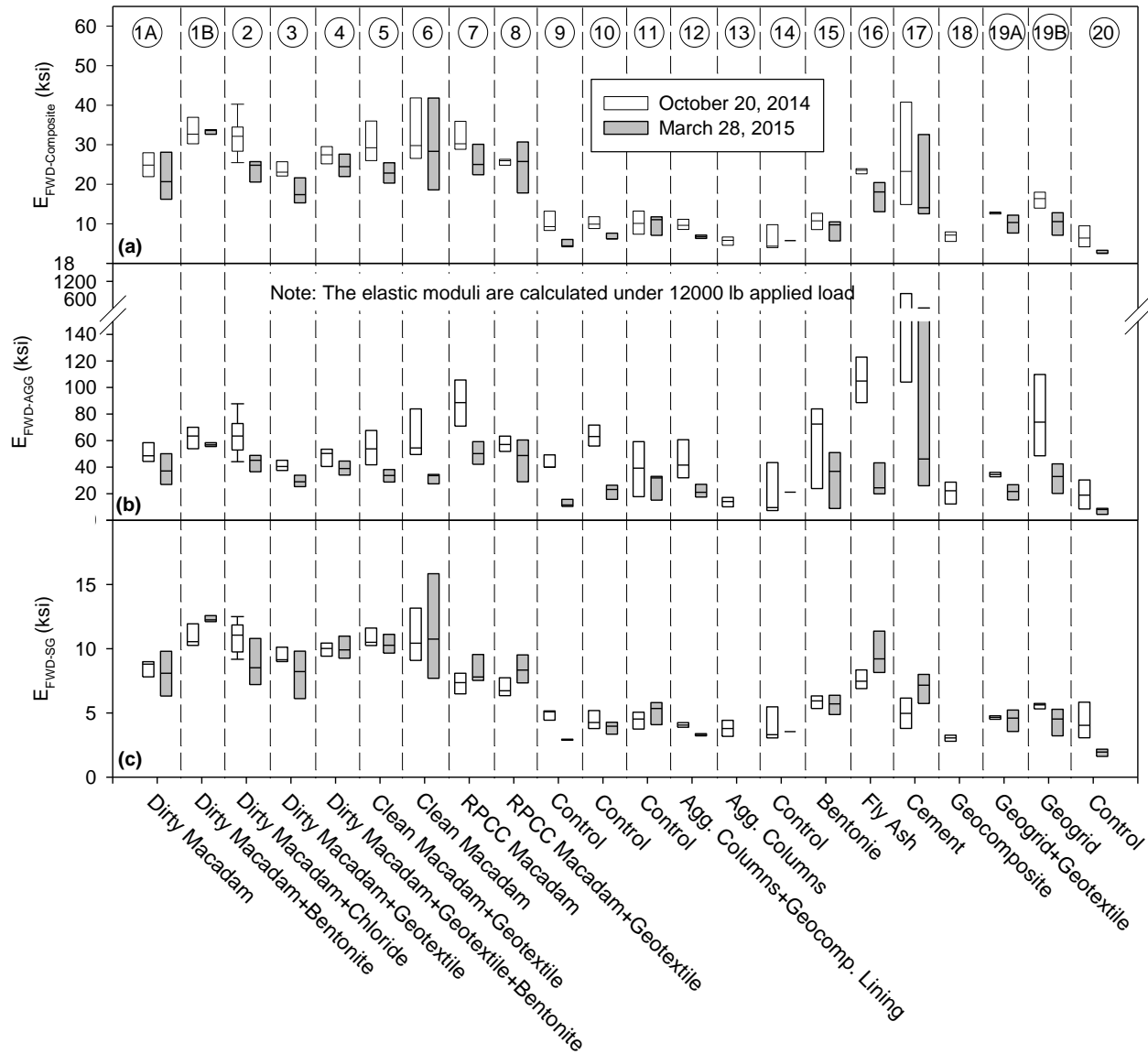
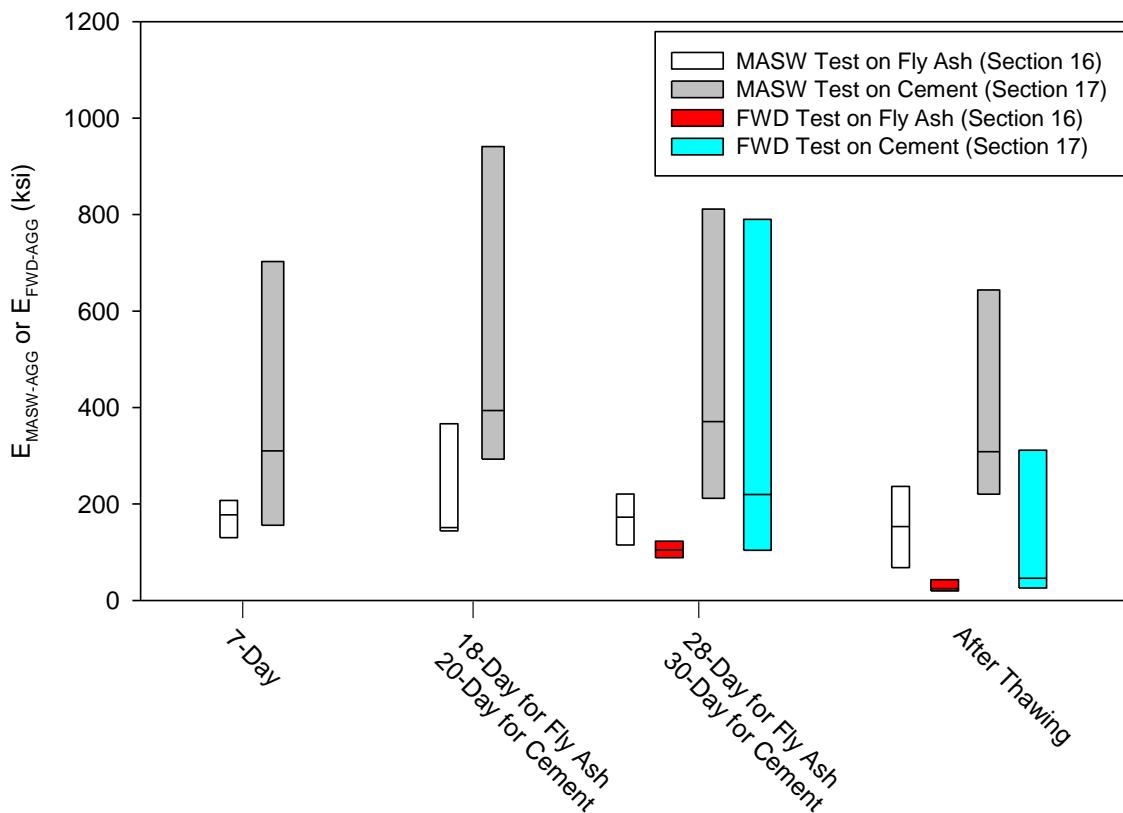


Figure 99. Summary boxplots of 2014 pre-freezing and 2015 post-thawing FWD tests on all sections: (a) $E_{FWD-Composite}$, (b) $E_{FWD-AGG}$, and (c) E_{FWD-SG}

The composite $E_{FWD-composite}$ and surface course $E_{FWD-AGG}$ values of the macadam Sections 1–8 were similar, and were much higher than the control sections. The fly ash- and cement-stabilized Sections 16 and 17 also had much higher $E_{FWD-composite}$ values than the control sections, but 2014–2015 was their first freeze-thaw cycle and they experienced greater reductions in $E_{FWD-AGG}$ than the macadam sections. The bentonite, BX-geogrid with NW-geotextile, and BX-geogrid sections (Sections 15, 19A, and 19B) showed slightly higher $E_{FWD-composite}$ and $E_{FWD-AGG}$ values than the control sections, while the aggregate column Sections 12 and 13 and geocomposite drain Section 18 had stiffnesses similar to the control sections.

6.5.3.3 MASW Test Results

MASW tests were performed on the fly ash- and cement-stabilized sections to measure the post-thawing small-strain elastic modulus of the surface course materials ($E_{\text{MASW-AGG}}$), and for comparison to the values measured during curing (Figure 100). The test results show that the average $E_{\text{MASW-AGG}}$ of the cement-stabilized surface course reached a maximum 20 days after construction, and decreased only slightly after the seasonal freeze-thaw cycle. Similarly, the average stiffness of the fly ash-stabilized section reached its maximum 18 days after construction, and remained relatively unchanged after the seasonal freeze-thaw cycle. The measurement values for the cement section also showed much more statistical variation than those of the fly ash section. The relative trends of MASW and FWD results were generally in agreement (with MASW modulus higher due to the smaller strain levels), but the average value and range of FWD modulus for the fly ash-stabilized Section 16 were much lower than the MASW values.



Middle line of box is median, box edges are 25th and 75th percentiles, and whiskers extend to most extreme data not considered outliers

Figure 100. Boxplots of surface course modulus of fly ash- and cement-stabilized sections from MASW and FWD tests during curing and after 2014-2015 seasonal freeze-thaw cycles

6.5.3.4 Survey Photos

Survey photos were also taken for the demonstration sections during freeze-thaw period of 2014-2015 to monitor and visually compare roadway surface conditions. Five groups of survey photos taken during this period can be found in Appendix C. The roadway surfaces of all sections in the thawing period of 2015 were generally in better condition than the thawing period of 2014. This is likely a result of the shorter thawing period, shallower maximum frost penetration depth, and lower precipitation in 2015 (see Figure 95 and Figure 96). However, the dirty macadam with chloride Section 2 showed a significant amount of ice lenses on the roadway surface during the winter freezing period (Figure 101a), which cannot be easily bladed off. During the thawing period, the chloride-treated Section 2 yielded many more potholes and much more washboarding (Figure 101b) compared to the other dirty macadam sections without the chloride treatment. Bergeson and Wahbeh (1990) found that chloride treatments are prone to potholes and washboarding due to maintenance restrictions. However, based on visual observations in this study during the freezing and thawing period, the potholes and washboarding may be caused by nonuniform chemical concentrations. Areas of high chemical concentrations with high osmotic potential can cause a significant amount of water transportation and accumulation, so the spots containing more ice lenses during freezing may have higher chemical concentrations, making them more prone to potholes and washboarding during thawing due to the heavy traffic loads and high pore-water pressures.

The geocomposite drain Section 18 suffered significant rutting (up to 4 in.) and depressions at some spots after the 2015 thawing period (see Figure 102). The Hamilton county maintenance department reported that the damage was caused by frost boils in the subgrade, because the damaged areas were very soft and spongy. The frost boils created soft spots that resulted in depressions, which further exacerbated the situation as water accumulated in the depressions instead of draining to the ditches. The significant rutting could have been caused by bearing capacity failure under wheel loads, due to the upper geosynthetic layer of the geocomposite providing good separation, but less shear resistance and lateral restraint at the base of the surface aggregate layer, compared to the typical scenario of the surface aggregate getting pressed into the subgrade. However, this problem requires further study to better understand the failure mechanisms involved. To correct the rutting in Section 18, approximately 80 tons of virgin aggregate was dumped on this section and bladed on June 12, 2014, approximately one week after construction. For the economic analysis in this study, the labor and materials costs for the virgin aggregate on Section 18 were therefore considered to be a construction cost rather than a recurring maintenance cost, because the original rock cover was not sufficient.

For the geogrid with geotextile Section 19A, the geosynthetics were exposed at several spots near the centerline after the second freeze-thaw cycle, as shown in Figure 103. This section was constructed on October 1, 2013, with a nominal 8 in. surface aggregate layer. Similar damage was also observed for a few spots of the macadam sections with the NW-geotextile. This damage was caused by degradation and/or loss of the surface aggregate, and the surface aggregate layer was thinnest at the centerline.

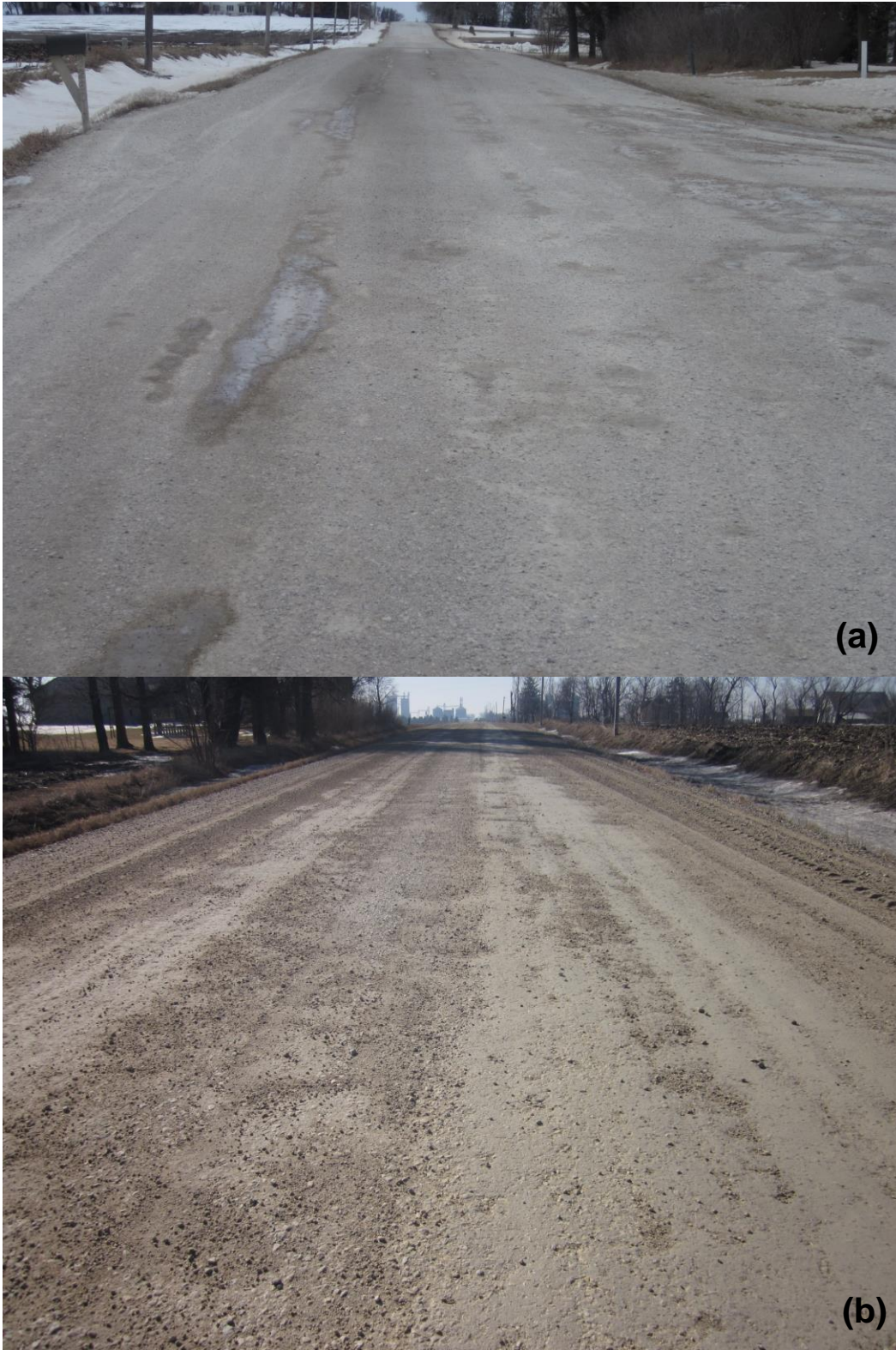


Figure 101. Surface conditions of dirty macadam plus chloride Section 2 during (a) freezing period (February 24, 2015) and (b) thawing period (March 10, 2015)



Figure 102. Surface condition of geocomposite drain Section 18 showing rutting (April 21, 2015)



Figure 103. Surface condition of BX-geogrid+NW-geotextile Section 19A showing exposed geosynthetics (May 20, 2015)

During the 2015 thawing period, the surface aggregate of the dirty macadam with bentonite Section 1B was much drier and tighter than the other sections (Figure 104). Representative surface aggregate specimens were collected from Sections 1A and 1B on April 4, 2014 to compare the gradation and plasticity of the two materials. The test results showed that the surface aggregate mixed with bentonite had more fines as expected (Figure 105). The surface aggregate of the dirty macadam Section 1A was non-plastic, whereas the plasticity index of the better performing Section 1B with bentonite was equal to 18. Detailed soil index properties for the samples from Sections 1A and 1B are summarized in Table 25.

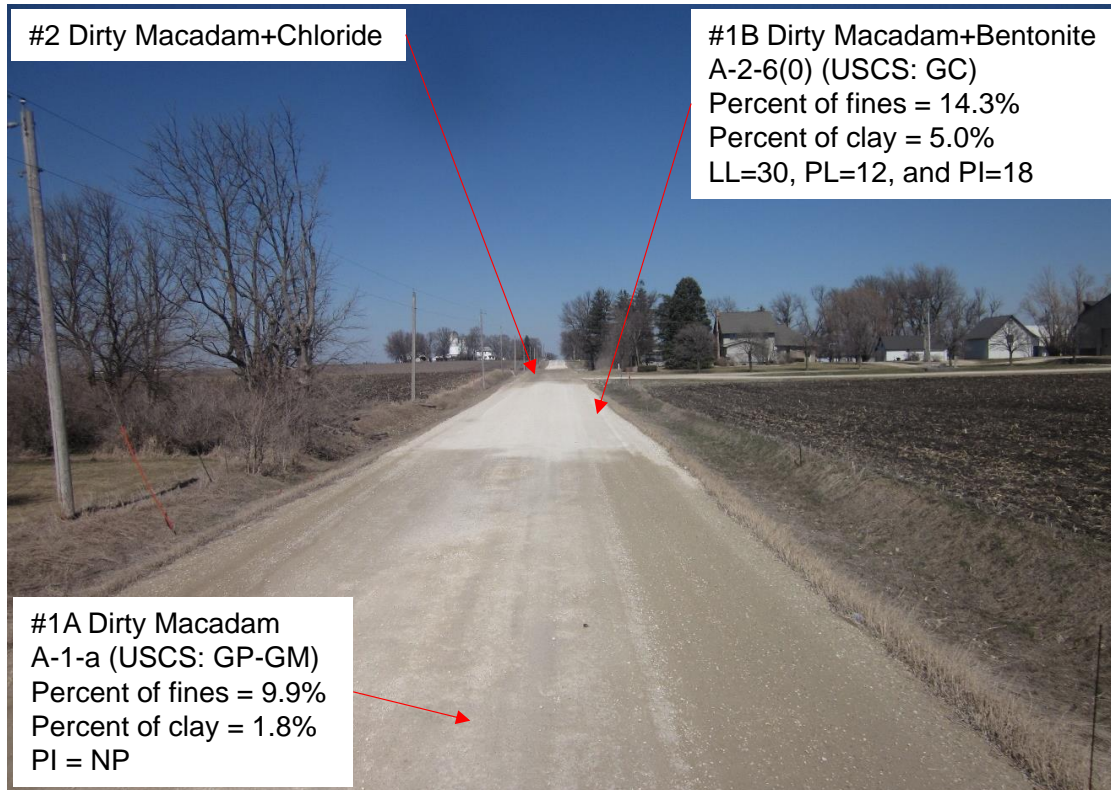


Figure 104. Surface conditions of dirty macadam, dirty macadam with bentonite, and calcium chloride Sections 1A, 1B, and 2 during 2015 thawing period (March 28, 2015)

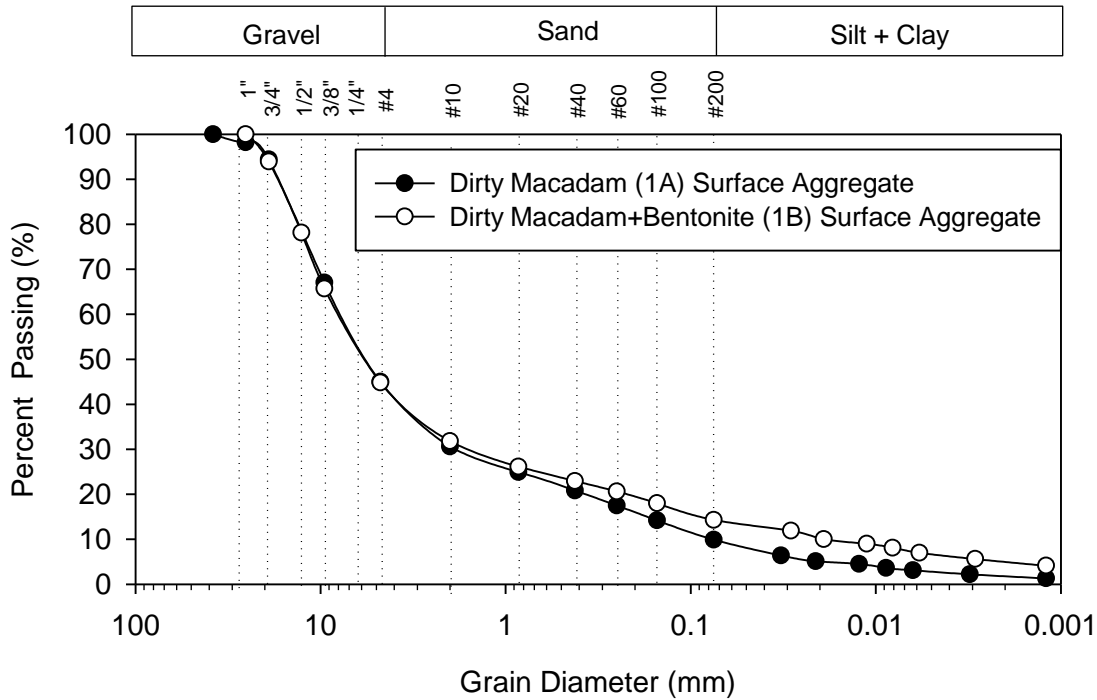


Figure 105. Particle size distribution curves of surface aggregate from dirty macadam Section 1A and dirty macadam with bentonite Section 1B

Table 25. Soil index properties of surface aggregate from dirty macadam Section 1A and dirty macadam with bentonite Section 1B

Parameter	Dirty Macadam Section 1A	Dirty Macadam with Bentonite Section 1B
Particle-size analysis results (ASTM D 422-03)		
Gravel content (%)	55.0	55.2
Sand content (%)	35.1	30.5
Silt content (%)	8.1	9.3
Clay content (%)	1.8	5.0
D ₁₀ (mm)	0.077	0.019
D ₃₀ (mm)	1.876	1.627
D ₆₀ (mm)	7.949	8.174
Coefficient of uniformity, c _u	103.74	423.79
Coefficient of curvature, c _c	5.78	16.79
Atterberg limits test results (ASTM D 4318-10e1)		
Liquid limit (%)	NP	30
Plastic limit (%)		12
AASHTO and USCS soil classification (ASTM D 2487-11 & D3282-09)		
AASHTO classification	A-1-a	A-2-6(0)
USCS classification	GP-GM	GC

6.5.3.5 SEM Results

Representative surface course samples were collected from the dirty macadam Section 1A, dirty macadam with chloride Section 2, bentonite-stabilized Section 15, fly ash-stabilized Section 16, and cement-stabilized Section 17 on May 19, 2015, approximately eight months after construction of the chemically stabilized sections. Scanning electron microscopy (SEM) with energy dispersive spectroscopy (EDS) was performed on the samples to compare their microstructural features and relative chemical proportions. All of the samples were first sieved through a No. 10 sieve and oven dried at a temperature of 100 °F for seven days.

The dirty macadam Section 1A was used as a control (untreated) sample, and showed high Ca and Mg content (Figure 106). The chemical compositions of typical Iowa limestone and typical Iowa dolomite as reported in Bergeson et al. (1995) are shown in Table 26. The limestone has an MgO content of only 0.3–4.3%, while the dolomite has a much higher MgO content of 13.2–18.8%. The x-ray spectra data therefore may indicate that the surface course material for the macadam-based sections was dolomite ($\text{CaMg}(\text{CO}_3)_2$) mixed with some limestone (CaCO_3) and alumino-silicates.

To compare the relative chemical proportions of the chemically treated surface course samples, the x-ray spectra for the different samples were normalized to the background in Figure 106a, and to Ca content in Figure 106b. However, normalizing to the background probably provides a better comparison, because the Ca content might change due to the different treatments and different surface course materials (i.e., the subgrade plus surface aggregate (SG+AGG) mixture for the fly ash- and cement-stabilized sections had 63% subgrade and 37% aggregate by volume).

For the dirty macadam with chloride Section 2, the sample was quite similar to the control sample (Figure 106a). As explained previously, the chloride treatment was sprayed by a local resident in summer 2014 for dust control, so the type and concentration of the liquid chloride was unknown. Compared to the control sample, the chloride-treated sample showed higher Cl and Mg and lower Ca content, indicating that the treatment may have been magnesium chloride rather than calcium chloride. However, the change in Mg was small, and Hamilton County does not allow the use of Magnesium Chloride, so the slight increase in Mg could therefore be due to sample variability and the Mg present in the dolomite. The chloride section sample was collected about one year after the treatment. However, based on the x-ray spectra and visual observations, the chloride treatment was still effective for dust control.

The bentonite Section 15 was constructed approximately one year after the macadam-based sections, and its surface course consisted of both existing and virgin aggregate. Compared to the control sample, the Section 15 sample showed lower Mg and higher Si and Al content as expected, because the bentonite used for this section had 59% SiO_2 and 21% Al_2O_3 (Table 12). Also, based on visual observations, the bentonite was still capable of dust reduction even after one seasonal freeze-thaw cycle.

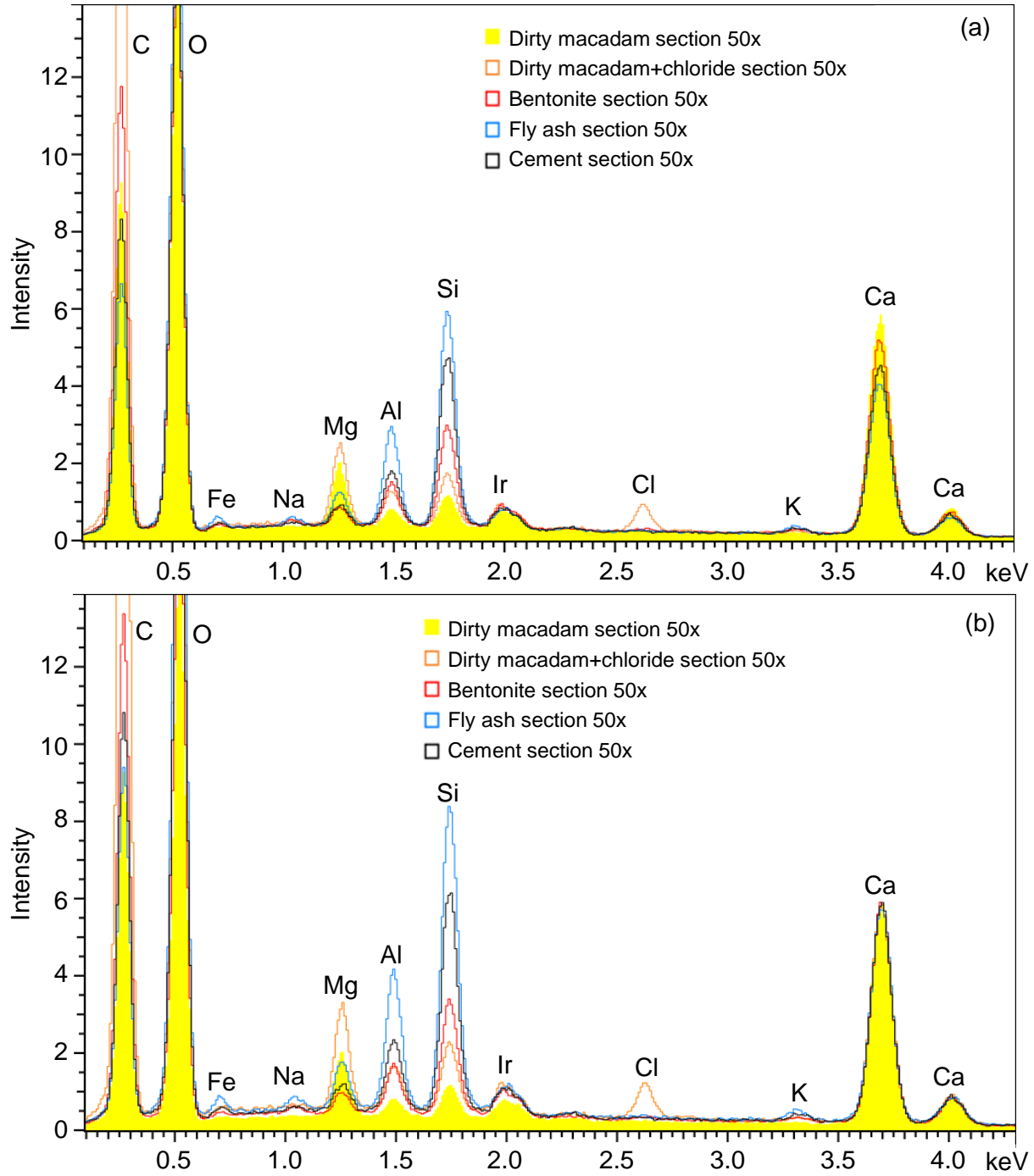


Figure 106. Comparison of X-ray spectra normalized to (a) background and (b) Ca content for the different surface course materials (collected at 50x magnification of SEM scan area)

Table 26. Chemical composition of typical Iowa limestone and dolomite (Bergeson et al. 1995)

Chemical Composition	Typical Iowa Limestone Ranges	Typical Iowa Dolomite Ranges
SrO ₃	0.02-0.04	0.01-0.02
MgO	0.29-4.34	13.18-18.84
CaO	47.40-54.89	29.76-34.38
Fe ₂ O ₃	0.16-0.60	0.20-0.94
TiO ₂	<0.01-0.02	0.01-0.03
SiO ₂	0.16-3.99	0.76-2.83
SO ₃	<0.01-0.20	<0.01-0.27
K ₂ O	0.01-0.14	0.06-0.18
P ₂ O ₅	<0.01-0.03	<0.01-0.07
Al ₂ O ₃	0.05-0.40	0.16-0.48
MnO	0.01-0.05	0.02-0.05
LOI ^a	42.30-44.10	45.00-46.80

^a LOI = loss on ignition @ 950°C

The surface courses of the fly ash- and cement-stabilized sections were SG+AGG mixtures, so their high Si and Al contents may be due to both the chemical stabilizers and subgrade materials. However, x-ray diffraction would be required to conclusively identify the sources of the Si and Al. Compared to the control sample, the fly ash treatment also led to increases in Fe, Na, and K, and reductions in Mg and Ca, as expected. The cement-treated sample also showed higher Al and Si and K content, but the Ca content was approximately the same as the fly ash-treated sample, possibly due to a low cement content in the collected sample because of non-uniform mixing during construction.

Representative SEM images were selected to visually compare the effectiveness of the chloride and bentonite treatments for dust control (Figure 107). Compared to the control and chloride-treated samples, the bentonite-treated samples had many more small particles adhered to the larger particles. However, based on the visual observations in the field, both the chloride- and bentonite-treated sections generated much less dust than the other sections, and the chloride-treated section showed the best performance. The two dust control methods use different principles, with bentonite functioning as an “electrochemical glue” to bond small particles to large particles, and magnesium chloride causing high osmotic potential to hold or absorb moisture from the environment to the road surface even under natural hot and dry conditions. However, the fact that the SEM images for the oven-dried chloride-treated samples showed fewer small particles adhering to the larger particles may be because they could not absorb moisture due to the extreme dryness in the oven, and some small particles were therefore blown away by compressed air in the SEM preparation process.

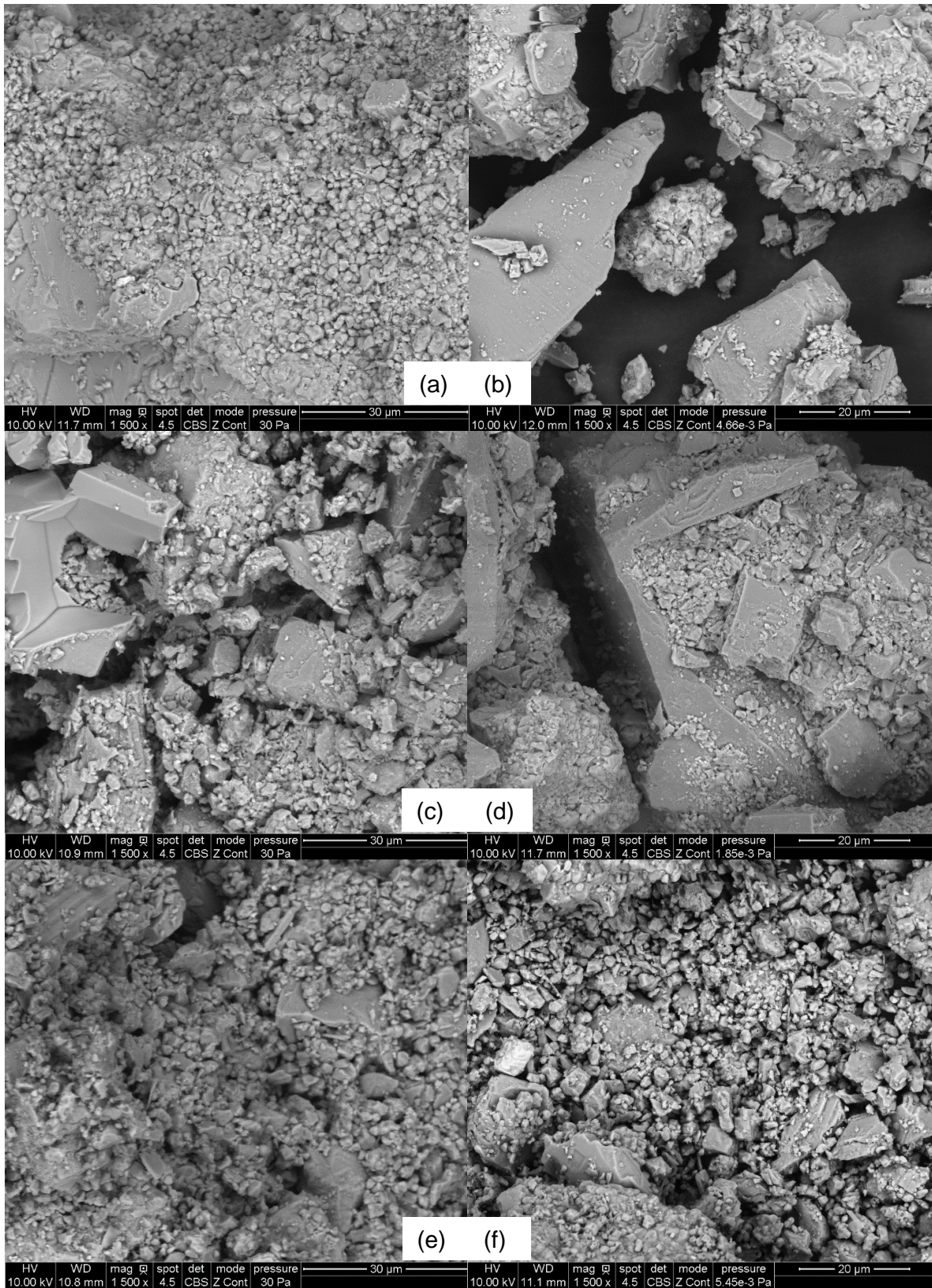


Figure 107. SEM images (1500x magnification) of (a and b) dirty macadam, (c and d) dirty macadam with chloride, and (d and e) bentonite-treated surface course samples

SEM images were also taken for surface course samples from the fly ash- and cement-stabilized Sections 16 and 17 to observe hydration of the chemical stabilizers and ettringite formation in the fly ash-stabilized material. For the fly ash-stabilized samples, very few intact (unhydrated) fly ash spheroids and no needle-like ettringite structures can be seen in Figure 108a and Figure 108b. Unhydrated fly ash could bring some long-term benefits as the pozzolanic reactions would continue, but long-term performance monitoring would be required to assess this. For the cement-stabilized samples, unhydrated cement particles were not observed in Figure 108d and Figure 108e. Also, the low Ca content (see Figure 106) might be a result of the collected samples having a very low cement content due to non-uniform mixing during construction, or because they might have been collected mainly from the wearing surface used to cover the chemically-stabilized materials after mixing.

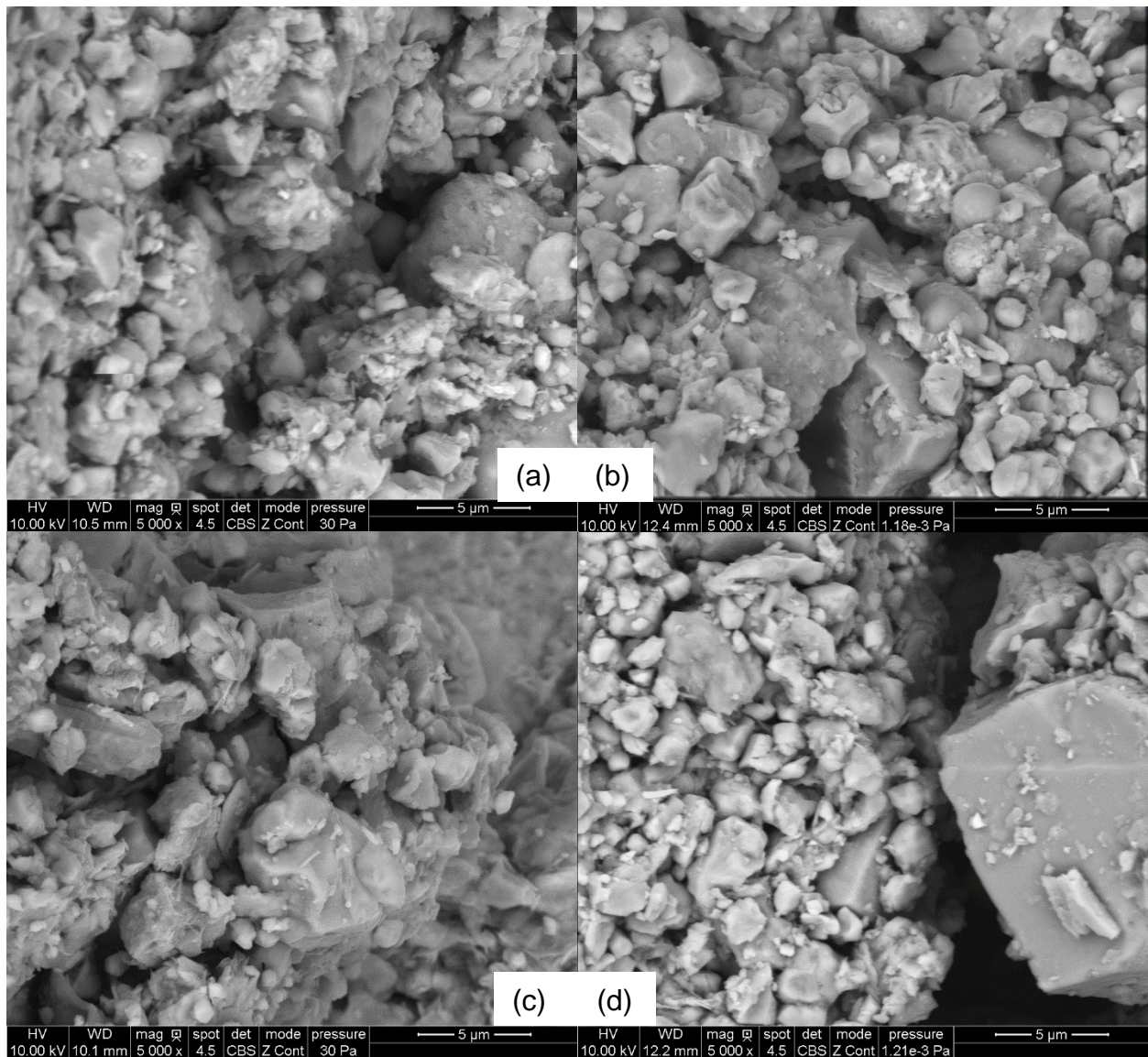


Figure 108. SEM images (5000x magnification) of surface course samples from (a and b) fly ash and (c and d) cement-stabilized sections

6.6 Construction Costs and Economic Analysis

To evaluate the relative cost-effectiveness of the various stabilization technologies for mitigating freeze-thaw damage, the construction costs and maintenance work-orders for the demonstration sections were documented by the Hamilton County secondary roads department.

6.6.1 Construction Costs

The construction costs are summarized in Figure 109 and detailed in Table 27. Since milling of the chemical stabilizers was performed by Manatts Inc., the labor and equipment costs were billed as a lump sum. For the macadam sections with bentonite (Sections 1B and 3), the construction costs were \$18.5 and \$20.2 per square yard. Construction costs for the other macadam sections ranged between \$8.6 and \$10.1 per square yard. However, the significantly higher labor and equipment costs for the two macadam sections with bentonite could be greatly reduced if the county secondary roads department were to perform the mixing using existing equipment such as dump trucks, motor graders, and water trucks. Detailed construction procedures and equipment for macadam construction were recommended in Bergeson et al. (1995). The calcium chloride in Section 2 was purchased and applied by a local resident for dust control, so the related material and labor costs were estimated by the County Engineer based on previous experience.

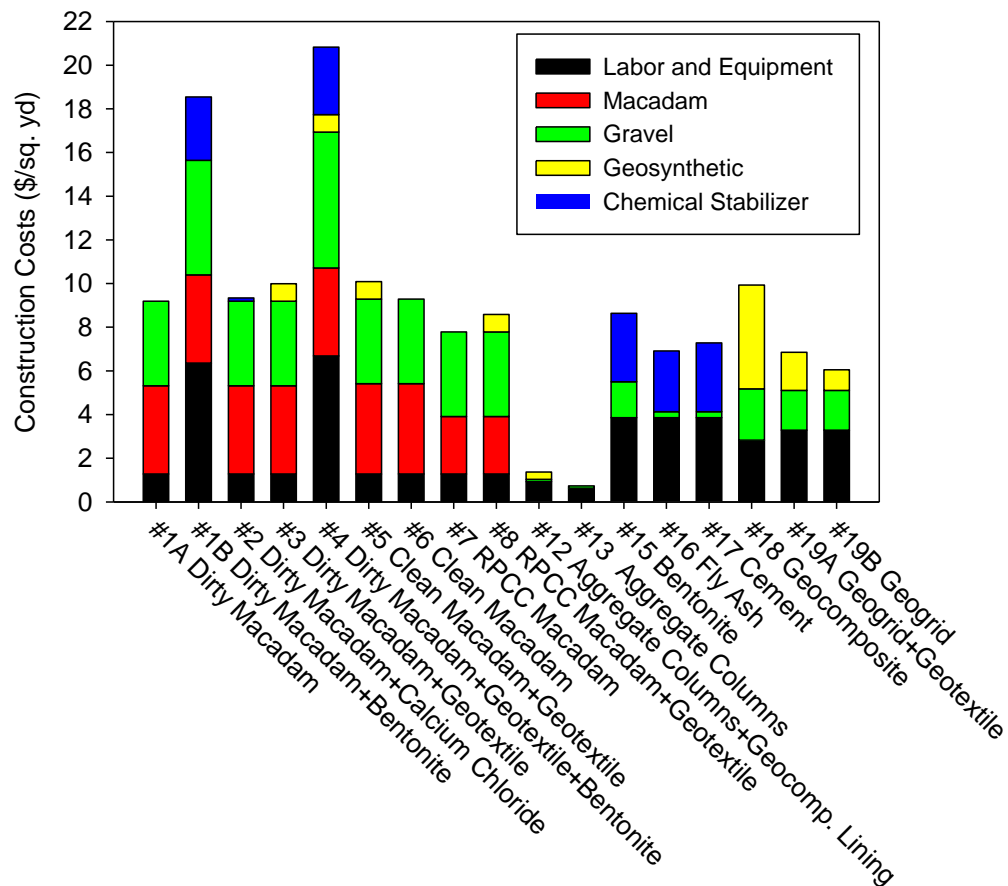


Figure 109. Construction costs (\$/sq. yd.) of the Vail Avenue demonstration sections

Table 27. Breakdown of construction costs for the Vail Avenue demonstration sections (\$/sq. yd.)

Description (Section Number)	Labor	Equip- ment	Macadam	Choke stone	Road Stone	Geosyn- thetic	Stabilizer	Total Cost
Dirty Macadam (1A)	0.47	0.82	4.03	2.25	1.62	–	–	9.19
Dirty Macadam+Bentonite (1B)	6.36 ^a		4.03	2.25	3.00	–	2.90	18.54
Dirty Macadam+Calcium Chloride (2)	0.47	0.82	4.03	2.25	1.62	–	0.15 ^b	9.34
Dirty Macadam +NW-geotextile (3)	0.47	0.82	4.03	2.25	1.62	0.80	–	9.99
Dirty Macadam+NW-geotextile+Bentonite (4)	6.68 ^a		4.03	2.25	3.97	0.80	3.09	20.82
Clean Macadam+NW-geotextile (5)	0.47	0.82	4.13	2.25	1.62	0.80	–	10.09
Clean Macadam (6)	0.47	0.82	4.13	2.25	1.62	–	–	9.29
RPCC Macadam (7)	0.47	0.82	2.63	2.25	1.62	–	–	7.79
RPCC Macadam+NW-geotextile (8)	0.47	0.82	2.63	2.25	1.62	0.80	–	8.59
Aggregate columns w/ geocomp. linings (12)	0.76	0.17	–	–	0.11	0.33	–	1.37
Aggregate columns (13)	0.46	0.17	–	–	0.11	–	–	0.74
Bentonite (15)	3.86 ^a		–	–	1.65	–	3.14	8.65
Fly ash (16)	3.86 ^a		–	–	0.28	–	2.78	6.92
Cement (17)	3.86 ^a		–	–	0.28	–	3.15	7.29
Geocomposite drain (18)	1.13	1.70	–	–	2.35	4.75	–	9.93
BX-geogrid+NW-geotextile (19A)	1.49	1.79	–	–	1.82	1.74	–	6.84
BX geogrid (19B)	1.49	1.79	–	–	1.82	0.94	–	6.04

^a Milling of chemical additives was performed by Manatts, Inc., so labor and equipment costs were billed as a lump sum.

^b Because the calcium chloride was sprayed by a local resident, quantity and total costs (i.e., material, equipment, and labor) were estimated by the County Engineer based on previous experience.

6.6.2 Maintenance Costs

In this section, the maintenance records from 2014 and 2015 are used to estimate annual maintenance costs per square yard for the demonstration sections. Through personal communication, the Hamilton County Engineer provided estimated annual maintenance costs for the two-mile stretch of Vail Avenue for years prior to the present project. However, the estimated costs do not include any overhead or engineering administration costs. This stretch of roadway was previously the most heavily used one in Hamilton County, requiring an estimated 350 tons of virgin aggregate per mile annually to maintain. The cost of the virgin aggregate varied between \$10 and \$15 per ton in recent years, which includes the cost of hauling from the quarry to a county stock-pile, but not the cost of loading and hauling material to the site. To account for local hauling costs, the higher \$15/ton rate was used to estimate the maintenance costs prior to building the stabilization demonstration sections. Also, the road required two bladings per week during heavily used harvest and planting seasons (approximately 4 months of the year), and each blading usually required approximately one hour per mile of labor and grader time. Calcium chloride liquid was also applied annually for stabilization, at a total cost of approximately \$0.16 per square yard. The unit costs for the materials, equipment, and labor provided by the Hamilton County Engineer are summarized in Table 28. Based on this information, the previous yearly maintenance cost of the Vail Avenue section between 310th and 330th streets was estimated at \$0.84/sq. yd., as shown in Table 29.

Table 28. Unit costs for materials, labor and equipment

Category	Unit Cost
Virgin aggregate	\$15.00 / ton
Average labor	\$31.00 / hr
Truck	\$53.71 / hr
Motor Grader	\$64.09 / hr
Loader	\$49.03 / hr
Chloride Stabilization	\$0.16 / sq. yd.

The maintenance records for the demonstration sections show that blading of the entire two-mile stretch of Vail Avenue was conducted three times during the thawing period of 2014. This was much less than required in previous years, as explained above. For the geocomposite drain Section 18, however, two maintenance work orders to spread additional aggregate and blade the surface due to excessive rutting were completed on June 12 and June 17, 2014. Since the additional aggregate was needed only one week after construction of Section 18 to remedy excessive rutting, these costs were considered one-time incremental construction costs rather than recurring maintenance costs. On November 6, 2014, two truckloads of virgin aggregate were spread on the clean macadam with NW-geotextile Section 5, and one truckload was spread on the RPCC macadam with NW-geotextile Section 8 to cover the exposed geotextile. On January 20, 2015, seven truckloads of aggregate were dumped and bladed for the fly ash Section 16 due to significant rutting after a short period of unusually warm weather (see Figure 93) and rainfall. During the thawing period of 2015, two truckloads of aggregate were dumped on Section 3 and 4 to cover exposed geotextile on March 5, 2015. Up through the last date of data

collection on April 28, 2015, only one motor grader blading was conducted during the thawing period of 2015.

Prior to 2013, the two-mile stretch of Vail Avenue required dumping and blading 350 tons of virgin aggregate per mile annually. After constructing the demonstration sections, only those sections having geocomposite, NW-geotextile, and fly ash required dumping and blading of virgin aggregate. Otherwise, blading of the entire two-mile stretch was only needed three times in 2014, and was only needed one time in the first quarter of 2015 (Table 29). Based on these outcomes, several of the stabilization technologies demonstrate the potential to significantly reduce the annual maintenance costs for such heavily traveled roads.

Table 29. Estimated annual maintenance costs for years prior to stabilization in 2013, and for stabilization demonstration sections in 2013-2015

Date	Description	Section Name (Section Number)	Material Cost	Equipment Cost	Labor Cost	Chloride Cost^a	Total Cost	Cost /sq. yd.
Per year prior to 2013	Maintenance costs based on previous experience	Per mile of Vail Avenue	\$5,250	\$3,849	\$2,077	\$2,707	\$13,883	\$0.845
Spring 2014 ^b	Total of three bladings (assumed 1 hr per mile)	Entire 2 miles ^c	NA	\$385	\$186	–	\$571	\$0.017
11/6/2014	Dumping 2 truckloads virgin aggregate and 0.7 hr blading	Clean Macadam + NW-geotextile (5)	\$600	\$197	\$114	–	\$911	\$1.171
11/6/2014	Dumping 1 truckload virgin aggregate and 0.3 hr blading	RPCC Macadam + NW-geotextile (8)	\$300	\$100	\$57	–	\$457	\$0.309
1/20/2015	Dumping 7 truckloads virgin aggregate and 3 hrs blading	Fly ash (16)	\$2,100	\$1,209	\$698	–	\$4,007	\$2.146
3/5/2015	Dumping 2 truckloads virgin aggregate and 0.5 hr blading	Sections with NW-geotextile (3 and 4)	\$600	\$238	\$140	–	\$977	\$0.209
4/27/2015	1.5 hrs blading	Entire 2 miles ^b	NA	\$96	\$47	–	\$143	\$0.004

^a Total cost including material, labor, and equipment estimated by Hamilton County Engineer

^b Estimated based on personal communication with Hamilton County Engineer.

^c Motor grader blading was conducted on the entire two mile stretch of roadway.

To determine the number of years until each technology would begin to provide cost savings (i.e., the break-even points) relative to continuation of previous maintenance practices, the construction costs and estimated annual maintenance costs were combined to determine cumulative yearly costs for the different stabilization technologies. These costs were then compared to the estimated annual maintenance costs from previous years for the unimproved two-mile stretch of Vail Avenue (Figure 110). For an accurate life-cycle analysis, it would be best to monitor the demonstration sections over several years to obtain more accurate average annual maintenance costs. However, the existing performance data through two freeze-thaw cycles can also be used to extrapolate out several years if the maintenance costs in Table 29 are assumed to hold constant.

The average annual maintenance costs for the first two years were calculated from the maintenance records during the project. The initial construction costs shown in Table 27 and Figure 109 were combined with the estimated annual maintenance costs for the various demonstration sections, and projected over a twenty-year period. Inflation and depreciation were not accounted for in the break-even analysis, because interest rates are variable from year to year, and blading was performed on the entire two-mile stretch at once since it was not practical for operators to record the amount of blading needed in each individual demonstration section. The maintenance costs of blading per square yard are therefore the same for all demonstration sections. However, some sections did require dumping of virgin aggregate while others did not, which results in different estimated annual maintenance costs. Additionally, it is assumed that the same interest rates would apply to the maintenance costs in the various sections. All cost comparisons were therefore done in terms of present-day dollars rather than future values. If future values of the present-day construction costs were considered, the break-even periods would be somewhat shorter.

The results are shown in Figure 110. The cost shown at 0 years is the construction cost for each section, which is \$0 for the current maintenance practice. The results show that compared to the costs of current maintenance practices, the aggregate column Sections 12 and 13 reached the break-even point within only two years of construction. After the break-even points, the cumulative cost would be less than the cost of continuing current maintenance practices. Most of the other sections, except for Sections 1B, 3, 4, 5, and 16 reached break-even points between 9 to 17 years after initial construction. For the macadam sections with bentonite (Sections 1A and 4), the construction costs were very high due to the labor costs of milling the bentonite as performed by Manatts Inc. As mentioned previously, these construction costs could be reduced if this work was performed by the county secondary roads department using their existing equipment.

Based on Figure 110, all of the macadam sections with NW-geotextile (Sections 3, 4, 5, and 8) required higher maintenance costs than the corresponding sections without the NW-geotextile, because virgin aggregates were dumped and bladed to cover some exposed geotextile. Also, the county maintenance crew reported that the geosynthetics placed below the surface aggregate caused maintenance restrictions, because to avoid damage the geosynthetics, the scarifier of the motor grader could not be used to break down the crust and reshape the roadway surface for these sections. The fly ash Section 16 did not require any additional maintenance beyond that performed on January 20, 2015, and the road conditions were similar to the cement-stabilized

Section 17 during the 2015 thawing period. Therefore, the projected maintenance costs may be overestimated for Section 16.

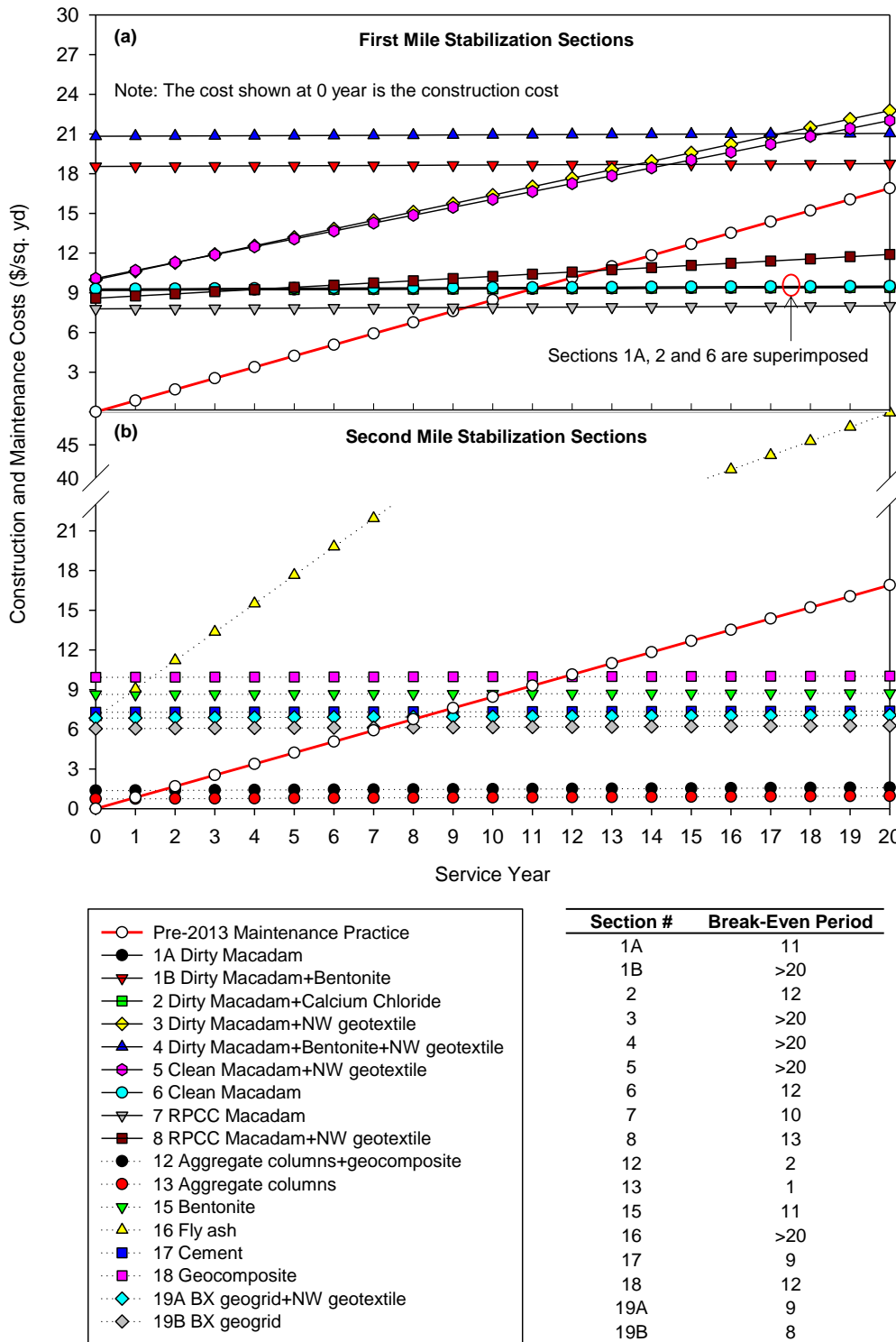


Figure 110. Projected cumulative (construction + annual maintenance) costs for the (a) first mile and (b) second mile stabilization sections, compared to cumulative cost of continuing pre-2013 maintenance practices

The construction costs of various stabilization methods may initially give the impression of being expensive. However, they should be viewed as an investment that will provide savings relative to current maintenance practice after a break-even point several years in the future. Additionally, other long-term economic and non-economic benefits will be realized such as significantly improved ride quality, and foundations that can serve as good base layers for future overlays or paved surface upgrades, especially for the macadam bases.

The basic economic analysis presented in this study could be improved by considering a life-cycle analyses and incorporating the overhead and engineering administration costs and time-value of money (i.e., present and future values considering interest and inflation). However, lifespan data is not currently available for all the variations of stabilization technologies examined in this study. Also, the actual long-term performance of the various sections as well as the related maintenance costs may differ from those observed over the 24 month period of this study. To determine more accurate annual maintenance and life-cycle costs, the project sections should be monitored and their performance and maintenance costs analyzed over a longer period. With such data, the most economical and effective stabilization methods in the long-term can be more clearly identified.

CHAPTER 7. CONCLUSIONS AND RECOMMENDATIONS

This chapter summarizes the key findings from construction, laboratory tests, field tests, weather and performance monitoring, and economic analysis for the Vail Avenue demonstration sections. Recommendations for future research and implementation are also provided.

7.1 Construction Processes and Requirements

Based on the observations of construction processes, most of the mechanical stabilization methods can be easily implemented by county secondary roads departments with existing crews and equipment. However, a full-depth reclaimer and vibratory sheep's-foot or pad-foot roller compactor are also needed for chemical stabilization using fly ash or cement, and a Jersey spreader is needed for placing macadam stone. During construction, all of the demonstration sections except for the chemically stabilized sections remained opened to traffic.

7.2 Laboratory Test Results

Comprehensive laboratory tests were conducted on the surface course and subgrade materials of the Vail Avenue demonstration sections. Soil index property tests and laboratory abrasion tests were conducted to evaluate the compaction and degradation characteristics of the different geomaterials. According to the laboratory L.A. abrasion test results, all three macadam material types met the Iowa DOT abrasion specifications for macadam stone materials (Table 4122.03-1 of Iowa DOT 2012). The clean macadam stone showed the greatest resistance to degradation, whereas the RPCC macadam showed more severe degradation (48.0%) than both the clean (34.8%) and dirty macadam (38.5%) specimens. The RPCC degradation was also close to the upper limit of the Iowa DOT specifications (50%).

Laboratory CBR and UCS tests were conducted to determine the shear strength properties of existing surface course and subgrade materials. The laboratory CBR results showed that the performance will degrade significantly when either material goes from fairly dry (as typically observed in the field) to near its optimum compaction moisture content. The UCS was also strongly dependent on the compaction moisture content, and reduced significantly when going from the OMC to vacuum-saturated states. Comparing the actual degree of saturation achieved in the soaked CBR and vacuum-saturated specimens, the vacuum-saturation process was much more effective than soaking for achieving a saturated state.

The laboratory mix design results showed that stabilization by 15% fly ash or 6% cement can effectively increase the peak UCS of the existing surface aggregate, subgrade, and subgrade and surface aggregate mixtures. However, the field performance of the chemically stabilized materials can be influenced significantly by their compaction moisture contents. The optimum compaction moisture contents $w_{opt(UCS)}$ for saturated UCS were within $\pm 1.5\%$ of the optimum compaction moisture contents w_{opt} for density from standard Proctor tests. Relative to the untreated materials, the materials stabilized with 15% fly ash yielded the highest maximum dry unit weights and lowest optimum moisture contents.

Laboratory freezing-thawing and wetting-drying tests were also conducted on field-compacted specimens to evaluate the durability of the fly ash- and cement-stabilized surface course materials. The results showed that the cement-stabilized specimens showed better freezing-thawing and wetting-drying durability than fly ash-stabilized specimens.

Laboratory permeameter tests were conducted on an existing subgrade specimen and surface aggregate specimens with and without an embedded geocomposite drainage layer. The results showed the subgrade material (AASHTO classification A-7-6(10)) can be considered impermeable due to the extremely low saturated hydraulic conductivity ($K_{sat} = 5.06 \times 10^{-5}$ ft/day). The geocomposite drainage layer effectively increased the K_{sat} of the surface aggregate specimens by three orders of magnitude.

7.3 Weather and Ground Temperature Profile Results

Using a weather station and thermocouples embedded between 0.6 in. and 5 ft depth, the subgrade was determined to undergo up to 34 freeze-thaw cycles during the 2013-2014 and 2014-2015 seasonal freeze-thaw periods. The maximum frost depth was determined to be near 5 ft in 2014, and 4.5 ft in 2015. The duration of the thaw period, during which time the granular surfaced road is most susceptible to moisture damage, was found to be 40 days in 2014 and 23 days in 2015. The last portion of frozen subgrade thawed at approximately 3.75 ft depth around April 21 in 2014, and approximately 2.5 ft depth around March 30 in 2015. Overall, the thawing season had more precipitation and a longer duration in 2014 than in 2015.

7.4 Field Test Results

Preconstruction, as-constructed, and post-thawing field tests were conducted on the Vail Avenue demonstration sections. The preconstruction tests showed that when the existing materials were dry, the surface aggregate course had a nominal thickness of 4.8 in. and rated as excellent at 7 out of 9 test locations and below good at the other 2 locations, whereas the subgrade rated from very poor to very good. The average ratings were excellent for the surface course and fair to good for the subgrade.

The as-constructed FWD test results showed that the composite elastic modulus ($E_{FWD-Composite}$) of the surface-and-subgrade system for the macadam Sections 1A–8 and fly ash- and cement-stabilized Sections 16 and 17 were about three times higher than the control sections. However, significant variation in $E_{FWD-Composite}$ was observed for the cement-stabilized section. The $E_{FWD-Composite}$ values of the BX geogrid with NW-geotextile and BX-geogrid Sections 19A and 19B were about two times higher than the control sections. Relative to the control sections, the $E_{FWD-Composite}$ moduli for the aggregate column Sections 12 and 13, bentonite Section 15 and geocomposite drain Section 18 were not significantly increased, but the freeze-thaw performance of the aggregate column section was improved.

For the as-constructed performance evaluations, two independent NDT methods, falling weight deflectometer (FWD) tests and multichannel analysis of surface wave (MASW) tests, were

performed. The MASW tests showed significant variation for the subgrade due to the small hammer used, which was selected to focus the energy on the surface course. To better measure the stiffness of the subgrade materials, a sledge hammer could be used to generate greater seismic energy at the subgrade depth.

The post-thawing field tests showed that the $E_{\text{FWD-Composite}}$ moduli of the macadam sections were about five times higher than the control sections. However, the macadam sections with NW-geotextile had lower moduli than the corresponding sections without the NW-geotextile. The chemically and geosynthetically stabilized sections also had significantly increased moduli. The moduli of the aggregate column and geocomposite sections were similar to the control sections. However, these two methods are aimed at improving freeze-thaw resilience by improving drainage, not by increasing stiffness.

Based on survey photos taken on 11 different dates during the two freeze-thaw periods, most of the stabilization methods can minimize frost boils and potholes and improve the granular surfaced road surface conditions to varying degrees. Even the roadway surface treated with bentonite was much drier and tighter than the other sections during the thawing period. However, the sections with chloride surface treatments showed more ice lenses during freezing, and were more prone to potholes and washboarding during the thawing period. Additionally, the geocomposite drain section suffered significant rutting during the 2015 thawing period, which may require further study.

7.5 Economic Analysis Results

The different stabilization technologies were evaluated on the basis of their documented construction costs and estimated maintenance costs compared to continuation of previous maintenance practices for the two-mile stretch of Vail Avenue. A break-even analysis was performed by projecting the cumulative total construction and maintenance costs per square yard over a twenty-year period. The initial construction costs of the various stabilization methods might be considered high, but over the long-term they may eventually provide a savings through reduced maintenance costs. The stabilization methods can also provide additional economic and non-economic benefits, such as creation of good-quality base layers for future overlays or surface upgrades, and significantly improved ride quality. However, the actual long-term performance of the various sections may be different from those predicted based upon the maintenance costs documented in this two-year project. Additional long-term monitoring is recommended to more accurately determine the life-cycle costs of each section and better identify the most economical and effective stabilization methods.

7.6 Recommendations

Some recommendations for future research activities and implementation are provided below:

- Continue monitoring and comparing the long-term performance of the various demonstration sections to better assess the maintenance requirements, estimate service lifespans, and more clearly identify the most effective and economical solutions for preventing and mitigating seasonal freeze-thaw damage.
- Install additional strings of thermocouples and sensors to monitor the ground temperature profiles and moisture contents under the different stabilization sections.
- Study the physics and mechanisms involved to understand why the chloride surface treatment caused more ice lenses on the roadway surface during freezing and was more prone to potholes and washboarding during thawing.
- Evaluate the feasibility of using MASW testing as a more economical alternative to FWD testing for measuring and monitoring the stiffness of the different layers of granular surfaced road systems.

Counties could benefit by immediately implementing some of the research project findings. First, the aggregate columns were very inexpensive to install, and appeared to reduce the occurrence of frost-boils and related washboarding and ice lenses on the surface. Some minor rutting was observed near the shoulders, which could be improved by installing more aggregate columns near the shoulders, as well as installing a denser grid of columns. The columns are believed to function primarily as drainage basins, so their effectiveness in any year may be a function of their depth, the depth of the water table, and the amount of seasonal precipitation. The aggregate columns had a break even period of 1 year (2 years with geocomposite linings), after which the cumulative construction and maintenance costs would be less than continuation of existing maintenance practices. As shown in Figure 59, the cost savings continue to add up after any given break-even point, assuming that the estimated annual maintenance costs hold.

After the aggregate columns, the biaxial (BX) geogrid sections had the next shortest break-even periods of 8 years without a geotextile layer, or 9 years with the geotextile, followed by cement (9 years), RPCC macadam (10 years), bentonite stabilization and dirty macadam (11 years), dirty macadam with chloride, clean macadam, and geocomposite (12 years), and RPCC macadam with NW-geotextile (13 years). Due to higher construction costs, the clean and dirty macadam sections with bentonite and/or NW-geotextile would have very long break-even periods (>20 years). For the dirty and clean macadam sections with NW-geotextile, virgin aggregates were dumped to cover spots where the geotextile was exposed, which led to higher projected annual maintenance costs. The recorded maintenance cost of the fly ash section was greater than the previous maintenance practices, so no break-even period exists for this section.

Overall, the BX geogrid and macadam-based sections had the best observed freeze-thaw performance in this study. They have larger initial costs and longer break-even periods than the aggregate columns, but counties should also weigh the benefits and savings that these solutions can provide as excellent foundations for future paving or surface upgrades.

REFERENCES

- AASHTO (1993). *AASHTO guide for design of pavement structures 1993*, American Association of State Highway and Transportation Officials, Washington, D.C.
- Aho, S., and Saarenketo, T. (2006). *Design and repair of roads suffering spring thaw weakening*. The Swedish Road Administration, Northern Region, Sweden.
- Alzubaidi, H. (1999). *Operation and Maintenance of Gravel Roads - A Literature Study*. Swedish National Road and Transport Research Institute, Linköping, Sweden, 231.
- Andersland, O. B., and Ladanyi, B. (2004). *Frozen Ground Engineering*, John Wiley & Sons, Hoboken, New Jersey.
- ASTM. (2013). "Standard Test Method for Resistance to Degradation of Large-Size Coarse Aggregate by Abrasion and Impact in the Los Angeles Machine." *Annual book of ASTM standards, ASTM C 535-12*, West Conshohocken, PA.
- ASTM. (2013). "Standard Specification for Coal Fly Ash and Raw or Calcined Natural Pozzolan for Use in Concrete." *Annual book of ASTM standards, ASTM C 618-12a*, West Conshohocken, PA.
- ASTM. (2013). "Standard practice for sampling aggregates." *Annual book of ASTM standards, ASTM D 75-13*, West Conshohocken, PA.
- ASTM. (2013). "Standard Test Method for Particle-Size Analysis of Soils." *Annual book of ASTM standards, ASTM D 422-03*, West Conshohocken, PA.
- ASTM. (2007). "Standard Test Methods for Wetting and Drying Compacted Soil-Cement Mixtures." *Annual book of ASTM standards, ASTM D 559-03*, West Conshohocken, PA.
- ASTM. (2007). "Standard Test Methods for Freezing and Thawing Compacted Soil-Cement Mixtures." *Annual book of ASTM standards, ASTM D 560-03*, West Conshohocken, PA.
- ASTM. (2013). "Standard test methods for laboratory compaction characteristics of soil using standard effort (12 400 ft-lb/ft³ (600 kN-m/m³))." *Annual book of ASTM standards, ASTM D 698-12e1*, West Conshohocken, PA.
- ASTM. (2013). "Standard Test Methods for Compressive Strength of Molded Soil-Cement Cylinders." *Annual book of ASTM standards, ASTM D 1633-00(2007)*, West Conshohocken, PA.
- ASTM. (2013). "Standard Test Method for CBR (California Bearing Ratio) of Laboratory-Compacted Soils." *Annual book of ASTM standards, ASTM D 1883-07e2*, West Conshohocken, PA.
- ASTM. (2013). "Standard Practice for Classification of Soils for Engineering Purposes (Unified Soil Classification System (USCS))." *Annual book of ASTM standards, ASTM D 2487-11*, West Conshohocken, PA.
- ASTM. (2013). "Standard Practice for Classification of Soils and Soil-Aggregate Mixtures for Highway Construction Purposes." *Annual book of ASTM standards, ASTM D 3282-09*, West Conshohocken, PA.
- ASTM. (2013). "Standard Test Methods for Liquid Limit, Plastic Limit, and Plasticity Index of Soils." *Annual book of ASTM standards, ASTM D 4318-10e1*, West Conshohocken, PA.
- ASTM. (2013). "Standard Practice for Correction of Unit Weight and Water Content for Soils Containing Oversize Particles." *Annual book of ASTM standards, ASTM D 4718-87(2007)*, West Conshohocken, PA.
- ASTM. (2013). "Standard Test Methods for Frost Heave and Thaw Weakening Susceptibility of Soils." *Annual book of ASTM standards, ASTM D 5918-13*, West Conshohocken, PA.

- ASTM. (2013). "Standard Test Method for Resistance of Coarse Aggregate to Degradation by Abrasion in the Micro-Deval Apparatus." *Annual book of ASTM standards, ASTM 6928-10*, West Conshohocken, PA.
- ASTM. (2013). "Standard Test Method for Measurement of Hydraulic Conductivity of Porous Material Using a Rigid-Wall, Compaction-Mold Permeameter." *Annual book of ASTM standards, ASTM 6951-09*, West Conshohocken, PA.
- Azadegan, O., Yaghoubi, E., and Li, J. (2013). "Evaluation of the performance of lime and cement treated base layers in unpaved roads." *Electronic Journal of Geotechnical Engineering*, 18(D), 647-660.
- Bahador, M., Evans, T. M., and Gabr, M. A. (2013). "Modeling effect of geocomposite drainage layers on moisture distribution and plastic deformation of road sections." *Journal of Geotechnical and Geoenvironmental Engineering*, 139(9), 1407-1418.
- Barnes, A. G. (1997). "Pavement thickness design using reclaimed hydrated Iowa class C fly ash as a base material." Master of Science Thesis, Iowa State University, Ames, Iowa
- Berg, K. C. (1998). "Durability and strength of activated reclaimed Iowa Class C fly ash aggregate in road bases." M.S. Thesis, Department of Civil Engineering, Iowa State University, Ames, IA.
- Bergeson, K. L., and Barnes, A. G. (1998). *Iowa thickness design guide for low volume roads using reclaimed Class C fly ash bases*. Iowa State University, Ames, IA.
- Bergeson, K. L., Waddingham, J. W., Brocka, S. G., and Lapke, R. K. (1995). *Bentonite treatment for economical dust reduction on limestone surface secondary roads*. HR-351, Iowa Department of Transportation, Ames, IA.
- Bergeson, K. L., and Wahbeh, A. M. (1990). *Development of an Economic Dust Palliative for Limestone Surfaced Secondary Roads*. HR-297, Iowa Department of Transportation, Ames, IA, 64.
- Berthelot, C., and Carpentier, A. (2003). "Gravel loss characterization and innovative preservation treatments of gravel roads: Saskatchewan, Canada." *Eighth International Conference on Low-Volume Roads 2003, June 22, 2003 - June 25, 2003*, National Research Council, Reno, NV, 180-184.
- Boussinesq, J. (1885). *Application des potentiels à l'étude de l'équilibre et du mouvement des solides élastiques: principalement au calcul des déformations et des pressions que produisent, dans ces solides, des efforts quelconques exercés sur une petite partie de leur surface ou de leur intérieur: mémoire suivi de notes étendues sur divers points de physique, mathématique et d'analyse*, Gauthier-Villars.
- Bushman, W. H., Freeman, T. E., and Hoppe, E. J. (2005). "Stabilization techniques for unpaved roads." *Transportation Research Record: Journal of the Transportation Research Board*, No. 1936, TRB, Washington, DC, pp. 28-33.
- Christopher, B. R., Hayden, S. A., and Zhao, A. (2000). "Roadway base and subgrade geocomposite drainage layers." *The Symposium of 'Testing and Performance of Geosynthetics in Subsurface Drainage', June 29, 1999 - June 29, 1999*, ASTM, Seattle, WA, 35-51.
- Crovetti, J. A., Shahin, M. Y., and Touma, B. E. (1989). "Comparison of two falling weight deflectometer devices, Dynatest 8000 and KUAB 2M-FWD." *First International Symposium on Nondestructive Testing of Pavements and Backcalculation of Moduli*, A. J. Bush, and G. Y. Baladi, eds., ASTM, Baltimore, MD, 59-69.
- Dempsey, B. J., and Thompson, M. R. (1973). "Vacuum Saturation Method for Predicting

- Freeze-Thaw Durability of Stabilized Materials." *52nd Annual Meeting of the Highway Research Board*, Highway Research Record, Washington, DC, 44-57.
- ERI (2009). *ERI Data Analysis User's Guide*. Engineering & Research International, Inc., Savoy, Illinois.
- Freeman, E. A. (2006). "Geotextile separators for dust suppression on gravel roads." Master of Science, University of Missouri--Columbia, Columbia, MO.
- Giroud, J. P., and Han, J. (2004a). "Design Method for Geogrid-Reinforced Unpaved Roads. I. Development of Design Method." *Journal of Geotechnical and Geoenvironmental Engineering*, 130(8), 775-786.
- Giroud, J. P., and Han, J. (2004b). "Design method for geogrid-reinforced unpaved roads. II. Calibration and applications." *Journal of Geotechnical and Geoenvironmental Engineering*, 130(8), 787-797.
- Henry, K. S. (1990). *Laboratory investigation of the use of geotextiles to mitigate frost heave*. U.S. Army Cold Regions Research and Engineering Laboratory, Washington, DC., 36.
- Henry, K. S. (1996). "Geotextiles to mitigate frost effects in soils: a critical review." *Transportation Research Record: Journal of the Transportation Research Board*, No. 1534, TRB, Washington, DC, 8-11.
- Henry, K. S., and Holtz, R. D. (2001). "Geocomposite capillary barriers to reduce frost heave in soils." *Canadian Geotechnical Journal*, 38(4), 678-694.
- Henry, K. S., Olson, J. P., Farrington, S. P., and Lens, J. (2005). *Improved performance of unpaved roads during spring thaw*. Engineer Research and Development Center Cold Regions Research and Engineering Laboratory, Hanover, NH, 179.
- Holtz, R. D., Christopher, B. R., and Berg, R. R. (2008). *Geosynthetic Design and Construction Guidelines*. FHWA-NHI-07-092, National Highway Institute, FHWA, U.S. DOT, Washington, DC.
- Hoover, J. M. (1973). *Surface improvements and dust palliation of unpaved secondary roads and streets*. Iowa Highway Research Board Project HR-151, Engineering Research Institute, Iowa State University, Ames, IA.
- Hoover, J. M., Pitt, J. M., Handfelt, L. D., and Stanley, R. L. (1981). "Performance of soil-aggregate-fabric systems in frost-susceptible roads, Linn County, Iowa." *Transportation Research Record: Journal of the Transportation Research Board*, No. 827, 6-14.
- Iowa DOT (2012). "Standard Specifications for Highway and Bridge Construction." Iowa Department of Transportation, Ames, IA.
- Jobgen, M. C., Tymkowicz, S., Harris, G., and Callahan, M. (1994). *Low cost techniques of base stabilization*. Project HR-312, Iowa Department of Transportation, Ames, IA., 40.
- Johnson, A. (2012). "Freeze-thaw performance of pavement foundation materials." M.S. Thesis, Dept. of Civil Construction and Environmental Engineering, Iowa State University, Ames, IA.
- Jones, D. (2003). "Toward fit-for-purpose certification of road additives." *Proc., Eight International Conference on Low-Volume Roads 2003, June 22, 2003 - June 25, 2003*, National Research Council, 208-217.
- Jones, D., and Surdahl, R. (2014). "New procedure for selecting chemical treatments for unpaved roads." *Transportation Research Record: Journal of the Transportation Research Board*, 2433(1), 87-99.
- Kestler, M. A. (2003). "Techniques for Extending the Life of Low-Volume Roads in Seasonal Frost Areas." *Proc., Eight International Conference on Low-Volume Roads 2003*,

- National Research Council, 275-284.
- Lai, Y., Zhang, S., and Yu, W. (2012). "A new structure to control frost boiling and frost heave of embankments in cold regions." *Cold Regions Science and Technology*, 79-80, 53-66.
- Less, R. A., and Paulson, C. K. (1977). *Experimental macadam stone base-Des Moines County*. Ames, IA.
- Lin, S. (2014). "Advancements in active surface wave methods: modeling, testing, and inversion." Doctor of Philosophy, Iowa State University, Ames, IA.
- Lin, S., and Ashlock, J. C. (2011). "A Study on issues relating to testing of soils and pavements by surface wave methods." *38th Annual Review of Progress in Quantitative Nondestructive Evaluation (QNDE 2011)* Burlington, VT, 1532-1539 (2012).
- Lynam, D., and Jones, K. (1979). *Pavement surfaced on macadam base-Adair County*. IHRB Project HR-209. Ames, IA.
- Lytton, R. L. (1989). "Backcalculation of pavement layers properties." *First International Symposium on Nondestructive Testing of Pavements and Backcalculation of Moduli*, A. J. Bush, and G. Y. Baladi, eds., ASTM, Baltimore, MD, p. 7-38.
- Odemark, N. (1949). "Investigations as to the elastic properties of soils and design of pavements according to the theory of elasticity." Statens Vaginstitut, Stockholm, Sweden.
- Park, C. B., Ivanov, J., Miller, R. D., Xia, J., and Ryden, N. (2001). "Seismic investigation of pavements by MASW method—geophone approach." *Proc., SAGEEP 2001, Denver, Colorado*.
- Park, C. B., Miller, R. D., and Xia, J. (1999). "Multichannel analysis of surface waves." *Geophysics*, 64(3), 800-808.
- Parsons, R. L., and Milburn, J. P. (2003). "Engineering Behavior of Stabilized Soils." *Transportation Research Record: Journal of the Transportation Research Board*, No. 1837, 20-29.
- Saarenketo, T., and Aho, S. (2005). *Managing Spring Thaw Weakening on Low Volume Roads: Problem description, load restriction, policies, monitoring and rehabilitation*. ROADX II, Northern Periphery, Inverness, Scotland.
- Shoop, S., Kestler, M., Stark, J., Ryerson, C., and Affleck, R. (2003). "Rapid stabilization of thawing soils: field experience and application." *Journal of Terramechanics*, 39(4), 181-194.
- Solanki, P., Zaman, M., and Khalife, R. (2013). "Effect of freeze-thaw cycles on performance of stabilized subgrade." *Sound Geotechnical Research to Practice: Honoring Robert D. Holtz II, Geotechnical Special Publication (GSP) No. 230*, R. D. Holtz, A. W. Stuedlein, and B. R. Christopher, eds., ASCE, Reston, VA, 567-581.
- Stormont, J. C., Ramos, R., and Henry, K. S. (2001). "Geocomposite capillary barrier drain systems with fiberglass transport layer." *Transportation Research Record: Journal of the Transportation Research Board*, No. 1772, 131-136.
- SUDAS (2015). *Design Manual Chapter 6 – Geotechnical, 6E-1 – Subgrade Design and Construction*, 2013 Edition, Statewide Urban Design and Specifications (SUDAS), Institute of Transportation, Iowa State University, Ames, IA.
- Ullidtz, P. (1987). *Pavement Analysis. Developments in Civil Engineering*, Elsevier, New York, NY.
- White, D., and Vennapusa, P. (2013). *Low-Cost Rural Surface Alternatives: Literature Review and Recommendations*. Center for Earthworks Engineering, Iowa State University, Ames, IA, 302p.

- White, D. J., Harrington, D., Ceylan, H., and Rupnow, T. (2005b). *Fly Ash Soil Stabilization for Non-Uniform Subgrade Soils, Volume II: Influence of Subgrade Non-Uniformity on PCC Pavement Performance*. IHRB Project TR-461, FHWA Project 4, Center for Transportation Research and Education, Iowa State University, Ames, IA.
- White, D. J., Harrington, D., and Thomas, Z. (2005a). *Fly Ash Soil Stabilization for Non-Uniform Subgrade Soils, Volume I: Engineering Properties and Construction Guidelines*. IHRB Project TR-461, FHWA Project 4, Center for Transportation Research and Education, Iowa State University, Ames, IA.
- White, D. J., Vennapusa, P., and Zhao, L. (2014). "Verification and repeatability analysis for the in situ air permeameter test." *Geotechnical Testing Journal*, 37(2).
- White, D. J., Vennapusa, P. K. R., Suleiman, M. T., and Dahren, C. T. (2007). "An in-situ device for rapid determination of permeability for granular bases." *Geotechnical Testing Journal*, 30(4), 282-291.
- Winterkorn, H., and Pamukcu, S. (1991). "Soil stabilization and grouting." *Foundation Engineering Handbook*, H.-Y. Fang, ed., Springer US, 317-378.

HEADWATERS		CB- 013540
RESOURCES		
17690 Applewood Road • Council Bluffs, IA 51503		COUNCIL BLUFFS <input type="checkbox"/> 1 <input type="checkbox"/> 2 <input type="checkbox"/> 3
1-800-537-7098		
DATE <u>10-7-14</u>	The material herein described has been sampled and tested as prescribed by the following agencies: Iowa DOT, SD-DOT, N-DOR and MINN-DOT. It complies with applicable specification requirements of Class C fly ash as defined in ASTM C618 and the above agencies.	
CUSTOMER'S NAME <u>Maple</u>	PROJECT NO. _____	
ADDRESS <u>Elkworth</u>	Signed _____ LOI = _____	
COMMODITY <u>Fly Ash Soil</u>	FINENESS = _____	
CARRIER <u>CPH</u>	LBS. GROSS _____	
	LBS. TARE - DRIVER ON _____ OFF _____	
	LBS. NET @ _____ PER LB. PRICE _____	
	SHIPPER <u>Maple</u>	
	WEIGHER _____	
WEIGHED ON A FAIRBANKS SCALE		

Figure 112. Receipt for class C fly ash used on Section 16



ORIGINAL

Lafarge North America Inc.

SEE OTHER CONDITIONS ON THE BACK

Received subject to the terms of any written transportation contract between the Carrier(s) transporting this shipment and Lafarge North America or its affiliates (Shipper) on the date of issue of this Bill of Lading the property described hereon, in apparent good order, except as noted, marked, consigned and destined as set forth hereon, which said Carrier(s) agrees to carry with reasonable dispatch to such destination. Carrier(s) shall verify the weight of the shipment and Carrier(s) agree to indemnify Shipper from any loss, cost or expense (including, but not limited to, attorney's fees) arising from or relating to the transportation of a load that exceeds the maximum allowable weight. Consignee accepts such shipment in accordance with Lafarge's standard terms and conditions. Page 1 of 1
NON-RECOURSE: If Shipper signs this provision, Shipper shall not be liable for freight charges and Carrier shall not deliver this shipment without advance payment of all shipping and related charges.

Signature of Shipper: _____

Branch/Plant :
66524
WEST DES MOINES TERMINAL
276 S 11TH ST
WEST DES MOINES IA 50265
(515) 225-7171

Shipped To :
281854
MANATTS INC
3435 ADVENTURLAND DR
ALTOONA IA 50009
()

BOL No.	5683706
Load No.	
Sales Order No.	48021509
Shipment No.	36368657
Shipment Date	09/30/14
Customer Requested Delivery Date	09/30/14
Customer Requested Delivery Time (ET)	00:00:00



Pallets Returned	
-------------------------	--

Sold To		Customer Purchase Order No.						
MANATTS INC								
Item Description	Item No.	Begin/End	Silo	Bags or Gross LB	PLT	Bag Wgt or Tare LB	Net LB	Total TS
TYPE I/II - LOW ALKALI	6L100007501	09:40 09:44	30	49,240		28,480	20,760	10,380
				6L100007501				
				49240 28480 20760 10380				
				71700 26780 44920 22400				
BULK	B_MIN_CHRG	FUEL-B	Total US	49,240	28,480	20,760	10,380	
STANDARD			Total CA					
Additional Sales Order No. - If Applicable								

Special Delivery Instructions :

Mode	Carrier Full Name	Carrier Code	Tractor/Rail Car	Trailer 1	Trailer 2
10	CUSTOMER PICKUP	99999	266406MANA	274614MANA	
Rail Route Description		Transportation Contract	Trailer 1 Seal No.	Trailer 2 Seal No.	

State Stamp :

The material here in described has been manufactured in the USA from domestically produced raw materials & has been tested as prescribed by the IA DOT & complies with applicable specification requirements for Type I/II Cement. This cement was produced at Buffalo IA, PC0502.

Collect

Shipper Signature/ Date

Driver Signature / Date

Customer Signature / Date

WARNING: Corrosive - May cause severe eye and skin burns. Toxic - May cause lung disease. Read Material Safety Data Sheet (MSDS) **CUSTOMER**

Figure 113. Receipt for type I/II cement used on Section 17

Mirafi[®] 160N

Mirafi[®] 160N is a nonwoven geotextile composed of polypropylene fibers, which are formed into a stable network such that the fibers retain their relative position. Mirafi geotextile is inert to biological degradation and resists naturally encountered chemicals, alkalis, and acids.

Mechanical Properties	Test Method	Unit	Minimum Average Roll Value	
			MD	CS
Grab Tensile Strength	ASTM D 4632	N (lbs)	712 (160)	712
Grab Tensile Elongation	ASTM D 4632	%	50	50
Trapezoid Tear Strength	ASTM D 4533	N (lbs)	267 (60)	267
Mullen Burst Strength	ASTM D 3786	kPa (psi)	2101 (305)	2101
Puncture Strength ¹	ASTM D 4833	N (lbs)	423 (95)	423
CBR Puncture Strength	ASTM D 6241	N (lbs)	1780 (400)	1780
Apparent Opening Size (AOS) ²	ASTM D 4751	mm (U.S. Sieve)	0.212 (70)	0.212
Permittivity	ASTM D 4491	sec ⁻¹	1.4	1.4
Flow Rate	ASTM D 4491	l/min/m ² (gal/min/ft ²)	4481 (110)	4481
UV Resistance (at 500 hours)	ASTM D 4355	% strength retained	70	70

¹ ASTM D 4833 has been replaced with ASTM D 6241

² ASTM D 4751: AOS is a Maximum Opening Diameter Value

Physical Properties	Test Method	Unit	Typical Value
Weight	ASTM D 5261	g/m ² (oz/yd ²)	220 (6.5)
Thickness	ASTM D 5199	mm (mils)	1.7 (65)
Roll Dimensions (width x length)	--	m (ft)	4.5 x 91 (15 x 300)
Roll Area	--	m ² (yd ²)	418 (500)
Estimated Roll Weight	--	kg (lb)	97 (215)

Disclaimer: TenCate assumes no liability for the accuracy or completeness of this information or for the ultimate performance of the product under any conditions of use. TenCate disclaims any and all express, implied, or statutory standards, warranties or guarantees, including without limitation any implied warranty as to merchantability or fitness for a particular purpose or arising from a course of dealing or usage of trade as to any equipment, materials, or information furnished herewith. This disclaimer should not be construed as engineering advice.

Figure 114. Product datasheet for NW-geotextile used on Sections 3, 4, 5, 8, and 19A

Mirafi® BXG110



Mirafi® BXG110 geogrid is composed of polypropylene resin which is extruded into a structure. Mirafi® BXG110 is inert to biological degradation and resistant to natural encountered chemicals, alkalis, and acids.

TenCate Geosynthetics Americas Laboratories are accredited by a2La (The American Association for Laboratory Accreditation) and Geosynthetic Accreditation Institute – Laboratory Accreditation Program (GAI-LAP).

Mechanical Properties	Test Method	Unit	Minimum Average Roll Value	
			MD	CD
Tensile Strength (at ultimate) ¹	ASTM D6637	lbs/ft (kN/m)	850 (12.4)	1300 (19.0)
Tensile Strength (at 2% strain)	ASTM D6637	lbs/ft (kN/m)	280 (4.1)	450 (6.6)
Tensile Strength (at 5% strain)	ASTM D6637	lbs/ft (kN/m)	580 (8.5)	920 (13.4)
Junction Efficiency ²		%	93	
Flexural Stiffness ³		mg-cm	250,000	
Aperture Stability ⁴		m-N/deg	0.32	
Resistance to Installation Damage ⁵		% SC/%SW/%GP	95 / 93/ 90	
Resistance to Long Term Degradation ⁶		%	100	
Resistance to UV Degradation ⁷		%	100	

¹ True resistance to elongation when initially subjected to a load determined in accordance with ASTM D6637 without deforming test mats under load before measuring such resistance or employing "secant" or "offset" tangent methods of measurement so as to overstate test properties.

² Load transfer capability expressed as a percentage of ultimate tensile strength.

³ Resistance to bending force determined in accordance with ASTM D5732, using specimens of width two ribs wide, with transverse ribs flush with exterior edges of longitudinal ribs (as a "ladder"), and of length sufficiently long to enable measurement of the overhanging dimension. The overall Flexural Stiffness is calculated as the square root of the product of MD and CD Flexural Stiffness values.

⁴ Resistance to in-plane rotational movement measured by applying a 20 kg-cm (2 m-N) moment to the central junction of a 9 inch x 9 specimen restrained at its perimeter in accordance with U.S. Army Corps of Engineers Methodology for measurement of Torsional Rigidity.

⁵ Resistance to loss of load capacity or structural integrity when subjected to mechanical installation stress in clayey sand (SC), well graded sand (SW), and crushed stone classified as poorly graded gravel (GP). The geogrid shall be sampled in accordance with ASTM D6818. Load capacity shall be determined in accordance with ASTM D6637.

⁶ Resistance to loss of load capacity or structural integrity when subjected to chemically aggressive environments in accordance with 9000 immersion testing.

⁷ Tested according to ASTM D4355.

Physical Properties	Unit	Typical Value	
Rib Thickness	in (mm)	0.03 (0.76)	0.03 (0.76)
Grid Aperture Size (MD)	in (mm)	1.0 (25.4)	
Grid Aperture Size (CMD)	in (mm)	1.3 (33.0)	
Roll Dimensions (width x length)	ft (m)	13 x 246 (4 x 75)	
Roll Area	yd ² (m ²)	355 (300)	

Junction Efficiency, Flexural Stiffness, Aperture Stability, Resistance to Installation Damage, Resistance to Long Term Degradation, Resistance to UV Degradation, Rib Thickness and Grid Aperture Size is not covered by our current A2LA accreditation.

Disclaimer: TenCate assumes no liability for the accuracy or completeness of this information or for the ultimate use by the purchaser. TenCate disclaims any all express, implied, or statutory standards, warranties or guarantees, including without limitation any implied warranty as to merchantability or fitness for a particular purpose or arising from a course of dealing or usage of trade as to any equipment, materials, or information furnished hereunder. This document should be construed as engineering advice.



Mirafi® is a registered trademark of Nicolon Corporation.

Copyright © 2014 Nicolon Corporation. All Rights Reserved.

385 South Holland Drive
Pendergrass, GA 30067
EGS000/13
ETOR6

Tel: 706 693 2226
Tel: 888 295 1818

Fax 706 693 4400
www.tencate.com



GAI-LAP-25-57

Testing Lab 1291.01 & 12

Figure 115. Product datasheet for BX-geogrid used on Sections 19A and 19B

MACDRAIN™ W 1051 DRAINAGE COMPOSITE

Geocomposite for planar drainage (GCD), realized by thermobonding a draining core in extruded monofilaments (GMA) with two filtering nonwoven geotextiles that may also be working as separation or protecting layers. The draining three dimensional core will have a "W" configuration as longitudinal parallel channels.

GEOCOMPOSITE (GCO)	Standard	Unit	Value		
Thickness at 40 psf (2 kPa)	ASTM D 5199	mils (mm)	197	5	(1)
Mass per unit area	ASTM D 5261	oz/y ² (g/m ²)	18	610	(1)
Tensile strength MD	ASTM D 5035	lbs/ft (kN/m)	12.500	17	(2)
Transmissivity MD	ASTM D 4716	m ² /s			(2)
Rigid/Soft contact	gradient i =	0.10	0.30	1.0	
	500 psf (20 kPa)	2.1x10 ⁻³	1.3x10 ⁻²	1.2x10 ⁻³	
	1000 psf (50 kPa)	1.6x10 ⁻³	1.1x10 ⁻²	1.0x10 ⁻³	
	2100 psf (100 kPa)	1.5x10 ⁻³	0.9x10 ⁻²	0.7x10 ⁻³	
	4150 psf (200 kPa)	6.0x10 ⁻⁴	7.0x10 ⁻⁴	0.6x10 ⁻³	

EXTERNAL FILTERS (GTX-N)

Structure: nonwoven geotextiles in compliance with class 3 AASHTO M288 designation

Raw Material: UV stabilized polyolefin

Mass per unit area	ASTM D 5261	oz/y ² (g/m ²)	3.4	115	(1)
Grab strength	ASTM D4632	lbs (N)	124	550	(3)
Grab elongation	ASTM D4632	%	50	50	(3)
Trapezoidal tear strength	ASTM D 4533	lbs (N)	67	300	(3)
Static puncture resistance	ASTM D 6241	lbs (N)	280	1250	(2)
Puncture resistance	ASTM 4833	lbs (N)	45	200	(3)
Flux perpendicular to the plane	ASTM 4491	gpm/ft ² (l/m ² min)	100	4100	(3)
Characteristic opening size O ₉₅	ASTM D 4751	US Sieve (micron)	70	80	(3)

DRAINAGE CORE (GMA)

Structure: three dimensional geomat made by extruded monofilaments set in longitudinal parallel channel configuration

Raw Material: polypropylene UV stabilized by carbon black

Mass per unit area	ASTM D 5261	oz/y ² (g/m ²)	11.2	380	(1)
--------------------	-------------	---------------------------------------	------	-----	-----

(1) Typical value

(2) Minimum Average Value defined as mean value minus one standard deviation and it's the value which is exceeded by 95% of the all test data; transmissivity is measured using water at 21±2°C (70 ±4°F) at the indicated gradient and confining pressure between a rigid plate (to simulate an hard contact surface like concrete walls, geomembrane or similar) and a smooth plate (to simulate a soft contact like soil or similar).

(3) Minimum Average Value defined as mean value minus one standard deviation and it's the value which is exceeded by 97.5% of the all test data.

MD: Longitudinal direction

CMD: Transversal direction

The producer, for his optimisation and improving process of the product's technical characteristics, has the faculty to modify the standards and the characteristics of the product without any pre-advise. All the information are given in base to our experience and is not intended as a warranty or guarantee; in any case no liability in connection with the use of these information could be referred to the producer or one of his distributors.

© 2014 Maccaferri. All rights reserved. Maccaferri will enforce Copyright.

Maccaferri, Inc.
10303 Governor Lane Blvd., Williamsport, MD 21795
Tel. (800) 638-7744 - Fax (301) 223-4590
E-mail: info@Maccaferri-usa.com - Web site: www.maccaferri-usa.com

Area Offices:
Phoenix, Arizona
Sacramento, California
Miami, Florida
St. Louis, Missouri

Trenton, New Jersey
Albuquerque, New Mexico
Caguas, Puerto Rico
Dallas/Ft. Worth, Texas



Figure 116. Product datasheet for NW-geotextile used on Sections 3, 4, 5, 8, and 19A

MACDRAIN™ W 1091 DRAINAGE COMPOSITE

Geocomposite for planar drainage (GCD), realized by thermobonding a draining core in extruded monofilaments (GMA) with two filtering nonwoven geotextiles that may also be working as separation or protecting layers. The draining three dimensional core will have a "W" configuration as longitudinal parallel channels.

GEOCOMPOSITE (GCO)	Standard	Unit	Value		
Thickness at 40 psf (2 kPa)	ASTM D 5199	mils (mm)	354	9	(1)
Mass per unit area	ASTM D 5261	oz/y ² (g/m ²)	29.2	980	(1)
Tensile strength MD	ASTM D 5035	lbs/ft (kN/m)	12.500	17	(2)
Transmissivity MD	ASTM D 4716	m ² /s			(2)
Rigid/Soft contact	gradient i =	0.03	0.10	0.30	
	1000 psf (50 kPa)	1.2x10 ⁻²	6.2x10 ⁻³	4.3x10 ⁻³	
	2100 psf (100 kPa)	1.0x10 ⁻²	4.6x10 ⁻³	4.0x10 ⁻³	
	4150 psf (200 kPa)	8.5x10 ⁻³	4.0x10 ⁻³	2.8x10 ⁻³	
	10000 psf (480 kPa)	4.0x10 ⁻³	2.7x10 ⁻³	1.2x10 ⁻³	

EXTERNAL FILTERS (GTX-N)

Structure: nonwoven geotextiles in compliance with class 3 AASHTO M288 designation

Raw Material: UV stabilized polyolefin

Mass per unit area	ASTM D 5261	oz/y ² (g/m ²)	3.4	115	(1)
Grab strength	ASTM D4632	lbs (N)	124	550	(3)
Grab elongation	ASTM D4632	%	50	50	(3)
Trapezoidal tear strength	ASTM D 4533	lbs (N)	67	300	(3)
Static puncture resistance	ASTM D 6241	lbs (N)	280	1250	(2)
Puncture resistance	ASTM 4833	lbs (N)	45	200	(3)
Flux perpendicular to the plane	ASTM 4491	gpm/ft ² (l/m ² min)	100	4100	(3)
Characteristic opening size O ₉₅	ASTM D 4751	US Sieve (micron)	70	80	(3)

DRAINAGE CORE (GMA)

Structure: three dimensional geomat made by extruded monofilaments set in longitudinal parallel channel configuration

Raw Material: polypropylene UV stabilized by carbon black

Mass per unit area	ASTM D 5261	oz/y ² (g/m ²)	22.4	760	(1)
--------------------	-------------	---------------------------------------	------	-----	-----

(1) Typical value

(2) Minimum Average Value defined as mean value minus one standard deviation and it's the value which is exceeded by 95% of the all test data; transmissivity is measured using water at 21±2°C (70 ±4°F) at the indicated gradient and confining pressure between a rigid plate (to simulate an hard contact surface like concrete walls, geomembrane or similar) and a smooth plate (to simulate a soft contact like soil or similar).

(3) Minimum Average Value defined as mean value minus one standard deviation and it's the value which is exceeded by 97.5% of the all test data.

MD: Longitudinal direction

CMD: Transversal direction



The producer, for his optimisation and improving process of the product's technical characteristics, has the faculty to modify the standards and the characteristics of the product without any pre-advise. All the information are given in base to our experience and is not intended as a warranty or guarantee; in any case no liability in connection with the use of these informations could be referred to the producer or one of his distributors.

© 2014 Maccaferri. All rights reserved. Maccaferri will enforce Copyright.

Maccaferri, Inc.
10303 Governor Lane Blvd., Williamsport, MD 21795
Tel. (800) 638-7744 - Fax (301) 223-4590
E-mail: info@Maccaferri-usa.com - Web site: www.maccaferri-usa.com

Area Offices:
Phoenix, Arizona
Sacramento, California
Miami, Florida
St. Louis, Missouri

Trenton, New Jersey
Albuquerque, New Mexico
Caguas, Puerto Rico
Dallas/Ft. Worth, Texas

Figure 117. Product datasheet for geocomposite used on Section 18



Roadway Drainage System

Specification Sheet – ROADRAIN 5 (RD-5)

ROADRAIN 5 is a Synthetic Subsurface Drainage Layer (SSDL) comprised of a tri-planar structure with thermally bonded 6 oz. nonwoven geotextiles on both sides. This product quickly removes subsurface water from pavement base and sub-base layers, while providing a void-maintaining system to work as a capillary break. ROADRAIN 5 also works as a separation layer. ROADRAIN 5 has properties conforming to the values and test methods listed below:

Property	Test Methods	Units	Value	Qualifier
Tri-Planar Core¹				
Density	ASTM D 792	g/cm ³	0.94 – 0.96	Range
Carbon Black	ASTM D 4218	%	2-3	Range
Rib Spacing (top & bottom)	Calipered	in. (mm)	0.4 (10)	Typical
Central Rib Spacing	Calipered	in. (mm)	0.5 (12.5)	Typical
Unsupported Aperture Area	Calipered	in. ² (mm ²)	0.3 (195)	MAX
Thickness	ASTM D 5199	mil (mm)	280 (7.1)	±10%
Nonwoven Geotextile¹				
Strength	AASHTO M 288		Exceeds Class 2	
U.V. Resistance (500 hrs)	ASTM D 4355	%	70	MARV
AOS	ASTM D 4751	US Std Sieve (mm)	70 (0.212)	MaxARV
Permittivity	ASTM D 4491	sec ⁻¹	1.4	MARV
Water Flow Rate	ASTM D 4491	gpm/ft ² (l/min/m ²)	110 (4481)	MARV
SSDL Performance				
Capillary Barrier	ASTM 5918		Effective	Notes ²
Coefficient of Permeability	ASTM D 4716	ft/day	56,700	Notes ³
Dimensions & Flow Orientation				
Roll Size			12.75 ft x 200 ft (3.89 m x 61 m)	
Direction of Primary Flow			Across the roll width @ approximately 45°	

Qualifiers: MARV = Minimum Average Roll Value (MARV), MAV = Minimum Average Value, MAX = Maximum Value, MaxARV = Maximum average roll value.

NOTES:

Geotextile and core properties listed are prior to lamination.

As tested by the USACE Cold Regions Research and Engineering Laboratory (CRREL).

Coefficient of permeability is calculated with the measured SSDL transmissivity and the nominal core thickness. SSDL transmissivity is tested along the primary flow direction with the boundary conditions as follows: steel plate/0.75 in. Ottawa sand/SSDL/0.75 in. Ottawa sand/steel plate, one hour seating period @ 5,000 psf and gradient 2%.



Tensar International Corporation
2500 Northwinds Parkway
Suite 500
Midvale, UT 84046

©2012, Tensar International Corporation. Certain products and/or applications described or illustrated herein are protected under one or more U.S. patents. Other U.S. patents are pending and certain foreign patents and patent applications may also exist. Trademark rights also apply as indicated herein. Final determination of the suitability of any information or material for the use

Figure 118. Product datasheet for geocomposite used on Section 12

APPENDIX B: HORIZONTAL PERMEAMETER TEST (HPT) SPECIMEN PREPARATION PROCEDURE



Figure 119. HPT soil tank set up: (a) place fine screen and screen support on top of inlet and outlet, (b, c, d, and e) place three screens with different opening sizes next to the screen support, (e) place specimen material in soil tank



Figure 120. HPT specimen compaction: (a) compact specimen in several lifts, (b) scarify surface after each compaction lift, and (c) place geocomposite at middle of specimen and seal gaps between geocomposite and soil tank using closed-cell foam

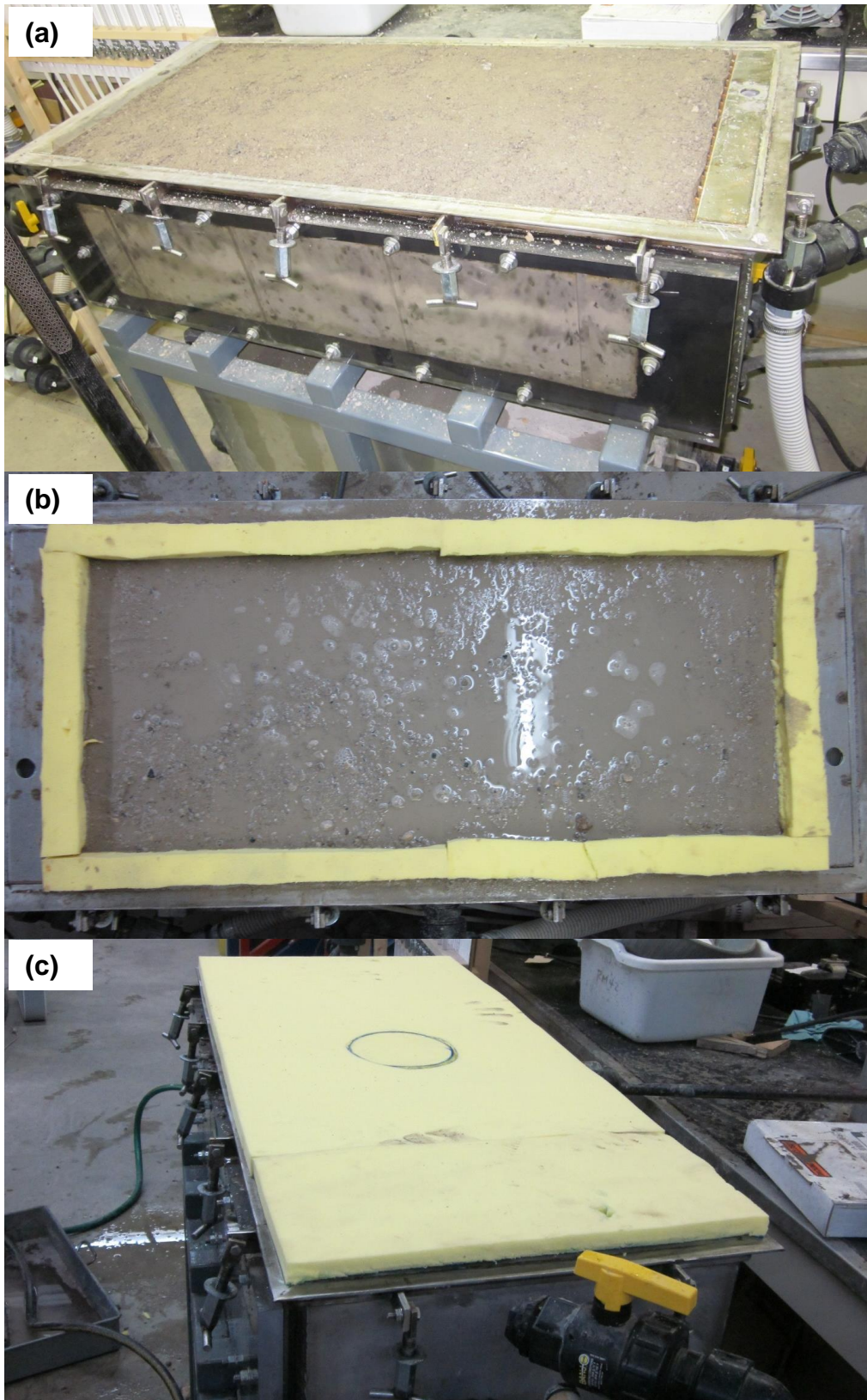


Figure 121. HPT specimen sealing: (a) level the specimen surface, (b) pre-soak specimen, and (c) seal top surface with closed-cell foam

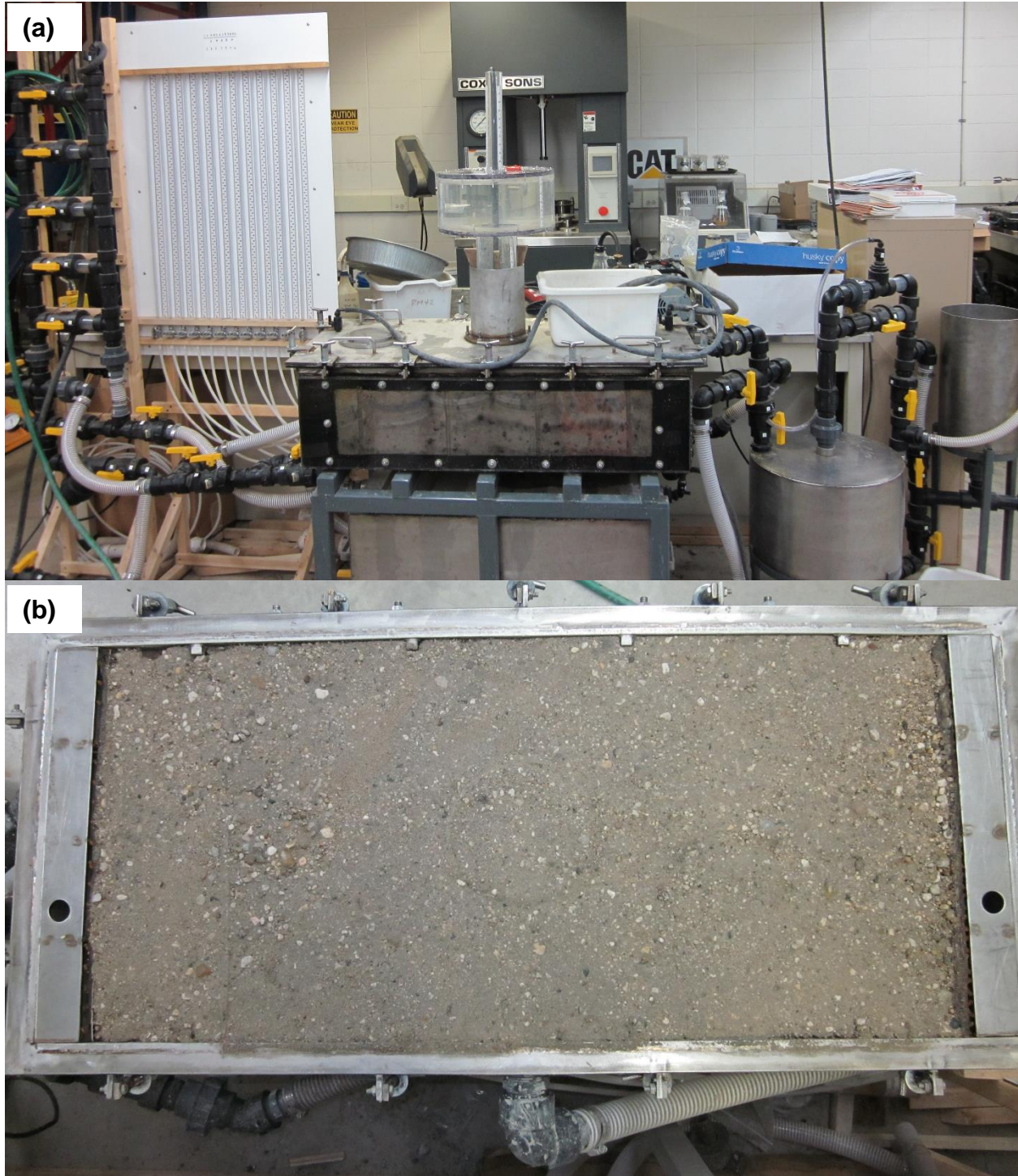


Figure 122. HPT specimen saturation and examination: (a) soak specimen using water supply placed on top of specimen, then vacuum saturate specimen, (b) examine specimen surface after test to check if water channeling occurred

APPENDIX C: SURVEY PHOTOS OF VAIL AVENUE DEMONSTRATION SECTIONS



Figure 123. Survey photos of Vail Avenue demonstration sections (March 8, 2014)



Figure 123. (continued). Survey photos of Vail Avenue demonstration sections (March 8, 2014)



Figure 123. (continued). Survey photos of Vail Avenue demonstration sections (March 8, 2014)



Figure 124. Survey photos of Vail Avenue demonstration sections (March 20, 2014)



Figure 124. (continued). Survey photos of Vail Avenue demonstration sections (March 20, 2014)



Figure 124. (continued). Survey photos of Vail Avenue demonstration sections (March 20, 2014)

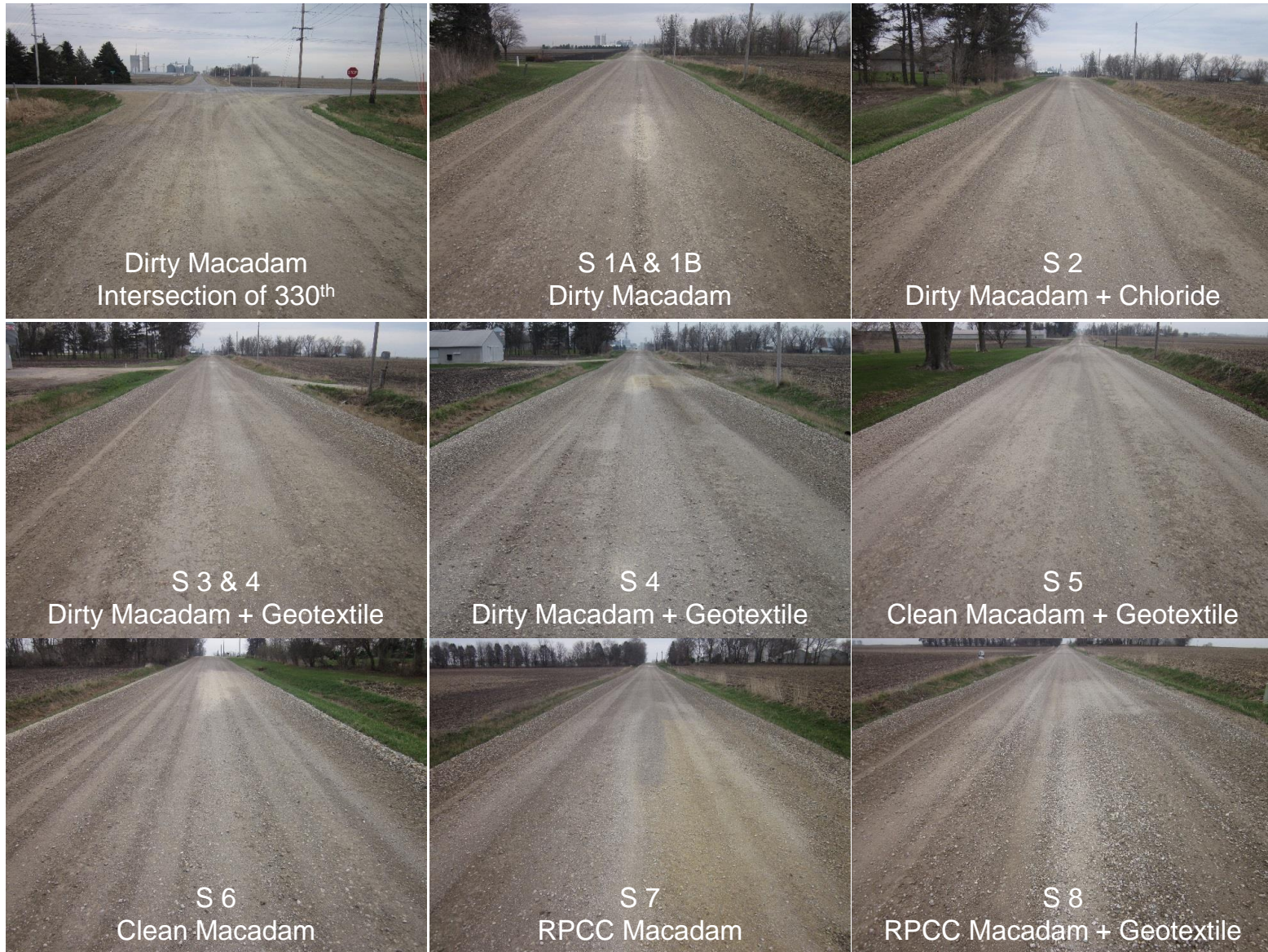


Figure 125. Survey photos of Vail Avenue demonstration sections (April 21, 2014)

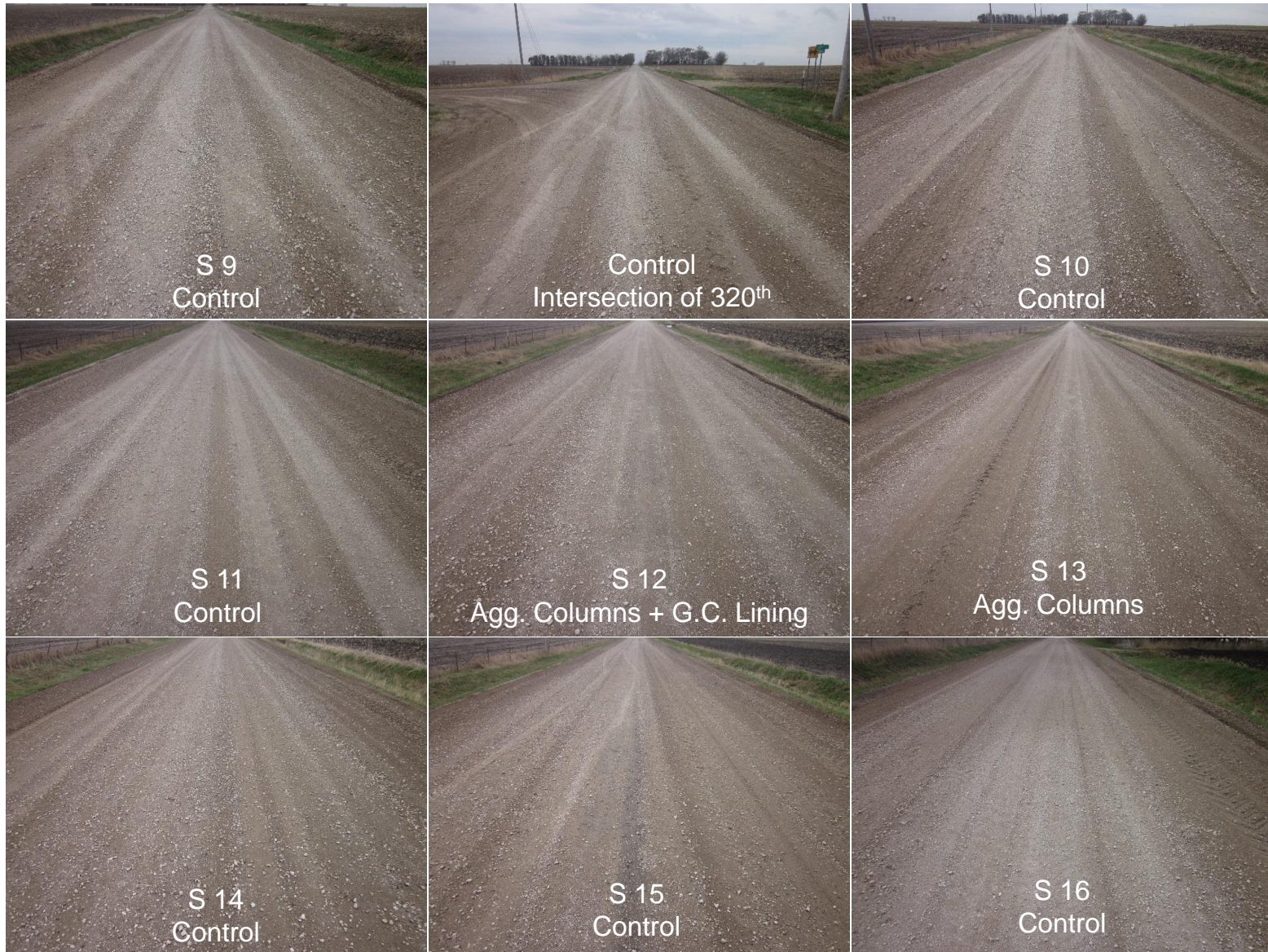


Figure 125. (continued). Survey photos of Vail Avenue demonstration sections (April 21, 2014)



Figure 125. (continued). Survey photos of Vail Avenue demonstration sections (April 21, 2014)



Figure 126. Survey photos of Vail Avenue demonstration sections (May 8, 2014)



Figure 126. (continued). Survey photos of Vail Avenue demonstration sections (May 8, 2014)



Figure 126. (continued). Survey photos of Vail Avenue demonstration sections (May 8, 2014)



Figure 127. Survey photos of Vail Avenue demonstration sections (June 6, 2014)



Figure 127. (continued). Survey photos of Vail Avenue demonstration sections (June 6, 2014)



Figure 127. (continued). Survey photos of Vail Avenue demonstration sections (June 6, 2014)



Figure 128. Survey photos of Vail Avenue demonstration sections (July 3, 2014)

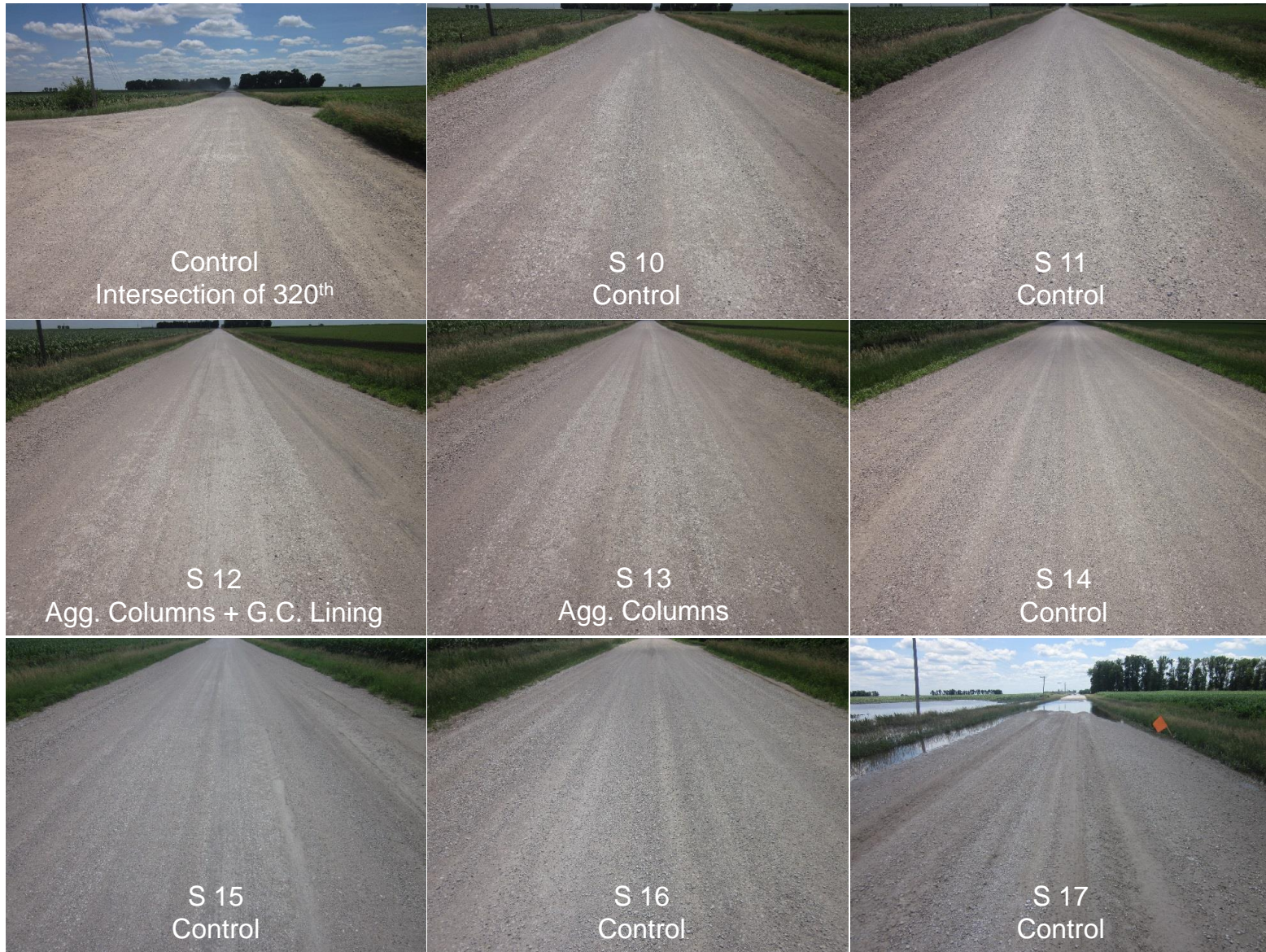


Figure 128. (continued). Survey photos of Vail Avenue demonstration sections (July 3, 2014)



Figure 128. (continued). Survey photos of Vail Avenue demonstration sections (July 3, 2014)



Figure 129. Survey photos of Vail Avenue demonstration sections (September 2, 2014)



Figure 129. (continued). Survey photos of Vail Avenue demonstration sections (September 2, 2014)



Figure 129. (continued). Survey photos of Vail Avenue demonstration sections (September 2, 2014)



Figure 130. Survey photos of Vail Avenue demonstration sections (January 20, 2015)



Figure 130. (continued). Survey photos of Vail Avenue demonstration sections (January 20, 2015)



Figure 130. (continued). Survey photos of Vail Avenue demonstration sections (January 20, 2015)

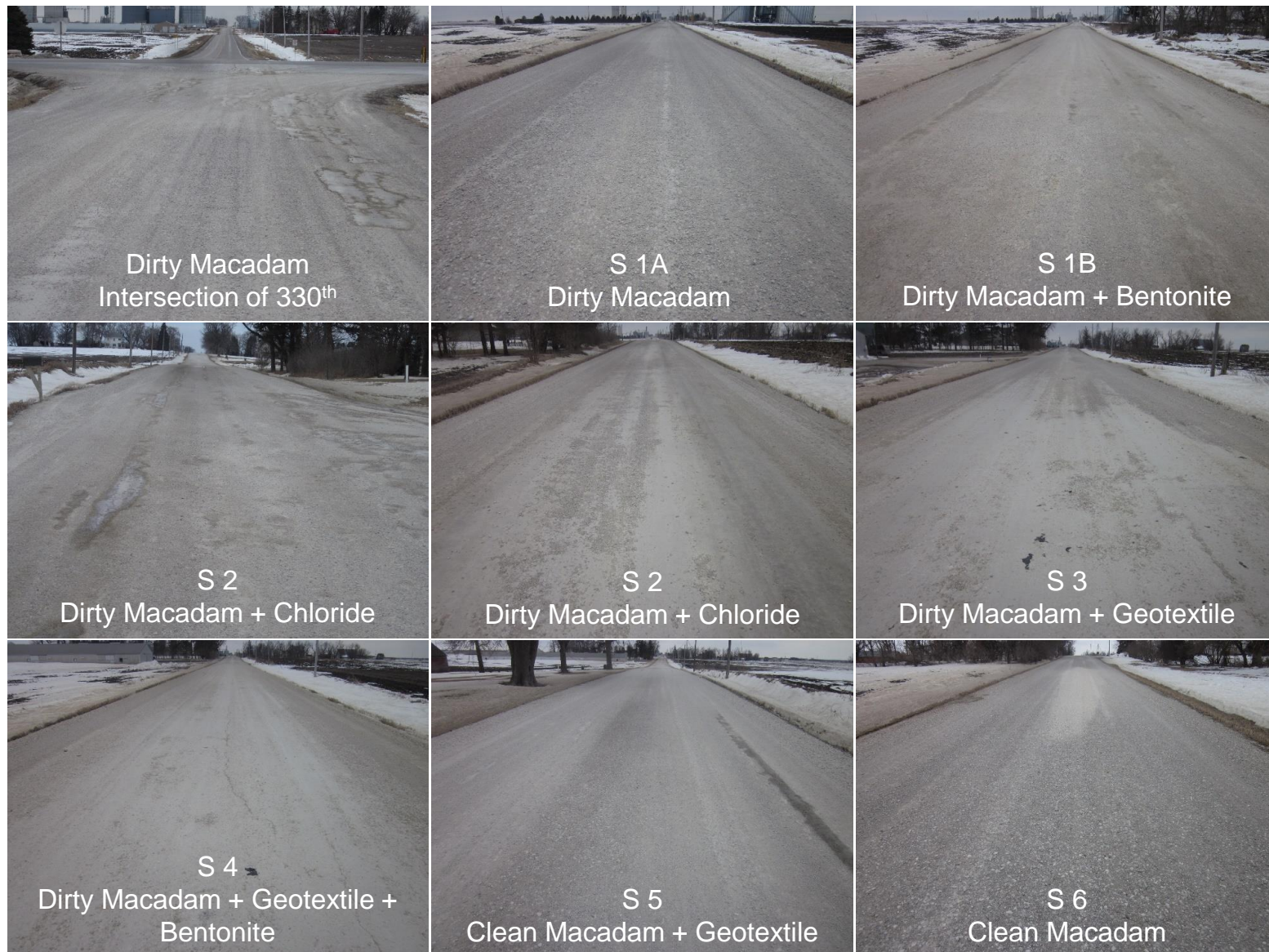


Figure 131. Survey photos of Vail Avenue demonstration sections (February 24, 2015)

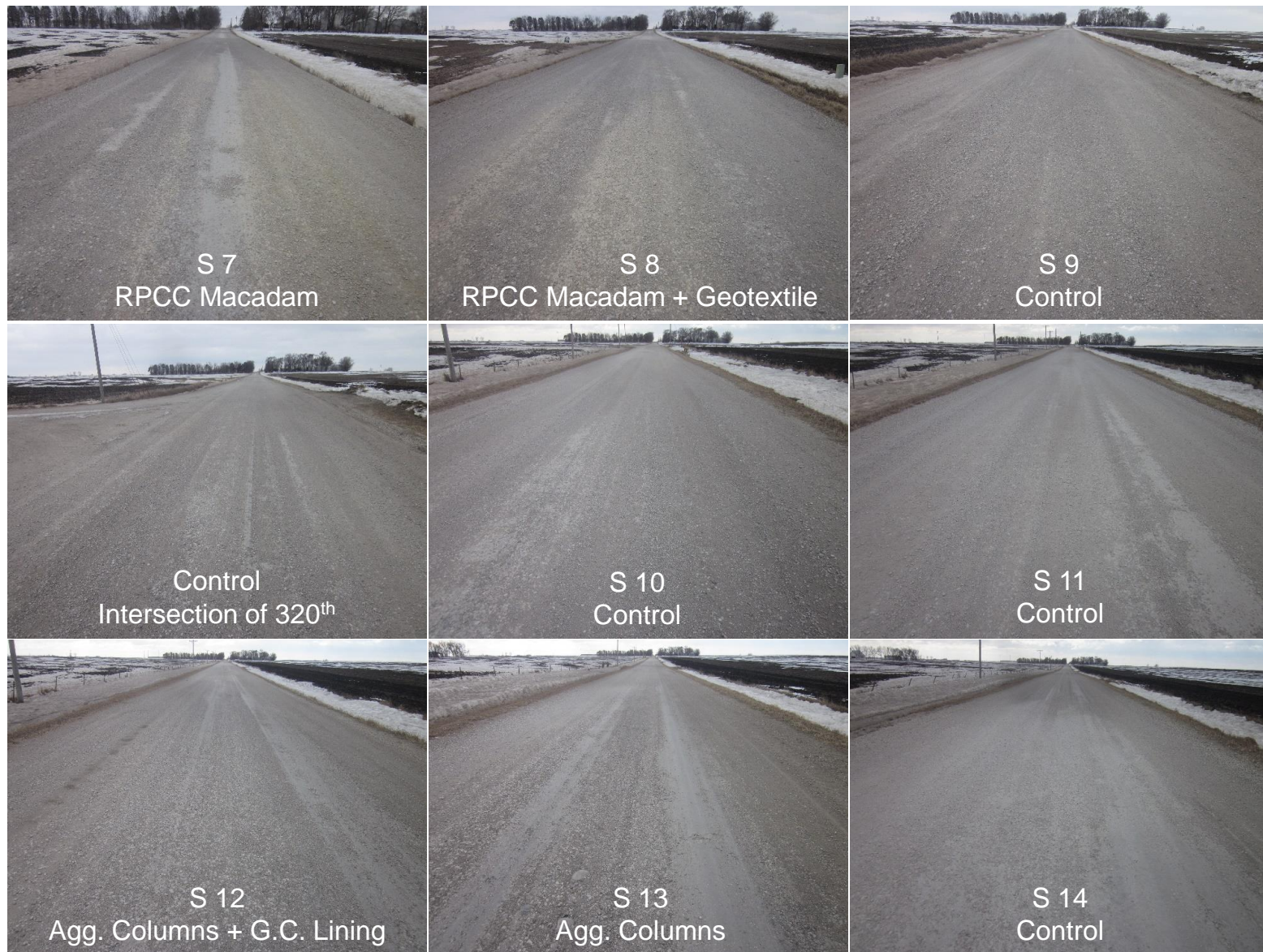


Figure 131. (continued). Survey photos of Vail Avenue demonstration sections (February 24, 2015)

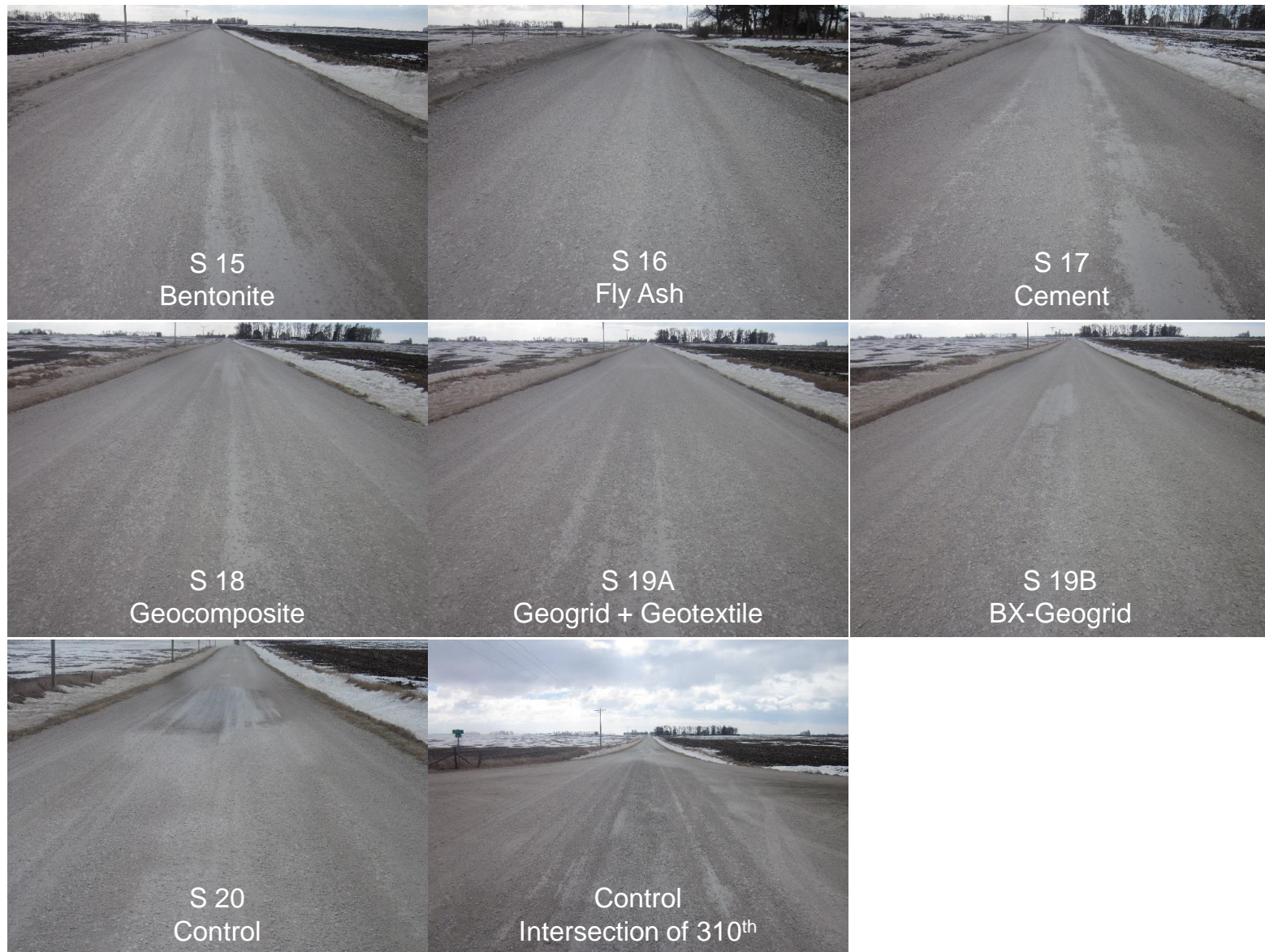


Figure 131. (continued). Survey photos of Vail Avenue demonstration sections (February 24, 2015)



Figure 132. Survey photos of Vail Avenue demonstration sections (March 10, 2015)

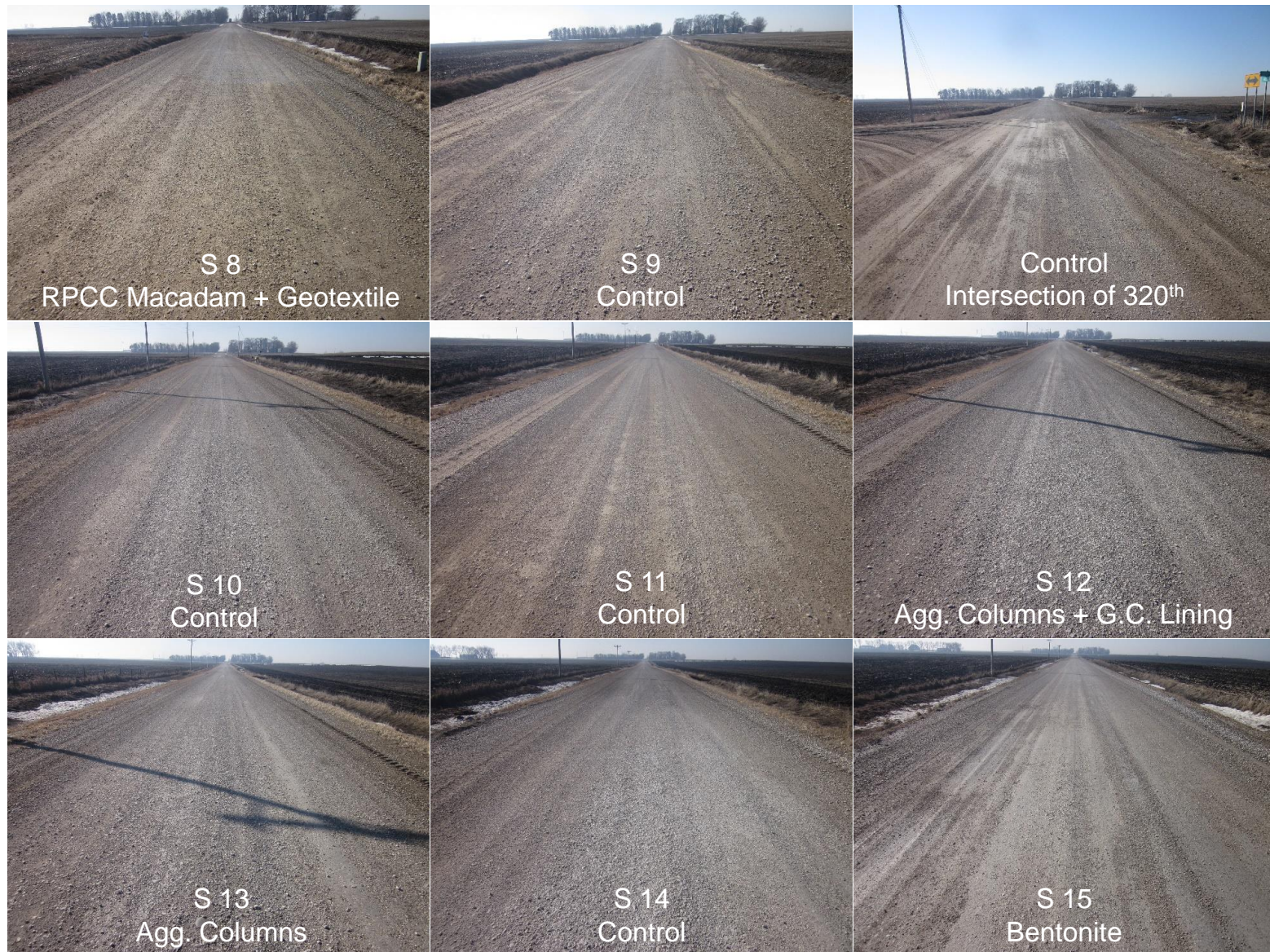


Figure 132. (continued). Survey photos of Vail Avenue demonstration sections (March 10, 2015)

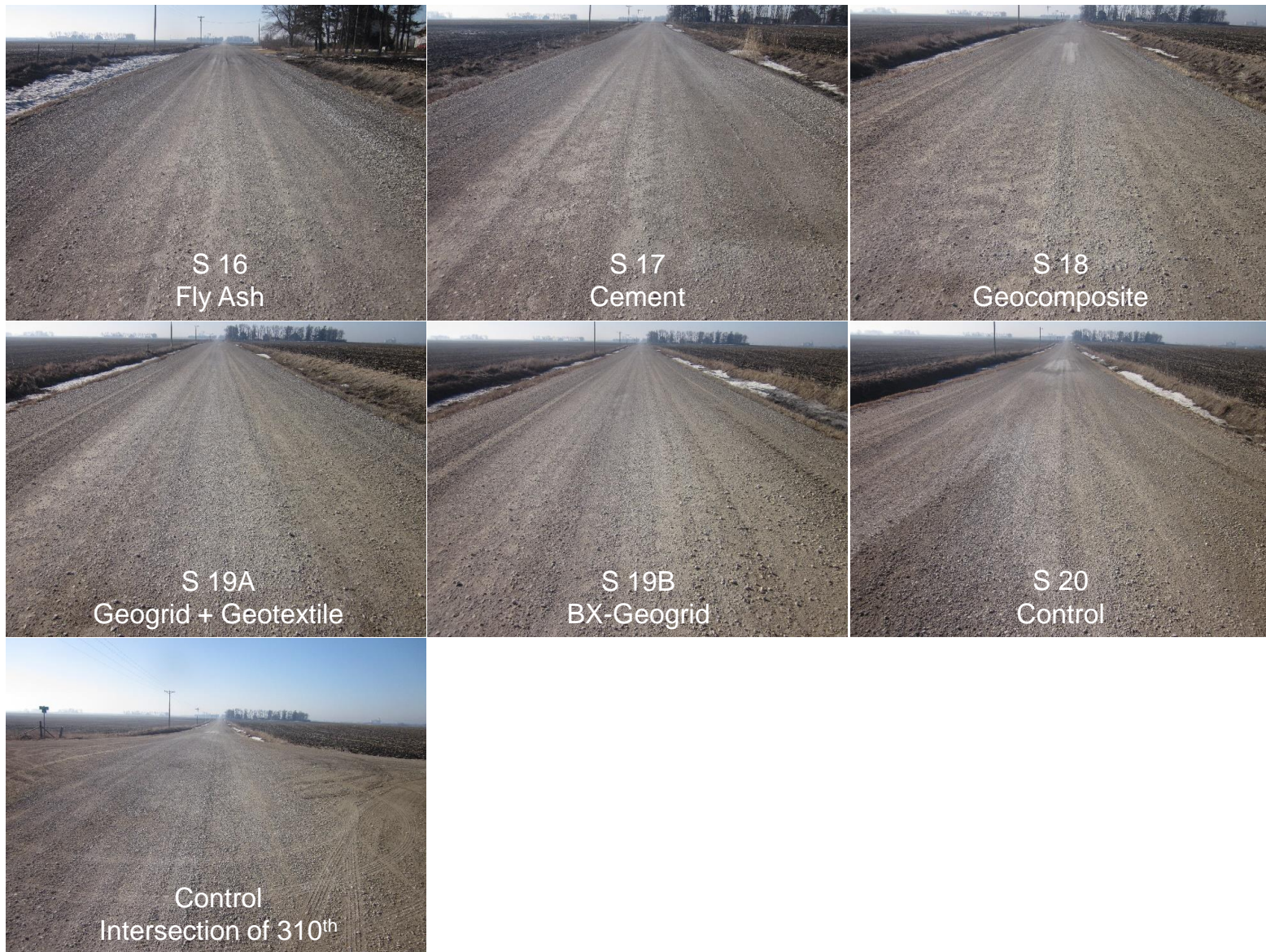


Figure 132. (continued). Survey photos of Vail Avenue demonstration sections (March 10, 2015)



Figure 133. Survey photos of Vail Avenue demonstration sections (April 21, 2015)



Figure 133. (continued). Survey photos of Vail Avenue demonstration sections (April 21, 2015)

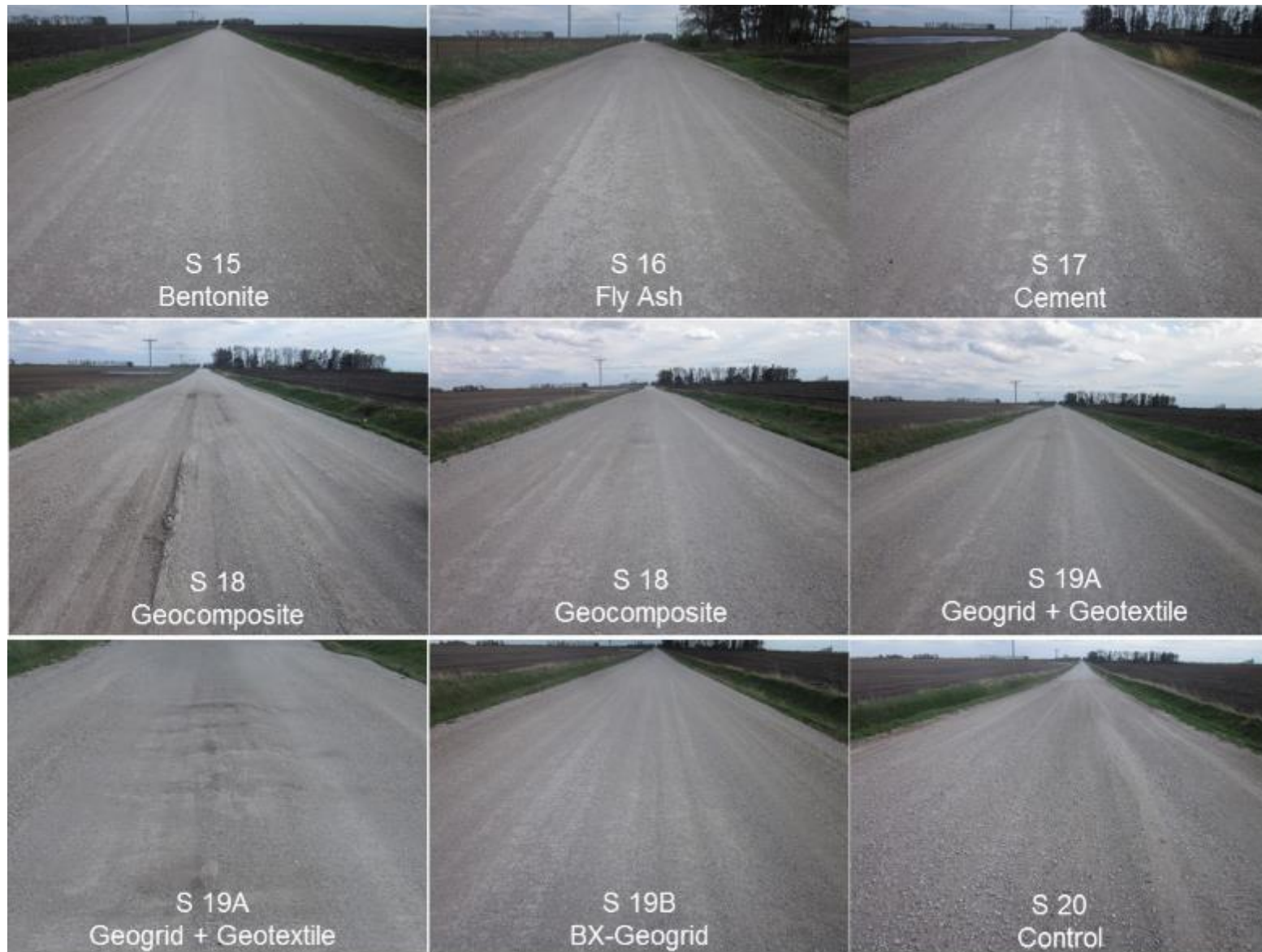


Figure 133. (continued). Survey photos of Vail Avenue demonstration sections (April 21, 2015)



Figure 134. Survey photos of Vail Avenue demonstration sections (May 19, 2015)



Figure 134. (continued). Survey photos of Vail Avenue demonstration sections (May 19, 2015)



Figure 134. (continued). Survey photos of Vail Avenue demonstration sections (May 19, 2015)